



UPPSALA  
UNIVERSITET

Examensarbete 30 hp  
Oktober 2016

# Tool wear in turning of titanium alloy Ti–6Al–4V

Challenges and potential solutions for crater  
wear, diffusion and chip formation

---

Erik Bamford





UPPSALA  
UNIVERSITET

Teknisk- naturvetenskaplig fakultet  
UTH-enheten

Besöksadress:  
Ångströmlaboratoriet  
Lägerhyddsvägen 1  
Hus 4, Plan 0

Postadress:  
Box 536  
751 21 Uppsala

Telefon:  
018 – 471 30 03

Telefax:  
018 – 471 30 00

Hemsida:  
<http://www.teknat.uu.se/student>

## Abstract

### Tool wear in turning of titanium alloy Ti–6Al–4V

---

Erik Bamford

Titanium alloys are major materials used in the airplane industry, and prospects show that airplane production will double in the next 20 years. Consequently, the demand for cutting tools for machining of titanium alloys will increase. The primary problem when machining titanium alloys is their low thermal conductivity. Crater wear is the main factor limiting tool life, and is generally caused by thermal diffusion due to high temperatures in the tool-chip interface.

This master's thesis was performed in collaboration with Sandvik Coromant, with the prospect to increase knowledge of how diffusion and chip formation influences crater wear progression. The aim was to study tool wear of cutting tools when turning Ti–6Al–4V. This was done by testing two different rake face geometries, both coated and uncoated, at cutting speeds of 30–115 m/min. Diffusion was investigated to learn about the impact it has on crater wear. Chips were examined to investigate chip formation and shear strain.

The coated modified rake face insert showed less crater wear only for the initial few seconds of machining. Uncoated inserts with a modified rake face showed higher diffusion rate and faster crater wear progression than did standard inserts. The standard inserts showed twice as long tool life as did the modified inserts. No significant differences in the chip formation mechanism were found between modified and standard inserts. Cracks were found within shear bands that were thinner than usual, which suggest that the generation of cracks allows less shear deformation.



***“Man is a tool-using animal. Without tools he is nothing, with tools he is all.”***

–Thomas Carlyle



## POPULÄRVETENSKAPLIG SAMMANFATTNING

### Verktygsslitage vid svarvning av titanlegeringen Ti-6Al-4V

*Utmaningar och möjliga lösningar för gropförslitning, diffusion och spånbildning*

Titanlegeringar används i stor utsträckning i flygplansindustrin, och prognoserna tyder på att flygplansproduktionen kommer att fördubblas under de kommande 20 åren. Följaktligen kommer efterfrågan på skärande verktyg för bearbetning av titan att öka. Några gemensamma fördelar med titanlegeringar är att de har låg densitet, hög styrka och är korrosionsbeständiga. Ett stort problem är dock att de har en mycket låg värmeförmedlingsförmåga, vilket gör att värmen koncentreras i skäreggen och leder till att skäreggen snabbt slits ut.

För att kunna forma ett arbetsmaterial måste skäret som bearbetar det vara hårdare. Vid svarvning av titanlegeringar används ofta skär utan beläggning tillverkade av en metall- och kerambaserad komposit av volframkarbid och kobolt. I andra skärprocesser använder man vanligtvis skärverktyg med skyddande ytskikt för att ytterligare reducera nötningshastigheten av det bearbetande skäret. Det finns fortfarande stora problem med att applicera tunna ytskikt på skär för svarvning i titanlegeringar eftersom beläggningen snabbt slits bort. En vanlig utslitningstyp vid svarvbearbetning är gropförslitning, vilket är den faktor som huvudsakligen påverkar verktygets livslängd vid konventionella skärhastigheter inom industrin. Gropförslitning orsakas av diffusion, det vill säga rörelse av atomer mellan det bearbetade materialet och skärverktyget, vilket orsakas av höga temperaturer i skäreggen. Detta leder till att bindningar mellan atomer försagas och att skärverktyget nöts ut. Det är således viktigt att undersöka denna nötningmekanism för att kunna utveckla nya skärande verktyg med längre livslängd.

Detta examensarbete utfördes i samarbete med Sandvik Coromant, ett världsledande företag som är specialiserade på skärverktyg för bearbetning i metaller. Syftet var att öka kunskapen om hur kemisk diffusion och spånbildning påverkar gropförslitning. Svarvtester genomfördes på ett cylinderformat ämne av titanlegeringen Ti-6Al-4V med skär

med och utan ytbeläggning vid skärhastigheter mellan 30–115 m/min. Eggen på de undersökta skären hade en modifierad spånsida, och jämfördes mot standardskär med en plan spånsida. Gropförslitningen undersöktes med mästinstrumentet Alicona för att få en tydlig bild av skärytans topografi, vilket visade hur ytan påverkats efter svarvning vid olika tidpunkter och skärhastigheter. Titan fastnar i gropen på skäret och diffusionen leder till att bitar avlägsnas från skärverktyget, vilket bidrar till förslitningsprocessen. Detta studerades genom att titta på tvärsnitt av skären med svepelektronmikroskop. Diffusionen av titan och kol studerades med elektronmikrosond för att mäta halten av titan och kol vid gränssnittet av titanskiktet och skärverktyget, samt för att undersöka skärets nötningshastighet.

Under bearbetningsprocessen bildas svinn i form av spånor. Tvärsnitt av spånor kan studeras för att få en inblick i hur spånbildningsprocessen påverkar gropförslitningen. Titanspånor har en segmenterad geometri, det vill säga att de är sågtandade. Interna spänningar under bearbetningsprocessen bidrar till att materialet skjuvas och kan avslöja hur materialet påverkas av deformationen under bearbetningen. Skjuvning är ett mått på hur mycket materialet deformeras utan volymförändring och uppkommer genom att två motsatta spänningar påfrestar materialet, vilket leder till att materialet töjs ut. Specifika dimensioner och vinklar i titanspåorna uppmättes med hjälp av ljusoptiskt mikroskop och graden av segmentering, segmentfrekvensen och skjuvningen i spåorna beräknades. Skjuvningen kan avbildas med ljusoptiskt- och svepelektronmikroskop och visar sig som smala skjuvningsband mellan segmenten. Energiröntgenspektroskop användes för att studera diffusion av partiklar från skärverktyg till titanspånor.

Tillämpning av beläggning på spånsidan av skärverktyget bidrog till en minskad kemisk diffusion, men beläggningen kan orsaka andra förslitningsmekanismer som påskyndar gropförslitning. Belagda skärverktyg med modifierad spånsida visade på en mindre gropförslitning de första sekunderna av bearbetning, vilket troligtvis beror på att beläggningen var kvar på en större yta än för standardskär. Skär utan beläggning med en modifierad spånsida visade högre diffusionshastighet och snabbare gropförslitningshastighet än standardskär. Mätning av fasförslitning visade att standardskär hade dubbelt så lång livslängd som modifierade skär. Förändringar i spånbildningen kan påverka gropförslitningen och bestäms genom att undersöka spångeometrin. Dock kunde inga signifikanta skillnader bekräftas mellan modifierade och standardskär.

## TABLE OF CONTENTS

<b>ABSTRACT .....</b>	<b>I</b>
<b>POPULÄRVETENSKAPLIG SAMMANFATTNING.....</b>	<b>V</b>
<b>ACKNOWLEDGEMENTS .....</b>	<b>XI</b>
<b>LIST OF ABBREVIATIONS.....</b>	<b>XII</b>
<b>LIST OF NOMENCLATURE.....</b>	<b>XIII</b>
<b>LIST OF FIGURES .....</b>	<b>XIV</b>
IN CHAPTER 1: INTRODUCTION .....	XIV
IN CHAPTER 2: THEORY .....	XIV
IN CHAPTER 3: LITERATURE REVEIW .....	XIV
IN CHAPTER 4: METHODOLOGY.....	XV
IN CHAPTER 5: RESULTS AND DISCUSSIONS .....	XV
IN APPENDIX B.....	XVI
IN APPENDIX C.....	XVI
IN APPENDIX D .....	XVI
IN APPENDIX F .....	XVII
IN APPENDIX G .....	XVII
IN APPENDIX H .....	XVII
<b>LIST OF TABLES.....</b>	<b>XVIII</b>
IN CHAPTER 1: INTRODUCTION .....	XVIII
IN CHAPTER 3: LITERATURE REVEIW.....	XVIII
IN CHAPTER 4: METHODOLOGY.....	XVIII
IN CHAPTER 5: RESULTS AND DISCUSSIONS .....	XVIII
IN APPENDIX A.....	XVIII
IN APPENDIX C.....	XIX
IN APPENDIX E .....	XIX
IN APPENDIX G .....	XIX
IN APPENDIX H .....	XIX
<b>LIST OF EQUATIONS .....</b>	<b>XX</b>

<b>CHAPTER 1 INTRODUCTION .....</b>	<b>1</b>
1.1 PROJECT BACKGROUND .....	1
1.1.1 HISTORY OF METAL MACHINING .....	2
1.1.2 APPLICATIONS AND COSTS OF TITANIUM ALLOYS .....	3
1.2 PROJECT DESIGN .....	3
1.2.1 PROBLEM STATEMENT .....	4
1.2.2 PROJECT OBJECTIVES AND ORGANIZATION.....	4
1.3 SCOPE OF THE PROJECT .....	5
<b>CHAPTER 2 THEORY .....</b>	<b>7</b>
2.1 TITANIUM MACHINING .....	7
2.1.1 MACHINABILITY OF TITANIUM AND ITS ALLOYS .....	7
2.1.2 LONGITUDINAL TURNING OPERATION.....	8
2.1.3 CLASSIFICATION OF TITANIUM ALLOYS .....	10
2.2 TOOL WEAR .....	11
2.2.1 BASICS OF DIFFUSION.....	12
2.2.2 CRATER WEAR.....	13
2.2.3 FLANK WEAR.....	14
2.2.4 TOOL LIFE.....	15
2.3 CHIP FORMATION .....	15
2.3.1 REASONS BEHIND CHIP SEGMENTATION.....	16
2.3.2 CATASTROPHIC SHEAR MODEL .....	17
2.3.3 DESCRIPTION OF CHIP GEOMETRY.....	19
2.3.4 CALCULATIONS REGARDING CHIP ANALYSIS.....	20
2.3.5 DEFINITIONS OF SHEAR STRESS AND SHEAR STRAIN.....	21
2.3.6 CALCULATIONS OF SHEAR STRAIN IN SHEAR-LOCALIZED CHIPS.....	21
2.4 ANALYTICAL METHODS .....	22
2.4.1 FOCUS VARIATION WITH ALICONA.....	23
2.4.2 LIGHT OPTICAL- AND STEREO MICROSCOPE.....	23
2.4.3 SCANNING ELECTRON MICROSCOPE .....	24
2.4.4 ELECTRON MICROPROBE ANALYZER .....	24
2.4.5 ENERGY-DISPERSIVE X-RAY SPECTROSCOPE .....	25
<b>CHAPTER 3 LITERATURE REVIEW.....</b>	<b>26</b>
3.1 PREVIOUS RESEARCH ON CRATER WEAR.....	27
3.2 PREVIOUS RESEARCH ON DIFFUSION WEAR .....	30
3.3 PREVIOUS RESEARCH ON CHIP FORMATION .....	32

<b>CHAPTER 4 METHODOLOGY .....</b>	<b>36</b>
4.1 TURNING TESTS .....	36
4.1.1 TURNING OPERATION SETUP.....	37
4.1.2 CUTTING PARAMETERS .....	37
4.1.2 CUTTING TOOLS .....	38
4.2 SAMPLE PREPARATION .....	38
4.3 WEAR CHARACTERIZATION .....	39
4.3.1 FOCUS VARIATION: CRATER WEAR PROGRESSION.....	40
4.3.2 SEM: FORMATION OF A TITANIUM BUILD-UP LAYER.....	41
4.3.3 EMA: DIFFUSION .....	41
4.3.4 STEREO MICROSCOPE: FLANK WEAR PROGRESSION.....	42
4.4 CHIP CHARACTERIZATION .....	43
4.4.1 LOM: CHIP GEOMETRY.....	43
4.4.2 EDS: DIFFUSION TO CHIP .....	44
4.4.3 EXCEL: STATISTICAL ANALYSIS OF VARIANCE ON CHIP PARAMETERS .....	44
<b>CHAPTER 5 RESULTS AND DISCUSSIONS .....</b>	<b>45</b>
5.1 WEAR CHARACTERIZATION .....	45
5.1.1 EFFECTS ON CRATER WEAR .....	45
5.1.2 IMPACT OF DIFFUSION AND TITANIUM BUILD-UP LAYER .....	48
5.1.3 FLANK WEAR AND TOOL LIFE.....	52
5.2 CHIP CHARACTERIZATION .....	54
5.2.1 GEOMETRICAL ANALYSIS OF CHIP FORMATION.....	54
5.2.2 SEGMENTATION FREQUENCY .....	57
5.2.3 SEGMENTATION- AND SHEAR ANGLES.....	58
5.2.4 EVOLUTION OF SHEAR STRAINS .....	60
5.2.5 DIFFUSION OF CUTTING TOOL PARTICLES INTO CHIPS.....	65
<b>CHAPTER 6 CONCLUSIONS AND RECOMMENDATIONS.....</b>	<b>66</b>
6.1 CONCLUSIONS .....	66
6.2 RECOMMENDATIONS .....	67
<b>REFERENCES .....</b>	<b>68</b>

<b>APPENDICES .....</b>	<b>76</b>
APPENDIX A1 – TURNING TEST DATA.....	76
APPENDIX A2 – TURNING TEST DATA (CONFIDENTIAL).....	78
APPENDIX B1 – SEM AND ALICONA IMAGES OF CRATER WEAR.....	79
APPENDIX B2 – SEM AND ALICONA IMAGES OF CRATER WEAR (CONFIDENTIAL).....	83
APPENDIX C1 – LINE SCAN ANALYSIS WITH EMA .....	84
APPENDIX C2 – POINT-TO-POINT ANALYSIS WITH EMA.....	107
APPENDIX D – IMAGES OF FLANK WEAR .....	124
APPENDIX E1 – CHIP GEOMETRY ( $D_O, P_O, \phi_{SEG}$ ) .....	126
APPENDIX E2 – CHIP GEOMETRY ( $T_{2MIN}, T_{2MAX}, G$ ) .....	129
APPENDIX E3 – CHIP GEOMETRY MEASUREMENTS ( $P_{SB}, \Delta_{SB}, P_{SEG}$ ) .....	135
APPENDIX F1 – DIFFERENCES BETWEEN COLLECTED CHIPS .....	136
APPENDIX F2 – SEM IMAGES OF COLLECTED CHIPS .....	140
APPENDIX G1 – CALUCULATIONS REGARDING CROSS-SECTIONS .....	142
APPENDIX G2 – ANALYSIS OF VARIATION AND CHIP STATISTICS .....	144
APPENDIX G3 – CALUCULATION OF THE SHEAR ANGLE .....	147
APPENDIX H – EDS ANALYSIS .....	148

## **ACKNOWLEDGEMENTS**

Firstly, I would like to express my sincere gratitude to my supervisor at Sandvik Coromant, Roland Bejjani, for all support throughout the work, and to the head of section, Johan Gullander, for the opportunity to perform my master's thesis at Sandvik Coromant. I want to acknowledge Christer Fahlgren, who was very helpful regarding polishing of titanium chips and SEM imaging; Karl-Olof Erixon, who performed the machining test; Elias Nyrot, who performed electron microprobe analysis; and Bo Lundberg, who performed energy-dispersive x-ray spectroscopy. I am also thankful for all help I got from other colleagues at Sandvik Coromant throughout the work. I am grateful to my subject reader Staffan Jacobson, examiner Erik Lewin and objector Emil Olsson at Uppsala University who gave suggestions for improvements on the thesis. Finally, I would like to give a special appreciation to my partner Lena Bergqvist who supported me during the work.

– Erik Bamford

## LIST OF ABBREVIATIONS

<b>ABBREVIATION</b>	<b>DEFINITION</b>
Al <sub>2</sub> O <sub>3</sub>	Aluminum Oxide
bcc	Body-centered cubic
BUE	Build-Up Edge
CNC	Computer Numerically Controlled
CVD	Chemical Vapor Deposition
EDS	Energy-Dispersive X-ray Spectroscopy
EMA	Electron Microprobe Analysis
hcp	Hexagonal close-packed
LOM	Light Optical Microscopy
MRS	Modified Rake Surface insert
PVD	Physical Vapor Deposition
SEM	Scanning Electron Microscopy
SI	Standard Insert
Ti-6Al-4V	Titanium alloy (6% Aluminum and 4% Vanadium)
TiCN	Titanium Carbo-Nitride
TiC	Titanium Carbide
TiN	Titanium Nitride
WC/Co	Tungsten Carbide/Cobalt
WDS	Wavelength-Dispersive X-ray Spectroscopy

## LIST OF NOMENCLATURE

<b>SYMBOL</b>	<b>DEFINITION</b>	<b>UNIT</b>
$\alpha$	Clearance/Relief angle	[°]
$\gamma$	Rake angle	[°]
$\gamma_e$	Engineering shear strain	-
$\gamma_c$	Shear strain in the adiabatic shear band	-
$\gamma_{sb}$	Total shear strain within the adiabatic shear band	-
$\gamma_{seg}$	Shear strain within the segment	-
$\delta_{sb}$	Shear band width	[μm]
$\kappa_r$	Entering angle	[°]
$\lambda_h$	Chip compression ratio	-
$\rho_{seg}$	Bulge angle	[°]
$\tau$	Shear stress	[N m <sup>-2</sup> ]
$\phi$	Shear angle	[°]
$\phi_{seg}$	Segmentation angle	[°]
$a_p = t_1$	Depth of cut	[mm]
$d$	Band spacing before upsetting phase	[μm]
$d_c$	Mean shear band spacing	[μm]
$D$	Diffusion coefficient	[m <sup>2</sup> s <sup>-1</sup> ]
$D_0$	Frequency factor	[s <sup>-1</sup> ]
$f_{seg}$	Segmentation frequency	[kHz]
$f_n$	Feed rate	[mm rev <sup>-1</sup> ]
$G$	Degree of segmentation	-
$J$	Diffusion flux	[kg m <sup>-2</sup> s <sup>-1</sup> ]
$K_T$	Maximum crater depth	[μm]
$p$	Pitch before upsetting phase	[μm]
$p_c$	Pitch, or Segment spacing	[μm]
$p_{sb}$	Shear band projection	[μm]
$Q$	Material removal rate	[m <sup>3</sup> s <sup>-1</sup> ]
$r$	Cutting ratio	-
$t_1 = a_p$	Depth of cut	[μm]
$t_2$	Average chip thickness	[μm]
$t_{2max}$	Maximum chip thickness	[μm]
$t_{2min}$	Minimum chip thickness	[μm]
$V_B$	Average flank wear	[μm]
$v_c$	Cutting speed	[m min <sup>-1</sup> ]
$v_{ch}$	Chip velocity	[m min <sup>-1</sup> ]

## LIST OF FIGURES

### **IN CHAPTER 1: INTRODUCTION**

FIGURE 1.1. DEVELOPMENT OF CUTTING TIME AND PRODUCTION RATE DURING THE LAST CENTURY .....	2
FIGURE 1.2. PROJECT DESIGN OF THE WORK IN THIS MASTER'S THESIS.....	3
FIGURE 1.3. FLOW CHART OVER THE PATHWAY FOR THE OBJECTIVE OF THIS MASTER'S THESIS PROJECT.....	4

### **IN CHAPTER 2: THEORY**

FIGURE 2.1. SCHEMATIC ILLUSTRATION OF A CUTTING TOOL IN ACTION .....	8
FIGURE 2.2. SCHEMATIC ILLUSTRATION OF THE SETUP IN THE TURNING CENTER MACHINE. ....	9
FIGURE 2.3. THE HCP AND BCC CRYSTAL STRUCTURES .....	10
FIGURE 2.4. THE BEHAVIORS OF TOOL WEAR MECHANISMS .....	11
FIGURE 2.5. THE DIFFUSION FLUX OF TITANIUM IN THE TOOL-CHIP INTERFACE.....	13
FIGURE 2.6. DEFINITION OF CRATER DEPTH MEASUREMENT. ....	14
FIGURE 2.7. DEFINITION OF FLANK WEAR MEASUREMENTS. ....	14
FIGURE 2.8. ADIABATIC SHEAR BANDS AND THE SECONDARY SHEAR ZONE IN A SERRATED CHIP. ....	16
FIGURE 2.9. STAGES DURING THE UPSETTING PHASE OF CHIP FORMATION.....	18
FIGURE 2.10. HOW GRAINS ELONGATE IN THE REGION NEAR THE ADIABATIC SHEAR BAND.....	18
FIGURE 2.11. GEOMETRIC PARAMETERS DESCRIBING CHIP DIMENSIONS IN THE CHIP.....	19
FIGURE 2.12. DEFINITION OF SHEAR STRAIN.....	21

### **IN CHAPTER 3: LITERATURE REVIEW**

FIGURE 3.1. TREND OF MATERIAL REMOVAL RATES, FROM 1980 TO PRESENT.....	26
FIGURE 3.2. TRENDS OF CHIP FORMATION, ADIABATIC SHEAR BANDS, CHIP MORPHOLOGY AND CHIP FORMATION SIMULATIONS, FROM 1980 TO PRESENT .....	33

## IN CHAPTER 4: METHODOLOGY

FIGURE 4.1. EXPERIMENTAL SETUP IN THE TURNING MACHINE .....	37
FIGURE 4.2. HOT MOUNTED BAKELITE PELLETS WITH CROSS-SECTIONS OF INSERTS AND CHIPS.....	39
FIGURE 4.3. METHOD OF MEASUREMENTS OF CRATER AREA IN ALICONA .....	40
FIGURE 4.4. TITANIUM BUILD-UP LAYER AND THE POSITION WHERE EMA LINE SCANS AND POINT-TO-POINT ANALYSIS WERE EXECUTED .....	41

## IN CHAPTER 5: RESULTS AND DISCUSSIONS

FIGURE 5.1. RESULTS OF CRATER DEPTH MEASUREMENT .....	46
FIGURE 5.2. CROSS-SECTIONAL SEM IMAGE OF OF CRATER WEAR.....	46
FIGURE 5.3. RESULTS OF CRATER AREA MEASUREMENT .....	47
FIGURE 5.4. EMA LINE SCANS (COATED, 75 M/MIN AFTER 3 S) .....	48
FIGURE 5.5. EMA LINE SCANS (UNCOATED, 75 M/MIN AFTER 60 S). ....	49
FIGURE 5. 6. EMA LINE SCANS (UNCOATED, 90 M/MIN AFTER 40 S).....	49
FIGURE 5.7. EMA POINT-TO-POINT ANALYSIS (UNCOATED, 90 M/MIN AFTER 40 S).....	50
FIGURE 5.8. EMA POINT-TO-POINT ANALYSIS (UNCOATED, 115 M/MIN AFTER 20/40 S).....	50
FIGURE 5.9. RESULTS OF AVERAGE FLANK WEAR MEASUREMENT. ....	52
FIGURE 5.10. TOOL LIFE INVESTIGATION. ....	53
FIGURE 5.11. MEAN SHEAR BAND SPACING .....	55
FIGURE 5.12. SEGMENT SPACING .....	55
FIGURE 5.13. DEGREE OF SEGMENTATION .....	56
FIGURE 5.14. COMPARISON OF TWO DIFFERENT CHIPS FROM THE SAME CUTTING CONDITIONS .....	56
FIGURE 5.15. CHIP SEGMENTATION FREQUENCY .....	57
FIGURE 5.16. COMPARISON OF CHIP SEGMENTATION FREQUENCY AT DIFFERENT CUTTING SPEEDS AND FEEDS .....	58
FIGURE 5.17. SEGMENTATION ANGLE.....	58
FIGURE 5.18. COMPARISON OF SEGMENTATION ANGLE AGAINST SHEAR ANGLE FOR STANDARD INSERTS .....	59
FIGURE 5.19. COMPARISONS OF SEGMENTATION ANGLE AGAINST SHEAR ANGLE FOR MODIFIED INSERTS.....	59
FIGURE 5.20. CHIPS COLLECTED FROM MACHINING TESTS.....	60
FIGURE 5.21. SHEAR STRAIN WITHIN THE SEGMENT .....	61
FIGURE 5.22. SHEAR STRAIN WITHIN THE ADIABATIC SHEAR BAND. ....	61
FIGURE 5.23. TOTAL SHEAR STRAIN WITHIN THE ADIABATIC SHEAR BAND.....	62
FIGURE 5.24. COMPARISON OF ADIABATIC SHEAR BANDS OF UNCOATED STANDARD INSERTS .....	62
FIGURE 5.25. COMPARISON OF ADIABATIC SHEAR BANDS OF UNCOATED MODIFIED INSERTS .....	63
FIGURE 5.26. THE RELATIONSHIP BETWEEN MEAN SHEAR BAND SPACING AND SHEAR STRAIN WITHIN SEGMENTS .....	64

## **IN APPENDIX B**

FIGURE B1. SAMPLE A4: COATED SI AT CUTTING SPEED OF 30 M/MIN AFTER 60 S .....	79
FIGURE B2. SAMPLE C2: COATED SI AT CUTTING SPEED OF 75 M/MIN AFTER 3 S. ....	80
FIGURE B3. SAMPLE E2: UNCOATED SI AT CUTTING SPEED OF 75 M/MIN AFTER 60 S.....	80
FIGURE B4. SAMPLE G3: UNCOATED SI AT CUTTING SPEED OF 90 M/MIN AFTER 40 S. ....	81
FIGURE B5. SAMPLE I1: UNCOATED SI AT CUTTING SPEED OF 115 M/MIN AFTER 3 S. ....	81
FIGURE B6. SAMPLE I3: UNCOATED SI AT CUTTING SPEED OF 115 M/MIN AFTER 40 S.....	82

## **IN APPENDIX C**

FIGURE C1. TEST G3, LINE 1. SPECTRA FROM EMA POINT-TO-POINT ANALYSIS .....	108
FIGURE C2. TEST G3, LINE 1. SPECTRA FROM EMA POINT-TO-POINT ANALYSIS .....	109
FIGURE C3. TEST G3, LINE 2. SPECTRA FROM EMA POINT-TO-POINT ANALYSIS .....	110
FIGURE C4. TEST G3, LINE 2. SPECTRA FROM EMA POINT-TO-POINT ANALYSIS .....	111
FIGURE C5. TEST H3, LINE 1. SPECTRA FROM EMA POINT-TO-POINT ANALYSIS .....	112
FIGURE C6. TEST H3, LINE 1. SPECTRA FROM EMA POINT-TO-POINT ANALYSIS .....	113
FIGURE C7. TEST H3, LINE 2. SPECTRA FROM EMA POINT-TO-POINT ANALYSIS .....	114
FIGURE C8. TEST H3, LINE 2. SPECTRA FROM EMA POINT-TO-POINT ANALYSIS .....	115
FIGURE C9. TEST I3, LINE 1. SPECTRA FROM EMA POINT-TO-POINT ANALYSIS .....	116
FIGURE C10. TEST I3, LINE 1. SPECTRA FROM EMA POINT-TO-POINT ANALYSIS.....	117
FIGURE C11. TEST I3, LINE 2. SPECTRA FROM EMA POINT-TO-POINT ANALYSIS. ....	118
FIGURE C12. TEST I3, LINE 2. SPECTRA FROM EMA POINT-TO-POINT ANALYSIS. ....	119
FIGURE C13. TEST J3, LINE 1. SPECTRA FROM EMA POINT-TO-POINT ANALYSIS.....	120
FIGURE C14. TEST J3, LINE 1. SPECTRA FROM EMA POINT-TO-POINT ANALYSIS.....	121
FIGURE C15. TEST J3, LINE 2. SPECTRA FROM EMA POINT-TO-POINT ANALYSIS.....	122
FIGURE C16. TEST J3, LINE 2. SPECTRA FROM EMA POINT-TO-POINT ANALYSIS.....	123

## **IN APPENDIX D**

FIGURE D1. FLANK WEAR PROGRESSION OF A1–4 (SI) TO THE LEFT AND B1–4 (MRS) TO THE RIGHT AT 1, 3, 10 AND 60 S .....	124
FIGURE D2. FLANK WEAR PROGRESSION OF C1–4 (SI) TO THE LEFT AND D1–4 (MRS) TO THE RIGHT AT 1, 3, 10 AND 60 S .....	124
FIGURE D3. FLANK WEAR PROGRESSION OF E1–2 (SI) TO THE LEFT AND F1–2 (MRS) TO THE RIGHT AT 30 AND 60 S .....	125
FIGURE D4. FLANK WEAR PROGRESSION OF G1–3 (SI) TO THE LEFT AND H1–3 (MRS) TO THE RIGHT AT 10, 20 AND 40 S .....	125
FIGURE D5. FLANK WEAR PROGRESSION OF I1–3 (SI) TO THE LEFT AND J1–3 (MRS) TO THE RIGHT AT 3, 5, 20 AND 40 S. ....	125

## IN APPENDIX F

FIGURE F1. DIFFERENCES BETWEEN THE TWO COLLECTED CHIPS FOR RESPECTIVE TEST SAMPLE, FOR $D_C$ , $P_C$ , $\phi_{SEG}$ AND $G$ .....	136
FIGURE F2. LOM IMAGES OF DIFFERENT CHIPS FROM CVD (SI) AT 30 M/MIN CUTTING SPEED. ....	136
FIGURE F3. LOM IMAGES OF DIFFERENT CHIPS FROM CVD (MRS) AT 30 M/MIN CUTTING SPEED.....	137
FIGURE F4. LOM IMAGES OF DIFFERENT CHIPS FROM CVD (SI) AT 75 M/MIN CUTTING SPEED. ....	137
FIGURE F5. LOM IMAGES OF DIFFERENT CHIPS FROM CVD (MRS) AT 75 M/MIN CUTTING SPEED.....	137
FIGURE F6. LOM IMAGES OF DIFFERENT CHIPS FROM U (SI) AT 75 M/MIN CUTTING SPEED .....	138
FIGURE F7. LOM IMAGES OF DIFFERENT CHIPS FROM U (MRS) AT 75 M/MIN CUTTING SPEED .....	138
FIGURE F8. LOM IMAGES OF DIFFERENT CHIPS FROM U (SI) AT 90 M/MIN CUTTING SPEED .....	138
FIGURE F9. LOM IMAGES OF DIFFERENT CHIPS FROM U (MRS) AT 90 M/MIN CUTTING SPEED .....	139
FIGURE F10. SEM IMAGES OF CHIPS OF CVD (SI) TO THE LEFT AND CVD (MRS) TO THE RIGHT AT 30 M/MIN. ....	140
FIGURE F11. SEM IMAGES OF CHIPS OF CVD (SI) TO THE LEFT AND CVD (MRS) TO THE RIGHT AT 75 M/MIN. ....	140
FIGURE F12. SEM IMAGES OF CHIPS OF U (SI) TO THE LEFT AND U (MRS) TO THE RIGHT AT 75 M/MIN .....	141
FIGURE F13. SEM IMAGES OF CHIPS OF U (SI) TO THE LEFT AND U (MRS) TO THE RIGHT AT 90 M/MIN .....	141

## IN APPENDIX G

FIGURE G1. SCHEMATIC ILLUSTRATION OF THE RAKE FACE CRATER .....	142
FIGURE G2. DISTRIBUTION OF DATA FOR $D_C$ , $P_C$ , $\phi_{SEG}$ AND $G$ .....	146

## IN APPENDIX H

FIGURE H1. EDS ANALYSIS OF THE BACK SIDE OF THE CHIPS EIGHT CHIPS AT DIFFERENT CUTTING CONDITIONS. ....	149
---	-----

## **LIST OF TABLES**

### **IN CHAPTER 1: INTRODUCTION**

TABLE 1.1. LIMITATIONS OF MACHINING TEST CUTTING TOOLS .....	6
TABLE 1.2. LIMITATIONS OF MACHINING TEST CUTTING CONDITION.....	6

### **IN CHAPTER 3: LITERATURE REVIEW**

TABLE 3.1. WEAR MECHANISMS AND WEAR TYPES AT DIFFERENT CUTTING CONDITIONS (1) .....	28
TABLE 3.2. WEAR MECHANISMS AND WEAR TYPES AT DIFFERENT CUTTING CONDITIONS (2). ....	29

### **IN CHAPTER 4: METHODOLOGY**

TABLE 4.1. ELEMENTAL COMPOSITION OF Ti–6Al–4V FROM TIMET .....	36
TABLE 4.2. PROPERTIES OF Ti–6Al–4V FROM TIMET .....	36
TABLE 4.3. CUTTING CONDITIONS DURING MACHINING TESTS .....	37
TABLE 4.4. DIVISION OF MACHINING TESTS .....	38
TABLE 4.5. ANALYTICAL METHODS AND THE REASONS FOR ANALYSIS. ....	40
TABLE 4.6. DISTANCECE BETWEEN ANALYZED POSITION IN THE EMA POINT-TO-POINT ANALYSIS. ....	42

### **IN CHAPTER 5: RESULTS AND DISCUSSIONS**

TABLE 5.1. RESULTS FROM EDS ANALYSIS .....	65
--	----

### **IN APPENDIX A**

TABLE A1. TURNING TEST DATA, MEASUREMENTS OF $V_B$ AND $K_T$ , AND METHODS OF ANALYSIS .....	76
TABLE A2. TURNING TEST DATA, MEASUREMENTS OF $V_B$ AND $K_T$ , AND METHODS OF ANALYSIS .....	77

## IN APPENDIX C

TABLE C1. DATA FROM EMA LINE SCAN OF SAMPLE C2 AND D2 REGARDING TITANIUM.....	84
TABLE C2. DATA FROM EMA LINE SCAN OF SAMPLE C2 AND D2 REGARDING CARBON.....	88
TABLE C3. DATA FROM EMA LINE SCAN OF SAMPLE E2 AND E2 REGARDING TITANIUM .....	92
TABLE C4. DATA FROM EMA LINE SCAN OF SAMPLE E2 AND F2 REGARDING CARBON.....	96
TABLE C5. DATA FROM EMA LINE SCAN OF SAMPLE G3 AND H3 REGARDING TITANIUM .....	100
TABLE C6. DATA FROM EMA LINE SCAN OF SAMPLE G3 AND H3 REGARDING CARBON. ....	103

## IN APPENDIX E

TABLE E1. MEAN VALUES, SD, MIN AND MAX VALUES CALCULATED FROM THE $D_c$ DATA SET .....	126
TABLE E2. MEAN VALUES, SD, MIN AND MAX VALUES CALCULATED FROM THE $P_c$ DATA SET.....	126
TABLE E3. MEAN VALUES, SD, MIN AND MAX VALUES CALCULATED FROM THE $\phi_{SEG}$ DATA SET.....	126
TABLE E4. RAW DATA OF $D_c$ , $P$ , AND $\phi_{SEG}$ , FROM LOM MEASUREMENTS .....	127
TABLE E5. MEAN VALUES, SD, MIN AND MAX VALUES CALCULATED FROM THE $G$ DATA SET.....	129
TABLE E6. RAW DATA OF $T_{2MAX}$ AND $T_{2MIN}$ , TOGETHER WITH THE CALCULATED VALUES OF $G$ FROM LOM MEASUREMENTS .....	129
TABLE E7. SHEAR BAND PROJECTION MEASUREMENTS .....	135
TABLE E8. SHEAR BAND WIDTH MEASUREMENTS .....	135
TABLE E9. BULGE ANGLE MEASUREMENTS .....	135

## IN APPENDIX G

TABLE G1. HEIGHT MEASUREMENT OF INSERT PELLETS.....	143
TABLE G2. HEIGHT MEASUREMENT OF CHIP PELLETS.....	143
TABLE G3. F-TESTS OF MEASURED GEOMETRICAL PARAMETERS AND CALCULATED SHEARS.....	144
TABLE G4. F-TESTS OF MEASURED GEOMETRICAL PARAMETERS AND CALCULATED SHEARS.....	144
TABLE G5. T-TESTS OF MEASURED GEOMETRICAL PARAMETERS AND CALCULATED SHEARS .....	145
TABLE G6. T-TESTS OF MEASURED GEOMETRICAL PARAMETERS AND CALCULATED SHEARS .....	145
TABLE G7. ANOVAs OF MEASURED GEOMETRICAL PARAMETERS AND CALCULATED SHEARS .....	145

## IN APPENDIX H

TABLE H1. RESULTS IN ATOMIC PERCENT FROM EDS ANALYSIS OF THE BACK SIDE OF THE CHIPS .....	148
---	-----

## LIST OF EQUATIONS

EQ. 1. MATERIAL REMOVAL RATE.....	8
EQ. 2. FICK'S FIRST LAW .....	12
EQ. 3. FICK'S SECOND LAW.....	12
EQ. 4. DIFFUSION FLUX .....	13
EQ. 5. MERCHANT'S EQUATION.....	15
EQ. 6. CRITERIA FOR CATASTROPHIC THERMOPLASTIC SHEAR.....	17
EQ. 7. AVERAGE CHIP THICKNESS .....	20
EQ. 8. DEGREE OF SEGMENTATION.....	20
EQ. 9. SEGMENTATION FREQUENCY.....	20
EQ. 10. CUTTING RATIO (SHEAR ANGLE) .....	20
EQ. 11. CUTTING RATIO (SEGMENTATION ANGLE) .....	20
EQ. 12. SHEAR STRESS .....	21
EQ. 13. ENGINEERING SHEAR STRAIN .....	21
EQ. 14. SHEAR STRAIN WITHIN SEGMENTS (SEGMENTATION ANGLE=CONSTANT) .....	22
EQ. 15. SHEAR STRAIN WITHIN SEGMENTS (SEGMENTATION ANGLE $\neq$ CONSTANT) .....	22
EQ. 16. CHIP COMPRESSION RATIO .....	22
EQ. 17. CONSTANT C .....	22
EQ. 18. SHEAR STRAIN IN THE ADIABATIC SHEAR BANDS.....	22
EQ. 19. TOTAL SHEAR STRAIN IN ADIABATIC SHEAR BANDS.....	22
EQ. 20. MOSELEY'S LAW .....	24
EQ. 21. SHEAR ANGLE (RAKE ANGLE=0) .....	44
EQ. 22. SHEAR ANGLE (RAKE ANGLE $\neq$ 0) .....	44
EQ. 23. CALCULATIONS REGARDING CROSS-SECTIONS (1) .....	142
EQ. 24. CALCULATIONS REGARDING CROSS-SECTIONS (2) .....	142

## **CHAPTER 1**

### **INTRODUCTION**

This master's thesis was made in collaboration with Sandvik Coromant, a world leading manufacturer and supplier of tools for metal cutting. In order to survive in the global market today, manufacturers have to keep up with the rapid development of new products and product solutions with superior properties. Therefore, it is important for Sandvik Coromant to continually carry out research on cutting tools to further improve tool life, to remain in the market and gain more market shares.

The purpose with this master's thesis was to study tool wear of cutting tools used to machine the common titanium alloy Ti–6Al–4V. This was done by testing two different rake face geometries, both coated and uncoated. Testing was performed by turning, at different cutting speeds and times, and chips were also studied.

#### **1.1 PROJECT BACKGROUND**

Titanium alloys are major materials used in the airplane industry. Forecasts predict that the aircraft fleet will double from 21,600 to 43,560 in less than 20 years, demanding the production of 38,050 new airplanes worldwide during this period [1], which is an average of roughly 2,000 units per year. However, the annual aircraft production was only around 1,500 in 2014 [2], so if this goal is to be achieved, the production has to increase substantially. This will certainly increase the demand for cutting tools made for titanium machining.

### 1.1.1 HISTORY OF METAL MACHINING

The history of metal processing extends far back to the inception of firearm production, but the key advancements in metal cutting came with the development of the steam engine in the 1760s [3]. During the nineteenth century, machines were belt- or hand-driven, and therefore very slow, until electrification of industries was introduced. The ongoing technological revolution definitely helped to improve the cutting process.

Taylor, sometimes called the father of industrial engineering and scientific management [4], introduced his new cutting tool in the early twentieth century. It operated in, at that time, extreme conditions: 40 m/min cutting speed, 1.6 mm feed and 4.8 mm cutting depth; and surprisingly remained sharp [5].

Further improvement of cutting tools and the introduction of automatic machinery, i.e. the computer numerically controlled (CNC) machine, which has up to two times as powerful engines as mechanically driven manually operated machines, paved the way to an enormous reduction in cutting time for machining operations [6]. The cutting time has reduced for the same turning operation during the twentieth century and is illustrated in Fig 1.1 [7]. The production rate of a certain component is also presented in Fig. 1.1 [5].

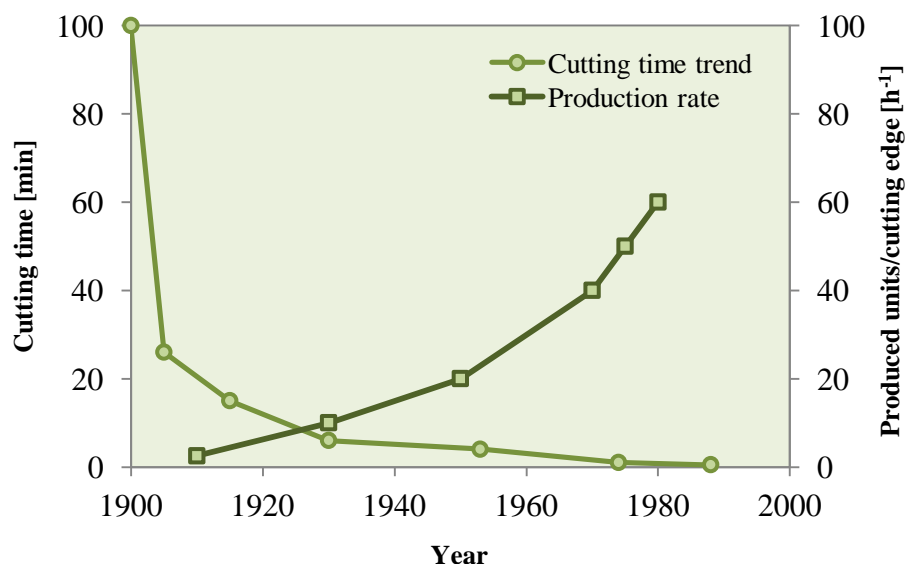


**Figure 1.1.** Development of cutting time, and production rate (i.e. produced components per cutting edge and hour) of turning operations, during the twentieth century [5,7].

### 1.1.2 APPLICATIONS AND COSTS OF TITANIUM ALLOYS

Titanium was discovered in 1790, although it was first purified in the early twentieth century, and has been commonly used in industry for the last 60 years [8]. Typical applications of titanium alloys are: gas turbine engines, compressor blades and landing gears in aerospace industry, subsea and chemical processing equipment, and orthopedic implants in biomedical industry. They are typically selected due to their low density, high strength, toughness and resistance to corrosion. [8–9] The density of titanium is 60% of that of steels or nickel-based alloys, and is therefore exceptional for use in the aerospace industry. However, the costs of titanium are comparable to other superalloys and around four times as high as the costs of stainless steels. [8] In 2005, 70% of all superalloys, including titanium alloys, were used in aerospace industry [10].

Many factors are involved in the total cost of a final product, such as workpiece material, cutting tool inserts and holders, the machining process, electricity, cutting fluids, reparations, and staff. Most of these costs may be hard to minimize, but according to Ezugwu [10], up to 20% of machining costs could be saved if correct cutting tools and cutting conditions are applied. Jiang et al. [11] claim that the machining cost component represents a minimum of 30% of the final product cost, and speculates that it could be up to 50% for difficult-to-cut materials. This emphasizes the importance of developing and improving cutting tools, especially for difficult-to-cut materials.

## 1.2 PROJECT DESIGN

The project is designed as shown in Fig. 1.2, which schematically illustrates the procedure, from research to thesis writing. All graphic illustrations in this master's thesis were made by the author.

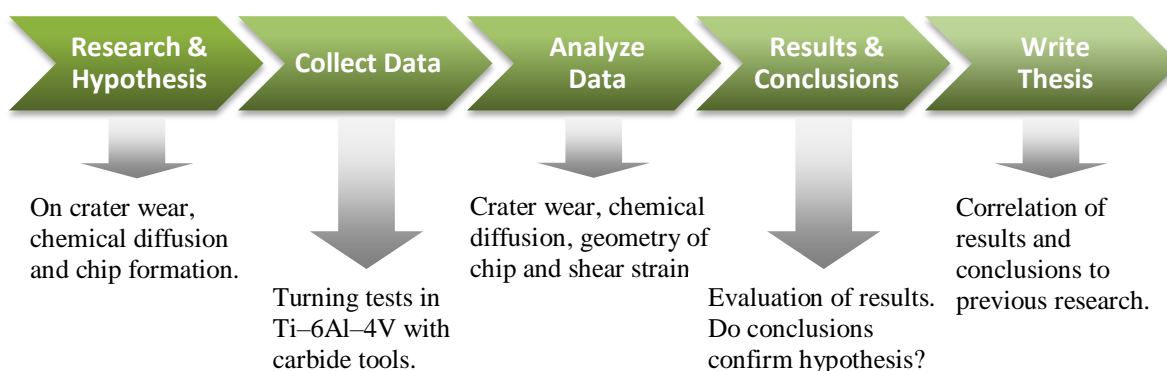


**Figure 1.2.** Project design of the work in this master's thesis.

### 1.2.1 PROBLEM STATEMENT

In general, tool wear needs to be controlled and reduced, in order to increase tool life and, consequently, minimize production costs. Crater wear on the rake surface is one of the major tool wear types when turning titanium alloys, and is often the limiting factor at cutting speeds between 60 and 120 m/min [12].

The contributor to this type of wear is mainly diffusion, which is located at the interface of the adhered titanium build-up layer and cutting tool insert. Another mechanism that affects the wear progression is chip formation, due to the fact that the interaction between chip and tool generates the crater. By investigating these two mechanisms, crater wear can be understood and controlled.

### 1.2.2 PROJECT OBJECTIVES AND ORGANIZATION

The main objective for this work was to investigate diffusion in the crater wear region and how to control the wear mechanism, as well as study the geometry and shear strain in titanium chips. A newly developed topography was investigated and compared against references at different cutting speeds. The modified rake surface was located in the crater wear region at the cutting edge of the cutting tool insert. Chip geometry, adiabatic shear bands and shear strain were believed to provide information about the chip formation mechanism. The organization and pathway of the thesis is schematically illustrated in Fig. 1.3.

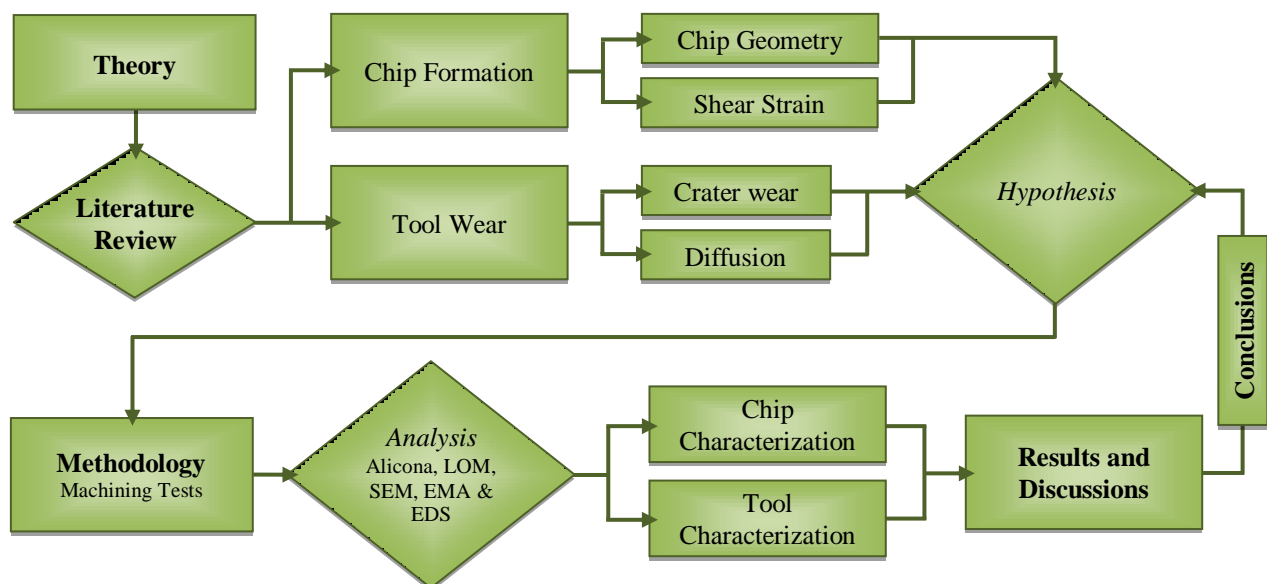


**Figure 1.3.** Systematic flow chart over the pathway for the objective of this master's thesis project.

The thesis is separated into six chapters, highlighted in bold. The theory chapter explains titanium machining, tool wear, chip formation and employed analytical methods. The literature review chapter presents previous research on crater wear, diffusion wear and chip formation. The methodology chapter explains the procedure of turning tests, sample preparation, as well as wear and chip characterizations. The results and discussions chapter presents and discusses the results from the wear and chip characterizations.

***Aims of this master's thesis:***

- Investigate how diffusion affects crater wear progression when turning the common titanium alloy Ti–6Al–4V.
- Investigate changes in titanium chips, relate them to the chip formation mechanism, and correlate them to crater wear progression.

***Research questions:***

- How does the modified rake surface affect crater wear in comparison to standard inserts, and does it reduce diffusion?
- Is there a difference in the chip formation mechanism between modified and standard inserts, and does it affect crater wear progression?

***Hypothesis:***

- The modified rake surface reduces diffusion and crater wear by altering the chip flow on the rake face of the cutting tool.

### **1.3 SCOPE OF THE PROJECT**

The scope of this master's thesis will be limited to the investigation of tool wear in external longitudinal turning of Ti–6Al–4V, focusing on crater wear, diffusion, chip formation, shear strain and chip geometry. The machining test cutting conditions are presented in Table 1.1, and a more detailed description of cutting tools, workpiece material and coolant is presented in Table 1.2. Standard inserts 29117 and 29119 are references.

**Table 1.1.** Machining test cutting conditions.

Cutting parameters	Cutting conditions
Cutting speeds ( $v_c$ )	30 m/min
	75 m/min
	90 m/min
	115 m/min
Feed rate ( $f_n$ )	0.2 mm/rev
Depth of cut ( $a_p, t_l$ )	2.0 mm
Entering angle ( $\kappa_r$ )	91°

**Table 1.2.** Machining test cutting tools, workpiece material and coolant.

	Specifications
<b>Cutting tool geometry</b>	TCMW16T308 Rake angle ( $\gamma$ ) = 0° Clearance angle ( $\alpha$ ) = 7°
<b>Substrate grade</b>	WC/Co
<b>Coating</b>	1. CVD: TiN, Al <sub>2</sub> O <sub>3</sub> , and TiCN 2. U: Uncoated
<b>Rake face topography</b>	1. Standard insert (SI) 2. Modified rake surface <sup>1</sup> (MRS)
<b>Inserts</b>	29117 = CVD (SI) 29118 = CVD (MRS) 29119 = U (SI) 29120 = U (MRS)
<b>Cutting tool holder</b>	C5-STGCL-35060-16
<b>Workpiece material</b>	Ti–6Al–4V
<b>Coolant</b>	Water/oil based emulsion (7%)

<sup>1</sup> Invention disclosure for patent protection. A detailed description of the invented topography is found in Appendix A2, only shown for employees at Sandvik.

## CHAPTER 2

### THEORY

This chapter presents some history and theories of titanium machining, tool wear, chip formation and some analytical methods.

#### 2.1 TITANIUM MACHINING

Machining is a term used to describe material removal in any form. Some examples of conventional cutting processes used when machining titanium alloys are turning, milling, drilling, threading and boring. One of the most common machining processes is turning, which can be separated into external and internal turning, and further divided into longitudinal turning, profiling and facing, depending on the application. This work will focus on external longitudinal turning. A schematic illustration of a cutting tool in action is shown in Fig. 2.1, where  $\gamma$  is the rake angle and  $\alpha$  is the clearance angle.

##### 2.1.1 MACHINABILITY OF TITANIUM AND ITS ALLOYS

There are many variables involved in the machining of metals. Workpiece conditions (e.g. chemical composition, hardness, microstructure), physical properties (e.g. thermal softening, thermal conductivity, work hardening), and cutting conditions (e.g. cutting parameters, tool geometry, tool material) affect the machinability of the workpiece material, in combination or independently [13]. Thermal softening is a process where the material loses its strength at elevated temperatures, and work hardening (i.e. strain hardening) is the hardening process that occurs in the machined material when it is plastically deformed [9]. Thermal softening and work hardening operate simultaneously in the workpiece material, and it has been reported that work hardening reduces the thermal softening effect [14].

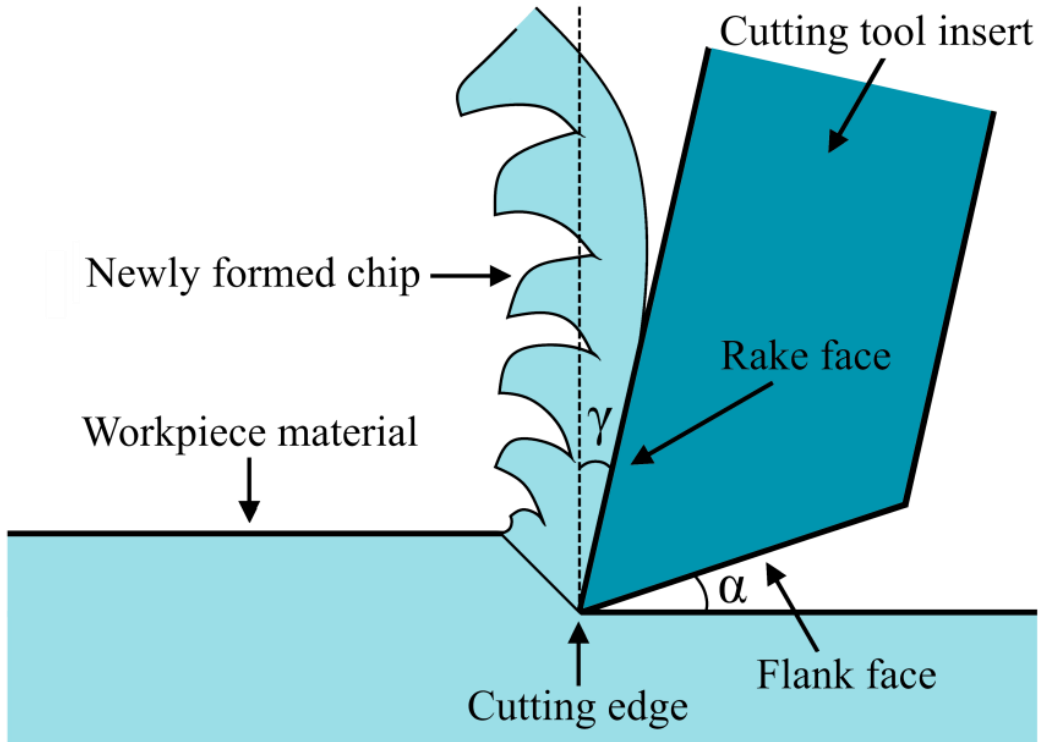


**Figure 2.1.** Cross-sectional illustration of a cutting tool in action, where  $\gamma$  is the rake angle and  $\alpha$  is the clearance angle.

Titanium is a difficult-to-cut material due to its low thermal conductivity and modulus of elasticity, high chemical reactivity and temperature strength [9,15–17]. Low thermal conductivity implies that the generated heat slowly conducts through the material. Young's modulus of elasticity ( $E$ ), is defined as the relationship between stress and strain, and  $E$  for titanium alloys is roughly half of that of most steels [18]. Titanium alloys are chemically stable at low temperatures, but if the temperature surpasses 500°C, they become highly reactive with cutting tool materials [15]. High temperature strength means that the material has high resistance to failure fracture at elevated temperatures [8–9].

### 2.1.2 LONGITUDINAL TURNING OPERATION

Longitudinal turning is a continuous machining operation, and industrial machining is nowadays performed in large turning centers with CNC technique. The material removal rate ( $Q$ ) is a good measure of how fast the machining operation removes the material from the workpiece. The material removal rate is calculated with Eq.1 [3].

$$Q = v_c * f_n * a_p \quad Eq. 1$$

A schematic illustration of longitudinal turning is presented in Fig. 2.2, where  $v_c$ ,  $f_n$ ,  $a_p$ , and  $\kappa_r$  represent the cutting speed [m/min], feed rate [mm/rev], depth of cut [mm] and entering angle [°], respectively. The illustration is not to scale.

The cutting tool edge is exposed to very high temperatures during machining operations, and about 98% of the mechanical work in cutting is transformed into heat. About 80% of the generated heat is conducted into the cutting tool when machining titanium alloys, i.e. 30 percentage points more than for steels, which results from the fast chip flow and low thermal conductivity of titanium alloys [15].

There is a variety of methods to lead generated heat away from the cutting process, e.g. usage of external cutting fluid, increasing thermal conductivity in the tool shank and holder, or cooling the tool shank and holder internally with liquid nitrogen [19]. Cutting with emulsion provides longer tool life, but demands more power and is less environmentally friendly [20]. However, dry machining is only effective at low cutting speeds for continuous machining of titanium alloys [21].

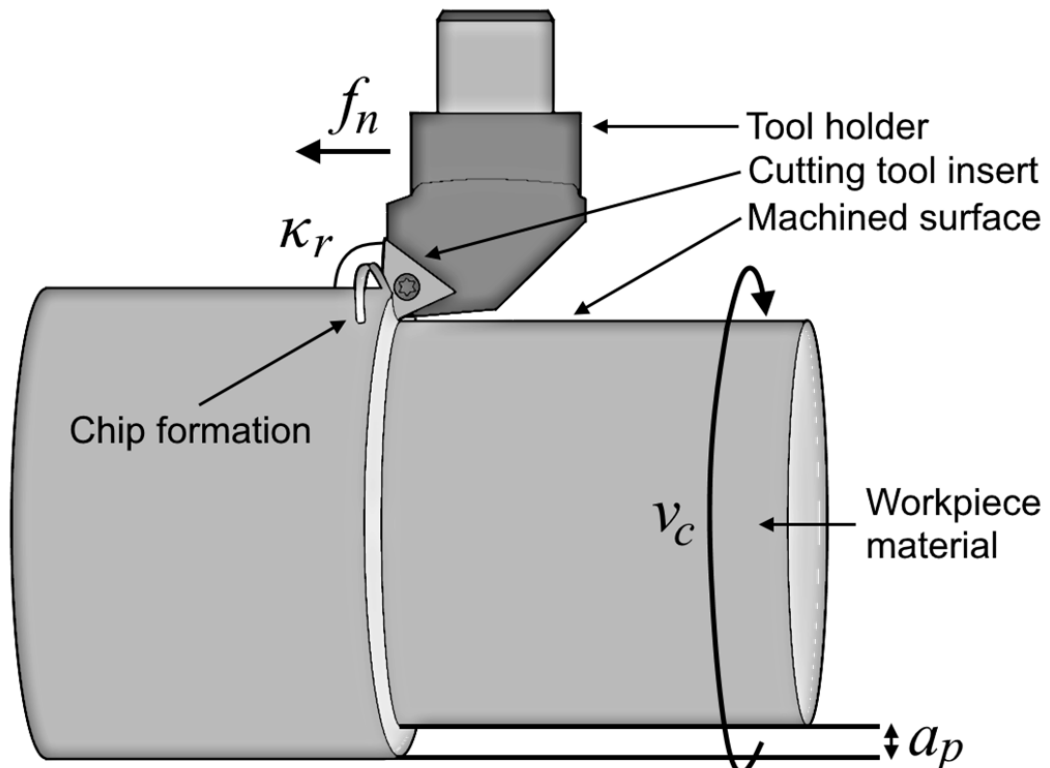


**Figure 2.2.** Schematic illustration of the setup in the turning center machine, where  $v_c$ ,  $f_n$ ,  $a_p$ , and  $\kappa_r$  represent the cutting speed, feed rate, depth of cut and entering angle, respectively. The illustration is not to scale.

### 2.1.3 CLASSIFICATION OF TITANIUM ALLOYS

Pure titanium, which is stable in  $\alpha$  phase in room temperature, has a hexagonal close-packed (hcp) crystal structure [22]. Unalloyed titanium undergoes alpha-to-beta transition, which is an allotropic transformation from hcp to body-centered cubic (bcc) crystal structure, at temperatures above 882°C, see Fig. 2.3 [9].

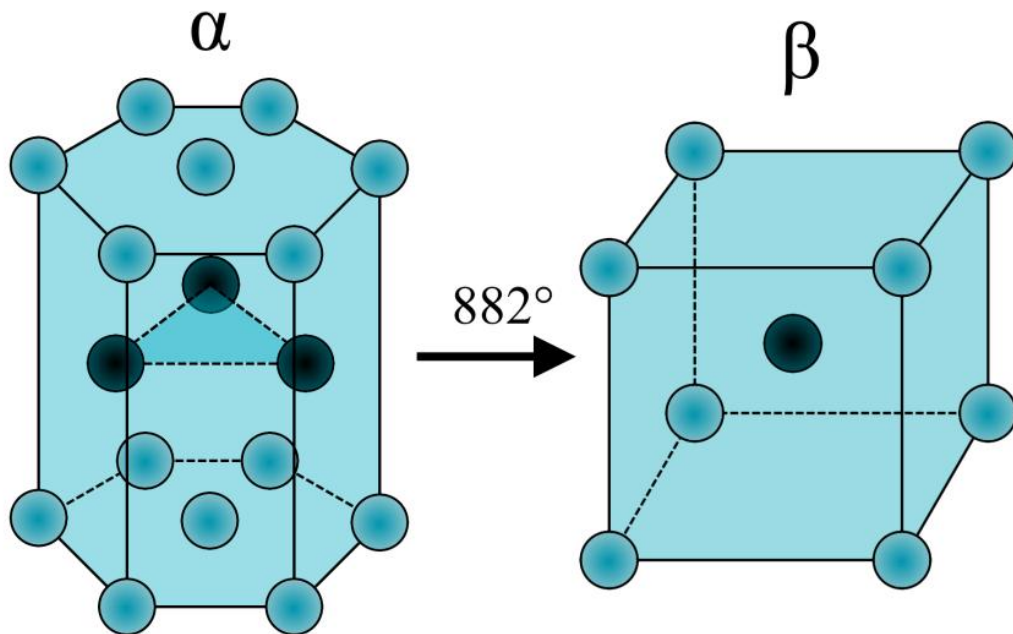


**Figure 2.3.** Hexagonal close-packed ( $\alpha$ ) and body-centered cubic ( $\beta$ ) crystal structures, and the allotropic transition temperature for pure titanium.

The presence of alloying elements strongly affects the transformation temperature [22].  $\alpha$ -stabilizers, e.g. aluminum, carbon and oxygen, are soluble in  $\alpha$ -titanium and increase the transition temperature. There are two types of  $\beta$ -stabilizers,  $\beta$ -isomorphs and  $\beta$ -eutectoids, which reduce the transition temperature.  $\beta$ -isomorphous stabilizers, e.g. vanadium and molybdenum, are equally soluble in  $\beta$ -titanium.  $\beta$ -eutectoids, e.g. copper and silicon, form interstitial compounds with the  $\beta$ -phase and therefore have restricted solubility in  $\beta$ -titanium. [15]

Titanium alloys can be divided into  $\alpha$ , near  $\alpha$ ,  $\alpha + \beta$ , metastable  $\beta$ , and  $\beta$  alloys [9]. Ti–6Al–4V is an  $\alpha + \beta$  alloy, because it is alloyed with aluminum, which is an  $\alpha$ -stabilizer and vanadium, which is a  $\beta$ -stabilizer. One characteristic among  $\alpha + \beta$  alloys is that they have lower work hardening rates compared to steels [14].

## 2.2 TOOL WEAR

Tool wear appears on the cutting tool during metal machining, regardless of the cutting conditions, due to contact between the tool and workpiece material. This is the reason for tool failure, and therefore it is essential to study and understand tool wear to further improve the performance and tool life of the cutting tool insert. There are many factors that can have an impact on tool wear, such as material and geometry of the tool, workpiece material, cutting fluids, and cutting parameters [23].

Tool wear can be described with wear types and wear mechanisms. Tool wear influences the rate of material removal, surface roughness of the machined component, control of chip formation, and economic accuracy [5]. Tool wear is located near the cutting edge of the rake and flank faces of the cutting tool insert. The main cause of tool damage is related to the adhesive-, mechanical- and thermal wear mechanisms, which are presented in Fig. 2.4. At low temperatures, the tool wear is related to adhesion, but at elevated temperatures thermal wear increases exponentially due to e.g. diffusion, and becomes the main contributor to tool wear. Thermal diffusion, chemical reaction and plastic deformation are temperature dependent, while abrasion, chipping, fatigue and fracture are dependent on mechanical factors. [6]

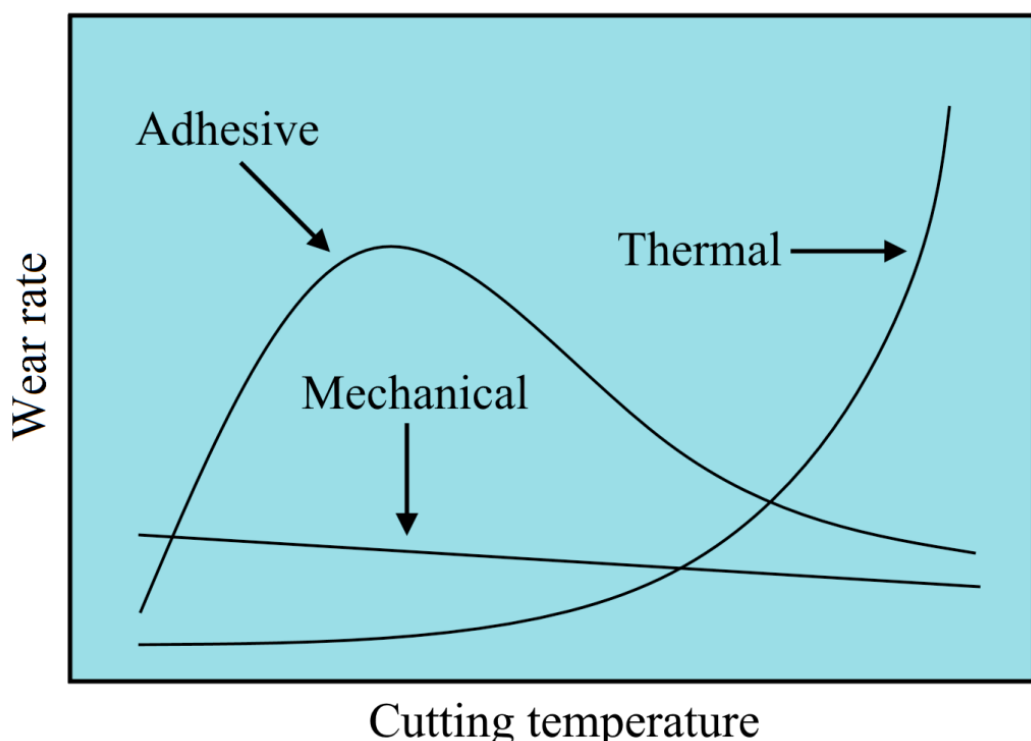


**Figure 2.4.** How the cutting temperature affects the wear rate for the adhesive-, mechanical- and thermal wear mechanisms. Based on Childs et al. [6]

The wear types can be divided into chipping, cracking, crater wear, flaking, flank wear, fracture, notch wear, plastic deformation, and smearing (build-up edge or build-up layer) [5]. Typical tool wear when turning difficult-to-cut materials are crater wear, flank wear, notch wear and adhesion [24].

### **2.2.1 BASICS OF DIFFUSION**

The basics of diffusion were pioneered in the nineteenth century by Fick and Brown. Fick's work describes diffusion with two fundamental laws, Fick's first and second laws. Brown's contribution to the diffusion theory was the Brownian motion, which Einstein later related to random walk. [25]

Fick's first law, presented in Eq.2, postulates that transportation of matter occurs from higher concentration to lower concentration through a concentration gradient.

$$J = -D \frac{\partial C}{\partial x} \quad Eq. 2$$

where  $J$  is the diffusion flux,  $D$  is the diffusion coefficient,  $C$  is the concentration, and  $x$  is the diffusion distance. Fick's second law, also called the diffusion equation, is presented in Eq.3, and describes how the concentration changes with time.

$$\frac{\partial C}{\partial t} = \nabla \cdot (D \nabla C) \quad Eq. 3$$

where  $C$  is the concentration,  $t$  is the time,  $\nabla$  is the gradient operator, and  $D$  is the diffusion coefficient. [25]

Diffusion in metals is often divided into two types, interdiffusion and self-diffusion. Interdiffusion occurs when atoms from one media diffuse into another, and self-diffusion takes place within the same media with no compositional changes [22]. Thus, elemental diffusion of titanium into WC/Co substrate is an interdiffusion process. The diffusion flux ( $J$ ) of titanium in the tool-chip interface is schematically illustrated in Fig. 2.5. The diffusion of titanium into the WC/Co substrate is marked with a dotted line.

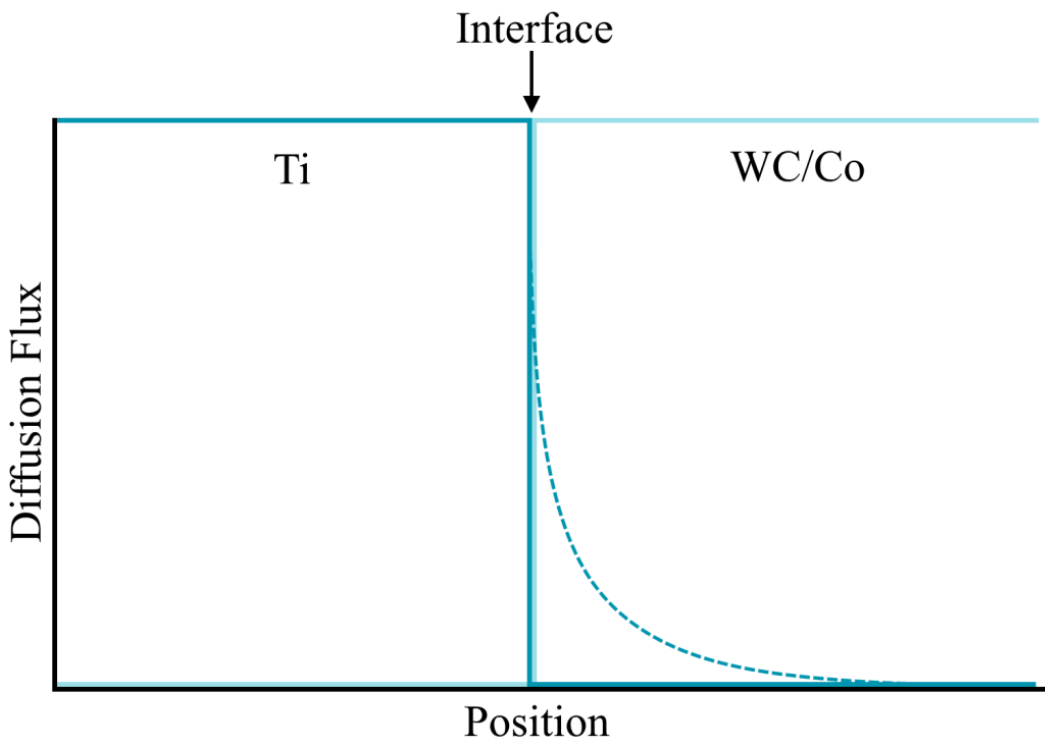


**Figure 2.5.** Schematic illustration of the diffusion flux of titanium in the tool-chip interface. The dotted line marks the diffusion of titanium into the WC/Co substrate.

There are several methods to determine  $D$ . These are separated into steady-state and non-steady methods. Non-steady methods are divided into diffusion couple, in- and out-diffusion, thin layer, and indirect methods [26]. The diffusion flux ( $D$ ) often obeys the Arrhenius relation and is calculated with Eq.4.

$$D = D_0 \left( -\frac{\Delta H}{RT} \right)$$

*Eq. Fel! Bokmärket är inte definierat.*

where  $D_0$  is the frequency factor,  $\Delta H$  is the activation enthalpy of diffusion,  $R$  is the gas constant and  $T$  is the temperature [25].

## 2.2.2 CRATER WEAR

Crater wear is a result of chip slipping along the tool edge on the rake face of the cutting tool insert. The wear mechanisms behind this are diffusion, adhesion and abrasion. The geometry of the cutting edge is strongly affected by crater wear, which results in differences in chip formation [5]. Adhesive wear can occur as a build-up layer that gets welded on the rake face and contributes to crater wear.

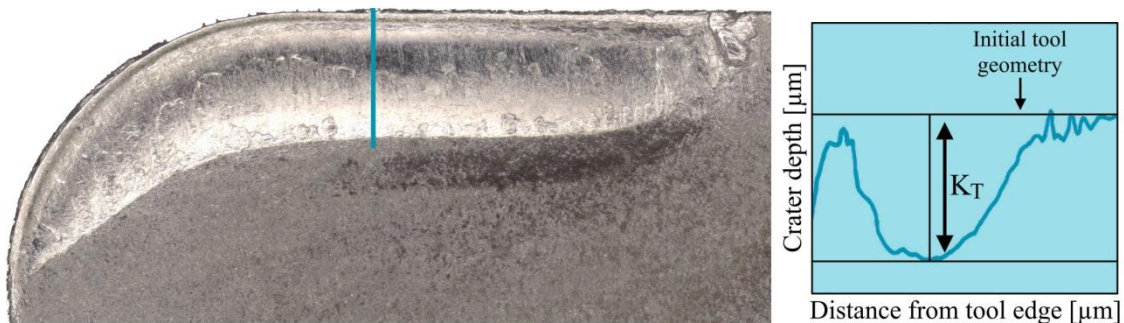


**Figure 2.6.** Typical crater wear on the rake face of an uncoated insert and the definition of crater depth measurements.

Maximum crater wear depth ( $K_T$ ) is measured as illustrated in Fig. 2.6. The contact area between the tool and chip is three times smaller for titanium alloy than for steels, at identical cutting conditions, resulting in a narrower crater width ( $K_B$ ) [15]. On the other hand,  $K_B$  increases with shear angle ( $\phi$ ), resulting in thinner chips [24].

### 2.2.3 FLANK WEAR

Flank wear ( $V_B$ ) is a type of abrasion wear that arises when contact occurs between the cutting tool insert and the workpiece material, on the flank face near the cutting edge of the cutting tool insert, and is primarily caused by the abrasive wear mechanism. If machining continues when flank wear becomes too exaggerated, the surface finish will quickly get ploughed and uneven [3,5]. Astakhov's [24] work shows that when flank wear surpasses the critical point for a given cutting tool insert, the surface roughness increases exponentially. A typical measurement of  $V_B$  is shown in Fig. 2.7. The region between the teal lines is the worn area (flank wear) and the yellow and red region is the unworn coating.

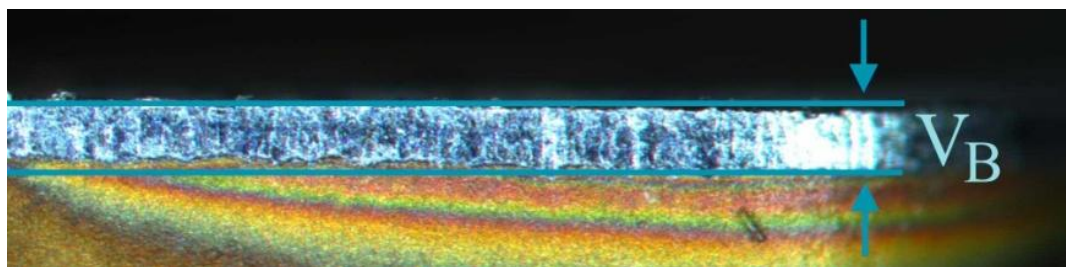


**Figure 2.7.** Typical flank wear on the flank face of a coated insert and the definition of flank wear measurements.

## 2.2.4 TOOL LIFE

Tool life refers to the amount of time a cutting tool insert is considered usable. Wear on the cutting tool insert has a direct effect on the point when it cannot longer produce a smooth surface on the workpiece material. Therefore, it is important to define the tool life criteria for every given type of tool wear. The tool life criteria recommendations for cemented carbide tool inserts are:

- $0.06 + 0.3 \times f_n$  mm for  $K_T$  ( $f_n$  is the feed)
- 0.3 mm for  $V_B$  (if regularly worn)

These recommendations were defined by ISO3685:1993 and recited by Astakhov and Davim [23]. However, in this thesis project the criterion for flank wear was established as 0.2 mm, due to the fact that relatively small inserts were used.

## 2.3 CHIP FORMATION

Ground-breaking work of chip formation was done by Tresca [27] and Mallock [28], who highlighted the importance of plasticity and tool-chip friction interactions already during the nineteenth-century [6]. However, it took over 60 years until Merchant [29–30] published his extensive work in 1945, which includes the fundamentals regarding geometry of continuous chip formation, force measurements and conditions of plasticity in orthogonal cutting. It is important to note that the cutting process produces either continuous, discontinuous or segmented chips, depending on the workpiece material.

Orthogonal cutting is applied when the cutting edge of the tool is perpendicular to the cutting direction. Longitudinal cutting is applied when the cutting edge of the tool has an entering angle ( $\kappa_r$ ) in the cutting direction. Merchant's equation is presented in Eq.5, derived from Merchant [29].

$$\phi = 45^\circ + \frac{\gamma}{2} - \frac{\theta}{2} \quad Eq. 5$$

where  $\phi$ ,  $\gamma$  and  $\theta$  are the shear, rake and friction angles, respectively, and predicts the shear angle that minimizes energy during orthogonal cutting. This is of great importance when improving cutting conditions, in order to reduce machining costs.

### 2.3.1 REASONS BEHIND CHIP SEGMENTATION

Titanium alloys, amongst other superalloys, form segmented chips due to their physical properties. The thermoplastic deformation that occurs within the chip is inhomogeneous when machining titanium alloys, which means that the chips will deform periodically as saw-tooth-like segments in distinct shear zones [31–33].

The primary shear zone is located between the tool-chip interface and the bulging segment in the upsetting phase, and shear occurs in the direction of the shear angle. The secondary shear zone is located in the region where tool-chip contact occurs and is extended along the backside of the chip. The adiabatic shear bands and secondary shear zone can easily be observed on chip cross-sections in SEM, see Fig. 2.8. Adiabatic shear bands are located between the segments of the chip, and shear occurs in the direction of the segmentation angle ( $\phi_{seg}$ ). The formation of these zones depends on heat concentration due to e.g. poor thermal conductivity [31]. The grey zones in Fig. 2.8 are  $\alpha$ -phase and the white zones are  $\beta$ -phase.

The shear-localized chip formation process starts when the shear stress in adiabatic shear bands is equal to, or lower than, the shear strength of the bulk material, and this occurs at a critical cutting speed for different materials [34]. Catastrophic thermoplastic shear practically appears at every conventional cutting speed for titanium alloys.

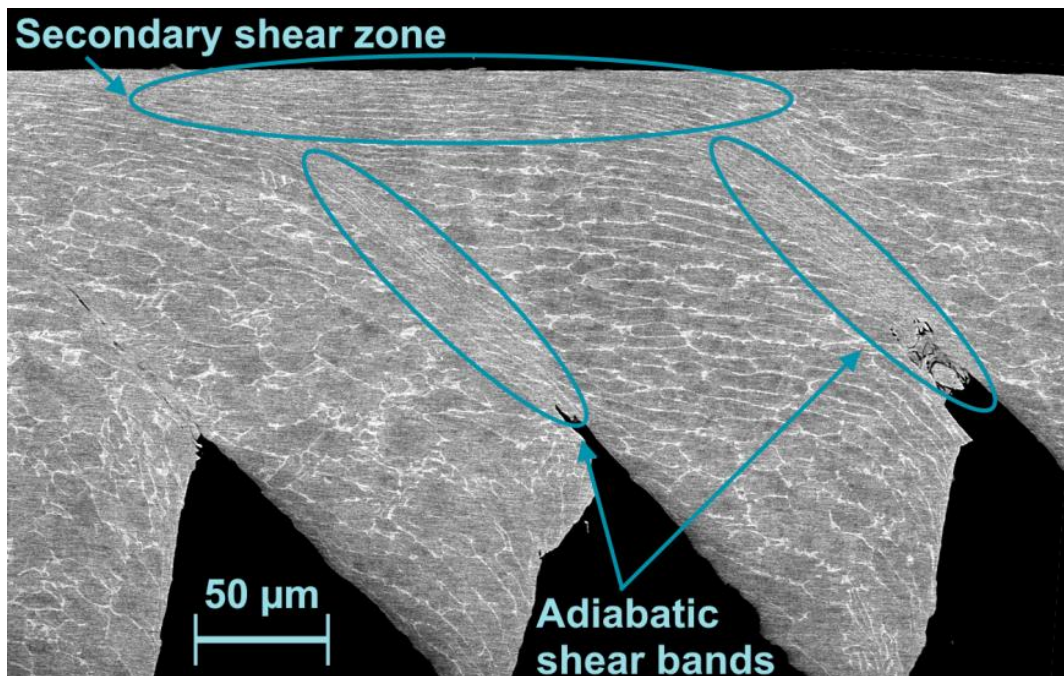


**Figure 2.8.** SEM image that illustrates the locations of adiabatic shear bands and the secondary shear zone in a serrated chip.

Shear strength is dependent on shear strain and temperature, and can be expressed as Eq.6, which indicates the criteria for catastrophic thermoplastic shear [35]:

$$0 \leq \frac{\frac{\delta_\tau}{\delta_{\gamma_e}}}{\frac{\delta_\tau}{\delta_{\theta_a}} * \frac{\delta_{\theta_a}}{\delta_{\gamma_e}}} \leq 1 \quad Eq. 6$$

where  $\tau$ ,  $\gamma_e$  and  $\theta_a$  are the shear stress, shear strain and temperature above ambient. The material will go through catastrophic shear if the ratio is between 0 and 1, and, consequently, form a serrated chip. Shear is distributed over the entire chip if the ratio is negative or above 1. Negative ratios result in temperature dependent hardening and ratios above 1 result in strain dependent hardening of the material. [35]

### 2.3.2 CATASTROPHIC SHEAR MODEL

The shear model in the present work is based on previous models by Komanduri and von Turkovich [32], and Turley et al. [33]. A schematic illustration of stages during the upsetting phase of chip formation is presented in Fig. 2.9. The cutting tool forces the material to deform from right to left, and is located at point F, F', D, and D' for stage 1–4, respectively. A detailed explanation of chip formation during the upsetting phase is accounted for below.

1. The parallelogram AEFD represents the undeformed area in the workpiece material, before chip formation, and is represented with dotted lines in stage 2–4.
2. At the beginning of the upsetting phase, E moves to E', F moves to F', and shearing occurs between E' and F' (primary shear zone). Stresses are compressive due to the fact that EF is longer than E'F'. Shearing also occurs along DF' (secondary shear zone).
3. When the cutting tool reaches the stalemate point, E' and F' have moved further to positions B and C, and forms the ABCD trapezoid chip segment. Shearing is finished in BC (primary shear zone) and the new surface CD has formed (secondary shear zone). Now, the whole segment has to move to further cut the material.
4. The end of the upsetting phase shows that the trapezoid ABCD slides in the AD direction to finally meet the end position of the newly formed segment A'B'C'D'. This process formed the new surface AA' and reduced the distance AD to AD'. Shearing is finished in AD' (primary shear zone), and AD' and B'C' are adiabatic shear bands.

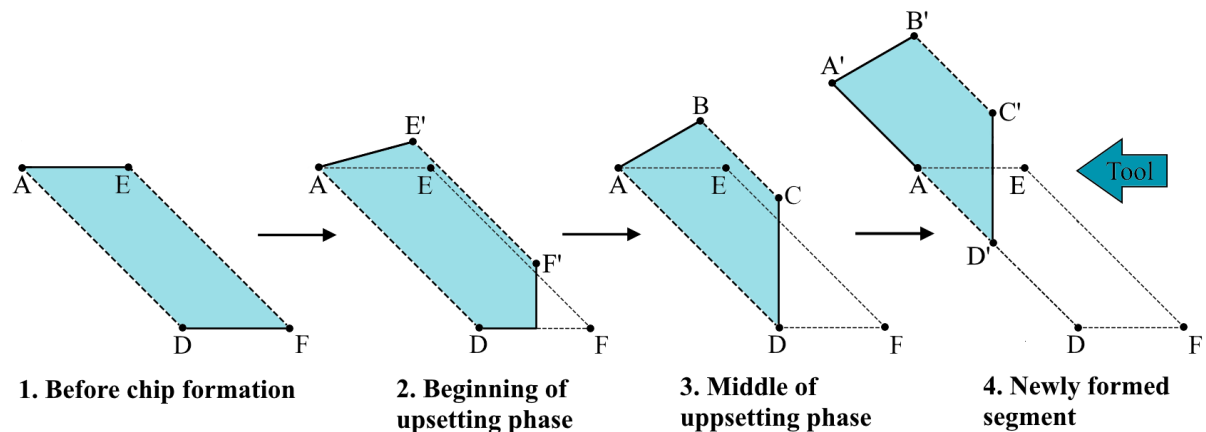


**Figure 2.9.** Stages during the upsetting phase of chip formation. 1. Undeformed area before chip formation, 2–3. Cutting tool forces deformation in the material and 4. The trapezoid segment slides along AD. The original parallelogram AEFD in stage 1 is illustrated in 2–4 with dotted lines.

A close-up view of shearing in Ti–6Al–4V is illustrated in Fig. 2.10, where the light colored grains are  $\alpha$ -phase and the darker colored boundaries are  $\beta$ -phase. The  $\alpha$ -phase grains and  $\beta$ -phase boundaries elongate in the adiabatic shear band region. The grains are progressively more elongated the closer they are to the adiabatic shear band. Black arrows indicate directions of elongation, and teal arrows indicate directions of shear stress.

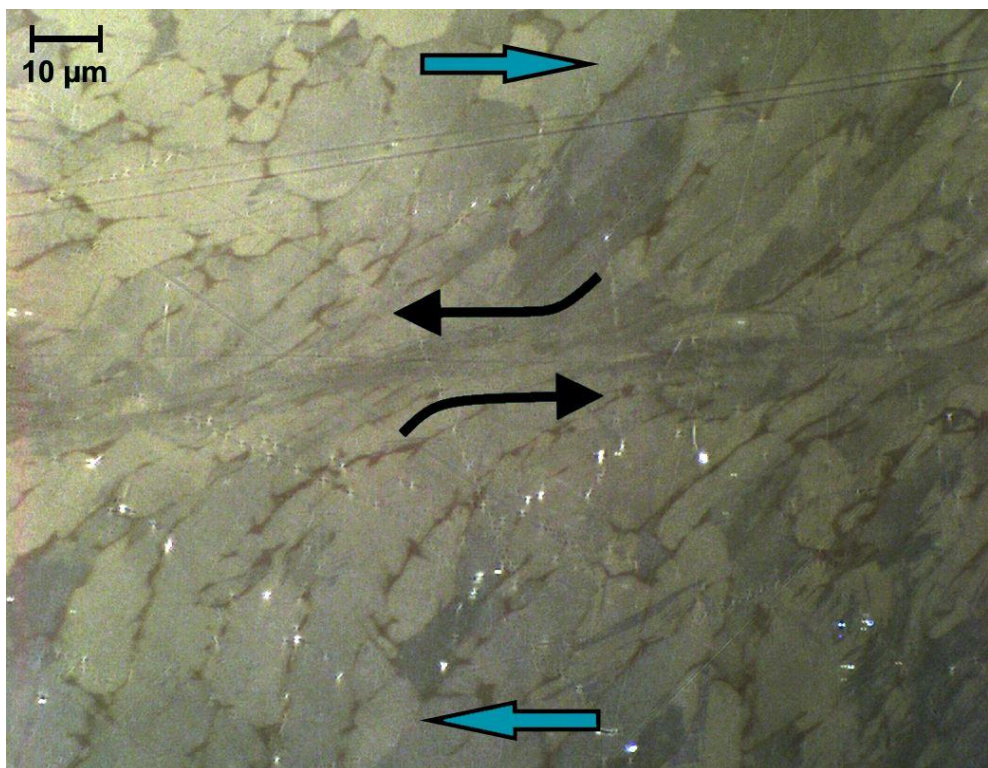


**Figure 2.10.** LOM image of how grains elongate in the region near the adiabatic shear bands. Black arrows indicate directions of elongation, and teal arrows indicate directions of shear.

### 2.3.3 DESCRIPTION OF CHIP GEOMETRY

Firstly, the assumption is made that all segments have the same size and are equally distributed all over the chip. The chip geometry is most easily explained with the aid of a schematic illustration; see Fig. 2.11, which shows chip segmentation during chip formation. The illustration was inspired by Gente and Hoffmeister [36] and Cotterell and Byrne [37].

The geometrical parameters describe chip dimensions before and after chip formation. The depth of cut is denoted as  $t_1$  (also  $a_p$ ), and  $t_2$  describes the average chip thickness (average of maximum and minimum chip thickness  $t_{2\max}$  and  $t_{2\min}$ ). Segment spacing before and after upsetting phase are denoted as  $p$  and  $p_c$ , and  $d$  and  $d_c$  represent mean shear band spacing before and after chip formation, respectively.

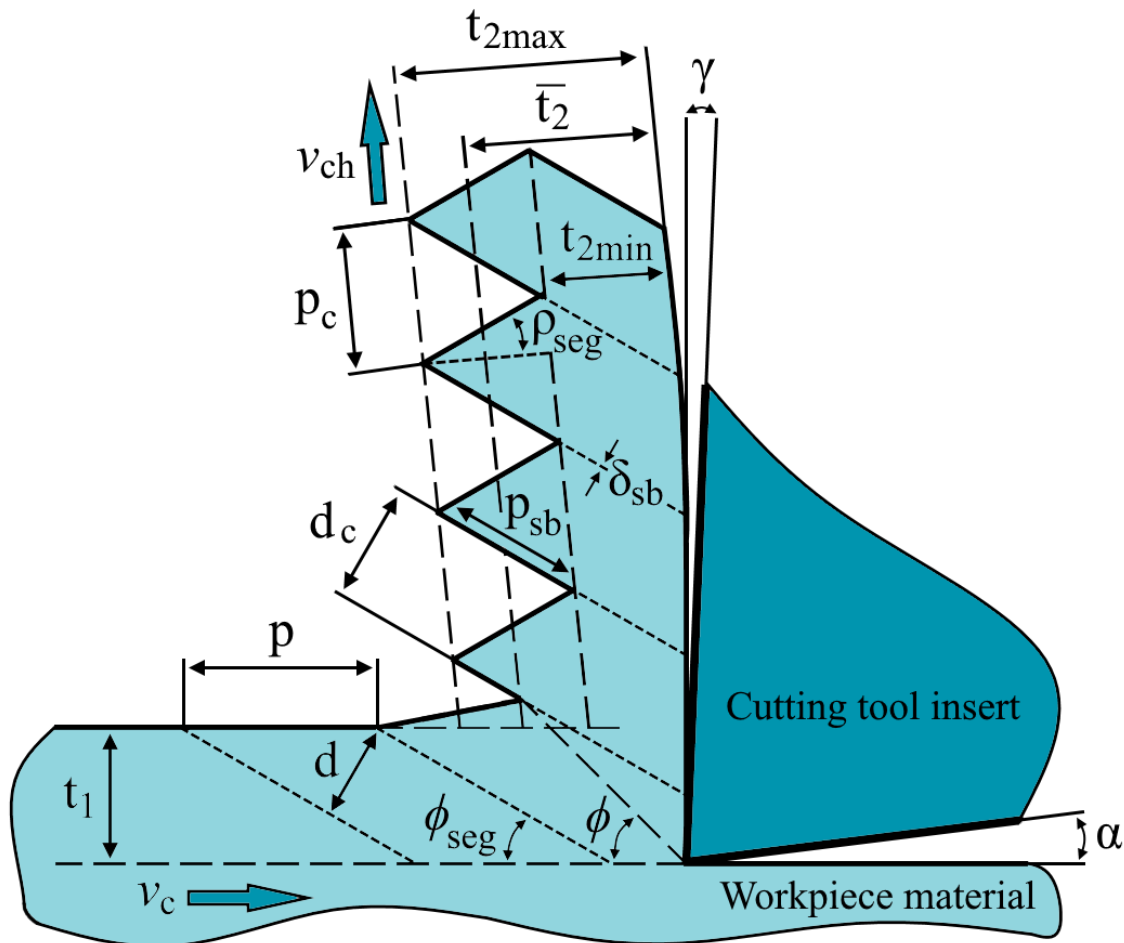


**Figure 2.11.** Schematic illustration of chip segmentation during chip formation, and representation of geometric parameters describing chip dimensions and cutting angles.  $t_1$  = depth of cut,  $t_2$  = average chip thickness of  $t_{2\max}$  and  $t_{2\min}$ ,  $p$  and  $p_c$  = segment spacing,  $d$  and  $d_c$  = mean shear band spacing,  $p_{sb}$  = shear band projection,  $\delta_{sb}$  = shear band width,  $\phi$  = shear angle,  $\phi_{seg}$  = segmentation angle,  $\rho_{seg}$  = bulge angle,  $\gamma$  = rake angle,  $\alpha$  = clearance angle,  $v_c$  = cutting speed, and  $v_{ch}$  = chip velocity. Inspired by Gente and Hoffmeister [36] and Cotterell and Byrne [37].

Shear band projection is denoted as  $p_{sb}$ , and  $\delta_{sb}$  is the shear band width. Shear- and segmentation angles are represented by  $\phi$  and  $\phi_{seg}$ , respectively. The bulge angle is denoted as  $\rho_{seg}$ . Rake and clearance (relief) angles are denoted as  $\gamma$  and  $\alpha$ , respectively. Finally,  $v_c$  and  $v_{ch}$  represents cutting speed and chip velocity, respectively.

### 2.3.4 CALCULATIONS REGARDING CHIP ANALYSIS

There are several ways to analyze a chip, e.g. compare average chip thickness, degree of segmentation, chips segmentation frequency, as well as shear- and segmentation angles. The average chip thickness ( $t_2$ ) is calculated according to Eq.7:

$$\bar{t}_2 = \frac{t_{2max} + t_{2min}}{2} \quad Eq. 7$$

The degree of segmentation ( $G$ ) is defined as the ratio between the distance of the bulging segment and the maximum thickness of the chip. Degree of segmentation is calculated with Eq.8 [38]:

$$G = \frac{t_{2max} - t_{2min}}{t_{2max}} \quad Eq. 8$$

The chip segmentation frequency ( $f_{seg}$ ) is defined as the number of segments per unit time given in [kHz] and calculated with Eq.9 [39]:

$$f_{seg} = \frac{1000v_c}{60p_c} \quad Eq. 9$$

It is evident that the cutting ratio ( $r$ ) in equations 10–11 are identical if the shear- and segmentation angles are equivalent ( $\phi = \phi_{seg}$ ), which results in that the band spacing before upsetting phase is equal to the mean shear band spacing ( $d = d_c$ ) and that the  $d_c/d$  ratio = 1 and remains constant during the upsetting phase [36]. If this is the case, shear strain will occur in the segments parallel to the adiabatic shear band [36–37].

$$r = \frac{p_c}{p} = \frac{v_{ch}}{v_c} = \frac{t_1}{\bar{t}_2} = \frac{\sin(\phi)}{\cos(\phi - \gamma)} \quad Eq. 10$$

$$r = \frac{p_c}{p} = \frac{d_c}{d} * \frac{\sin(\phi_{seg})}{\cos(\phi_{seg} - \gamma)} \quad Eq. 11$$

where  $\gamma$  is the rake angle.

### 2.3.5 DEFINITIONS OF SHEAR STRESS AND SHEAR STRAIN

The shear stress ( $\tau$ ) is defined by Eq.12 [18]:

$$\tau = \frac{F_s}{A} \quad Eq. 12$$

where  $F_s$  is the applied force and  $A$  is the loaded area. When a material experiences shear stress, it induces shear strain as illustrated in Fig. 2.12. The engineering shear strain ( $\gamma_e$ ) is defined by Eq.13 [18].

$$\gamma_e = \frac{w}{l} = \tan(\phi) \quad Eq. 13$$

where  $w$  is the width,  $l$  is the length and  $\phi$  is the shear angle.

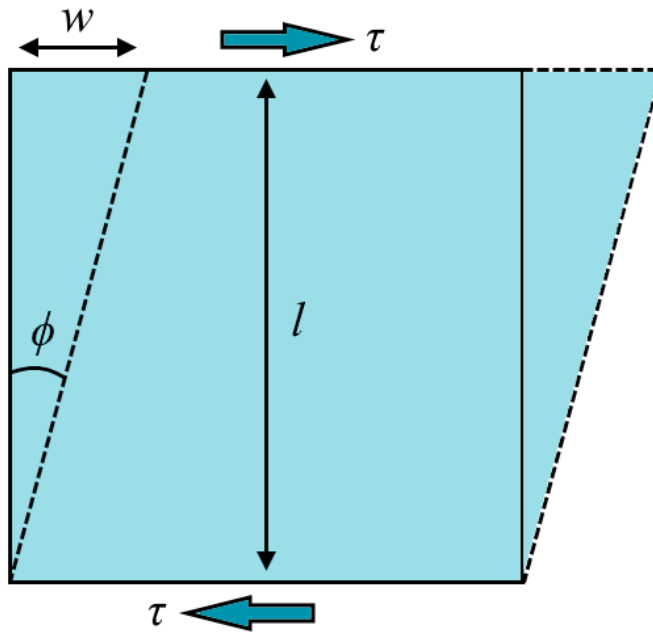


**Figure 2.12.** Definition of shear strain.  $w$  is the width,  $l$  is the length,  $\phi$  is the shear angle and  $\tau$  is the applied shear stress.

### 2.3.6 CALCULATIONS OF SHEAR STRAIN IN SHEAR-LOCALIZED CHIPS

Turley et al. [32] initiated the interest in calculating shear strain in titanium chips. Shear strain has been calculated in diverse ways and differs significantly between continuous and segmented chips [32,34,36–37,40–41]. Shear strain between the adiabatic shear bands is defined as shear strain within the segments ( $\gamma_{seg}$ ).

Eq.14 calculates the shear strain within the segment when the segmentation angle is constant, although this is rarely the case [32,36–37].

$$\gamma_{seg} = \frac{\sin(\rho_{seg})}{\sin(\phi_{seg}) \sin(\phi_{seg} + \rho_{seg})} \quad Eq. 14$$

Cotterell and Byrne [37], have investigated the case when the segmentation angle is not constant, which resulted in equations 15–17. If equations 14–15 are equal, shear- and segmentation angles are equivalent ( $\phi = \phi_{seg}$ ).

$$\gamma_{seg} = \frac{1}{\lambda_h \sin(\phi_{seg})} \sqrt{C^*} \quad Eq. 15$$

where  $\lambda_h$  is the chip compression ratio and  $C^*$  is a constant

$$\lambda_h = \frac{\bar{t}_2}{t_1} \quad Eq. 16$$

$$C^* = \lambda_h^2 - \frac{2\lambda_h \cos(\rho_{seg})}{\sin(\phi_{seg} + \rho_{seg})} + \frac{1}{\sin^2(\phi_{seg} + \rho_{seg})} \quad Eq. 17$$

Shear strain in the adiabatic shear band ( $\gamma_c$ ) is calculated with Eq.18 [32].

$$\gamma_c = \frac{p_{sb}}{\delta_{sb}} \quad Eq. 18$$

The total shear strain within the adiabatic shear band ( $\gamma_{sb}$ ) is the summation of the shear strain within the segments during the upsetting phase and the shear strain in the adiabatic shear band. The total shear strain in the adiabatic shear bands is calculated with Eq.19 [32].

$$\gamma_{sb} = \gamma_{seg} + \gamma_c \quad Eq. 19$$

## 2.4 ANALYTICAL METHODS

General analytical methods were performed to characterize wear patterns on cutting tools, and to study diffusion and measure chip geometry. The utilized instruments were the following: focus variation with Alicona, stereo microscope, light optical microscope (LOM), scanning electron microscope (SEM), electron microprobe analyzer (EMA) and energy-dispersive x-ray spectroscope (EDS).

### **2.4.1 FOCUS VARIATION WITH ALICONA**

There are numerous methods available for measuring surface topography, such as atomic force microscopy, confocal microscopy, focused variation, phase shifting interferometry, and white light interferometry [42]. Among these, focused variation is a fairly new technique, even though the theory was first published by von Helmholtz in 1867, and later translated to English by Southall [43] in 1924 [42].

Alicona InfiniteFocusSL is a focus variation instrument that employs optics to image areal surface topography and to measure depth. The instrument performs vertical scans at different focused depths by changing depth of field and, subsequently, builds up a 3D image of the surface texture [44]. The 3D image can have realistic colors, or pseudo colors to facilitate visualization of depth variations. Amongst other functions in the Alicona IF-MeasureSuit software, a line across the 3D image surface yields a 2D graph of the surface profile.

### **2.4.2 LIGHT OPTICAL- AND STEREO MICROSCOPE**

The first optical microscope was developed in the early seventeenth-century and was constructed of one single convex lens, which had huge magnification limitations due to severe image distortion. To reduce the aberration, two lenses were used, the objective and the projector, which also enable a higher degree of magnification. [45] The stereo microscope is constructed in a similar fashion to the LOM, but is simpler and has lower zoom resolution.

LOMs are fitted with a light source to illuminate the specimen. The light is diverged with the aim of a condenser lens system to either transmit through or reflect against the sample. Apertures are located near the condenser lens, to control the illuminated area of the specimen, and near the objective lens, to control the angular spread of the light reflected from the sample.

Resolution and contrast can be corrected by adjusting the objective lens aperture. The most important components in the LOM are the objective and the condenser. Nowadays, LOMs are far more complex than described here, with components such as collector and tube lenses, filters, polarizers and retarders. Multiple lenses in the objective and tube lenses help reduce aberration even more. [45–46]

### **2.4.3 SCANNING ELECTRON MICROSCOPE**

The first proposal of an electron microscope was described by Knoll and Ruska in the early 1930s, and alongside with von Ardenne [47], they paved the way for the modern SEM by letting the electron beam scan over the specimen and move in a so-called raster pattern [48].

SEM gives information about the surface, or near surface, of the studied sample. The construction of a typical SEM is based on an electron gun that, with the help from condenser and objective lenses, irradiates the specimen with an electron beam. The selected area of interest is scanned in a raster pattern. Electrons interact with the sample surface, absorb or scatter back as e.g. secondary electrons, backscattered electrons or x-rays, and are collected in different types of detectors. The most common detectors that create final images of the sample surface are the secondary electron and the backscattered electron detectors. The secondary electron detector generates images with more topographical contrast, while the backscattered electron detector gives more contrast from elemental composition. The SEM operates in high vacuum, since that minimizes the amount of electron scattering before they reach the sample surface. [49–51]

### **2.4.4 ELECTRON MICROPROBE ANALYZER**

During the early 1950s, Castaing developed EMA, also recognized as the electron probe microanalyzer (EPMA), or electron micro probe analyzer (EMPA). EMA is one of many experimental techniques to study diffusion in solids, and is the leading device to analyze diffusion, both qualitatively and quantitatively. Most EMAs can operate as a SEM, which makes it easy to identify the regions of interest, and the information about elemental distribution can either be obtained through point-by-point analysis, line scans or x-ray distribution maps. [25,52] The EMA utilizes a focused electron beam to irradiate a selected area of a few microns or less on the sample. The beam of electrons will locally excite x-rays, which are collected and measured in a crystal diffraction spectrometer, also called a wavelength-dispersive x-ray spectrometer (WDS). Moseley's law, shown in Eq.20, is used to relate a certain element to its respective spectral line.

$$\frac{1}{\lambda} = k(Z - \sigma)^{1/2} \quad Eq. 20$$

where  $\lambda$  is the wavelength of emitted x-rays,  $Z$  is the atomic number,  $k$  is the constant for a given x-ray spectral line and  $\sigma$  is the constant related to the atomic screening effect. [52]

#### **2.4.5 ENERGY-DISPERSIVE X-RAY SPECTROSCOPE**

SEMs are often equipped with an EDS detector for the possibility to perform chemical analysis on the examined sample [49]. The EDS detector collects characteristic x-rays emitted from the irradiated area. The EDS has higher count rates than WDS, and is therefore advantageous at low electron beam currents [50]. However, the spectral resolution is much poorer for EDS. This means that EDS has great limitations when it comes to quantification of elements, which is preferred with WDS.

## CHAPTER 3

### LITERATURE REVIEW

This chapter presents an overview of the major observations from previous research with focus on crater wear, diffusion wear and chip formation when turning in titanium alloys. Numerous investigations regarding turning titanium alloys with WC/Co cutting tools can be found in the literature. Some of them are accounted for in tables 3.1–2, which present the most expected wear mechanisms and wear types, when turning in titanium alloys at different cutting conditions, i.e. cutting parameters, tool and work materials, and usage of coolant.

The trend of material removal rate (MRR) for some investigations when turning titanium alloys with carbide tools is shown in Fig. 3.1, from 1980 to present [12,16,19,53–82]. The MRR was calculated with Eq.1.

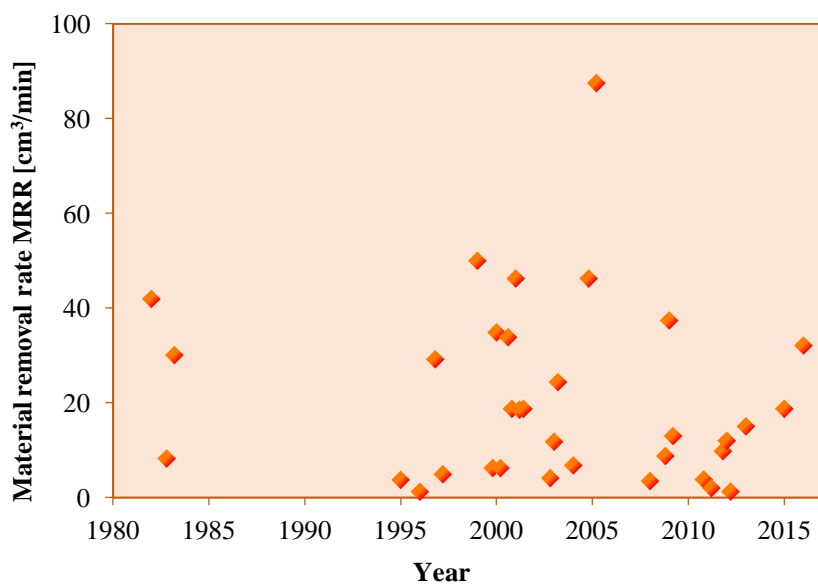


**Figure 3.1.** Trend of investigations about turning titanium alloys with carbide tools, with respect to MRRs, from 1980 to present.

### 3.1 PREVIOUS RESEARCH ON CRATER WEAR

Titanium and its alloys are well known to be very difficult to machine due to their low thermal conductivity and high chemical reactivity. Heat transfer between cutting tool and newly formed chip is low and chip flow is rapid, which leads to high temperatures in the interface between the cutting tool insert and the workpiece material [15,19]. Turning of titanium alloys with uncoated and coated carbide tools makes alloys likely to suffer from crater wear at cutting speeds exceeding 60 m/min, and flank wear ( $V_B$ ) commonly occurs at all cutting speeds [12].

Hartung and Kramer [12] studied tool wear when turning Ti–6Al–4V, and compared many different cutting tools, including WC/Co tools. Crater wear was found to be the limiting factor of WC/Co tools between cutting speeds of 61 and 122 m/min. Crater depth ( $K_T$ ) was measured and crater wear rates were calculated for two different uncoated WC/Co tools, which showed that crater wear rates were 2–3  $\mu\text{m}/\text{min}$  for  $v_c = 61 \text{ m/min}$ , 5–10  $\mu\text{m}/\text{min}$  for  $v_c = 76 \text{ m/min}$  and 10–15  $\mu\text{m}/\text{min}$  for  $v_c = 122 \text{ m/min}$ .

Nabhani [70] performed dry single-point turning tests, with coated WC tools, in titanium alloy TA 48 at cutting conditions  $v_c = 75 \text{ m/min}$ ,  $f_n = 0.25 \text{ mm/rev}$  and  $a_p = 1.0 \text{ mm}$ . The study concluded that the coating was removed very fast in the crater wear region, which left the WC/Co surface subjected to further crater progression. Titanium alloys will quickly dissolve into, or chemically react with, most of the tool materials available today when in contact during metal machining. A stable coherent build-up layer on the rake face was found to be protective against crater wear, which resulted in lower wear rate. Detached WC particles from the cutting tool were observed on the backside of the chips, which indicates strong bonds between workpiece material and tool surface. It was concluded that coated carbide tools accelerated crater wear.

Jawaid and Olajire [84] investigated the cuttability of chemical vapor deposited (CVD) and physical vapor deposited (PVD) coated carbides in high strength low alloy steel, which is a difficult-to-cut material. Delamination of all layers on a Ti(C,N)/Al<sub>2</sub>O<sub>3</sub>/TiN CVD multicoated insert was observed and attributed to variations in thermal expansion of the different layers.

**Table 3.1.** Wear mechanisms and wear types at different cutting conditions when dry turning common titanium alloys with universal cutting tool materials. The cutting parameters are: cutting speed ( $v_c$ ), feed rate ( $f_n$ ) and depth of cut ( $a_p$ ).

Work material	Dry/Wet	Tool materials	Cutting Parameters	Wear mechanisms	Wear types	References
Ti-64	Dry	Uncoated carbide	$v_c = 20\text{--}120 \text{ m/min}$ $f_n = 0.1 \text{ mm/rev}$ $a_p = 0.5 \text{ mm}$	60 m/min: Diffusion, abrasion 120 m/min: Diffusion, oxidation, abrasion	20 m/min: Small wear 60 m/min: K <sub>T</sub> , V <sub>B</sub> 120 m/min: K <sub>T</sub> , V <sub>B</sub>	Jianxin et al. [73]
Ti-64	Dry	Uncoated carbide	$v_c = 55\text{--}110 \text{ m/min}$ $f_n = 0.1 \text{ mm/rev}$ $a_p = 0.5 \text{ mm}$	55 m/min: Adhesion 70 m/min: Adhesion 110 m/min: Adhesion, diffusion	110 m/min: K <sub>T</sub> , V <sub>B</sub>	Ribeiro et al. [74]
Ti-64	Dry	Uncoated carbide	$v_c = 70\text{--}117 \text{ m/min}$ $f_n = 0.20 \text{ mm/rev}$ $a_p = 2 \text{ mm}$	70 m/min: Abrasion, adhesion 100 m/min: Dissolution/diffusion, adhesion, abrasion 117 m/min: Dissolution/diffusion, adhesion, abrasion	70 m/min: V <sub>B</sub> 100 m/min: K <sub>T</sub> , flaking, V <sub>B</sub> 117 m/min: K <sub>T</sub> , flaking, V <sub>B</sub>	Venugopal et al. [72]
Ti-64	Dry	Uncoated carbide	$v_c = 90 \text{ m/min}$ $f_n = 0.1 \text{ mm/rev}$	90 m/min: Abrasion, adhesion, diffusion	90 m/min: K <sub>T</sub> , V <sub>B</sub> ,	Yang et al. [85]
Ti-64	Dry	1. Uncoated carbide, 2. Cermet, 3. TiC, 4. Ceramic, 5. CBN	$v_c = 60\text{--}200 \text{ m/min}$ $f_n = 0.10 \text{ mm/rev}$ $a_p = 0.5 \text{ mm}$	100–200 m/min: Diffusion, adhesion, abrasion	100 m/min: 1-5. K <sub>T</sub> , V <sub>B</sub> , chipping, 4-5. Notch 200 m/min: Fast fracture, V <sub>B</sub>	Narutaki and Murakoshi [19]
Ti-64	Dry		$v_c = 61\text{--}610 \text{ m/min}$ $f_n = 0.1 \text{ mm/rev}$ $a_p = 1.25 \text{ mm}$	61–122: Diffusion, adhesion, abrasion 122–610: Thermo-mechanical, diffusion, abrasion	61–122: K <sub>T</sub> , BUE, V <sub>B</sub> 122–610: P <sub>D</sub> , K <sub>T</sub> , V <sub>B</sub>	Hartung and Kramer [12]
Ti-64	Dry	Coated carbide (TiAlN)	$v_c = 20\text{--}65 \text{ m/min}$ $f_n = 0.1 \text{ mm/rev}$	20 m/min: Thermo-mechanical, adhesion 65 m/min: Adhesion, thermo-mechanical, diffusion	20 m/min: Chipping, V <sub>B</sub> 65 m/min: V <sub>B</sub> , Flaking	Nouari and Makich [88]

**Abbreviations:**  $v_c$  = cutting speed,  $f_n$  = feed rate,  $a_p$  = depth of cut, K<sub>T</sub> = crater wear, V<sub>B</sub> = flank wear, P<sub>D</sub> = plastic deformation, BUE = build-up edge, and Ti-64 = Ti-6Al-4V.

**Table 3.2.** Wear mechanisms and wear types at different cutting conditions when wet and dry turning common titanium alloys with universal cutting tool materials. The cutting parameters are: cutting speed ( $v_c$ ), feed rate ( $f_n$ ) and depth of cut ( $a_p$ ).

Work material	Dry/Wet	Tool materials	Cutting Parameters	Wear mechanisms	Wear types	References
Ti-64	Wet	Uncoated carbide	$v_c = 50\text{--}90 \text{ m/min}$ $f_n = 0.1 \text{ mm/rev}$ $a_p = 2 \text{ mm}$	50 m/min: Adhesion, (abrasion) 80 m/min: Diffusion, adhesion 90 m/min: Diffusion, abrasion	50 m/min: BUE, (V <sub>B</sub> ) 80 m/min: K <sub>T</sub> , BUE, notch, (V <sub>B</sub> ) 90 m/min: K <sub>T</sub> , V <sub>B</sub>	Arrazola et al. [75]
Ti-64	Wet	Uncoated carbide	$v_c = 70\text{--}117 \text{ m/min}$ $f_n = 0.20 \text{ mm/rev}$ $a_p = 2 \text{ mm}$	70 m/min: Dissolution/diffusion, adhesion, (abrasion) 100 m/min: Dissolution/diffusion, adhesion, abrasion 117 m/min: Dissolution/diffusion, adhesion, abrasion	70 m/min: K <sub>T</sub> , flaking, (V <sub>B</sub> ) 100 m/min: K <sub>T</sub> , flaking, V <sub>B</sub> 117 m/min: K <sub>T</sub> , flaking, V <sub>B</sub>	Venugopal et al. [72]
Ti-64	Wet	1. Uncoated carbide, 2. Cermet, 3. TiC, 4. Ceramic, 5. CBN	$v_c = 60\text{--}200 \text{ m/min}$ $f_n = 0.10 \text{ mm/rev}$ $a_p = 0.5 \text{ mm}$	100–200 m/min: Diffusion, adhesion, abrasion	100 m/min: 1-5. K <sub>T</sub> , (V <sub>B</sub> ), (chipping), 4-5. Notch 200 m/min: Fast fracture, V <sub>B</sub>	Narutaki and Murakoshi [19]
Ti-64	Wet	PVD-coated carbide (TiN, TiN/TiCN/TiC)	$v_c = 63\text{--}100 \text{ m/min}$ $f_n = 0.13\text{--}0.25 \text{ mm/rev}$ $a_p = 2.00 \text{ mm}$	76 m/min: Adhesion 100 m/min: Adhesion, diffusion thermo-mechanical	76 m/min: V <sub>B</sub> 100 m/min: V <sub>B</sub> , cracking, chipping, flaking, fracture	Ezugwu et al. [16]
Ti-5553	Dry	Coated carbide (TiAlN)	$v_c = 20\text{--}65 \text{ m/min}$ $f_n = 0.1 \text{ mm/rev}$	20 m/min: Abrasion 65 m/min: Diffusion, abrasion, thermo-mechanical	20 m/min: V <sub>B</sub> 65 m/min: K <sub>T</sub> , V <sub>B</sub> , P <sub>D</sub> , cracking	Nouari and Makich [88]
Ti-5553	Wet	Uncoated carbide	$v_c = 40\text{--}60 \text{ m/min}$ $f_n = 0.1 \text{ mm/rev}$ $a_p = 2 \text{ mm}$	50 m/min: Diffusion, abrasion, adhesion	50 m/min: K <sub>T</sub> , V <sub>B</sub> , BUE	Arrazola et al. [75]
Ti-6246	Dry	Uncoated carbide	$v_c = 60\text{--}100 \text{ m/min}$ $f_n = 0.25\text{--}0.35 \text{ mm/rev}$ $a_p = 2.0 \text{ mm}$	60 m/min: Dissolution/diffusion, adhesion, abrasion 100 m/min: Dissolution/diffusion, adhesion, thermo-mech., abrasion	60 m/min: K <sub>T</sub> , V <sub>B</sub> , chipping 100 m/min: Chipping, K <sub>T</sub> , V <sub>B</sub> , flaking, P <sub>D</sub>	Jawaid et al. [71], Che-Haron [76]

**Abbreviations:**  $v_c$  = cutting speed,  $f_n$  = feed rate,  $a_p$  = depth of cut, K<sub>T</sub> = crater wear, V<sub>B</sub> = flank wear, P<sub>D</sub> = plastic deformation, BUE = build-up edge, Ti-64 = Ti-6Al-4V, Ti-5553 = 5Al-5Mo-5V-3Cr and Ti-6246 = Ti-6Al-2Sn-4Zr-6Mo.

Jawaid et al. [71] verified that the main contributing factors to crater wear progression for WC/Co cutting tools are adhesion, dissolution and diffusion. The same observations were made by Venugopal et al. [72], who executed machining tests on Ti–6Al–4V in both dry and wet conditions at almost the same cutting conditions as the present work ( $v_c = 70\text{--}117$  m/min,  $f_n = 0.20$  mm/rev and  $a_p = 2.0$  mm). Recited from [72], Dearnly and Grearson [84] concluded that the short contact length between cutting tool and chip during titanium machining resulted in elevated temperatures and narrow crater width, which increases the probability of adhesion, dissolution and diffusion.

Recently, Yang et al. [85] presented a tool wear model by combining Usui and Shirakashi's [86] empirical adhesive wear model and Takeyama and Murata's [87] abrasive and diffusion wear model. The model resulted in reliable prediction of crater depth and flank wear. They concluded that the most favorable cutting parameters when cutting Ti–6Al–4V with uncoated WC/Co tools were:  $v_c = 50\text{--}100$  m/min and  $f_n = 0.15\text{--}0.25$  mm/rev.

### 3.2 PREVIOUS RESEARCH ON DIFFUSION WEAR

Diffusion and dissolution are one of the main problems when cutting metals, due to the fact that material from the cutting tool tends to dissolve into the workpiece [89]. This wear progression eventually results in tool failure, and in order to improve tool life, diffusion and dissolution have to be investigated. Temperature has a decisive role when it comes to both chemical solubility and diffusivity, and higher cutting speeds result in elevated temperature at the cutting tool edge [88]. Solubility is exponentially dependent on temperature, and therefore much more prominent at high cutting speeds, which results in more progressive tool wear [89].

Prior investigations on turning titanium alloys indicates that (1) an induced build-up layer of titanium adheres on the cutting edge, which contributes to diffusion and crater wear; and (2) a hard and protective layer of titanium carbide (TiC) forms to slow down diffusion and dissolution [12]. According to Hartung and Kramer [12], Ti–6Al–4V is adhering strongly to the interfacial region of the cutting tool and workpiece material. However, it is believed that the diffusion of tool material to the chips is limited due to the adhered titanium build-up layer [77]. This infers that tool wear would decrease.

A stable layer of TiC was discovered, through Auger electron spectroscopy, in the crater region of WC/Co tools at cutting conditions comparable to those studied in the present work. This confirms a reaction between adhered titanium and carbon from the cutting tool [12]. The hard TiC layer is believed to protect the insert from further tool wear as well as reduce the diffusion speed in the tool-chip interface, because of minor relative contact between the cutting tool and the workpiece material. This proposal was strengthened through Arrazola et al.'s [75] EDS analysis in wet cutting conditions. They found evidence of carbon diffusion into the adherent titanium build-up layer, which indicated that a reaction between the titanium and carbon into TiC might have occurred.

Ezugwu et al. [16] confirmed that carbon diffuses into titanium chips, but that the TiC layer slows down the diffusion. However, carbon is the fastest diffusing element in the cutting tool insert, yet it has a low solubility in both  $\alpha$ -phase titanium (1.1 atomic percent) and  $\beta$ -phase titanium (0.60 atomic percent). It is important to recognize that carbon tends to diffuse to the surface of the cutting edge due to high temperatures in this area, which leads to accumulation of carbon. This means that a greater amount of carbon atoms can react with the adhered titanium build-up layer and form a protective TiC layer.

An investigation by Jianxin et al. [73], in dry turning Ti–6Al–4V, was performed with uncoated WC/Co tools at cutting speeds between 20 and 120 m/min. The feed rate was constant at 0.1 mm/rev, and depth of cut was set to 0.5 mm. It was observed that the main wear mechanisms at the rake face wear land were adhesion and diffusion wear. They performed diffusion couple tests at 400, 600, and 800°C, to study how prominent the diffusion is at different temperatures. Titanium diffusion into the cutting tool, and tungsten and cobalt diffusion into the workpiece material were examined. Evidence of diffusion was observed for all three elements after 90 min for 600 and 800°C, and for the latter, the penetration depth was 20  $\mu\text{m}$ . Hardness tests near the interface revealed lower performance where elemental diffusion had occurred.

The diffusion process that causes crater wear have been explained in two different models, by Molinari and Nouari [90] when machining 1018 steel, and Hou and Shivpuri [91] when machining Ti–6Al–4V. Molinari and Nouari's model relates the cause of crater wear to WC particle diffusion into the steel chips. Their model describes that mass transfer of tungsten, from the crater to the chip, is directly influenced by chip velocity, and indirectly affected by the diffusion rate, which is dependent on average contact temperature in the tool-chip interface [90]. Hou and Shivpuri's model declares that cobalt diffusion is the dominant factor

causing crater wear since the diffusion coefficient ( $D$ ) of WC at  $\sim 1000^\circ\text{C}$  is  $1 \times 10^{-8} \text{ mm}^2/\text{s}$  and much lower than  $D$  of Co  $8 \times 10^{-4} \text{ mm}^2/\text{s}$ , when machining Ti–6Al–4V [91]. It is worth noting that normal cutting temperature when machining Ti–6Al–4V is around  $600\text{--}700^\circ\text{C}$ . They concluded that cobalt diffusion results in less cobalt binder surrounding the brittle WC particles, which consequently results in particles detaching from the substrate and adhering on the sliding chip. Zhang et al. [92] observed WC particles and cobalt atoms on titanium chips with SEM and EDS, and agreed with Hou and Shivpuri that diffusion of cobalt into chips results in crater wear and detachment of WC particles due to less cobalt binder.

### 3.3 PREVIOUS RESEARCH ON CHIP FORMATION

Numerous publications discuss the topics chip formation, adiabatic shear banding, chip morphology and chip formation simulations when machining titanium alloys. The trend of published journal papers where these topics are covered is illustrated in Fig. 3.2, from 1980 to present. The searching was carried out in the Uppsala University Library database [93], and separate searches were done on each topic together with the keyword “titanium alloys”. The number of papers for every topic was separated into ranges of five years.

As can be seen, the number of published journal papers increases exponentially, which likely depends on the skyrocketing market for titanium alloys due to their superior properties. Some of those journal papers, regarding chip formation [31,33–34,36–37,78–81,94–102], adiabatic shear banding [38,78,94,103–116], chip morphology [38,75,77,82,88,117] and chip formation simulations [79,95–97,103–105], covered machining in Ti–6Al–4V, which is studied in the present work. The classical model of catastrophic shear instability was developed by Recht [35] in 1964. Several models have later been presented to explain catastrophic thermoplastic shear in chip formation of difficult-to-cut materials [31–32,34–35,40,93,107]. Recited from Boothroyd and Reinhart [118], the rate of crater wear is dependent on the chip formation mechanism [119]. Consequently, the mechanism of chip formation is important to study.

Nouari and Makich [88] showed that thermal softening becomes more prominent at elevated temperatures, which causes lower yield stress. They discovered that the rate of strain hardening increased at the same time as the thermal softening increased, which implies contradictory behaviors. The thermal softening rate is higher than the work hardening rate when machining titanium alloys, resulting in catastrophic shear localized chips [98].

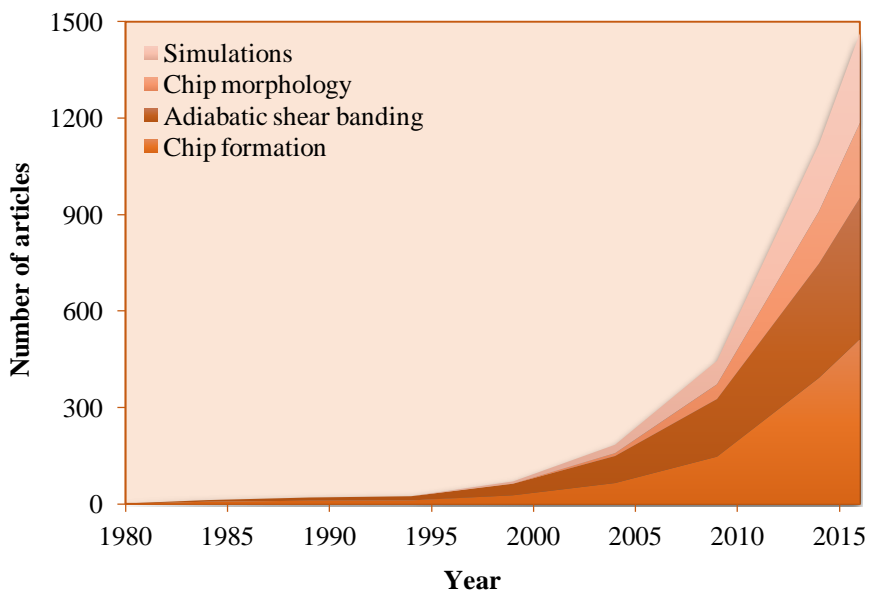


**Figure 3.2.** Numbers of published investigations regarding chip formation, adiabatic shear banding, chip morphology and chip formation simulations, from 1980 to present. This is an approximation with just below 1500 articles.

In a publication by Xie et al. [108], thermal softening was reported as the major cause of catastrophic shear localization and that temperature was of great importance for the flow instability in the chip formation process. The high cutting temperatures of titanium alloys can contribute to shape- and size changes of the grains in the microstructure.

Barry et al. [100] observed that the welding process of titanium build-up layers on the rake face of the cutting tool insert accelerates with increased cutting speed. They believed that this process is responsible for the comparatively high average chip compression ratio ( $\lambda_h$ ) for titanium alloys, compared to other metals, e.g. hardened steels. The chip compression ratio decreases with feed and approaches a constant value for feed between 20 and 100  $\mu\text{m}$ . However, the feed becomes less dependent on the chip compression ratio when increasing the cutting speed from 15 to 180 m/min. Chip compression ratios are always greater than 1.

According to Wan et al. [78], segment spacing, shear band width and degree of segmentation increase with cutting speed (30–178 m/min) for Ti–6Al–4V. Segment spacing was observed to increase with cutting speed to a stagnated value and observations indicated that the shear band width increases at higher speeds due to heat elevation. They concluded that if the cutting speed or feed is high enough, degree of segmentation is asymptotic to 1, which results in separation of each segment into individual chips.

Sutter and List [38], and Sima and Özal [97] agreed with Wan et al. [78] that degree of segmentation increases with cutting speed, but disagree with them about the increment of segment spacing. Their results indicate the opposite that the segment spacing decreases with cutting speed. Miguélez et al. [103] and Molinari et al. [110] came to the conclusion that the shear band width becomes thinner with increment of the cutting speed, which contradicts Wan et al.'s results. They also concluded that the mean shear band spacing ( $d_c$ ) was independent of cutting speed over 60 m/min.

Bayoumi and Xie [99] investigated how the mean shear band spacing was influenced by cutting speed and feed rate, and concluded that the mean shear band spacing had a great impact on the chip formation mechanism. Mean shear band spacing decreased with increasing cutting speed or decreasing feed rate. The latter was believed to have greater effect on mean shear band spacing.

Bayoumi and Xie [99] observed a non-diffusional  $\beta$  to  $\alpha$  phase transformation within adiabatic shear bands, when machining Ti–6Al–4V. The result of this very high speed process was grain changes. Consequently, no changes in chemical composition were observed in the material. However, Wan et al.'s [78] observations of adiabatic shear bands revealed that cutting speed greatly influenced the deformed area. Adiabatic shear bands are deformed at lower speeds and transformed at higher speeds, which is a result of  $\alpha$  to  $\beta$  transformation.

Observations of chip cross-sections indicate that a chip can be segmented and continuous simultaneously [38]. Cracks are often found in adiabatic shear bands of titanium chips, and are related to ductile fracture due to void nucleation, growth of voids and void coalescence within the adiabatic shear band at high cutting speeds [100].

Cotterell and Byrne [101] observed cracks at the chip surface and inside the chip, along the adiabatic shear bands, and related them to the elongation of  $\beta$ -phase as well as void nucleation and coalescence. They also studied the chip segmentation frequency ( $f_{seg}$ ), and concluded that it increased with increasing cutting speed and decreased with increasing feeds. It was later confirmed that the chip segmentation frequency increased with increasing cutting speed [38–39], and additionally confirmed that the chip segmentation frequency was linearly dependent on cutting speed [103].

In another publication by Cotterell and Byrne [37], chip formation was investigated at cutting speeds from 4 to 120 m/min during orthogonal cutting in Ti–6Al–4V with uncoated carbide tools. They observed an increase of the segmentation angle (from about 32–40°) and a decrease of the bulge angle (from about 30–27°) with cutting speed between 4–140 m/min. Shear strain within the segment ( $\gamma_{seg}$ ) slightly decreases with cutting speed, from about 1 to a constant value of 0.75.

Gente and Hoffmeister [36], and Sutter and List [38] investigated chip formation at extreme cutting conditions and observed that shear and segmentation angles were equivalent at very high cutting speeds. Shear strain within the segment was constant around 0.5 at very high cutting speeds (300–4800 m/min) [36].

## CHAPTER 4

### METHODOLOGY

This chapter summarizes the testing methods and sample preparation, as well as the wear and chip characterization.

#### 4.1 TURNING TESTS

A 180x400 mm billet of forged and annealed Ti–6Al–4V alloy from TIMET was used as workpiece material. The elemental composition of the alloy is presented in Table 4.1. The turning tests were performed with external longitudinal cutting in an Okuma Space Turn LB4000 EX-II, CNC controlled turning center, and using water based cutting fluid with 7% oil. Inserts were mounted into a C5-STGCL-35060-16 cutting tool holder. Properties of the Ti–6Al–4V workpiece material are presented in Table 4.2.

**Table 4.1.** Elemental composition of Ti–6Al–4V from TIMET. Titanium is balanced up to 100%.

Element	Ti	Al	V	Fe	O	C	N	H	Residuals
Min [%]	Bal.	5.5	3.5	-	-	-	-	-	-
Max [%]	Bal.	6.75	4.5	0.4	0.2	0.08	0.05	0.015	0.4

**Table 4.2.** Properties of Ti–6Al–4V from TIMET.

Density	Beta Trans	Tensile Strength	Yield Strength	Shear Modulus	Young's Modulus	Thermal Conductivity
4.42 g cm <sup>-3</sup>	996±14 °C	1016±121 MPa	948±120 MPa	41–45 GPa	107–122 GPa	6.6 W m <sup>-1</sup> K <sup>-1</sup>

#### 4.1.1 TURNING OPERATION SETUP

The experimental setup of the turning test is illustrated in Fig. 4.1.  $v_c$ ,  $f_n$ ,  $a_p$ , and  $\kappa_r$  represent the cutting speed, feed rate, depth of cut and entering angle, respectively.

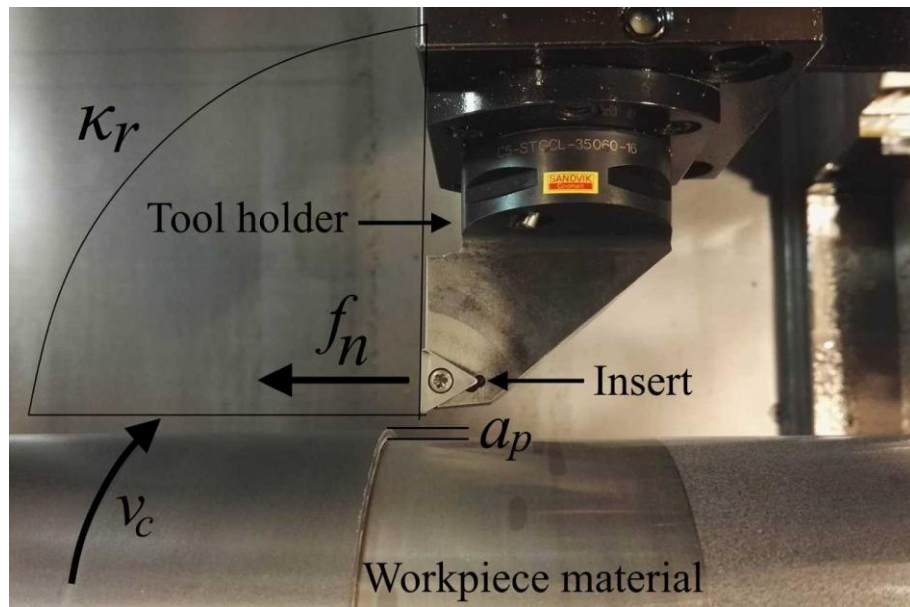


**Figure 4.1.** Experimental setup of the turning machine.  $v_c$  = cutting speed,  $f_n$  = feed rate,  $a_p$  = depth of cut and  $\kappa_r$  = entering angle.

#### 4.1.2 CUTTING PARAMETERS

Cutting conditions are presented in Table 4.3. Four cutting speeds between 30 and 115 m/min were investigated. Cutting feed, depth of cut and entering angle were kept constant at 0.2 mm/rev, 2.0 mm and 91°, respectively.

**Table 4.3.** Cutting conditions during machining tests.

Parameter	Cutting condition			
Cutting speed ( $v_c$ )	30 m/min	75 m/min	90 m/min	115 m/min
Cutting feed rate ( $f_n$ )	0.2 mm/rev	0.2 mm/rev	0.2 mm/rev	0.2 mm/rev
Depth of cut ( $a_p$ )	2.0 mm	2.0 mm	2.0 mm	2.0 mm
Entering angle ( $\kappa_r$ )	91°	91°	91°	91°

#### 4.1.2 CUTTING TOOLS

All investigated cutting tool inserts had TCMW16T308 geometry. The substrate grade was composed of hard tungsten carbide grains in a soft cobalt matrix (WC/Co). Inserts were produced with powder metallurgy, sintered at Sandvik Coromant. The variants were designed with a modified rake surface (MRS) and were either uncoated or coated with CVD. The variants were compared to standard inserts (SIs) without a modified surface. The CVD coating consisted of layers of TiCN, Al<sub>2</sub>O<sub>3</sub>, TiN, and binding layers. Further information about the cutting tool insert is confidential.

A total of 40 turning tests were performed during the machining. Results from these tests can be found in Appendix A1. These were parted into 10 groups (A–J) according to cutting speeds, coating, and rake face topography, see Table 4.4.

**Table 4.4.** Division of machining tests into test groups A–J.

Test group	Cutting speed [m/min]	Coating	Rake Face Topography
A	30	CVD	SI
B	30	CVD	MRS
C	75	CVD	SI
D	75	CVD	MRS
E	75	-	SI
F	75	-	MRS
G	90	-	SI
H	90	-	MRS
I	115	-	SI
J	115	-	MRS

#### 4.2 SAMPLE PREPARATION

Cross-sections were prepared for selected cutting tool inserts from tests A–J, and for titanium chips from tests A–H, see appendices A1–2 for further information regarding selected samples. Inserts were washed with water, detergent and ethanol, and in a Bandelin Sonorex ultrasonic bath before preparation. Selected samples were mounted into conducting Bakelite with ATM Opal 460 hot mounting presses. A Heidenhain Length Gauges MT 30 altimeter was used to measure the height of the Bakelite pellets, in order to control the amount of grinded material. Further information about height measurements and calculation can be found in Appendix G1. Examples of cross-sections of inserts and chips are shown in Fig. 4.2.

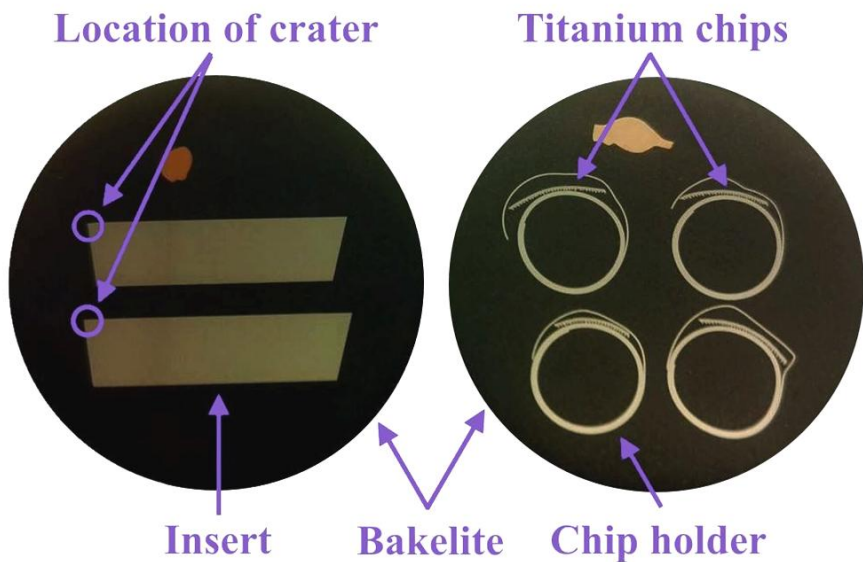


**Figure 4.2.** Hot mounted Bakelite pellets with cross-sections of inserts to the left and titanium chips to the right.

Samples were grinded with Struers Rotopol-V grinding machine and polished with Struers RotoPol-31 and RotoForce-4 polishing machines. They were first polished on paper using 9 µm diamond slurry and oil, and then with 1 µm diamond slurry and oil. Titanium is easily scratched when polished, due to its high ductility; therefore, it was polished in several steps. Application of special polishing equipment, i.e. using Struers Pedemat with 1200/600/220 SiC grits on magnetic polishing pads and fumed silica slurry, resulted in a smoother surface finish. Samples were washed between all steps with water, detergent and ethanol, and between some steps in ultrasonic bath. Illustrative images of hot mounted Bakelite pellets with cross-sections of inserts and titanium.

#### 4.3 WEAR CHARACTERIZATION

Crater wear was measured and imaged with focus variation technique for all test samples A–J. Scanning electron microscope (SEM) was used to investigate the titanium build-up layer for A4, B4, C2, C4, D2, D4, E2, F2, G3, H3, I1, I3, J1, and J3. Electron microprobe analyzer (EMA) was used to analyze diffusion on C2, D2, E2, F2, G3, H3, I3, and J3. The analytical methods and the reason for the analysis are illustrated in Table 4.5. Flank wear was measured and imaged with stereo microscope for all test samples A–J. See appendices A1–2 for further information about the turning test samples.

**Table 4.5.** Analytical methods and the reasons for analysis.

Analysis methods	Reasons for analysis
<b>Wear characterization</b>	
<b>Alicona</b>	$K_T$ measurement Study topography of crater
<b>SEM</b>	Study titanium build-up layer
<b>EMA</b>	Study diffusion of titanium and carbon
<b>Chip characterization</b>	
<b>LOM</b>	Measure geometry of chip Study adiabatic shear bands
<b>SEM</b>	Study adiabatic shear bands
<b>EDS</b>	Study diffusion of WC/Co particles to chips

#### 4.3.1 FOCUS VARIATION: CRATER WEAR PROGRESSION

The crater wear, crater depth ( $K_T$ ) and crater area were documented and measured after the test section, using focus variation with the instrument Alicona InfiniteFocusSL and Alicona IF-MeasureSuit software. All samples from the turning tests were analyzed with focus variation because it was the primary method to image the crater wear region and measure the crater depth and area. Crater depth was measured by identifying the deepest point in the crater wear region, and the crater area was measured by selecting the area of interest, as shown in Fig. 4.3. Selected images on craters in pseudo color can be found in appendices B1–2.

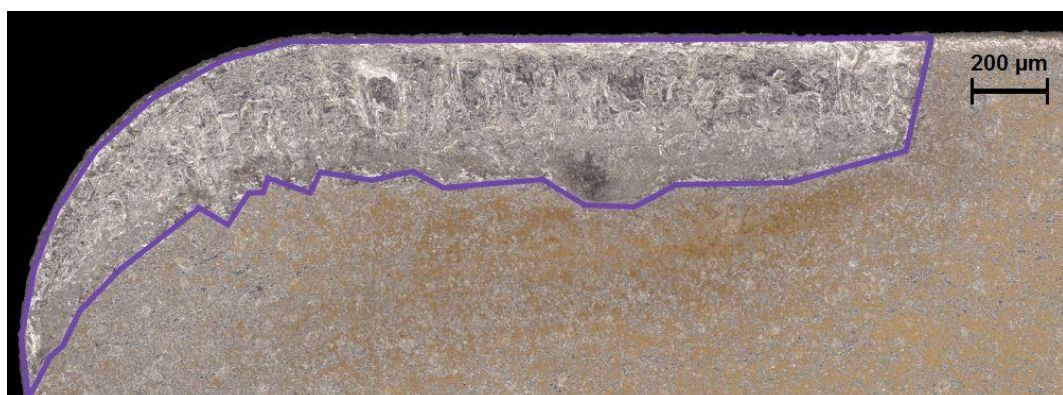


**Figure 4.3.** Method of measurements of crater area in Alicona.

#### 4.3.2 SEM: FORMATION OF A TITANIUM BUILD-UP LAYER

Samples for SEM were selected to study the adhered titanium build-up layer and to image the crater wear profile. A Zeiss Gemini Supra 40 Smart SEM was used to examine cross-sections of cutting tool inserts and titanium chips. A voltage of 10–20 kV was used on most of the micrographs and working distance was set to 10–14 mm. The samples were cleaned with cold water and detergent, placed in ultrasonic bath for a few minutes, rinsed with ethanol, and dried before they were placed into the SEM vacuum chamber.

The insert cross-sections were imaged with backscattered electron (BSE) detector to facilitate inspection with elemental contrast, while titanium chips were imaged with both secondary electron (SE) and BSE detectors. Selected SEM images on the titanium build-up layer can be found in appendices B1–2.

#### 4.3.3 EMA: DIFFUSION

Chemical analysis of titanium, carbon, tungsten and cobalt was executed using a Jeol JXA-8530F HyperProbe EMA. Line scans were performed in the crater area on test sample C2, D2, E2, F2, G3 and H3. The following samples were selected because those had shown interesting results in the Alicona instrument. A schematic illustration of how the EMA line scans and point-to-point analysis were performed is presented in Fig. 4.4.

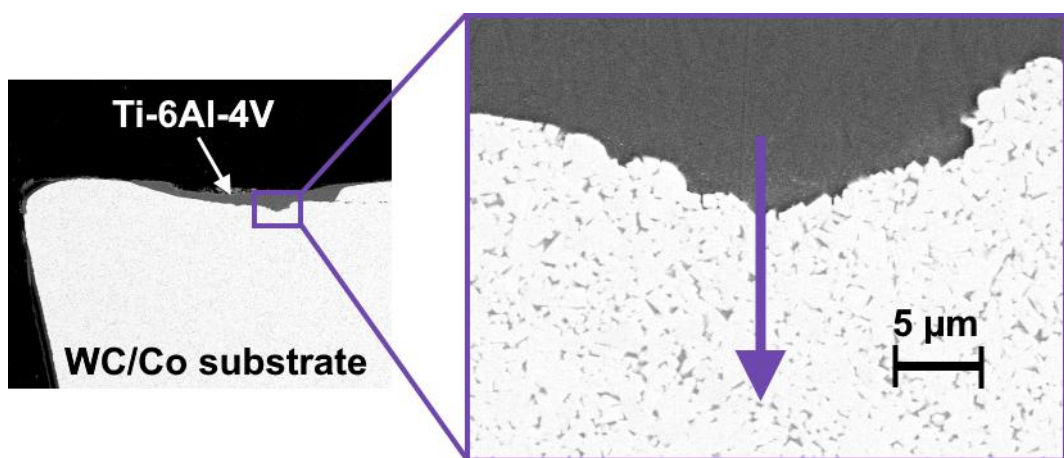


**Figure 4.4.** Cross-sectional SEM image of the crater with titanium build-up layer to the left. A magnification of the corresponding area is illustrated in the SEM image to the right. The arrow schematically indicates the position at which the line scans and point-to-point analysis were executed.

**Table 4.6.** Distance from the first analyzed position, from the titanium build-up layer into the WC/Co substrate.

Point-to-point analysis												
Position	1	2	3	4	5	6	7	8	9	10	11	12
Distance [μm]	0.5	1	1.5	2	2.5	3	3.5	4	5	6	7	12

Line scans were executed at two different locations for C2, E2 and G3, and at four different locations for D2, F2 and H3, due to the irregular topography of the MRS. Raw data from EMA line scans can be found in Appendix C1. Point-to-point analyses were carried out in the crater area on test sample G3, H3, I3 and J3. The analysis was performed at one location for G3 and I3, and at two different locations for H3 and J3, due to the irregular MRS topography. The raw data spectra from the EMA point-to-point analysis is found in Appendix C2.

Table 4.5 presents the positioning of EMA point-to-point measurements along the analyzed line. The exact region where the titanium-WC/Co interface is located is difficult to define due to the low resolution of the microprobe (0.5 μm), but it is expected to be located between position 3 and 5, see Table 4.6. It is assumed that all titanium diffusion passes through the cobalt metal matrix of the WC/Co substrate, due to the higher solubility of titanium in cobalt than in tungsten carbide.

Titanium diffusion into WC/Co substrate is taken into account, not vice versa, due to the fact that the same region of the cutting tool insert is exposed to diffusion continuously, while the workpiece material only is in contact with the insert for a very short time. This means that diffusion of elements in the WC/Co substrate to titanium chips is very small and difficult to analyze. However, large particles of WC/Co will detach from the substrate and adhere to the chips. This process is called particle diffusion, and is analyzed with the aid of energy-dispersive x-ray analysis (EDS).

#### 4.3.4 STEREO MICROSCOPE: FLANK WEAR PROGRESSION

Flank wear was documented using a Nikon SMZ1000 stereoscopic zoom microscope with a Lumenera Infinity 2-2 digital CCD camera. It was measured continuously, with Sandvik's software CoroImage 3.0, after each partial test. Stereo microscope images of flank wear can be found in Appendix D, for all test samples.

## 4.4 CHIP CHARACTERIZATION

Titanium chips were collected for the CVD coated samples at 30–75 m/min and at 75–90 m/min for the uncoated samples. Chips were collected at the beginning of each test, since crater wear leads to changes in the chip mechanism, thus resulting in changes in the chip formation and geometry. Light optical microscope (LOM) was utilized to measure chip geometry parameters, as well as to study chip shape and adiabatic shear bands. SEM was used to image adiabatic shear bands. The samples were cleaned with cold water and detergent, placed in ultrasonic bath for a few minutes, rinsed with ethanol, and dried before they were placed into the SEM vacuum chamber. EDS was performed to examine particle diffusion from cutting tool inserts to titanium chips. F-tests, t-tests and ANOVAs were performed in Microsoft Excel to verify if measurements and other calculated parameters were significantly different between MRSs and SIs, as well as between cutting speeds.

### 4.4.1 LOM: CHIP GEOMETRY

An Olympus BX51M LOM system with an Allied Vision Pike camera was used with the software Picsara Industrial, to image the microstructure, and measure the geometrical parameters mean shear band spacing ( $d_c$ ), segment spacing ( $p_c$ ),  $t_{2max}$ ,  $t_{2min}$ , shear band width ( $\delta_{sb}$ ), segmentation angle ( $\phi_{seg}$ ), shear band projection ( $p_{sb}$ ), and bulge angle ( $\rho_{seg}$ ). For further information about these parameters, see Fig. 2.10.

The segmentation angle, mean shear band spacing, segment spacing, and average chip thickness were measured on about 50 segments of two collected chips. Raw data regarding measurements of mean shear band spacing, segment spacing,  $t_{2max}$ ,  $t_{2min}$ , segmentation angle, and calculations of degree of segmentation, can be found in appendices E1–2. Differences between collected chips were studied to control that the collected chips had similar result, and are presented in Appendix F1.

Degree of segmentation ( $G$ ) was calculated with Eq.8, and chip segmentation frequency was calculated with Eq.9. Shear angles ( $\phi$ ) were calculated from Eq.21, which was derived from Eq.10.

$$\phi = \tan^{-1} \left( \frac{t_1}{\bar{t}_2} \right) \quad Eq. 21$$

For rake angles other than  $0^\circ$ , the shear angle is calculated with Eq.22, which also was derived from Eq.10, see calculation in Appendix G3.

$$\phi = \tan^{-1} \left( \frac{\left(\frac{t_1}{t_2}\right) \cos(\gamma)}{1 - \left(\frac{t_1}{t_2}\right) \sin(\gamma)} \right) \quad Eq. 22$$

where  $t_1$  is the depth of cut,  $t_2$  is the average chip thickness and  $\gamma$  is the rake angle. Shear strain in the adiabatic shear band ( $\gamma_c$ ), shear strain within the segment ( $\gamma_{seg}$ ) and total shear strain within the adiabatic shear band ( $\gamma_{sb}$ ) were calculated with equations 14–19. Shear band width, bulge angle and shear band projection was measured on five segments of two collected chips. Measurements of shear band width, shear band projection, and bulge angle can be found in Appendix E3.

#### **4.4.2 EDS: DIFFUSION TO CHIP**

An Oxford X-MAS EDS system connected to a Hitachi S-4300 FEG-SEM was used to observe whether particles from the cutting tool were attached to the backside of the chips. The analyzed area was  $60 \times 40 \mu\text{m}$ . EDS spectra can be found in Appendix H.

#### **4.4.3 EXCEL: STATISTICAL ANALYSIS OF VARIANCE ON CHIP PARAMETERS**

Statistical analyses of variance were performed with F-tests, t-tests and ANOVAs in Microsoft Excel in order to investigate chip parameters and shear strains ( $d_c$ ,  $p_c$ ,  $t_2$ ,  $\delta_{sb}$ ,  $\phi_{seg}$ ,  $p_{sb}$ ,  $\rho_{seg}$ ,  $G$ ,  $\gamma_c$ ,  $\gamma_{seg}$ , and  $\gamma_{sb}$ ). Data were assumed to be normally distributed. F-tests were performed to determine whether the variances of SIs and MRSs were equal. If this was the case, a t-test with the assumption of equal variances was selected, if not, a t-test with the assumption of unequal variances was selected. The t-test determined if SI and MRS could be assumed to be derived from the same underlying population, or whether a significant difference between the two samples could be found. ANOVAs indicated whether the distribution of data for a specific parameter between groups of SIs and MRSs and different cutting speeds were significantly different or not. All test results of F-tests, t-tests and ANOVAs can be found in Appendix G2.

## CHAPTER 5

### RESULTS AND DISCUSSIONS

This chapter presents and discusses the results for wear characterization, followed by the results for chip characterization.

#### 5.1 WEAR CHARACTERIZATION

This section covers crater wear, diffusion of titanium, titanium build-up layer, as well as flank wear and tool life. It is important to note that every new measurement, i.e. points in Fig. 5.1 and 5.3 and 5.9, represents a new cutting edge, due to the fact that continuous cutting was performed.

##### 5.1.1 EFFECTS ON CRATER WEAR

Results from Alicona crater depth ( $K_T$ ) measurements are summarized in Fig. 5.1. Since the inserts were not etched, an adhered titanium build-up layer was still present in the crater area. This leads to uncertainties regarding depth measurements. The titanium build-up layer was left on the crater to be studied at a later point.

There is no big difference between the modified rake surface inserts (MRSs) and the standard inserts (SIs) for CVD coated samples at a cutting speed of 30 m/min, represented by green lines in the left graph in Fig 5.1. The MRS seems to be more resistant to crater wear during the first seconds of machining although only one repetition may be too few to draw any conclusions. When performing only one single repetition of each turning test, there is a risk of obtaining large variations of tool wear. This may be the case for the coated SI at a cutting speed of 75 m/min after 3 s, which resulted in an equally deep crater as the SI after 60 s at the same cutting speed. The explanation to this behavior is likely related to the CVD coating, which is possibly not very well adhered to the substrate.

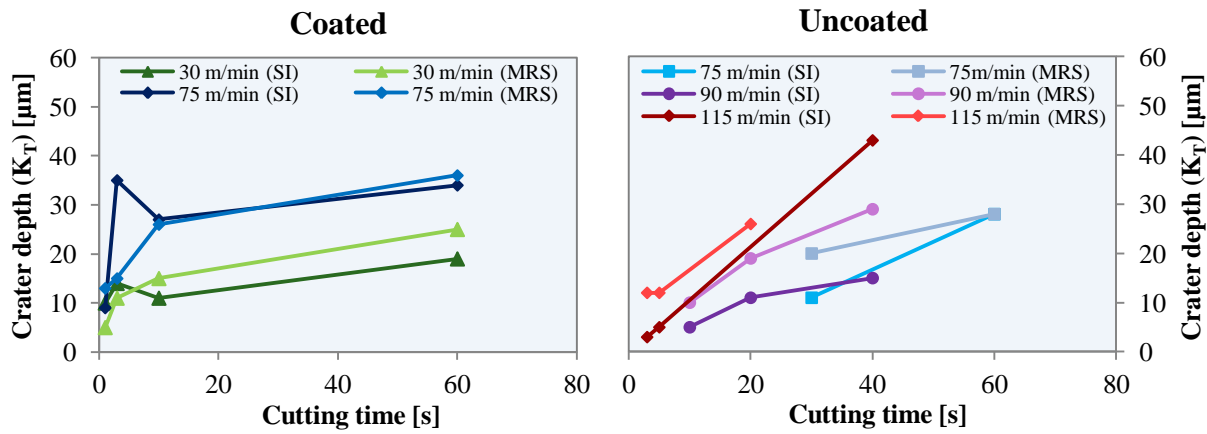


**Figure 5.1.** Summarized results of crater depth measurement for all investigated speeds, separated into MRSs and SIs. The CVD coated inserts are presented in the left graph and the uncoated in the right. Every measurement represents a new cutting edge.

The cross-section of sample C2, coated SI at 75 m/min after 3 s, is shown in Fig. 5.2 and shows a lateral crack in the crater region, parallel to the rake face. This kind of crack was only observed in one case. However, it is possible that this lateral crack was caused by the fast removal of the coating due to mechanical damage although this could not be verified. The coating is much harder than the substrate and could easily damage the substrate by physically crushing the surface. It is therefore suggested that the coating removal process has an effect on the detachment of larger pieces of WC/Co material from the substrate. If this suggestion is correct, lateral cracks could result in faster-than-normal crater wear rate.

As can be seen in Fig. 5.2, the coating was removed instantly, and the blue arrow reveals a small area of coating that is still present at the cutting edge. Appendices B1–2 present focus variation images of the topography of the crater in pseudo color taken with Alicona instrumentation, SEM images of crater cross-sections and surface profile diagrams near the cross-sections for 12 of the investigated inserts. The CVD coated inserts have a larger crater area than the uncoated inserts at similar cutting speed and time, and is illustrated in Fig. 5.3. This probably depends on the quick coating removal process.

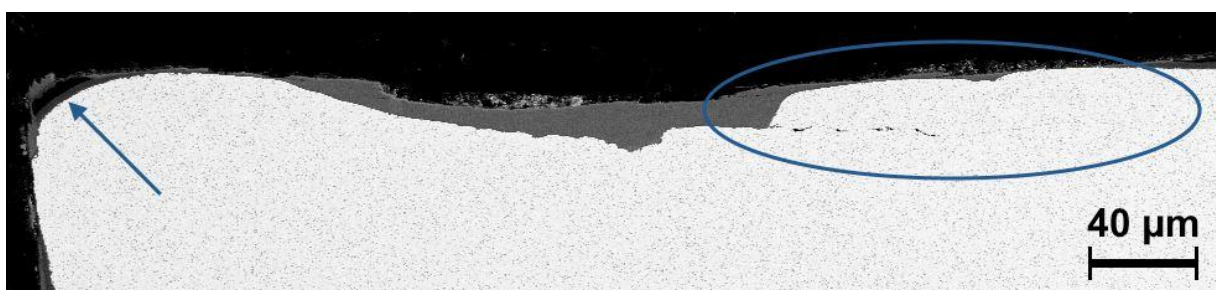


**Figure 5.2.** Cross-section of the crater of sample C2. The blue ellipsis shows a lateral crack in the crater area. The blue arrow shows the CVD coating.

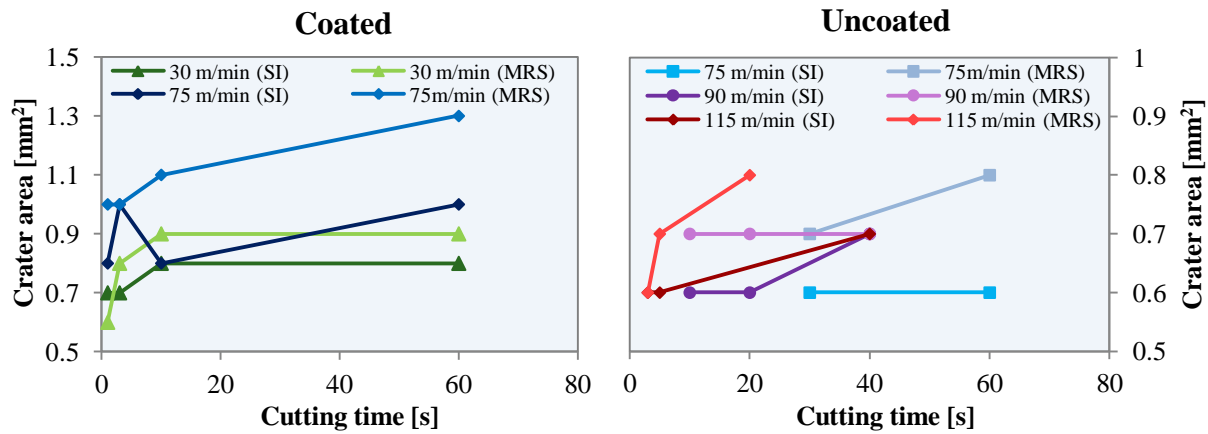


**Figure 5.3.** Summarized results of crater area measurement for all investigated speeds, separated into MRS and SI. The CVD coated inserts are presented in the left graph and the uncoated inserts are presented in the right graph in the right. Every measurement represents a new cutting edge.

Sample C2 (Appendix B1) reveals large areas of removed material, while sample D2 (Appendix B2) appears to be more resistant to large material removal, which may be related to the topography of the MRS. It is observed that coated inserts produce a more unevenly worn crater than uncoated inserts, and that sample B4 and D2 (MRSs) retain the coating longer than A4 and C2 (SIs), see appendices B1–2. This can also be related to the topography of the MRS, which might prevent the very quick removal process of the CVD coating. However, the coating did not last long enough to meet the qualities required in the machining industry. After the coating removes, MRSs wear out faster than SIs. Results presented in the right graph in Fig. 5.1 shows that uncoated MRSs have greater crater depth than SIs at all investigated speeds. It is concluded that MRSs retain the coating for a longer time than SIs, and that the coating removes in a matter of seconds. It is also observed that crater wear progression is greater on MRSs than on SIs after coating is totally worn.

It is observed that the CVD coating is worn outside the tool-chip contact zone and therefore causes a larger crater area, while the uncoated inserts are only affected the regions where contact has occurred. The size of the crater area is not changed much during machining. However, uncoated MRSs at a cutting speed of 115 m/min show a difference of 0.2 mm<sup>2</sup> within 20 s. This can be explained by the high cutting speed and that the topography of MRSs is a contributing factor. Alicona, SEM, crater depth and crater area measurements strengthen the suggestion that CVD coated inserts have a higher probability of developing large lateral cracks than uncoated inserts, which result in higher wear rate. Application of coatings is therefore believed to shorten tool life due to that it is quickly worn out. Bear in mind that only one lateral crack proposes this suggestion and further investigation is needed to verify it. However, crater wear was greater on MRS than on SI inserts after coating removal.

### 5.1.2 IMPACT OF DIFFUSION AND TITANIUM BUILD-UP LAYER

Titanium diffusion into the WC/Co substrate and the level of carbon near the tool-chip interface were studied with EMA. The titanium and carbon content is presented in counts, and is a measurement of concentration. However, the titanium counts can be regarded as the diffusion flux ( $J$ ) of titanium. Results from the EMA analysis are presented in figures 5.4–8 and appendices C1–2. As can be seen in figures 5.4–8, the titanium diffusion is comparable to the diffusion flux shown in Fig. 2.5.

Figures 5.4–6 represent EMA line scans, and figures 5.7–8 represent EMA point-to-point analysis. Lower graphs show diffusion from left to right, starting 4  $\mu\text{m}$  before the substrate, either in the titanium build-up layer (for all uncoated inserts and top positions of coated inserts), or in the CVD coating (for the bottom positions of the coated inserts). The 0 point is the interface and illustrated with a dotted line. Upper graphs illustrate separate magnifications of titanium and carbon diffusion from the highlighted area in the lower graph. Titanium is presented in blue colors and carbon is presented in red colors. Same colors define line scans, or point-to-point analyses, at different positions on the same sample.

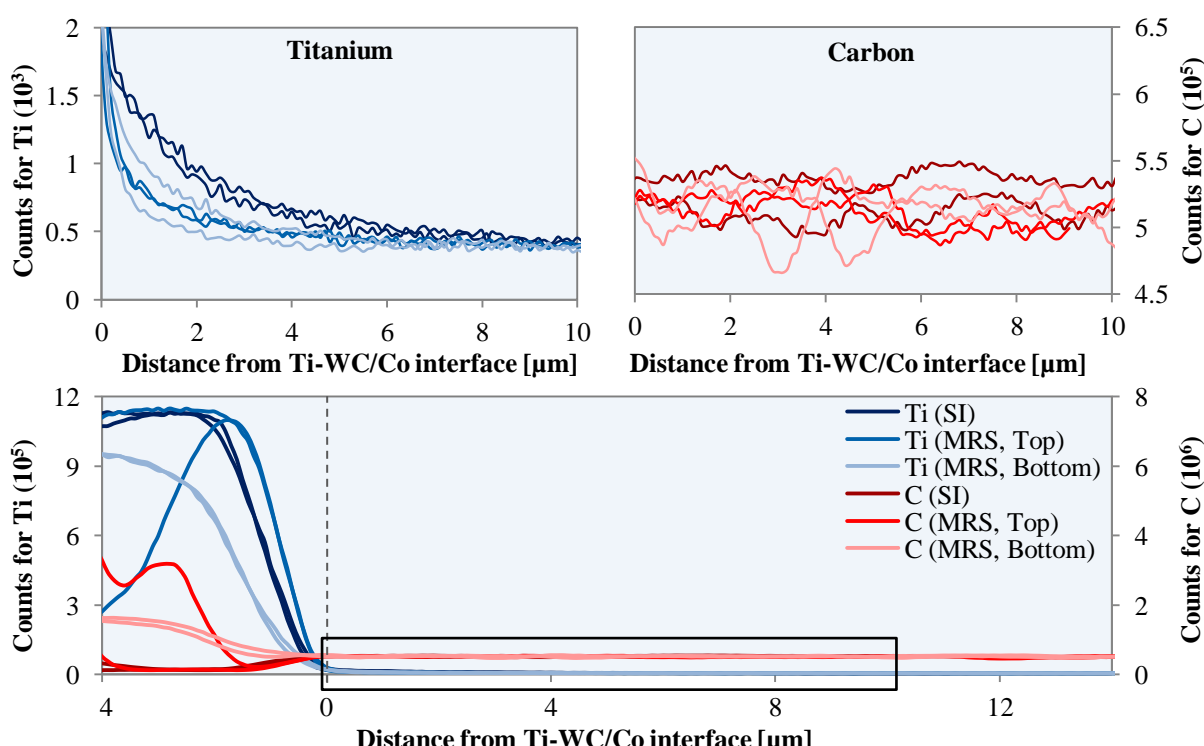


**Figure 5.4.** Coated, 75 m/min after 3 s. The graphs represent EMA signals of titanium (blue) and carbon (red), respectively. The upper graphs are magnifications of the highlighted area in the lower graph. Each line in the respective diagrams corresponds to one EMA line scan. The dotted line at zero marks the interface.

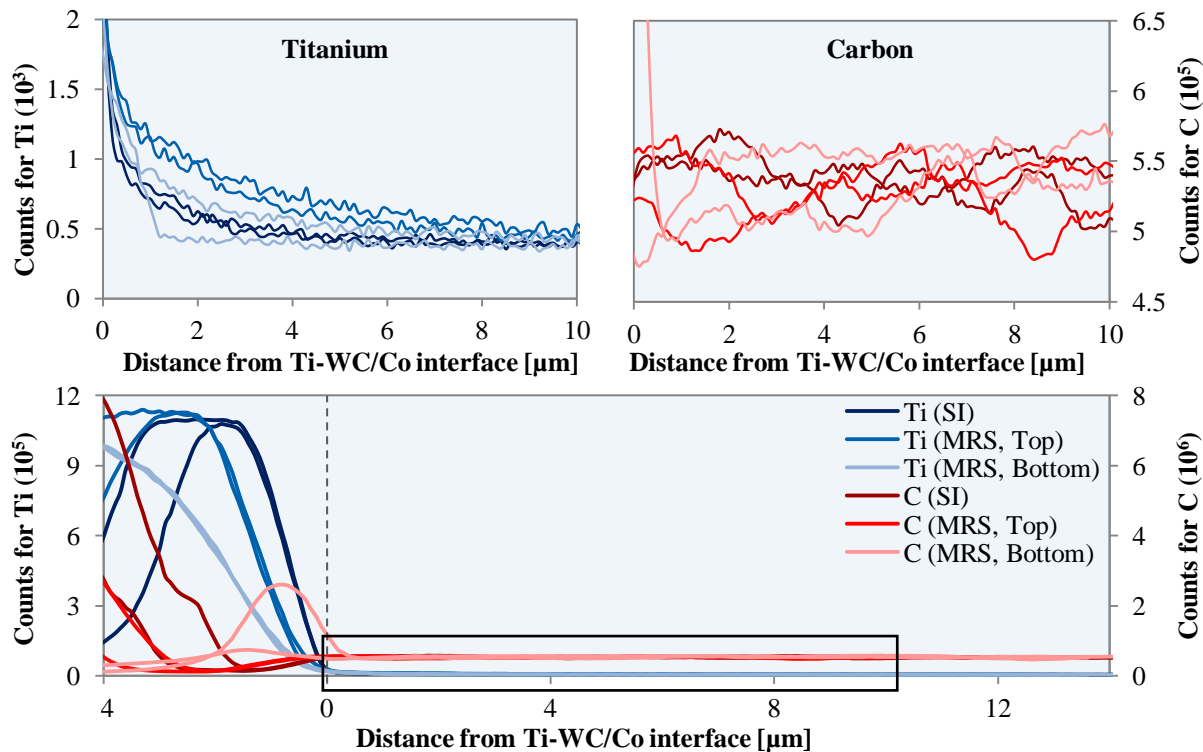


**Figure 5.5.** Uncoated, 75 m/min after 60 s. The graphs represent EMA signals of titanium (blue) and carbon (red), respectively. The upper graphs are magnifications of the highlighted area in the lower graph. Each line in the respective diagrams corresponds to one EMA line scan. The dotted line at zero marks the interface.

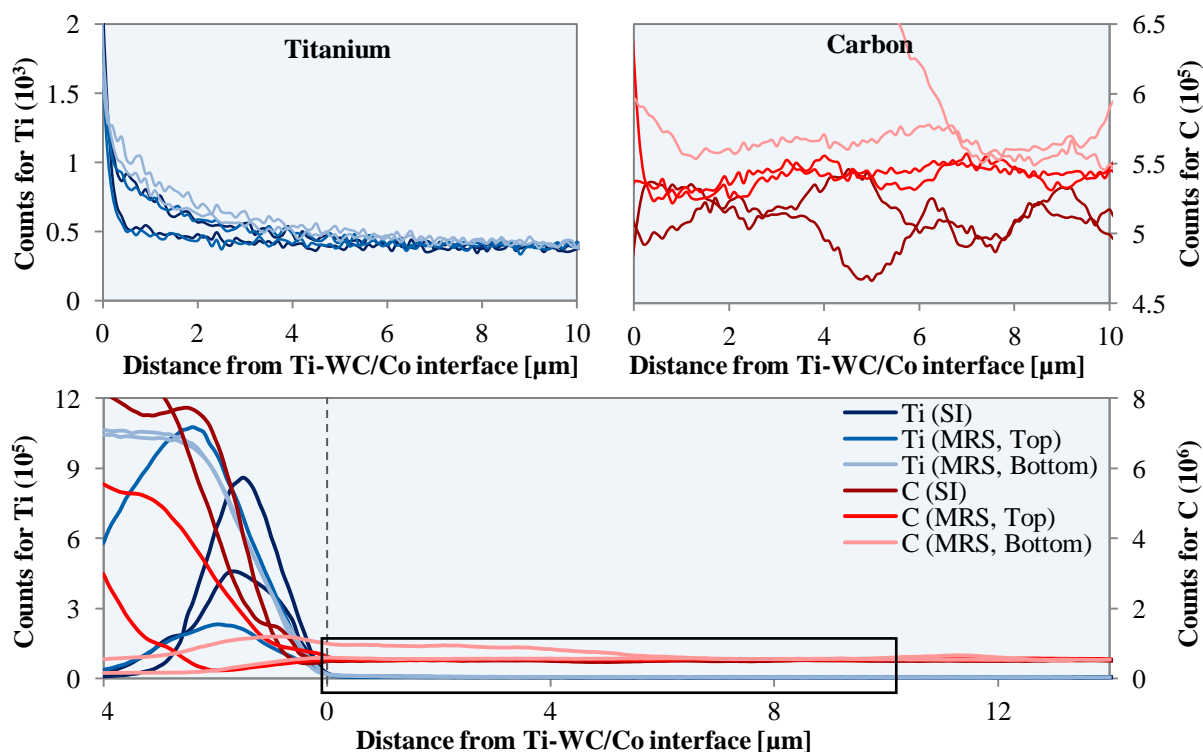


**Figure 5.6.** Uncoated, 90 m/min after 40 s. The graphs represent EMA signals of titanium (blue) and carbon (red), respectively. The upper graphs are magnifications of the highlighted area in the lower graph. Each line in the respective diagrams corresponds to one EMA line scan. The dotted line at zero marks the interface.

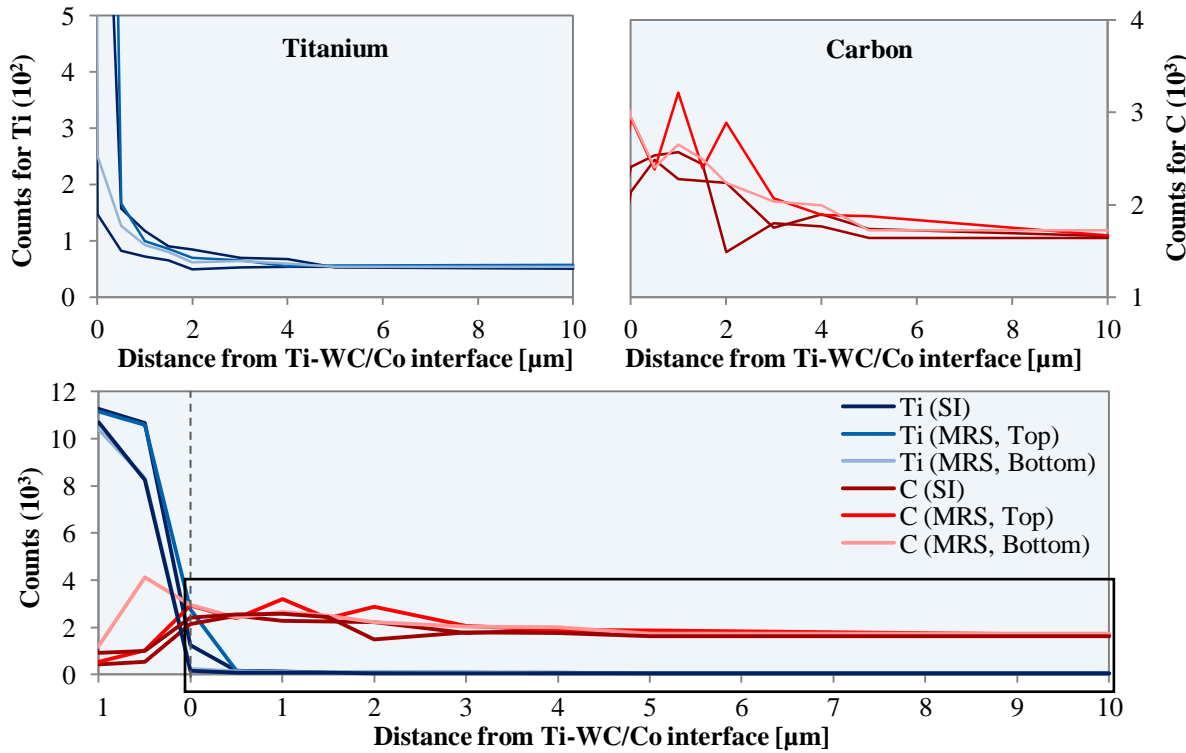


**Figure 5.7.** Uncoated, 90 m/min after 40 s. The graphs represent EMA signals of titanium (blue) and carbon (red), respectively. The upper graphs are magnifications of the highlighted area in the lower graph. Each line in the respective diagrams corresponds to one EMA point-to-point analysis. The dotted line at zero marks the interface.

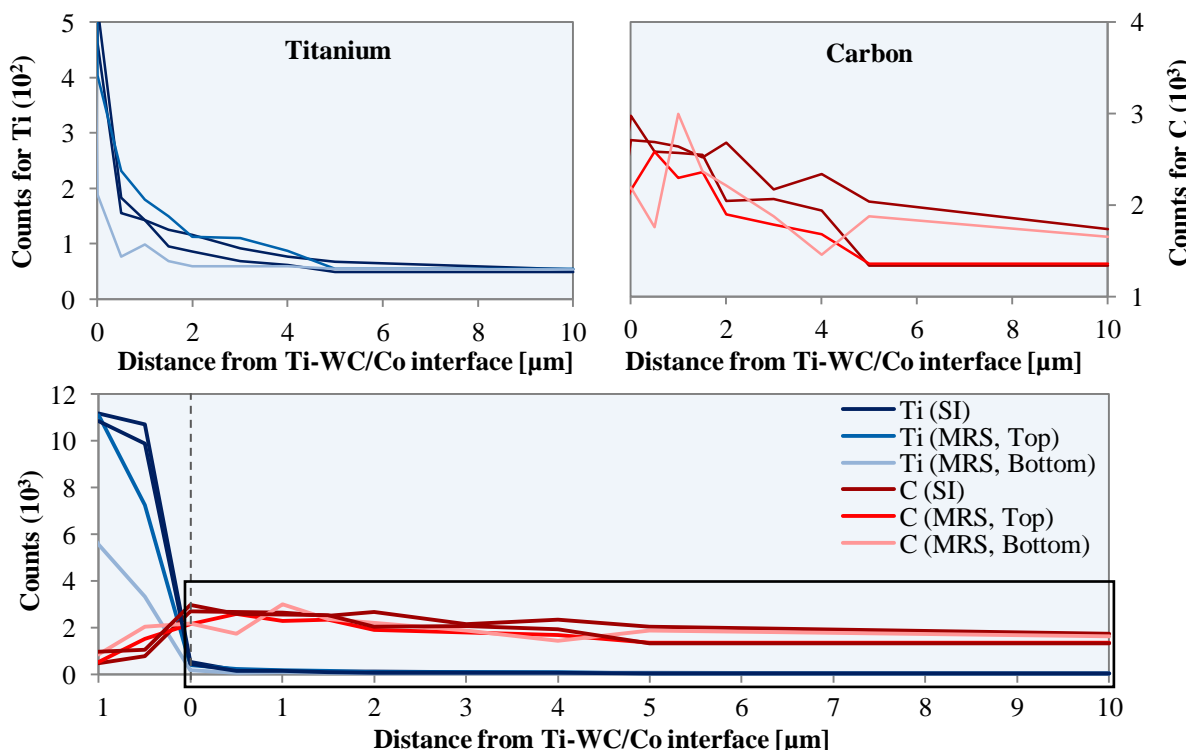


**Figure 5.8.** Uncoated, 115 m/min after 20 s for MRS and 40 s for SI. The graphs represent EMA signals of titanium (blue) and carbon (red), respectively. The upper graphs are magnifications of the highlighted area in the lower graph. Each line in the respective diagrams corresponds to one EMA point-to-point analysis. The dotted line at zero marks the interface.

The diffusion in samples C2 and D2 are presented in Fig. 5.4. The upper left graph illustrates that the diffusion flux for titanium is more predominant for SIs than MRSs in the early stage of the machining process. This is probably related to coating removal process, which is also discussed in 5.1.1. MRSs still had coatings left after 3 s, while the coatings on SIs were totally worn out. Thus, it is believed that the CVD coating prevents diffusion of titanium. MRS top positions should be exposed to a higher degree of diffusion than MRS bottom positions, if the coating does prevent the diffusion flux, since the coating is still present at bottom positions and not at top positions. This is clearly observed in the SEM image on sample D2 in Appendix B2. However, one of the MRS bottom line scans (light blue line between darker blue lines), in Fig. 5.4, has higher diffusion flux than the MRS top, which is difficult to explain. An uncoated insert machined at a cutting speed of 75 m/min after 60 s is shown in Fig. 5.5. The upper left graph indicates that titanium seems to have diffused more for SIs than MRSs, although carbon is at a constant level in the interface for all inserts. It reveals that uncoated SIs are exposed to titanium diffusion to a lower extent than coated SIs, and that uncoated MRSs are exposed to titanium diffusion to a higher extent than coated MRSs. This is related to the MRS, which has a larger contact area than the plane rake face of SIs.

The diffusion of titanium into the WC/Co substrate seems to be at approximately the same level at the same depths but different cutting times. Therefore, it is believed that the diffusion rate of titanium into the substrate has the same rate as the crater wear progression, which demonstrates that trace amounts of titanium in WC/Co make the substrate less resistant to crater wear. This indicates that the wear rate is dependent on titanium diffusion. However, previous research related crater wear to cobalt diffusion from tool substrate into titanium chips. This was believed to make WC particles detach, due to undermined bonds between cobalt and WC particles [91–92]. This was not investigated in the present work, and therefore, further research is recommended to verify these suggestions. Uncoated inserts at a cutting speed of 115 m/min are presented in Fig. 5.8. MRS was machining for 20 s and SI for 40 s. Although exposed to different cutting times, the MRS top position had a higher diffusion flux of titanium than the two different positions for SI, and MRS bottom position had diffused the least amount of titanium. CVD coating on top positions of the MRS was worn out as quickly as for SIs, but bottom positions of the MRS retained the coating for a longer time and observations from EMA suggest that the CVD coating prevents diffusion. This may indicate that MRSs control diffusion better than SIs.

The lower graph in figures 5.4–8 shows carbon diffusion into the titanium BUL, which indicates that a reaction between titanium and carbon may have occurred to form TiC. This possible TiC layer might have reduced the diffusion of titanium into the substrate, as previous research has concluded [12,16,75]. However, there were no observations of a TiC layer in EMA or SEM and no further analysis to detect TiC was executed.

Large amounts of carbon were also detected for some of the MRSs and SIs for all investigated samples, which for coated samples can be related to carbon from the coating. Though, this is not the case for the uncoated samples, where 10 times as high carbon content was detected for SIs at 90 m/min as for titanium in the titanium BUL, see Fig. 5.6. Figures 5.6–7 illustrates the same uncoated insert at the same cutting speed of 90 m/min after 40 s, performed with EMA line scan and point-to-point analysis, respectively. However, the presented results appear to be very diverse and hard to explain. Line scans show that carbon is at a constant level in the WC/Co substrate, see figures 5.4–6, but EMA point-to-point analysis reveals that carbon has a tendency to accumulate in the tool-chip interface, see figures 5.7–8. Carbon accumulation near the interface was also observed by Ezugwu et al. [16], and was believed to increase the TiC formation.

### 5.1.3 FLANK WEAR AND TOOL LIFE

Flank wear ( $V_B$ ) increases with cutting time and cutting speed, which can be seen in Fig. 5.9 and Appendix D. It is noticed that something critical happened for the 115 m/min SI after 3 s (sample I1), which has as much flank wear as the 115 m/min SI after 40 s. Though, the fact

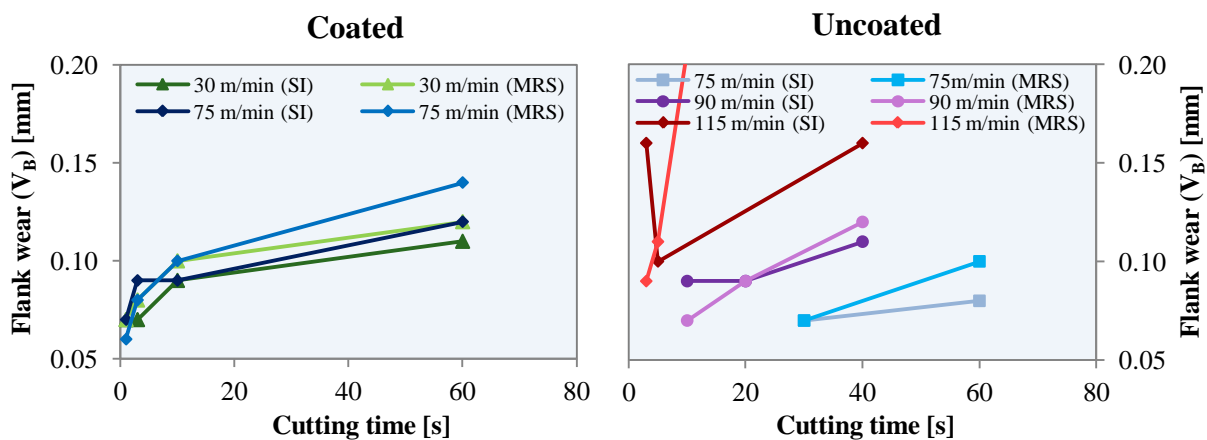


**Figure 5.9.** Summarized results of average flank wear measurement for all investigated speeds, separated into MRSs and SIs. The CVD coated inserts are presented in the left graph and the uncoated in the right. Every measurement represents a new cutting edge.

that every measurement represents a new cutting edge makes it possible that sample I1 was affected by variations during machining, which resulted in severe flank wear even after 3 s. Another variation for uncoated tools at 115 m/min arose after 20 s for the MRS tool (sample J3), which depended on that maximum flank wear was measured instead of average  $V_B$ , see Fig. D5 in Appendix D. This resulted in a sky-high point outside the graph in Fig. 5.9. When the standard and modified inserts were coated they showed almost no difference in flank wear. However, MRS at a cutting speed of 30 m/min (green) seems to wear out at a slower rate after 3 s and MRS at a cutting speed of 75 m/min (blue) after 10 s compared to respective SIs. However, flank wear was generally greater on MRS than on SI inserts.

A tool life investigation considering flank wear was performed at the cutting speed of 75 m/min, and illustrated in Fig. 5.10. The tool life criterion of  $V_B$  was set to be 0.20  $\mu\text{m}$ , marked as a dotted line in the left hand graph. Surprisingly, flank wear was the factor that limited tool life. The results show that SIs have longer tool life than MRSs. Tool life was 4 and 5 min for SIs and only 2 min for MRSs, which points out that SIs showed lower flank wear than MRSs. Worth noting is that the machining operations were performed in tough cutting conditions because it was desired to form a crater at a short cutting time. Consequently, this resulted in shorter tool life than what is required in the machining industry. It is possible that different cutting conditions have an effect on how the crater wear progression develop for MRSs compared to SIs, which can result in great differences in tool life for MRSs compared to SIs, at smoother cutting conditions. SIs are observed to have twice as long tool life as MRSs for both CVD- and uncoated inserts at 75 m/min.

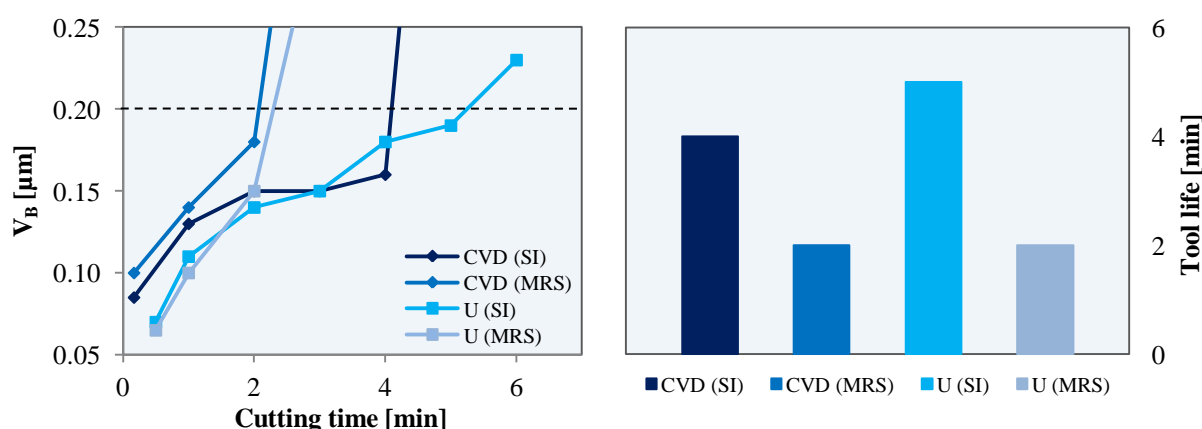


**Figure 5.10.** Summation of tool life tests at 75 m/min for CVD coated SI (C6) and MRS (D3–6), as well as uncoated SI (E4) and MRS (F1–4). Flank wear progression at measured on the same insert during the whole process. The dotted line marks the tool life criteria.

By summing the results from the wear characterization section, it is believed that the CVD coating reduce diffusion. However, application of coating can cause other wear mechanisms that accelerate crater wear progression. Diffusion is reduced for modified inserts, due to the fact that parts of coating at bottom positions remain for a longer time than coating on standard inserts. Results from EMA also show that uncoated inserts with modified surface have higher diffusion rate than standard inserts. The crater depth measurements present deeper craters for modified inserts than standards, which indicate a faster crater wear progression. Standard inserts have around twice as long tool life as modified inserts for both coated and uncoated inserts at a cutting speed of 75 m/min.

## 5.2 CHIP CHARACTERIZATION

This section covers chip geometry, degree of segmentation, segmentation frequency, segmentation- and shear angles, shear strains, as well as particle diffusion into chips. The investigated chips are denoted as follows:

- CVD (MRS) = coated inserts with modified rake surface
- U (MRS) = uncoated inserts with modified rake surface
- CVD (SI) = coated inserts with standard surface
- U (SI) = uncoated inserts with standard surface

### 5.2.1 GEOMETRICAL ANALYSIS OF CHIP FORMATION

As illustrated in Fig. 5.11, the mean shear band spacing ( $d_c$ ) of the chips has a tendency to increase between cutting speeds of 30 and 75 m/min, for CVD (MRS), but decrease for CVD (SI). The trend is the opposite for U (MRS) at cutting speeds between 75 and 90 m/min; mean shear band spacing is greater at 75 m/min than at 90 m/min. U (SI) increases between these cutting speeds.

Previous research suggested that mean shear band spacing decreased with increasing cutting speed [99], which corresponds well to CVD (MRS) and U (SI) in Fig. 5.11. However, ANOVA indicated no significant difference of mean shear band spacing between the cutting speeds, and t-tests only indicated a significant difference between MRS and SI at 90 m/min. Based on this, the conclusion is that the modified rake surface influences mean shear band spacing to decrease at 90 m/min.

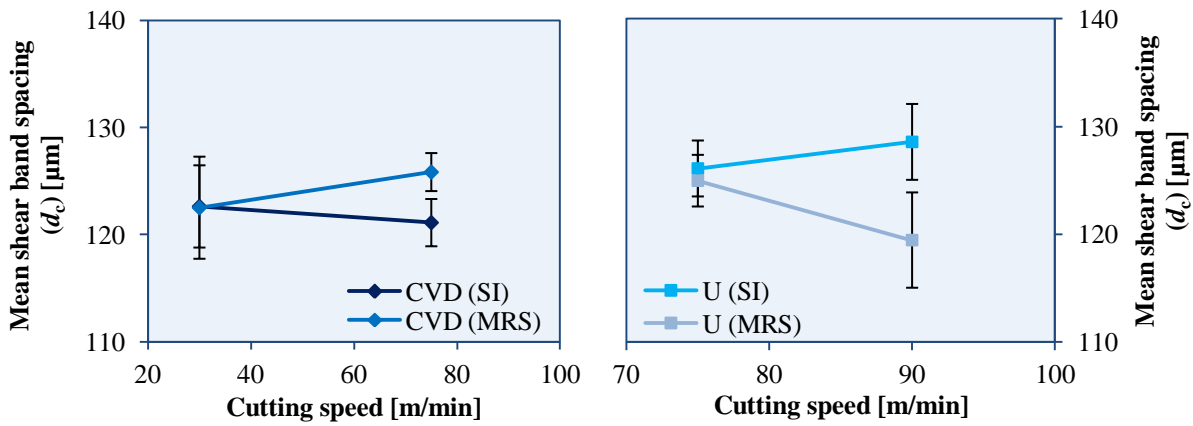


**Figure 5.11.** Mean shear band spacing, with standard error, for CVD- and uncoated SI and MRS inserts at different speeds: 30, 75, and 90 m/min. Every point is a mean value of 50.

The segment spacing ( $p_c$ ) is presented in Fig. 5.12, which is greater at 75 m/min than at 30 m/min for both CVD (MRS) and CVD (SI) although MRSs render a steeper curve. Segment spacing have the same divergent appearance as mean shear band spacing for U (MRS) and U (SI) at cutting speed between 75 and 90 m/min. Segment spacing decreases for U (MRS), while it has a tendency to increase for U (SI). ANOVA indicated significant differences for  $p_c$  between the cutting speeds, and t-tests indicated that there are significant differences between CVD (MRS) and CVD (SI) at 75 m/min, as well as between U (MRS) and U (SI) at 90 m/min. This concludes that the segment spacing increases with cutting speed for SIs, that it increases at lower speeds and decreases at higher speed for MRSs. It is possible that the CVD coating changes the chip formation mechanism differently from the uncoated tools due to coating removal. As shown in Fig. 5.13, the degree of segmentation ( $G$ ) looks very similar to the corresponding graphs of  $p$ . The similarities of results in Fig. 5.11–13 designates that the measurements have been done accurately.

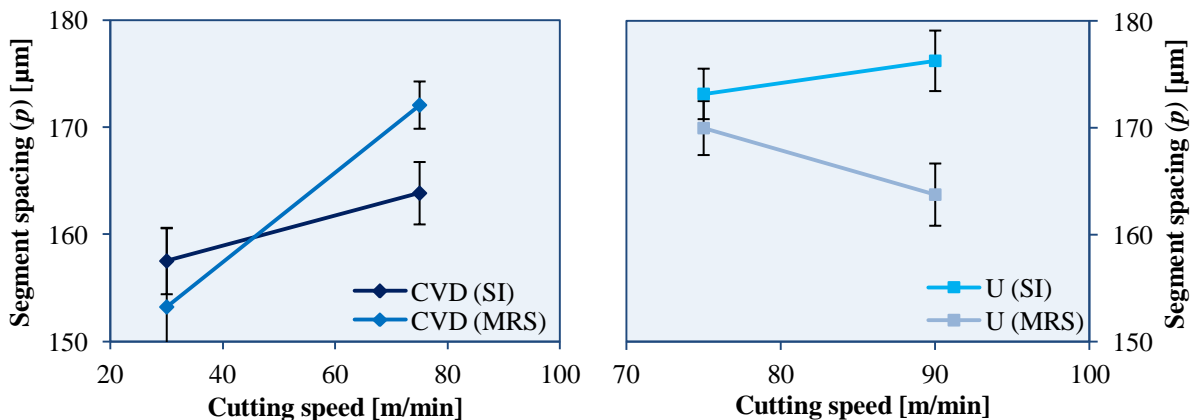


**Figure 5.12.** Segment spacing, with standard error, for CVD- and uncoated SI and MRS inserts at different speeds: 30, 75, and 90 m/min. Every point is a mean value of 50.

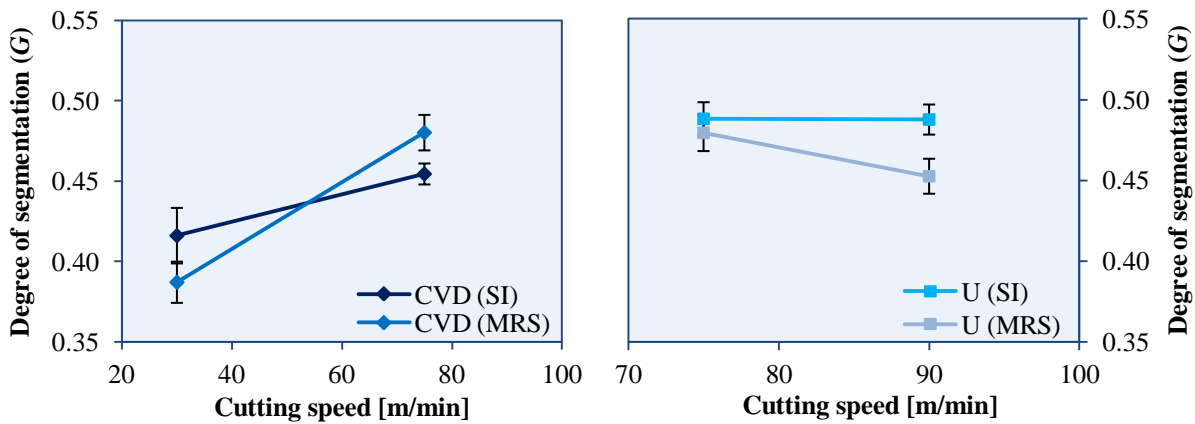


**Figure 5.13.** Degree of segmentation, with standard error, for CVD- and uncoated SI and MRS inserts at different speeds: 30, 75, and 90 m/min. Every point is a mean value of 50.

ANOVA indicated significant differences of  $G$  between the cutting speeds, and t-tests indicated that there are differences between CVD (MRS) and CVD (SI) at 75 m/min, as well as between U (MRS) and U (SI) at 90 m/min. This indicates that the degree of segmentation increases with cutting speed for SIs, but stagnates at higher speeds. Degree of segmentation increases with a steeper incline at lower speeds for MRSs than for SIs, and decreases at higher speeds for MRSs. Previous researches support that degree of segmentation increases with increasing cutting speed [38,78,97]. However, observations indicate that the degree of segmentation does not change at higher cutting speeds for chips machined with uncoated inserts.

Appendix F1 presents differences between the two collected chips from the same cutting conditions. For all tests but one, there were no considerable differences between the chips, but for mean shear band spacing at 30 m/min there was a difference of 8  $\mu\text{m}$ , when cutting with MRS tools. This can be explained by the large variances of chip geometry between the two chips, see Fig 5.14.

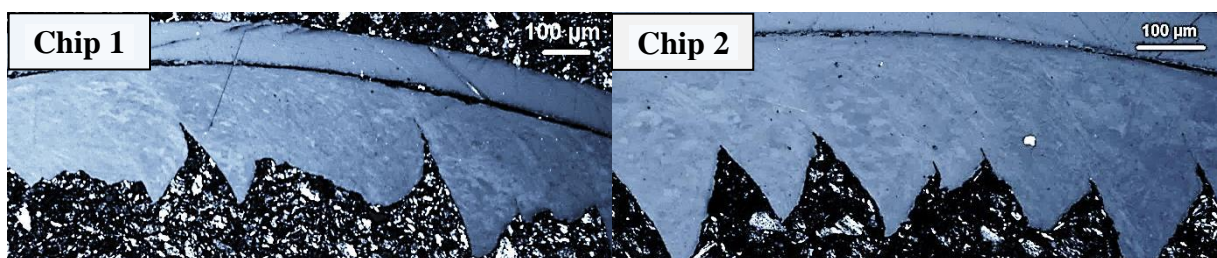


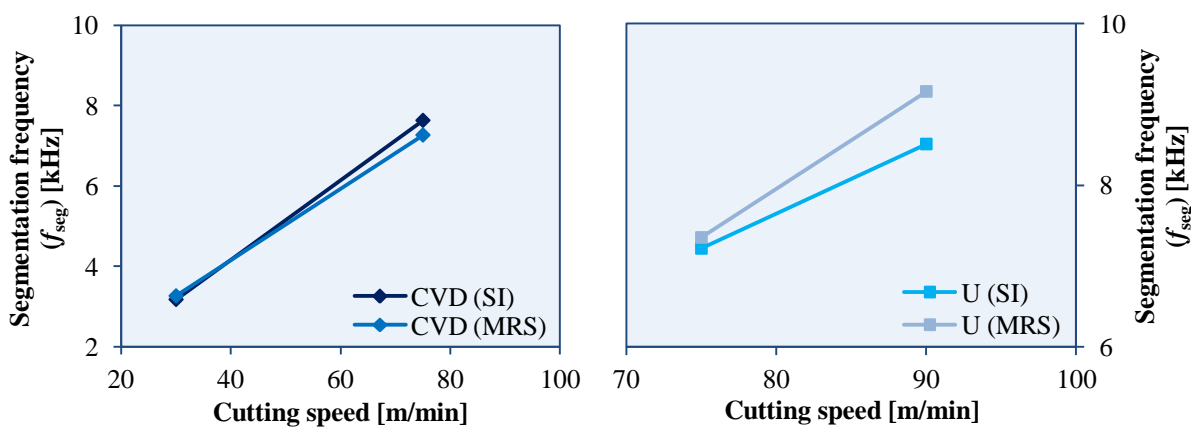
**Figure 5.14.** Comparison of two different chips from the same cutting conditions (Cutting speed: 30 m/min when cutting with MRS tools).

Some parts of chip 1 had regions with almost no serration, compared to the more regular serration of chip 2. Another reason behind this geometrical irregularity could be that the pellet was grinded too much, see Appendix F1. This means that the cross-section of these chips was not located in the middle of the chips, but rather to the edge, where the serration is more asymmetrical.

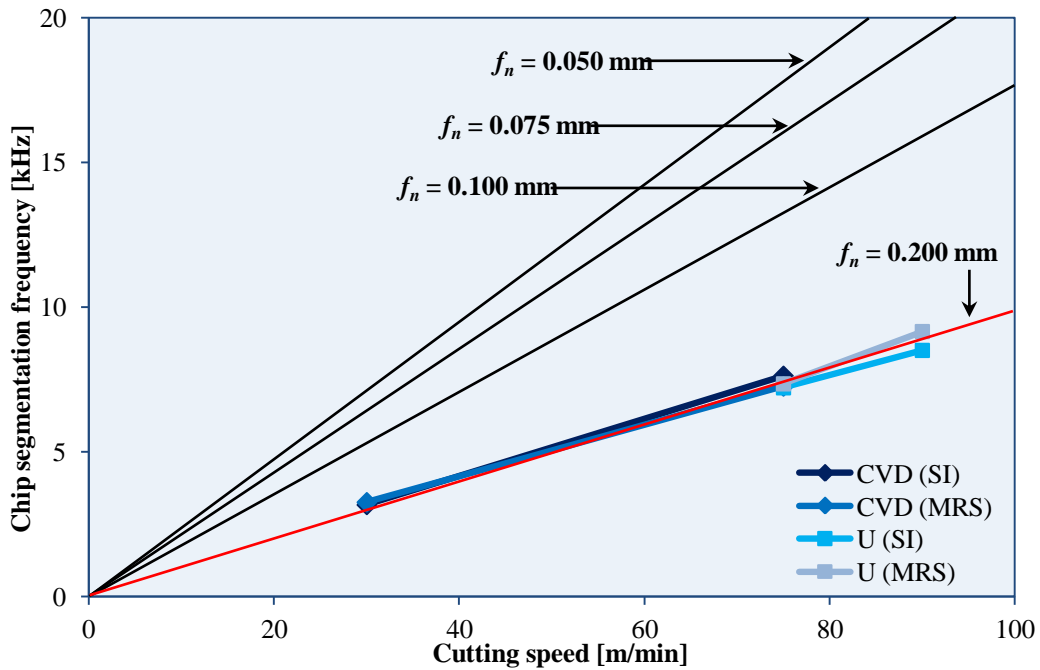
### 5.2.2 SEGMENTATION FREQUENCY

Fig 5.15 illustrates that the chip segmentation frequency ( $f_{seg}$ ) increases with increasing cutting speed for both uncoated and CVD coated inserts. However, no significant difference is observed between MRSs and SIs. Although the segment spacing decreases at higher cutting speed for MRSs, chip segmentation frequency clearly increases with increasing speed for both MRSs and SIs. This corresponds to previous results [37–38,97].

Trend lines from previous data (black lines) [97] versus a trend line from the present work (red line) are presented in Fig. 5.16, and shows that the same trend continues for  $f_n = 0.200$  mm. It is evident that the slopes decrease from the feed of 0.050 to 0.200 mm, and that chip segmentation frequency is linear against cutting speed. This indicates that chip segmentation frequency is less dependent on cutting speeds at greater feeds. Worth mentioning is that [97] performed orthogonal cutting, while the present work performed oblique cutting.



**Figure 5.15.** Chip segmentation frequency ( $f_{seg}$ ) at different cutting speeds for MRS and SI. Every point is a mean value of 50.



**Figure 5.16.** Chip segmentation frequency at different cutting speeds and feed rates ( $f_n$ ). The black lines are comparative lines at feed rates 0.050 to 0.100 from [97], and the red line illustrates the trend from the present work. Every point is a mean value of 50.

### 5.2.3 SEGMENTATION- AND SHEAR ANGLES

As illustrated in Fig. 5.17, the segmentation angle ( $\phi_{\text{seg}}$ ) decreases for CVD (MRS) and CVD (SI), between cutting speeds of 30 and 75 m/min. However, the segmentation angle has a tendency to increase for U (MRS) and U (SI), at cutting speeds between 75 and 90 m/min. The chips appear to have slightly larger segmentation angle when cutting with MRS tools compared to SIs, at all investigated cutting conditions.

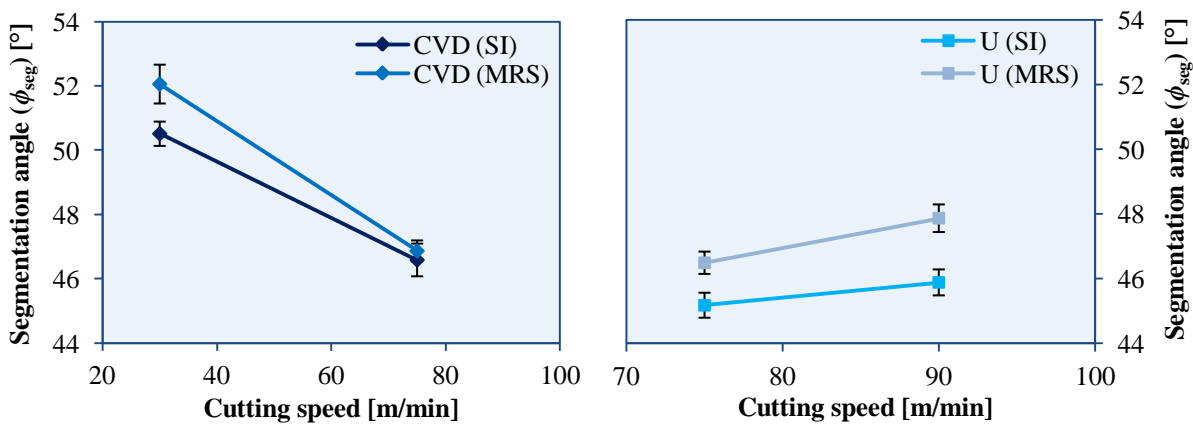


**Figure 5.17.** Segmentation angle, with standard error, for CVD- and uncoated SI and MRS inserts at speeds: 30, 75, and 90 m/min. Every point is a mean value of 50.

ANOVA indicated significant differences for  $\phi_{\text{seg}}$  between the cutting speeds, although t-tests only indicated significant differences at cutting speeds of 75 and 90 m/min between U (MRS) and U (SI). According to Cotterell and Byrne [37], the segmentation angle should increase with cutting speed for uncoated carbide tools, which is the case in the present work. Coating the tool seems to increase the segmentation angle, which can be caused by the quickly worn out coating.

Figures 5.18–19 illustrate measured and calculated values of segmentation angle and shear angle, respectively. Comparisons between SIs, and MRSs is presented in Fig. 5.18 and 5.19, respectively. The calculated values of the shear angle ( $\phi$ ) are stable right below  $45^\circ$  at all investigated cutting speeds, which corresponds well to [36] (although that result was obtained at extreme cutting speeds). However, the segmentation angle seems to reach a minimum at 75 m/min cutting speed for both MRS and SI.

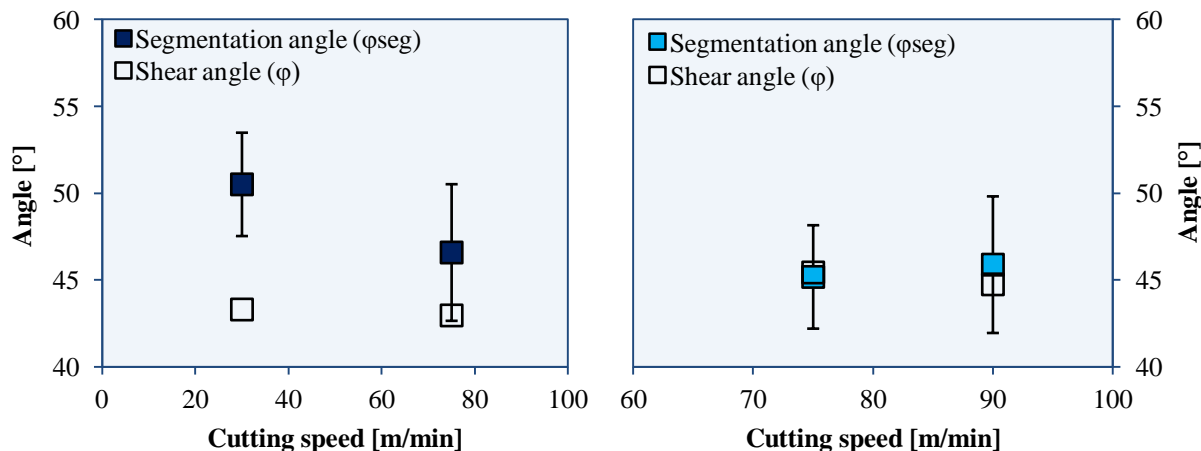


**Figure 5.18.** Comparisons of segmentation angle against shear angle from chip measurements with standard deviation and calculated value of shear angle for SIs.

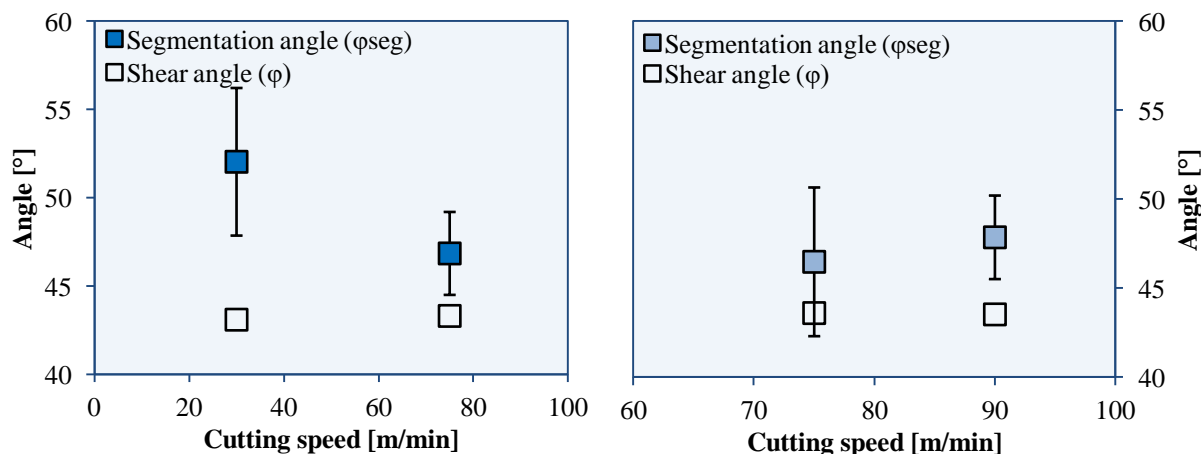


**Figure 5.19.** Comparisons of segmentation angle against shear angle from chip measurements with standard deviation and calculated value of shear angle for MRSs.

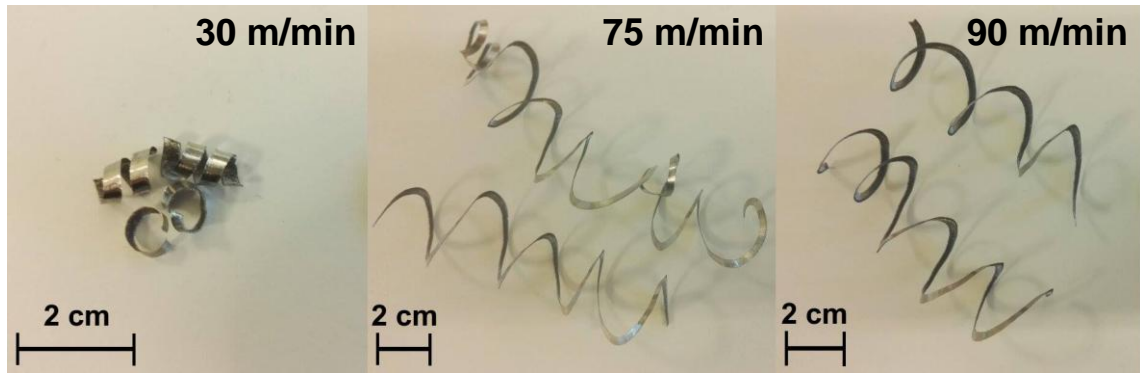


**Figure 5.20.** Chips collected from machining tests. Cutting speeds from left to right: 30, 75 and 90 m/min. Note that the scales are different for each speed.

The greatest difference observed between shear- and segmentation angles is at a cutting speed of 30 m/min. The reason for this can be that this speed had a steeper curvature of the helical chips than the curvature rendered at higher speeds, and therefore it is harder to measure exactly. Differences in size of the chips between various cutting speeds are shown in Fig. 20. Machining at a cutting speed of 30 m/min produces much smaller chips. Apart from this, lower cutting speeds produce chips where the serration faces the center, while higher cutting speeds produce chips where the serration faces upwards, like a spiral staircase.

#### 5.2.4 EVOLUTION OF SHEAR STRAINS

Results from calculation of shear strains are presented in figures 5.21–23, as average values of five calculations respectively. Shear strain within the segments ( $\gamma_{seg}$ ) is presented in Fig. 5.21, and appears to reduce with increased cutting speed. CVD (MRS) appears to undergo greater shear stress than CVD (SI)s at cutting speeds of 30–75 m/min. However, the results from the uncoated inserts are contradictory due to the fact that U (SI)s have higher shear strains than U (MRS)s. ANOVA indicated significant differences of  $\gamma_{seg}$  between the cutting speeds, although t-tests indicated no significant difference between CVD (MRS) and CVD (SI), or U (MRS) and U (SI) at the various cutting speeds. Shear strain within the adiabatic shear band ( $\gamma_c$ ) is presented in Fig. 5.22 and is much higher than the shear strain within the segment, which was expected. It is observed that shear strain in the adiabatic shear band does not change for CVD (MRS)s for cutting speeds of 30–75 m/min. It was a great increase of shear strain in the adiabatic shear band for CVD (SI)s at cutting speeds of 30–75 m/min, from 9.6 to 12.7, and also for U (MRS) from 11.6 to 12.9 at cutting speeds of 75–90 m/min. However, the results from the uncoated inserts differ due to the fact that the shear strain for U (SI) decreases from 12.3 to 9.5 at cutting speeds between 75–90 m/min.

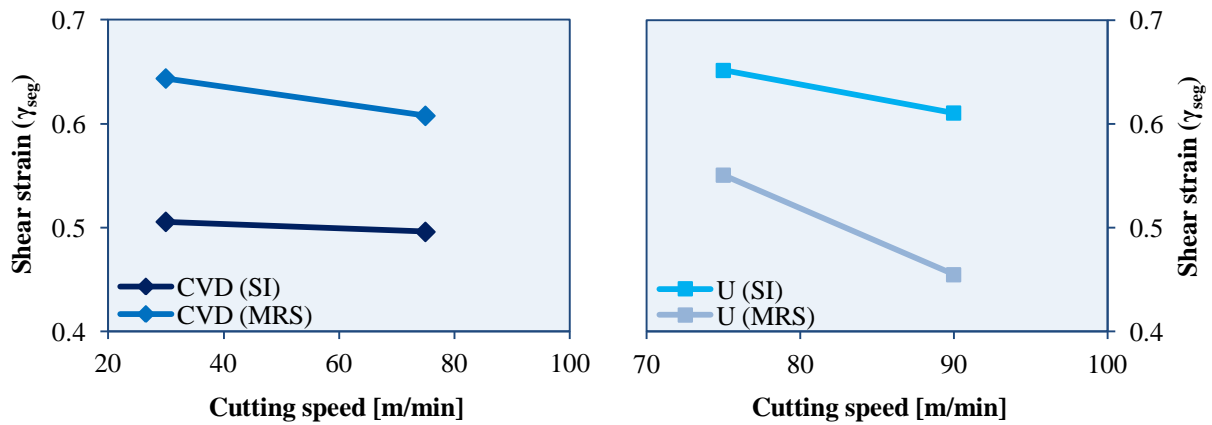


**Figure 5.21.** Shear strain within the segment ( $\gamma_{seg}$ ) at  $f_n = 0.20$  mm and  $a_p = 2.0$ . Left graph represents the chips machined with CVD-coated inserts and the right graph represents the chips machined with uncoated inserts. Every point is a mean value of five.

ANOVA did not indicate significant differences of  $\gamma_c$ , but t-tests indicated significant differences between U (MRS) and U (SI) at 90 m/min. The differences of shear strain in the adiabatic shear band depend on the fact that the shear band width ( $\delta_{sb}$ ) is thinner for MRSs than for SIs, 17.1  $\mu\text{m}$  compared to 22.2  $\mu\text{m}$ , see Appendix E3. Another contributing factor is that the shear band projection ( $p_{sb}$ ) was 9  $\mu\text{m}$  longer for MRSs than for SIs. This means that MRSs might have greater crack initiation along the adiabatic shear bands than SIs have. Total shear strain within the adiabatic shear band ( $\gamma_c$ ) is defined as the addition of shear strain in the adiabatic shear band and shear strain within the segment ( $\gamma_c + \gamma_{seg}$ ), and is presented in Fig. 5.23. As can be seen, total shear strain within the adiabatic shear band has the same appearance as shear strain in the adiabatic shear band, but higher values due to that shear strain within the segment is small and does not affect the shear strain in the adiabatic shear bands so much.

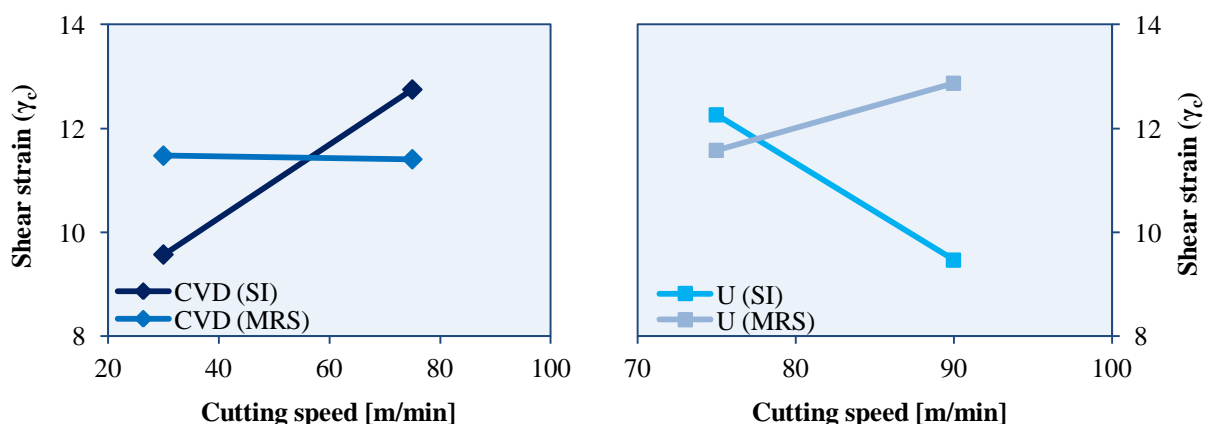


**Figure 5.22.** Shear strain within the adiabatic shear band ( $\gamma_c$ ) at  $f_n = 0.20$  mm and  $a_p = 2.0$ . Left graph represents the chips machined with CVD-coated inserts and the right graph represents the chips machined with uncoated inserts. Every point is a mean value of five.

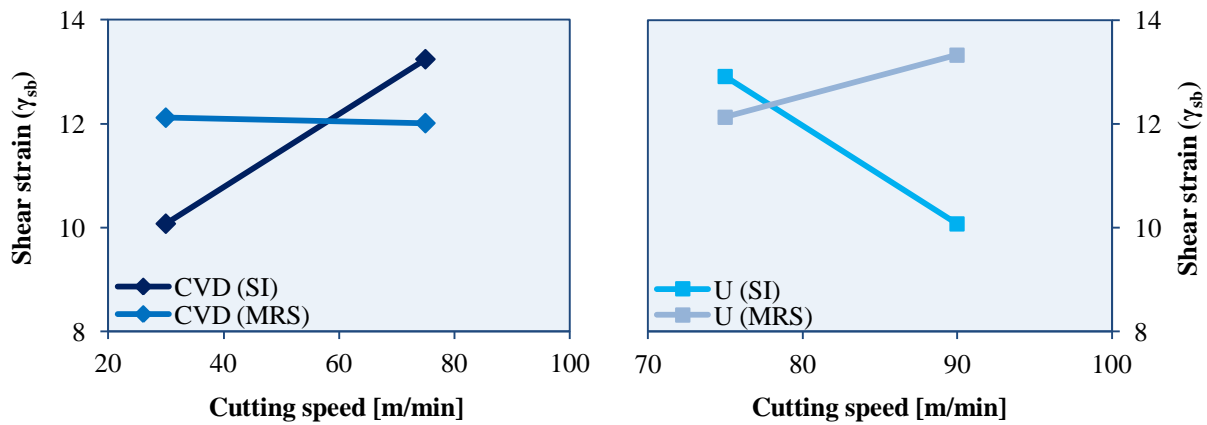


**Figure 5.23.** Total shear strain within the adiabatic shear band ( $\gamma_{sb}$ ) at  $f_n = 0.20$  mm and  $a_p = 2.0$ . Left graph represents the chips machined with CVD-coated inserts and the right graph represents the chips machined with uncoated inserts. Every point is a mean value of five.

ANOVA indicated no significant difference of  $\gamma_{sb}$  between the cutting speeds, although t-tests indicated that there are significant differences between U (MRS) and U (SI) at 90 m/min. The same conclusions as stated earlier for shear strain in the adiabatic shear band apply to total shear strain within the adiabatic shear band as well. Values of  $\gamma_{seg}$  tends to be between 0.45 and 0.65, and values of  $\gamma_{sb}$  tend to be between 10.1 and 13.3. This results correlate well with previous research. Turley et al. [32] calculated  $\gamma_{seg}$  to 1.3 and  $\gamma_{sb}$  to 8, when machining titanium. Cotterell and Byrne [101] calculated  $\gamma_{seg}$  to 0.6 at 30 m/min and 0.5 at 90 m/min, when machining Ti-6Al-4V, although in orthogonal cutting with  $f_n = 0.10$  mm. SEM images of adiabatic shear bands are presented in figures 5.24–25 and illustrates that cracks are located inside the adiabatic shear band. When cracks form within the adiabatic shear band, they become much thinner.

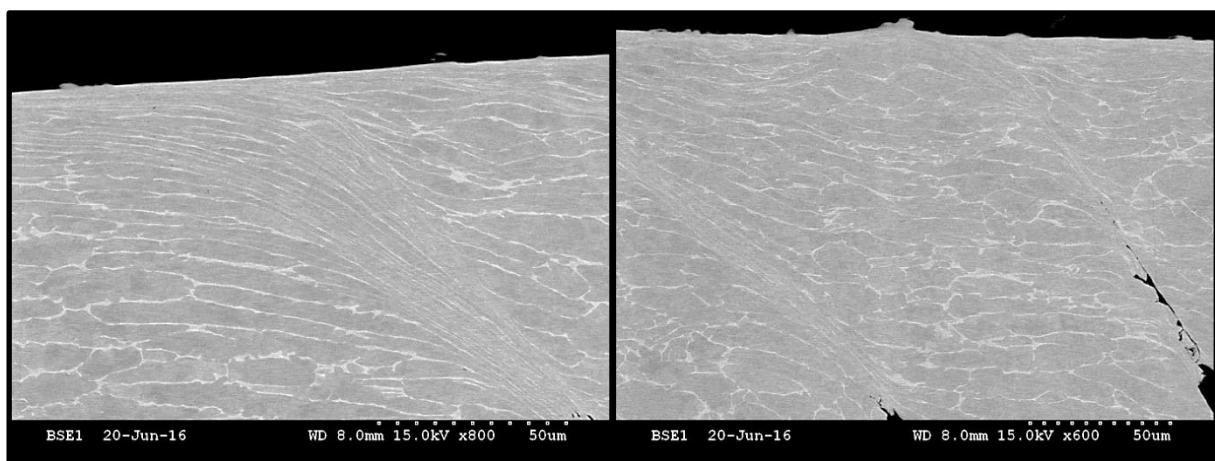


**Figure 5.24.** Adiabatic shear bands on uncoated standard inserts at 90 m/min.

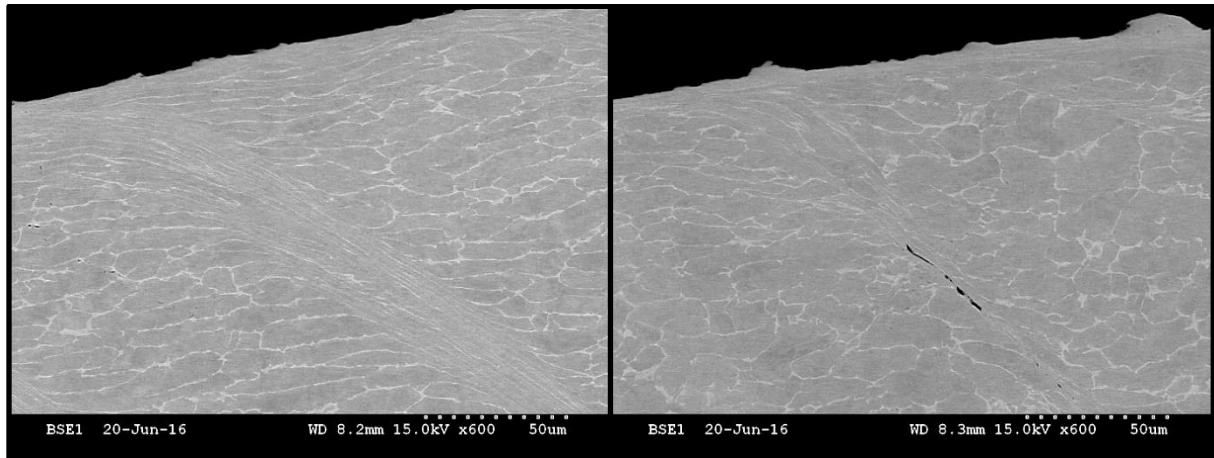


**Figure 5.25.** Adiabatic shear bands on uncoated modified inserts at 90 m/min.

It is also observed that shear band width varies very much within the same speed, which seems to be caused by the presence of cracks. Appendix F2 presents SEM images of chips at all cutting speeds. It is important to note that some of the shear band width and shear band projection measurements were taken on places where a small initiating crack was located, which could have an imminent effect on the shear strain results. However, no measurements of shear band width and shear band projection were taken on large initiating cracks, or on cracks within the adiabatic shear band.

The chip formation mechanism can be described by the mean shear band spacing, chip segmentation frequency, segmentation angle, shear strain within the segment, shear strain in the adiabatic shear band and total shear strain within the adiabatic shear band ( $G$ ,  $d_c$ ,  $f_{seg}$ ,  $\phi_{seg}$ ,  $\gamma_{seg}$ ,  $\gamma_c$ , and  $\gamma_{sb}$ , respectively). To observe differences in the chip formation mechanism between standard and modified inserts, it is important to correlate and find relations between these parameters. Turley et al. [32] calculated shear strain within the segment by using mean shear band spacing, while the present work used equations from Cotterell and Byrne [37], without evolving the mean shear band spacing. This implies that shear strain within the segment should be dependent on mean shear band spacing. By plotting those parameters against each other it was possible to observe that this was the case, see Fig. 5.26.

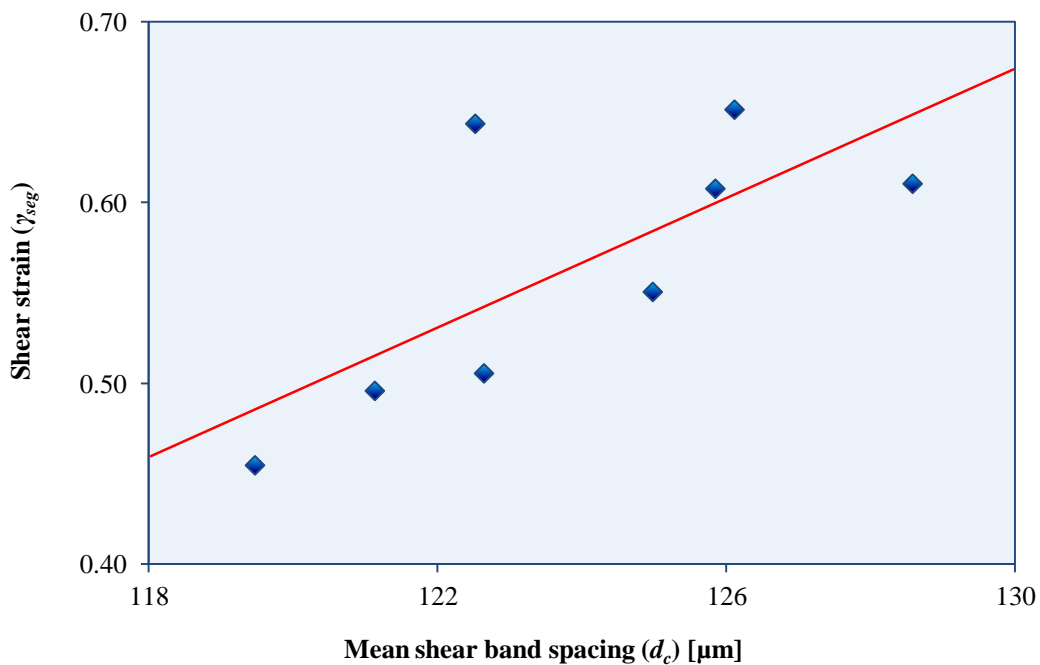


**Figure 5.26.** The relationship between mean shear band spacing ( $d_c$ ) and shear strain within segments ( $\gamma_{seg}$ ). The red line is the trend of the blue markers.

It is possible that the CVD coating changes the chip formation mechanism due to the coating removal process, but no relation between chip formation and crater wear progression could be proven. Greater distance between adiabatic shear bands results in greater shear strain within the segment. This result shows that mean shear band spacing is linearly dependent on shear strain within the segments of the chips. Mean shear band spacing increases with shear strain, which indicates that chips with larger mean shear band spacing are subjected to greater shear stress during chip formation.

Cracks at the chip surface and inside the chip, along the adiabatic shear bands, could be related to the elongation of  $\beta$ -phase as well as void nucleation and void coalescence, as previously observed [101]. Cracks are found in adiabatic shear bands where shear band width is thinner than usual. This suggests that the generation of cracks allows the necessary displacement between chip segments with less plastic shear deformation. The underlying reason for this demands further investigation although a suggestion by the author is that cracks inside adiabatic shear bands diminish shear band width and results in less shear strain. It was observed that shear band width are thinner for MRSs than for SIs. Therefore, chips machined with MRSs might have more cracks along the adiabatic shear bands than chips machined with SIs, which could be related to the chip formation mechanism.

### 5.2.5 DIFFUSION OF CUTTING TOOL PARTICLES INTO CHIPS

The EDS analysis on chips from turning tests at cutting speeds of 30, 75, and 90 m/min is presented in Table 5.1. EDS spectrums can be found in Appendix H. Previous observations indicated that WC particles and cobalt binder diffused into the newly formed chips [90–92].

However, no evidence of cutting tool material, adhesion or diffusion, was observed on investigated chips in the present study. It is observed that the minimum and maximum content of aluminum for CVD coated SIs and uncoated MRSs, respectively, at cutting speed of 75 m/min, exceeds the limit specified by the manufacturer, tabulated in Table 4.1. The titanium content is also higher than expected for uncoated MRSs at a cutting speed of 75 m/min. This is most likely related to the limitations behind EDS analysis, i.e. the uncertainty of element quantification.

**Table 5.1.** Results from EDS analysis on the backside of titanium chips at different cutting conditions. Values are presented in weight percent with mean, SD, max and min.

Cutting speed [m/min]	Coating	Insert	Aluminum [%]	Titanium [%]	Vanadium [%]
30	CVD	SI	7.12	89.35	3.53
30	CVD	MRS	6.12	90.00	3.88
75	CVD	SI	7.40	88.67	3.93
75	CVD	MRS	6.04	89.91	4.05
75	-	SI	6.32	89.79	3.89
75	-	MRS	4.55	91.55	3.90
90	-	SI	6.44	90.06	3.50
90	-	MRS	6.83	89.36	3.81
<b>Mean</b>			6.35	89.84	3.81
<b>SD</b>			0.82	0.78	0.18
<b>Max</b>			7.40	91.55	4.05
<b>Min</b>			4.55	88.67	3.50

## CHAPTER 6

### CONCLUSIONS AND RECOMMENDATIONS

This chapter presents the highlights of this master's thesis and proposes recommendations for future outlooks.

#### 6.1 CONCLUSIONS

- The claimed hypothesis (section 1.2.2) was verified for the following conditions: The coated modified rake face insert showed less crater wear only for the initial few seconds of machining. However, the hypothesis was not verified for the uncoated inserts.
- For our flank wear criteria of  $VB = 0.2$  mm, the standard inserts showed about twice as long tool life as did the modified inserts. This was true for both coated and uncoated inserts at a cutting speed of 75 m/min.
- Changes in the chip formation mechanism may affect crater wear progression and can be determined by investigating the chip geometry. However, no significant differences were found between chips machined with the modified and standard inserts.
- Cracks were found within those adiabatic shear bands (between chip segments) that were thinner than usual. This suggests that the generation of cracks allows the necessary displacement between chip segments with less plastic shear deformation. Inserts with the modified rake surface gave thinner shear bands than did the standard inserts.

## **6.2 RECOMMENDATIONS**

- Further research is necessary to verify how the modified rake surface affects crater wear progression and diffusion when machining titanium alloys. This is interesting because it is easier to redesign the rake surface geometry when you understand the link between crater wear and an irregular surface.
- It is recommended to investigate the possibility to retain a coating on inserts with a modified rake face longer than in the present work.
- Further research is necessary to confirm if crater wear is dependent on diffusion of titanium when machining titanium alloys.
- It is recommended to carry out more research on the differences in the chip formation mechanism between modified and standard inserts.

## REFERENCES

- [1] Deloitte. 2016 Global aerospace and defense sector outlook – Poised for a rebound [Internet]. Deloitte Touche Tohmatsu Limited; 2016 [cited 2016 July 6]. 25 p. Available from: <http://www2.deloitte.com/global/en/pages/manufacturing/articles/global-a-and-d-outlook.html#>
- [2] Boeing. Current market outlook 2015–2034 [Internet]. Boeing; 2015 [cited 2016 July 6]. 58 p. Available from: <http://www.boeing.com/commercial/market/long-term-market/downloads/>
- [3] Trent EM, Wright PK. Metal cutting. 4<sup>th</sup> ed. Woburn, MA: Butterworth-Heinemann; 2000. p. 2–11.
- [4] Martin-Vega LA. Chapter 1.1: The purpose and evolution of industrial engineering. In: Zandin KB, editor. Maynard's Industrial Engineering Handbook: Section 1 – Industrial engineering: Past, present, and future. 5<sup>th</sup> ed. New York, NY: McGraw-Hill; 2001. p. 1.3–1.11.
- [5] Sandvik Coromant. Modern metal cutting – A practical handbook. First north American ed. Fair Lawn, NJ: Sandvik Coromant, Technical Editorial dept; 1996. p. 2–IV-27.
- [6] Childs THC, Maekawa K, Obikawa T, Yamane Y. Metal machining: Theory and applications. Oxford: Elsevier Ltd; 2000. p. 1–19.
- [7] Juneja BL, Sekhon GS, Seth N. Fundamentals of metal cutting and machine tools. 2<sup>nd</sup> ed. New Delhi: New Age International (P) Ltd Publishers; 2003. p. 81–82.
- [8] Donachie MJ. Titanium: A technical guide. 2<sup>nd</sup> ed. Materials Park, OH: ASM International; 2000. p. 1–104.
- [9] Hosseini A, Kishawy HA. Cutting Tool Materials and Tool Wear. In: Davim JP, editor. Machining of titanium alloys. New York, NY: Springer-Verlag; 2014. p. 31–56.
- [10] Ezugwu EO. Key improvements in the machining of difficult-to-cut aerospace superalloys. Int J Mach Tools Manuf. 2005;45(12):1353–1367.
- [11] Jiang L, Haenninen H, Paro J, Kauppinen V. Active wear and failure mechanisms of TiN-coated high speed steel and TiN-coated cemented carbide tools when machining powder metallurgically made stainless steels. Metall Mater Trans A. 1996;27(9):2796–2808.
- [12] Hartung PD, Kramer BM, von Turkovich BF. Tool wear in titanium machining. CIRP Ann. 1982;31(1):75–80.

- [13] Schneider Jr G. Chapter 3: Machinability of Metals. *Am Mach.* 2009;153(12):48.
- [14] Yang X, Liu CR. Machining titanium and its alloys. *Mach Sci Technol.* 1999;3(1):107–139.
- [15] Ezugwu EO, Wang ZM. Titanium alloys and their machinability - a review. *J Mater Process Technol.* 1997;68(3):262–274.
- [16] Ezugwu EO, Wang ZM, Machado AR. Wear of coated carbide tools when machining nickel (Inconel 718) and titanium base (Ti-6Al-4V) alloys. *Tribol Trans.* 2000;43(2):263–268.
- [17] Niknam SA, Khettabi R, Songmene V. Machinability and machining of titanium alloys: A review. In: Davim JP, editor. *Machining of titanium alloys*. New York, NY: Springer-Verlag; 2014. p. 1–30.
- [18] Ashby MF, Jones DRH. *Engineering materials 1: An introduction to properties, applications, and design*. 4<sup>th</sup> ed. Oxford: Elsevier Ltd; 2012. p. 29–39.
- [19] Narutaki N, Murakoshi A, Motonishi S, Takeyama H. Study on Machining of Titanium Alloys. *CIRP Ann.* 1983;32(1):65–69.
- [20] Diniz AE, Micaroni R. Cutting conditions for finish turning process aiming: the use of dry cutting. *Int J Mach Tools Manuf.* 2002;42:899–904.
- [21] Rahman M, Wang Z-G, Wong Y-S. A review on high-speed machining of titanium alloys. *JSME Int J, Ser C.* 2006;49(1):11–20.
- [22] Callister WD, Rethwisch DG. *Material science and engineering*. 8<sup>th</sup> ed. Hoboken, NJ: John Wiley & Sons Pte Ltd; 2011. p. 122–413.
- [23] Astakhov VP, Davim JP. Tools (geometry and material) and tool wear. In: Davim JP, editor. *Machining: Fundamentals and Recent Advances*. London: Springer-Verlag; 2008. p. 29–58.
- [24] Grzesik W. Mechanics of cutting and chip formation. In: Davim JP, editor. *Machining of hard materials*. London: Springer-Verlag; 2011. p. 87–114.
- [25] Mehrer H. *Diffusion in solids: Fundamentals, methods, materials, diffusion-controlled processes*. New York, NY: Springer-Verlag; 2007. p. 1–36.
- [26] Brandes EA, Brook GB (editors). *Smithells metals reference book*. 7<sup>th</sup> ed. Oxford: Butterworth-Heinemann; 1998 p. 13-4–13-9.
- [27] Tresca HM. On further applications of the flow of solids. *J Franklin Inst.* 1878;106(4):263–270.
- [28] Mallock A. The action of cutting tools. *Proc R Soc London.* 1881;33:127–139.
- [29] Merchant ME. Mechanics of the metal cutting process. I. Orthogonal cutting and a type 2 chip. *J Appl Phys.* 1945;16(5):267–275.

- [30] Merchant ME. Mechanics of the metal cutting process. II. Plasticity conditions in orthogonal cutting. *J Appl Phys.* 1945;16(6):318–324.
- [31] Komanduri R, von Turkovich BF. New observations on the mechanism of chip formation when machining titanium alloys. *Wear.* 1981;69(2):179–188.
- [32] Turley DM, Doyle ED, Ramalingam S. Calculation of shear strains in chip formation in titanium. *Mater Sci Eng.* 1982;55(1):45–48.
- [33] Komanduri R. Some clarifications on the mechanics of chip formation when machining titanium alloys. *Wear.* 1982;76(1):15–34.
- [34] Komanduri R, Hou ZB. On thermoplastic shear instability in the machining of a titanium alloy (Ti–6Al–4V). *Metall Mater Trans A.* 2002;33(9):2995–360.
- [35] Recht RF. Catastrophic thermoplastic shear. *J Appl Mech.* 1964;31(2):189–193.
- [36] Gente A, Hoffmeister HW, Evans CJ. Chip formation in machining Ti6A40V at extremely high cutting speeds. *CIRP Ann.* 2001;50(1):49–52.
- [37] Cotterell M, Byrne G. Characterisation of chip formation during orthogonal cutting of titanium alloy Ti–6Al–4V. *CIRP J Manuf Sci Technol.* 2008;1(2):81–85.
- [38] Sutter G, List G. Very high speed cutting of Ti–6Al–4V titanium alloy – change in morphology and mechanism of chip formation. *Int J Mach Tool Manuf.* 2013;66:37–43.
- [39] Bejjani R, Aramesh M, Balazinski M, Kishawy H, Attia H. Chip morphology study of titanium metal matrix composites. *23<sup>rd</sup> CANCAM.* 2011;499–502.
- [40] Nakayama K, Arai M, Kanda T. Machining Characteristics of Hard Materials. *CIRP Ann.* 1988;37(1):89–92.
- [41] He N, Lee TC, Lau WS, Chan SK. Assessment of deformation of a shear localized chip in high speed machining. *J Mater Process Technol.* 2002;129(1):101–104.
- [42] Danzl R, Helmli F, Scherer S. Focus variation – a robust technology for high resolution optical 3D surface metrology. *J Mech Eng.* 2011;57(3):245–256.
- [43] Southall JPC, editor. Helmholtz's treatise on physiological optics – Volume II: The sensations of vision. 3<sup>rd</sup> ed. Menasha, WI: Optical Society of America; 1924.
- [44] Helmli F. Focus Variation Instruments. In: Leach R, editor. Optical measurement of surface topography. Berlin, Heidelberg: Springer-Verlag; 2011. p. 131–166.
- [45] Goodhew PJ, Beanland R, Humphreys FJ. Electron microscopy and analysis. 3<sup>rd</sup> ed. London: Taylor & Francis; 2001. p. 1–19.

- [46] Murphy DB, Davidson MW. Fundamentals of light microscopy and electronic imaging. 2nd ed. Hoboken, NJ: John Wiley & Sons, Inc; 2012. p. 1–16.
- [47] von Ardenne M. Das elektronen-rastermikroskop: Theoretische grundlagen [in German]. Z Phys. 1938;109:553–572.
- [48] McMullan D. The early development of the scanning electron microscope. In: Pawley J, Schatten H, editors. Biological low-voltage scanning electron microscopy. 25<sup>th</sup> ed. New York, NY: Springer Verlag; 2008. p. 1–25.
- [49] Khursheed A. Scanning electron microscope optics and spectrometers. Singapore: World Scientific Publishing Co Pte Ltd; 2011. p. 1–9.
- [50] Exner HE, Weinbruch S. Scanning Electron Microscopy. In: Vander Voort GF, editor. ASM handbook, vol. 9: Metallography and microstructures. Fort Lauderdale: ASM International Inc; 2004. p. 355–367.
- [51] Goldstein JI, Newbury DE, Joy DC, Lyman CE, Echlin P, Lifshin E, et al. Scanning electron microscopy and x-ray microanalysis. 3<sup>rd</sup> ed. New York, NY: Kluwer Academic / Plenum Publishers; 2003. p. 21–29.
- [52] Lifshin E. Electron Microprobe Analysis. In: Buschow KHJ, Cahn RW, Flemings MC, Ilschner B, Kramer EJ, Mahajan S, editors. Encyclopedia of Materials: Science and Technology, vol. 3: D–Fa. Oxford: Elsevier Science Ltd; 2001. p. 2565–2571.
- [53] Komanduri R, Reed WR. Evaluation of carbide grades and a new cutting geometry for machining titanium alloys. Wear. 1983;92(1):113–123.
- [54] Bhaumik SK, Divakar C, Singh AK. Machining Ti–6Al–4V alloy with a wBN-cBN composite tool. Mater Des. 1995;6(4):221–226.
- [55] Kitagawa T, Kubo A, Maekawa K. Temperature and wear of cutting tools in high-speed machining of Inconel 718 and Ti–6Al–6V–2Sn. Wear. 1997;202(2):142–148.
- [56] Wang ZM, Ezugwu EO. Performance of PVD-coated carbide tools when machining Ti-6Al-4V. Tribol Trans. 1997;40(1):81–86.
- [57] Mantle AL, Aspinwall DK. Surface integrity and fatigue life of turned gamma titanium aluminide. J Mater Process Technol. 1997;72(3):413–420.
- [58] Zoya ZA, Krishnamurthy R. The performance of CBN tools in the machining of titanium alloys. J Mater Process Technol. 2000;100(1):80–86.
- [59] Hong SY, Markus I, Jeong W. New cooling approach and tool life improvement in cryogenic machining of titanium alloy ti-6Al-4V. Int J Mach Tools Manuf. 2001;41(15):2245–2260.

- [60] Fitzsimmons M, Sarin VK. Development of CVD WC–Co coatings. *Surf Coat Technol.* 2001;137(2):158–163.
- [61] Nabhani F. Wear mechanisms of ultra-hard cutting tools materials. *J Mater Process Technol.* 2001;115(3):402–412.
- [62] Cherukuri R, Molian P. Lathe turning of titanium using pulsed laser deposited, ultra-hard boride coatings of carbide inserts. *Mach Sci Technol.* 2003;7(1):119–135.
- [63] Corduan N, Himbart T, Poulachon G, Dessoly M, Lambertin M, Vigneau J, et al. Wear mechanisms of new tool materials for Ti-6Al-4V high performance machining. *CIRP Ann.* 2003;52(1):73–76.
- [64] Kishawy HA, Becze CE, McIntosh DG. Tool performance and attainable surface quality during the machining of aerospace alloys using self-propelled rotary tools. *J Mater Process Technol.* 2004;152(3):266–271.
- [65] Che-Haron CH, Jawaaid A. The effect of machining on surface integrity of titanium alloy Ti–6% Al–4% V. *J Mater Process Technol.* 2005;166(2):188–192.
- [66] Dearnley PA, Schellewald M, Dahm KL. Characterisation and wear response of metal-boride coated WC–Co. *Wear.* 2005;259(7):861–869.
- [67] Zareena AR, Veldhuis SC. Tool wear mechanisms and tool life enhancement in ultra-precision machining of titanium. *J Mater Process Technol.* 2012;212(3):560–570.
- [68] Braham-Bouchnak T, Germain G, Morel A, Lebrun JL. The influence of laser assistance on the machinability of the titanium alloy Ti555-3. *Int J Adv Manuf Technol.* 2013;68(9):2471–2481.
- [69] Rahman Rashid RA, Palanisamy S, Sun S, Dargusch MS. Tool wear mechanisms involved in crater formation on uncoated carbide tool when machining Ti6Al4V alloy. *Int J Adv Manuf Technol.* 2016;83(9):1457–1465.
- [70] Nabhani F. Machining of aerospace titanium alloys. *Rob Comput Integr Manuf.* 2001;17(1):99–106.
- [71] Jawaaid A, Che-Haron CH, Abdullah A. Tool wear characteristics in turning of titanium alloy ti-6246. *J Mater Process Technol.* 1999;92(1):329–334.
- [72] Venugopal KA, Paul S, Chattopadhyay AB. Growth of tool wear in turning of Ti-6Al-4V alloy under cryogenic cooling. *Wear.* 2007;262(9):1071–1078.
- [73] Jianxin D, Yousheng L, Wenlong S. Diffusion wear in dry cutting of Ti–6Al–4V with WC/Co carbide tools. *Wear.* 2008;265(11):1776–1783.
- [74] Ribeiro MV, Moreira MRV, Ferreira JR. Optimization of titanium alloy (6Al–4V) machining. *J Mater Process Technol.* 2003;143–144:458–463.

- [75] Arrazola PJ, Garay A, Iriarte LM, Armendia M, Marya S, Le Maître F. Machinability of titanium alloys (Ti6Al4V and Ti555.3). *J Mater Process Technol.* 2009;209(5):2223–2230.
- [76] Che-Haron CH. Tool life and surface integrity in turning titanium alloy. *J Mater Process Technol.* 2001;118(1):231–237.
- [77] Bejjani R, Shi B, Attia H, Balazinski M. Laser assisted turning of titanium metal matrix composite. *CIRP Ann.* 2011;60(1):61–65.
- [78] Wan ZP, Zhu YE, Liu HW, Tang Y. Microstructure evolution of adiabatic shear bands and mechanisms of saw-tooth chip formation in machining Ti6Al4V. *Mater Sci Eng, A.* 2012;531:155–163.
- [79] Bejjani R, Shi B, Attia H, Balazinski M. Simulation of segmented chip formation in laser assisted machining of titanium metal matrix composite. *Int J Mach Tools Manuf.* 2012. (Ref: IJMACTOOL-D-12-00567).
- [80] Bejjani R, Balazinski M, Shi B, Attia H, Kishawy H. Machinability and chip formation of titanium metal matrix composites. *IJAMS.* 2011;13(1).
- [81] Sun S, Brandt M, Dargusch MS. Characteristics of cutting forces and chip formation in machining of titanium alloys. *Int J Mach Tools Manuf.* 2009;49(7):561–568.
- [82] Cedergren S, Frangoudis C, Archenti A, Pederson R, Sjöberg G. Influence of work material microstructure on vibrations when machining cast Ti–6Al–4V. *Int J Adv Manuf Technol.* 2016;84(9):2277–2291.
- [83] Jawaid A, Olajire KA. Cuttability Investigation of Coated Carbides. *Mater Manuf Processes.* 1999;14(4):559–580.
- [84] Dearnly PA, Grearson AN. Evaluation of principal wear mechanisms of cemented carbides and ceramics used for machining titanium alloy IMI 318. *Mater Sci Technol.* 1986;2:47–58.
- [85] Yang S, Zhu G, Xu J, Fu Y. Tool wear prediction of machining hydrogenated titanium alloy Ti6Al4V with uncoated carbide tools. *Int J Adv Manuf Technol.* 2013;68(1):673–682.
- [86] Usui E, Shirakashi T. Analytical prediction of cutting tool wear. *Wear.* 1984;100:129–151.
- [87] Takeyama H, Murata R. Basic investigation of tool wear. *J Eng Ind Trans ASME.* 1963;85(1):33–38.
- [88] Nouari M, Makich H. Experimental investigation on the effect of the material microstructure on tool wear when machining hard titanium alloys: Ti–6Al–4V and Ti–555. *Int J Refract Met Hard Mater.* 2013;41:259–269.
- [89] Kramer BM, von Turkovich BF. A comprehensive tool wear model. *CIRP Ann.* 1986;35(1):67–70.

- [90] Molinari A, Nouari M. Modeling of tool wear by diffusion in metal cutting. *Wear*. 2002;252:135–149.
- [91] Hua J, Shrivpuri R. A cobalt diffusion based model for predicting crater wear of carbide tools in machining titanium alloys. *J Eng Mater Technol*. 2005;127:136–144.
- [92] Zhang S, Li JF, Deng JX, Li YS. Investigation on diffusion wear during high-speed machining Ti-6Al-4V alloy with straight tungsten carbide tools. *Int J Adv Manuf Technol*. 2009;44:17–25.
- [93] Uppsala University Library [internet]. [cited 2016 June 26]. Available from: [uu.summon.serialssolutions.com](http://uu.summon.serialssolutions.com).
- [94] Semiatin SL, Rao SB. Shear localization during metal cutting. *Mater Sci Eng*. 1983;61:185–192.
- [95] Xie JQ, Bayoumi AE, Zbib HM. FEA modeling and simulation of shear localized chip formation in metal cutting. *Int J Mach Tools Manuf*. 1998;38(9):1067–1087.
- [96] Calamaz M, Coupard D, Girot F. A new material model for 2D numerical simulation of serrated chip formation when machining titanium alloy Ti-6Al-4V. *Int J Mach Tools Manuf*. 2008;48(3):275–288.
- [97] Sima M, Öznel T. Modified material constitutive models for serrated chip formation simulations and experimental validation in machining of titanium alloy Ti-6Al-4V. *Int J Mach Tools Manuf*. 2010;50(11):943–960.
- [98] Machado AR, Wallbank J. Machining of titanium and its alloys—a review. *Proc Inst Mech Eng*. 1990;204:53–60.
- [99] Bayoumi AE, Xie JQ. Some metallurgical aspects of chip formation in cutting Ti-6wt.%Al-4wt.%V alloy. *Mater Sci Eng, A*. 1995;190(1):173–180.
- [100] Barry J, Byrne JG, Lennon D. Observations on chip formation and acoustic emission in machining Ti-6Al-4V alloy. *Int J Mach Tools Manuf*. 2001;41(7):1055–1070.
- [101] Cotterell M, Byrne G. Dynamics of chip formation during orthogonal cutting of titanium alloy Ti-6Al-4V. *CIRP Ann*. 2008;57(1):93–96.
- [102] Wegener K, Ugarte A, M'Saoubi R, Garay A, Arrazola PJ. Machining behaviour of Ti-6Al-4V and Ti-5553 alloys in interrupted cutting with PVD coated cemented carbide. *Procedia CIRP*. 2012;1:202–207.
- [103] Miguélez MH, Soldani X, Molinari A. Analysis of adiabatic shear banding in orthogonal cutting of Ti alloy. *Int J Mech Sci*. 2013;75:212–222.
- [104] Ye GG, Xue SF, Jiang MQ, Tong XH, Dai LH. Modeling periodic adiabatic shear band evolution during high speed machining Ti-6Al-4V alloy. *Int J Plast*. 2013;40:39–55.

- [105] Liu J, Fan Q, Cai H, Wang F. Underlying mechanism of periodical adiabatic shear bands generated in Ti–6Al–4V target by projectile impact. *Mater Des*. 2015;87:231–237.
- [106] Timothy SP, Hutchings IM. The structure of adiabatic shear bands in a titanium alloy. *Acta Metall*. 1985;33(4):667–676.
- [107] Shahani AR, Karimi Taheri A. Adiabatic shear bands in titanium and titanium alloys: A critical review. *Mater Des*. 1993;14(4):243–250.
- [108] Xie JQ, Bayoumi AE, Zbib HM. A study on shear banding in chip formation of orthogonal machining. *Int J Mach Tools Manuf*. 1996;36(7):835–847.
- [109] Liao SC, Duffy J. Adiabatic shear bands in a Ti–6Al–4V titanium alloy. *J Mech Phys Solids*. 1998;46(11):2201–2231.
- [110] Molinari A, Musquar C, Sutter G. Adiabatic shear banding in high speed machining of Ti–6Al–4V: Experiments and modeling. *Int J Plast*. 2002;18(4):443–459.
- [111] Xue Q, Meyers MA, Nesterenko VF. Self-organization of shear bands in titanium and Ti–6Al–4V alloy. *Acta Mater*. 2002;50(3):575–596.
- [112] Zhang J, Tan C, Yu R, Yu X, Ma H, Wang F, et al. Adiabatic shear fracture in Ti–6Al–4V alloy. *T Nonferr Metal Soc*. 2011;210(11):2396–2401.
- [113] Bejjani R, Balazinski M, Attia H, L’Espérance G. On the adiabatic shear banding and microstructure evolution when machining titanium metal matrix composites. *J Manuf Sci Eng*. 2012;12:1170.
- [114] Peirs J, Tirry W, Amin-Ahmadi B, Coghe F, Verleysen P, Rabet L, et al. Microstructure of adiabatic shear bands in Ti6Al4V. *Mater Charact*. 2013;75:79–92.
- [115] Sun K, Yu X, Tan C, Ma H, Wang F, Cai H. Effect of microstructure on adiabatic shear band bifurcation in Ti–6Al–4V alloys under ballistic impact. *Mater Sci Eng, A*. 2014;595:247–256.
- [116] Mendoza I, Villalobos D, Alexandrov BT. Crack propagation of Ti alloy via adiabatic shear bands. *Mater Sci Eng, A*. 2015;645:306–310.
- [116] Nurul Amin AKM, Ismail AF, Nor Khairusshima MK. Effectiveness of uncoated WC–Co and PCD inserts in end milling of titanium alloy—Ti–6Al–4V. *J Mater Process Technol*. 2007;192:147–158.
- [118] Boothroyd G, Reinhart LE. Effect of chip forming devices on tool-wear in metal cutting, in: Proc. 1<sup>st</sup> NAMRC, Hamilton, Ontario. 1973;2:13–33.
- [119] Wanigarathne PC, Kardekar AD, Dillon OW, Poulachon G, Jawahir IS. Progressive tool-wear in machining with coated grooved tools and its correlation with cutting temperature. *Wear*. 2005;259:1215–1224.

## APPENDICES

### APPENDIX A1 – TURNING TEST DATA

Data about turning tests, measurements of flank wear ( $V_B$ ) and crater depth ( $K_T$ ), and methods of analysis, is presented in table A1–2. Cutting speed ( $v_c$ ) and time ( $t$ ) was varied, while feed ( $f_n = 0.2 \text{ mm/rev}$ ) and depth of cut ( $a_p = 2.0 \text{ mm}$ ) was kept constant during the tests.

**Table A1.** Turning test data, measurements of  $V_B$  and  $K_T$ , and methods of analysis.

Test	Insert (edge)	$v_c$ [m/min]	Coating	Rake face topog.	$t$ [s]	$V_B$ [mm]	$K_T$ [μm]	Analysis methods
A1	29117 (2-1)	30	CVD	SI	1	0.07	10	Alicona, LOM
A2	29117 (2-2)	30	CVD	SI	3	0.07	14	Alicona, LOM
A3	29117 (2-3)	30	CVD	SI	10	0.09	11	Alicona, LOM
A4	29117 (4-1)	30	CVD	SI	60	0.11	19	Alicona, LOM, SEM
B1	29118 (3-1)	30	CVD	MRS	1	0.07	5	Alicona, LOM
B2	29118 (3-2)	30	CVD	MRS	3	0.08	11	Alicona, LOM
B3	29118 (3-3)	30	CVD	MRS	10	0.10	15	Alicona, LOM
B4	29118 (2-2)	30	CVD	MRS	60	0.12	25	Alicona, LOM, SEM
C1	29117 (3-1)	75	CVD	SI	1	0.07	9	Alicona, LOM
C2	29117 (3-2)	75	CVD	SI	3	0.09	35	Ali., LOM, SEM, EMA
C3	29117 (5-2)	75	CVD	SI	10	0.09	27	Alicona, LOM
C4	29117 (3-3)	75	CVD	SI	60	0.12	34	Alicona, LOM, SEM
D1	29118 (1-1)	75	CVD	MRS	1	0.06	13	Alicona, LOM
D2	29118 (1-2)	75	CVD	MRS	3	0.08	15	Ali., LOM, SEM, EMA
D3	29118 (1-3)	75	CVD	MRS	10	0.10	26	Alicona, LOM
D4	29118 (2-1)	75	CVD	MRS	60	0.14	36	Alicona, LOM, SEM
E1	29119 (1-2)	75	-	SI	30	0.07	11	Alicona, LOM
E2	29119 (1-3)	75	-	SI	60	0.08	28	Ali., LOM, SEM, EMA
F1	29120 (1-1)	75	-	MRS	30	0.07	20	Alicona, LOM
F2	29120 (1-2)	75	-	MRS	60	0.10	28	Ali., LOM, SEM, EMA
G1	29119 (4-2)	90	-	SI	10	0.09	5	Alicona, LOM
G2	29119 (3-1)	90	-	SI	20	0.09	11	Alicona, LOM
G3	29119 (3-2)	90	-	SI	40	0.11	15	Ali., LOM, SEM, EMA
H1	29120 (3-3)	90	-	MRS	10	0.07	10	Alicona, LOM
H2	29120 (3-1)	90	-	MRS	20	0.09	19	Alicona, LOM
H3	29120 (3-2)	90	-	MRS	40	0.12	29	Ali., LOM, SEM, EMA
I1	29119 (2-2)	115	-	SI	3	0.16	3	Alicona, LOM, SEM
I2	29119 (3-3)	115	-	SI	5	0.10	5	Alicona, LOM
I3	29119 (5-1)	115	-	SI	40	0.14	43	Ali., LOM, SEM, EMA
J1	29120 (1-3)	115	-	MRS	3	0.09	12	Alicona, LOM, SEM
J2	29120 (2-3)	115	-	MRS	5	0.11	12	Alicona, LOM
J3	29120 (5-1)	115	-	MRS	20	0.40	26	Ali., LOM, SEM, EMA

**Table A2.** Turning test data, measurements of  $V_B$  and  $K_T$ , and methods of analysis.

Test	Insert (edge)	$v_c$ [m/min]	Coating	Rake face topog.	$t$ [s]	$V_B$ [mm]	$K_T$ [ $\mu\text{m}$ ]	Analysis methods
C5	29117 (4-3)	75	CVD	SI	180	0.15	59	Alicona, LOM
					60	0.13		
					120	0.15		
C6	29117 (1-3)	75	CVD	SI	180	0.15	-	Alicona, LOM
					240	0.16		
					300	0.58		
D5	29118 (4-3)	75	CVD	MRS	120	0.18	-	Alicona, LOM
D6	29118 (4-2)	75	CVD	MRS	180	0.48	54	Alicona, LOM
E3	29119 (4-3)	75	-	SI	180	0.19	38	Alicona, LOM
					60	0.11		
					120	0.14		
E4	29119 (4-1)	75	-	SI	180	0.15	-	Alicona, LOM
					240	0.18		
					300	0.19		
F3	29120 (4-3)	75	-	MRS	120	0.15	-	Alicona, LOM
					180	0.32	40	Alicona, LOM
F4	29120 (4-1)	75	-	MRS				

## **APPENDIX A2 – TURNING TEST DATA (CONFIDENTIAL)**

The content in Appendix A2 is confidential and not presented in this version.

## APPENDIX B1 – SEM AND ALICONA IMAGES OF CRATER WEAR

Figures B1–12 in appendices B1 and B2 presents SEM and Alicona images of crater wear.

**A** illustrates the topography of the crater wear on the rake face of the insert in pseudo colors.

**B** shows a SEM micrograph of the cross-section of the insert near the surface profile line, and

**C** illustrates a diagram of the profile line.

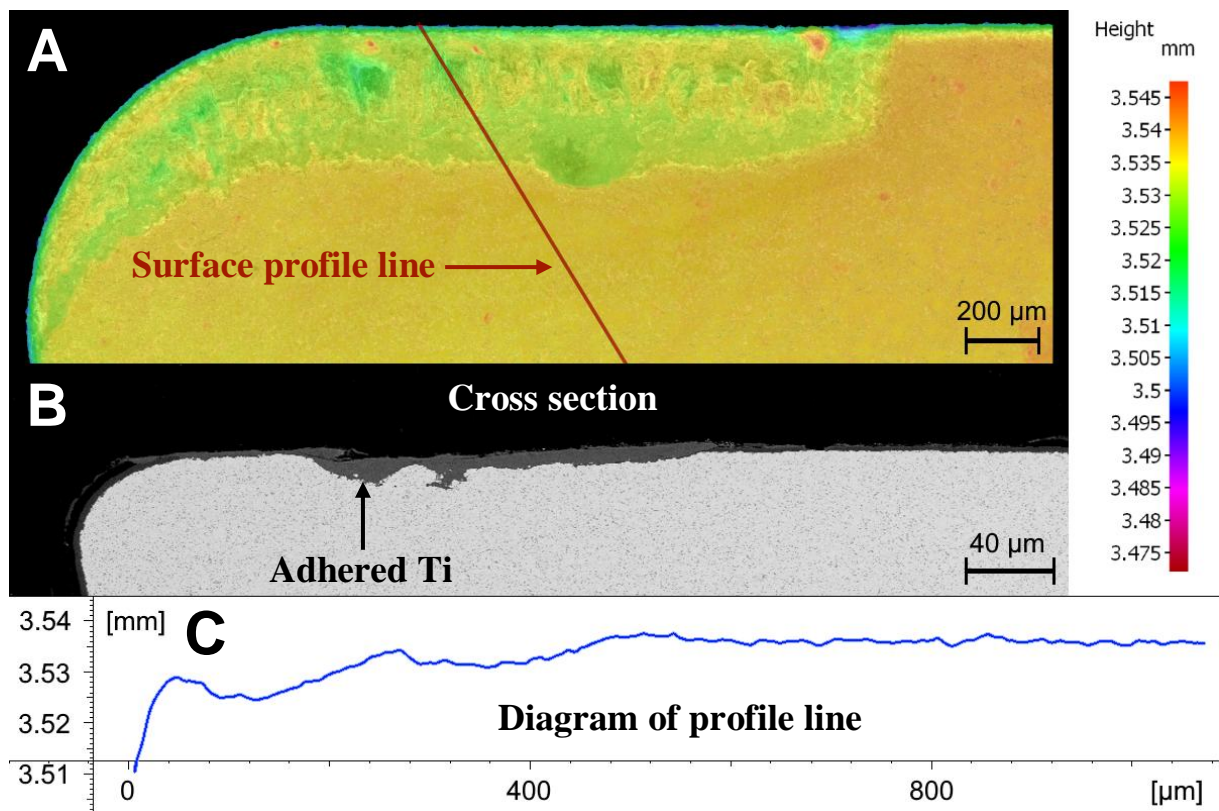


**Figure B1.** Sample A4: Coated SI at cutting speed of 30 m/min after 60 s.

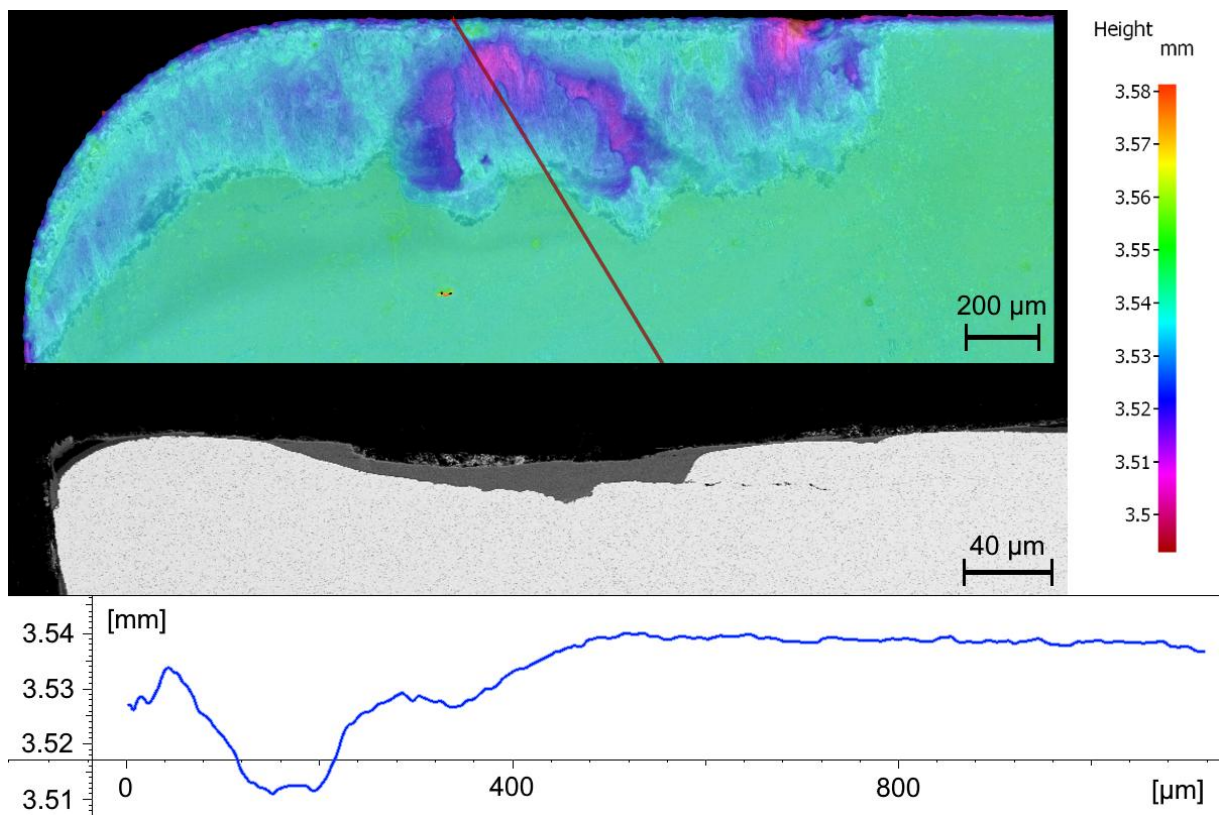


**Figure B2.** Sample C2: Coated SI at cutting speed of 75 m/min after 3 s.

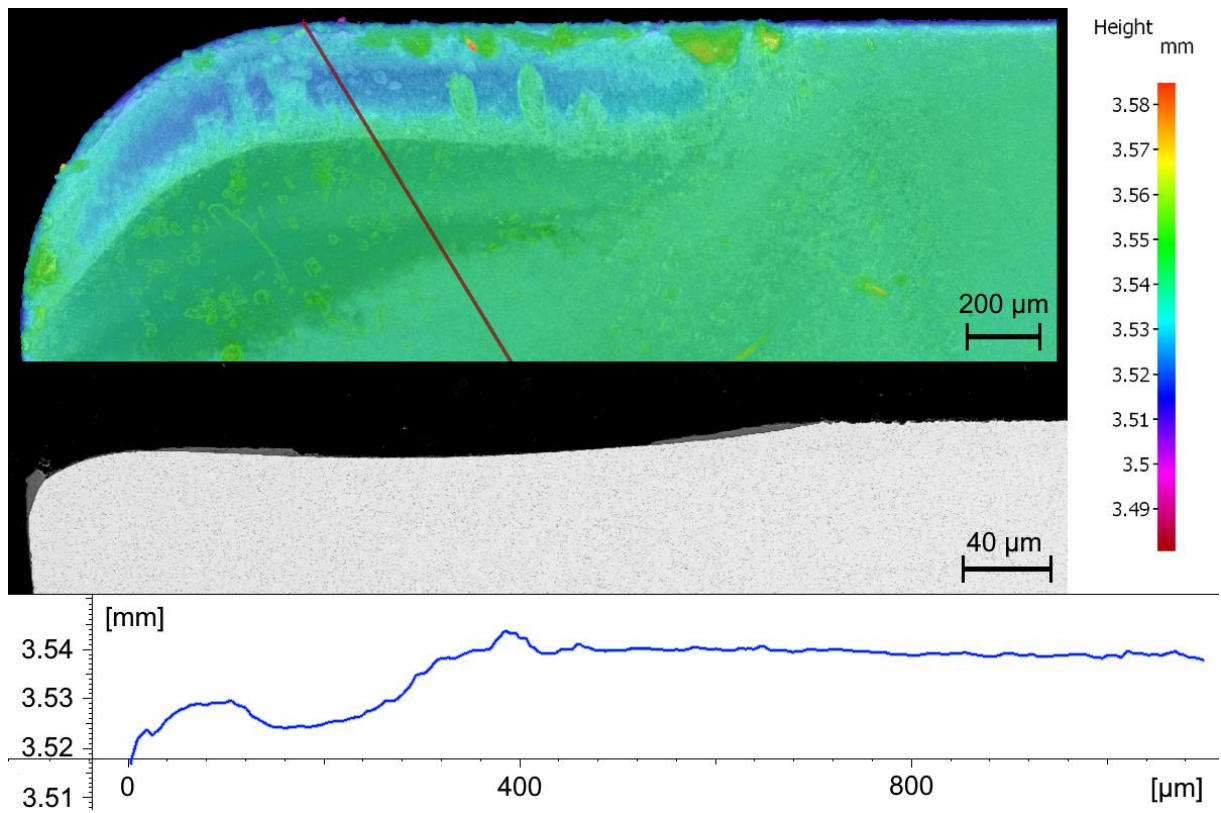


**Figure B3.** Sample E2: Uncoated SI at cutting speed of 75 m/min after 60 s.

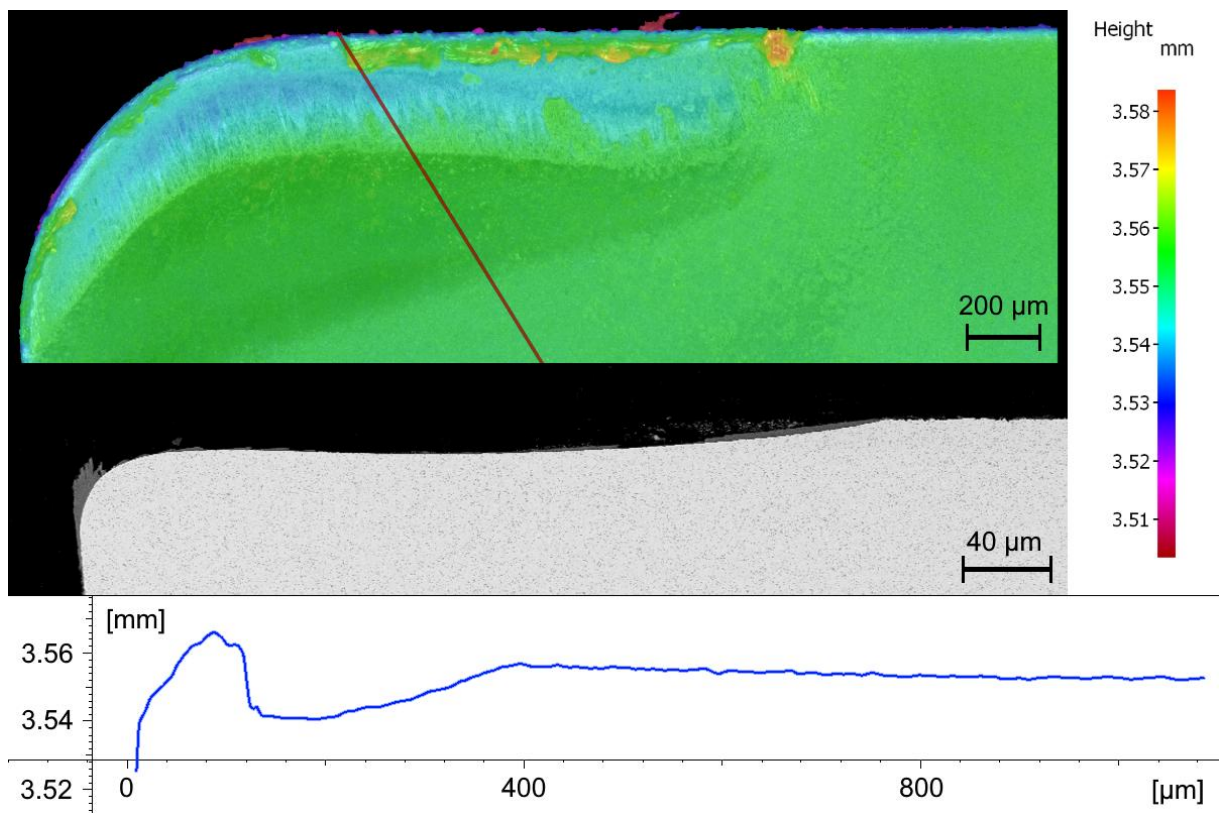


**Figure B4.** Sample G3: Uncoated SI at cutting speed of 90 m/min after 40 s.

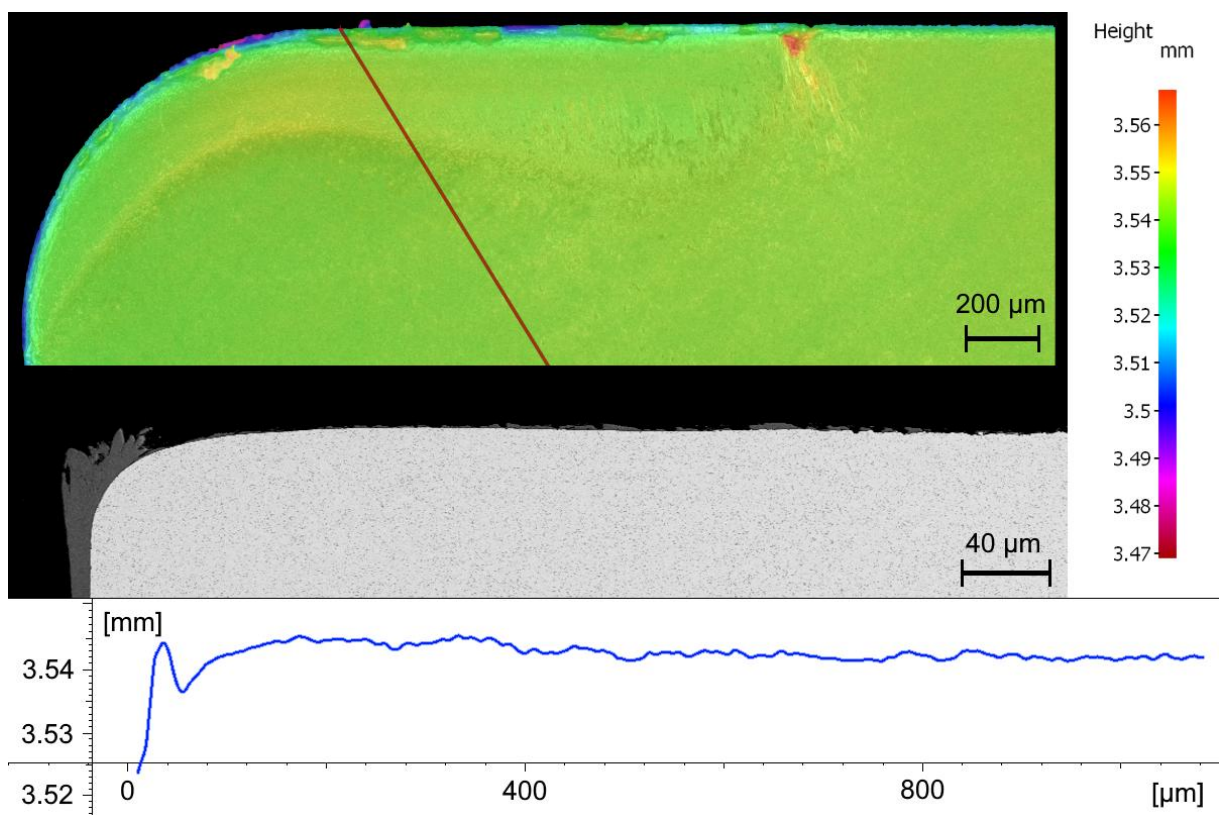


**Figure B5.** Sample I1: Uncoated SI at cutting speed of 115 m/min after 3 s.

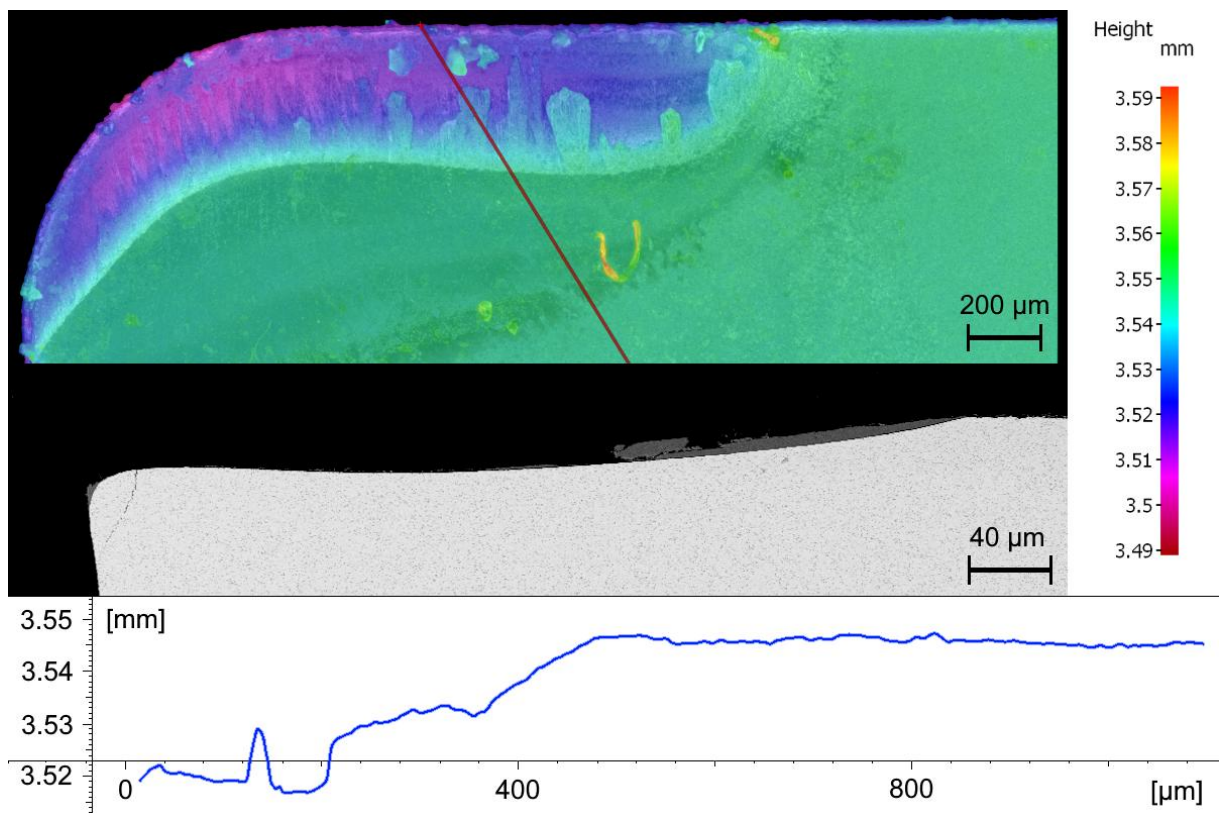


**Figure B6.** Sample I3: Uncoated SI at cutting speed of 115 m/min after 40 s.

## **APPENDIX B2 – SEM AND ALICONA IMAGES OF CRATER WEAR (CONFIDENTIAL)**

The content in Appendix B2 is confidential and not presented in this version.

## APPENDIX C1 – LINE SCAN ANALYSIS WITH EMA

Tables C1–6 presents data from EMA line scans. Graphs in figures 5.4–6 were adjusted so that interfaces were at the same location for all positions. Data in bold text in boxed areas were used to construct each line in respective graphs. The highlighted box near the middle of respective boxed area is the point where the interface is most likely to be located.

**Table C1.** Data from EMA line scan of sample C2 and D2 regarding titanium.

Distance from start [μm]	Titanium					
	C2		D2			
	SI (Position 1)	SI (Position 2)	MRS Top (Position 1)	MRS Top (Position 2)	MRS Low (Position 1)	MRS Low (Position 2)
0	112400	113171	<b>6568</b>	35239	82785	<b>97300</b>
0.1	112142	<b>113012</b>	<b>7755</b>	41978	85544	<b>97041</b>
0.2	112376	<b>113135</b>	<b>9151</b>	48388	88587	<b>97224</b>
0.3	112356	<b>113589</b>	<b>10678</b>	54947	91059	<b>97178</b>
0.4	113119	<b>113283</b>	<b>12868</b>	<b>62423</b>	92645	<b>96379</b>
0.5	112475	<b>113784</b>	<b>15124</b>	<b>69201</b>	94108	<b>96294</b>
0.6	112531	<b>113850</b>	<b>18025</b>	<b>76712</b>	95137	<b>96939</b>
0.7	113476	<b>113474</b>	<b>20295</b>	82737	<b>95785</b>	<b>96376</b>
0.8	112167	<b>113209</b>	<b>22601</b>	<b>89159</b>	<b>96254</b>	<b>95802</b>
0.9	112762	<b>113390</b>	<b>25066</b>	<b>96391</b>	<b>96570</b>	<b>94970</b>
1	112509	<b>112948</b>	<b>27104</b>	<b>101724</b>	<b>96884</b>	<b>95254</b>
1.1	112124	<b>112895</b>	<b>29477</b>	<b>105787</b>	<b>96749</b>	<b>94943</b>
1.2	112487	<b>113344</b>	<b>31648</b>	<b>108548</b>	<b>96970</b>	<b>94768</b>
1.3	111497	<b>112716</b>	<b>33674</b>	<b>109564</b>	<b>96338</b>	<b>94400</b>
1.4	111838	<b>113376</b>	<b>35533</b>	<b>111014</b>	<b>96177</b>	<b>93709</b>
1.5	111443	<b>112824</b>	<b>38390</b>	<b>112299</b>	<b>95438</b>	<b>93338</b>
1.6	111563	<b>112895</b>	<b>41620</b>	<b>112387</b>	<b>95246</b>	<b>92587</b>
1.7	111436	<b>112343</b>	<b>44416</b>	<b>113365</b>	<b>95022</b>	<b>92019</b>
1.8	110780	<b>112522</b>	<b>49304</b>	<b>112959</b>	<b>93916</b>	<b>91629</b>
1.9	111084	<b>112671</b>	<b>55083</b>	<b>113815</b>	<b>94184</b>	<b>90456</b>
2	111227	<b>112408</b>	<b>59748</b>	<b>114146</b>	<b>94475</b>	<b>89197</b>
2.1	110567	<b>112230</b>	<b>66224</b>	<b>114182</b>	<b>93588</b>	<b>87742</b>
2.2	110213	<b>112081</b>	<b>71812</b>	<b>114579</b>	<b>92264</b>	<b>86821</b>
2.3	109586	<b>113175</b>	<b>77115</b>	<b>114066</b>	<b>91605</b>	<b>85525</b>
2.4	109789	<b>112626</b>	<b>82631</b>	<b>114875</b>	<b>91010</b>	<b>83841</b>
2.5	108642	<b>113333</b>	<b>87858</b>	<b>113926</b>	<b>90572</b>	<b>82297</b>
2.6	108900	<b>112662</b>	<b>92868</b>	<b>114905</b>	<b>89384</b>	<b>80174</b>
2.7	108596	<b>112762</b>	<b>96851</b>	<b>114332</b>	<b>88098</b>	<b>76495</b>
2.8	107734	<b>112634</b>	<b>101105</b>	<b>113909</b>	<b>87744</b>	<b>74189</b>
2.9	107050	<b>111769</b>	<b>103879</b>	<b>114830</b>	<b>86241</b>	<b>69996</b>
3	105990	<b>111366</b>	<b>106945</b>	<b>114103</b>	<b>84727</b>	<b>66880</b>
3.1	105430	<b>110027</b>	<b>108668</b>	<b>113980</b>	<b>83472</b>	<b>62560</b>
3.2	105198	<b>109015</b>	<b>109765</b>	<b>113779</b>	<b>82125</b>	<b>56785</b>
3.3	104527	<b>104914</b>	<b>109633</b>	<b>113543</b>	<b>80532</b>	<b>52687</b>
3.4	104041	<b>98817</b>	<b>108831</b>	<b>113612</b>	<b>78568</b>	<b>46905</b>
3.5	103598	<b>92876</b>	<b>106613</b>	<b>112411</b>	<b>75602</b>	<b>42584</b>

3.6	102846	84397	102998	111324	72644	38115
3.7	102981	77098	97591	109518	68942	33561
3.8	102343	69333	90906	107962	64049	29714
3.9	102555	60521	82205	104065	59738	25653
4	102559	53365	73676	100845	53957	22520
4.1	102972	45024	63187	94461	48697	19155
4.2	103485	37955	54076	89108	44078	15448
4.3	104036	31380	45833	81010	38216	13093
4.4	104701	23663	35701	72246	33397	10521
4.5	105000	17734	27454	63748	27513	8483
4.6	106074	11949	17892	53192	23100	6692
4.7	106751	7769	10954	44256	19255	5031
4.8	107305	5181	5639	35827	15238	3773
4.9	107413	3110	2739	26282	12251	2710
5	108446	2405	1826	18494	9638	2071
5.1	109179	1932	1322	11508	8017	1621
5.2	109847	1803	1153	7165	6585	1225
5.3	110650	1673	1038	4654	5047	1080
5.4	110690	1597	948	2870	3940	959
5.5	111577	1555	973	2195	3012	810
5.6	111996	1511	865	1487	2458	770
5.7	112485	1381	826	1246	2134	699
5.8	112905	1376	873	1063	1735	650
5.9	112494	1364	840	982	1537	656
6	113284	1293	791	924	1433	616
6.1	113175	1189	735	819	1299	595
6.2	112656	1248	706	826	1197	581
6.3	112850	1206	695	785	1126	589
6.4	112478	1084	689	746	1070	561
6.5	111900	1049	676	744	1014	539
6.6	110285	1049	673	697	1001	541
6.7	108484	991	696	708	949	540
6.8	106151	951	683	681	908	500
6.9	102911	897	666	660	897	497
7	98349	920	596	669	833	498
7.1	93305	909	585	615	843	505
7.2	88196	880	632	606	779	447
7.3	81618	839	591	586	811	449
7.4	74550	758	593	585	749	454
7.5	68950	784	576	560	745	458
7.6	62678	843	595	538	746	442
7.7	57087	727	539	581	677	438
7.8	47288	737	532	573	672	454
7.9	41022	748	570	559	738	470
8	35062	686	501	562	634	442
8.1	28235	735	533	533	658	452
8.2	21232	717	517	542	624	478
8.3	15475	660	514	522	606	433
8.4	11014	694	533	511	592	441
8.5	7253	709	499	502	567	447
8.6	5014	679	502	501	570	411
8.7	3514	623	492	526	533	430
8.8	2699	625	476	524	559	397

8.9	2196	649	496	515	575	394
9	1931	600	459	496	549	398
9.1	1679	647	478	517	524	423
9.2	1658	596	495	463	517	407
9.3	1493	597	494	485	505	371
9.4	1504	533	479	492	506	367
9.5	1468	540	462	482	523	389
9.6	1342	551	476	489	520	403
9.7	1330	538	488	477	521	388
9.8	1358	547	509	464	523	401
9.9	1353	502	453	502	494	411
10	1206	568	494	456	481	360
10.1	1186	523	444	507	497	358
10.2	1148	539	473	424	478	377
10.3	1154	559	415	469	507	394
10.4	1070	452	431	406	473	376
10.5	1130	528	446	401	469	352
10.6	962	512	440	455	462	372
10.7	985	491	426	447	464	379
10.8	941	527	417	472	444	413
10.9	978	478	433	421	449	399
11	927	501	464	452	450	400
11.1	880	514	432	462	442	380
11.2	877	470	462	435	435	375
11.3	896	485	385	419	421	386
11.4	863	467	391	443	453	381
11.5	800	526	434	440	416	396
11.6	793	489	418	428	441	368
11.7	829	461	414	436	442	408
11.8	793	497	450	414	393	387
11.9	796	448	456	429	417	415
12	748	492	431	430	438	382
12.1	725	455	418	454	408	383
12.2	701	440	404	427	404	421
12.3	699	466	432	381	405	358
12.4	676	437	419	373	368	388
12.5	679	474	439	385	424	385
12.6	703	478	425	429	423	420
12.7	657	482	439	427	369	358
12.8	668	485	410	398	434	369
12.9	646	445	407	465	384	387
13	648	443	369	427	433	381
13.1	604	450	394	408	452	396
13.2	651	486	408	410	423	368
13.3	627	420	420	395	431	403
13.4	653	431	444	417	420	369
13.5	583	448	389	433	411	410
13.6	612	425	407	438	416	415
13.7	587	406	395	384	440	368
13.8	559	412	378	413	397	382
13.9	621	449	423	412	407	376
14	562	447	363	400	413	396
14.1	602	426	400	444	433	402
14.2	589	434	395	413	422	362

14.3	<b>579</b>	<b>451</b>	<b>387</b>	<b>420</b>	<b>425</b>	<b>383</b>
14.4	<b>558</b>	<b>401</b>	<b>375</b>	<b>430</b>	<b>402</b>	<b>416</b>
14.5	<b>565</b>	<b>403</b>	<b>398</b>	<b>405</b>	<b>355</b>	<b>375</b>
14.6	<b>552</b>	<b>422</b>	<b>376</b>	<b>429</b>	<b>414</b>	<b>385</b>
14.7	<b>506</b>	<b>462</b>	<b>414</b>	<b>396</b>	<b>395</b>	<b>364</b>
14.8	<b>549</b>	<b>430</b>	<b>416</b>	<b>398</b>	<b>396</b>	<b>382</b>
14.9	<b>532</b>	<b>419</b>	<b>388</b>	<b>400</b>	<b>387</b>	<b>347</b>
15	<b>511</b>	<b>411</b>	<b>406</b>	<b>390</b>	<b>378</b>	<b>362</b>
15.1	<b>498</b>	<b>408</b>	<b>411</b>	<b>410</b>	<b>411</b>	<b>351</b>
15.2	<b>486</b>	<b>385</b>	<b>426</b>	<b>413</b>	<b>380</b>	<b>373</b>
15.3	<b>505</b>	<b>429</b>	<b>429</b>	<b>420</b>	<b>373</b>	<b>371</b>
15.4	<b>488</b>	413	409	<b>386</b>	<b>397</b>	348
15.5	<b>530</b>	422	381	<b>392</b>	<b>389</b>	357
15.6	<b>539</b>	426	373	<b>423</b>	<b>384</b>	388
15.7	<b>504</b>	377	409	427	<b>393</b>	386
15.8	<b>520</b>	384	378	414	<b>403</b>	351
15.9	<b>493</b>	396	418	373	<b>404</b>	364
16	<b>514</b>	410	389	449	412	394
16.1	<b>472</b>	435	389	426	381	408
16.2	<b>473</b>	402	365	415	372	357
16.3	<b>506</b>	375	371	399	375	390
16.4	<b>496</b>	415	411	373	382	406
16.5	<b>491</b>	382	391	382	409	367
16.6	<b>467</b>	390	373	392	351	358
16.7	<b>489</b>	402	359	413	390	402
16.8	<b>510</b>	437	371	371	392	376
16.9	<b>429</b>	413	363	393	378	387
17	<b>498</b>	382	378	385	411	347
17.1	<b>484</b>	415	381	380	403	370
17.2	<b>480</b>	419	344	393	396	344
17.3	<b>442</b>	381	398	381	400	388
17.4	<b>462</b>	426	402	347	403	391
17.5	<b>457</b>	417	391	406	382	376
17.6	<b>453</b>	382	375	372	395	384
17.7	<b>418</b>	394	347	386	343	351
17.8	<b>418</b>	390	384	417	372	367
17.9	<b>431</b>	389	364	377	379	372
18	<b>419</b>	397	400	430	370	386
18.1	<b>438</b>	437	351	399	422	378
18.2	<b>421</b>	400	408	413	397	368
18.3	<b>404</b>	397	412	374	365	356
18.4	<b>425</b>	376	421	385	406	368
18.5	<b>436</b>	384	400	372	365	371
18.6	<b>447</b>	364	402	363	338	337
18.7	<b>425</b>	390	408	354	379	415
18.8	<b>454</b>	398	427	382	395	352
18.9	<b>432</b>	365	382	366	368	368
19	<b>422</b>	380	396	367	363	413
19.1	434	432	395	373	425	383
19.2	448	401	379	391	360	366
19.3	460	384	388	415	381	428
19.4	409	367	398	423	375	380
19.5	414	376	377	412	393	389
19.6	448	358	352	375	378	393

19.7	409	400	363	396	381	412
19.8	395	392	402	337	409	373
19.9	431	440	398	400	351	370

**Table C2.** Data from EMA line scan of sample C2 and D2 regarding carbon.

Distance from start [μm]	Carbon					
	C2		D2			
	SI (Position 1)	SI (Position 2)	MRS Top (Position 1)	MRS Top (Position 2)	MRS Low (Position 1)	MRS Low (Position 2)
0	15739	9804	<b>524897</b>	209352	123707	<b>161469</b>
0.1	13979	<b>9622</b>	<b>524679</b>	207339	131903	<b>162317</b>
0.2	12854	<b>9571</b>	<b>519096</b>	207360	138089	<b>162654</b>
0.3	12055	<b>9277</b>	<b>509936</b>	206108	145377	<b>162341</b>
0.4	11661	<b>9496</b>	<b>496147</b>	<b>202039</b>	150028	<b>162966</b>
0.5	10957	<b>9762</b>	<b>481559</b>	<b>196877</b>	153422	<b>162674</b>
0.6	10617	<b>10087</b>	<b>459200</b>	<b>188926</b>	155570	<b>162604</b>
0.7	10522	<b>10208</b>	<b>433082</b>	<b>183908</b>	<b>157186</b>	<b>163738</b>
0.8	10295	<b>10352</b>	<b>401434</b>	<b>176970</b>	<b>159006</b>	<b>163834</b>
0.9	10384	<b>10651</b>	<b>361800</b>	<b>170281</b>	<b>159574</b>	<b>164110</b>
1	10508	<b>10788</b>	<b>328094</b>	<b>156475</b>	<b>159482</b>	<b>163397</b>
1.1	10390	<b>11219</b>	<b>294082</b>	<b>124632</b>	<b>159405</b>	<b>163412</b>
1.2	10634	<b>11379</b>	<b>273312</b>	<b>96331</b>	<b>158353</b>	<b>163788</b>
1.3	10763	<b>11337</b>	<b>260219</b>	<b>72307</b>	<b>157553</b>	<b>162870</b>
1.4	11158	<b>11934</b>	<b>256000</b>	<b>51132</b>	<b>157554</b>	<b>161950</b>
1.5	11549	<b>11856</b>	<b>262805</b>	<b>38230</b>	<b>155842</b>	<b>161063</b>
1.6	11840	<b>12230</b>	<b>276707</b>	<b>27533</b>	<b>154719</b>	<b>160485</b>
1.7	12360	<b>12172</b>	<b>288627</b>	<b>21986</b>	<b>153898</b>	<b>158557</b>
1.8	12868	<b>12495</b>	<b>303672</b>	<b>17975</b>	<b>152385</b>	<b>157023</b>
1.9	13638	<b>12788</b>	<b>312133</b>	<b>14987</b>	<b>151406</b>	<b>155156</b>
2	14459	<b>12857</b>	<b>316043</b>	<b>13622</b>	<b>149776</b>	<b>153403</b>
2.1	15641	<b>12695</b>	<b>318309</b>	<b>12533</b>	<b>148649</b>	<b>151340</b>
2.2	16551	<b>12864</b>	<b>318484</b>	<b>12190</b>	<b>147360</b>	<b>148089</b>
2.3	18064	<b>12757</b>	<b>315455</b>	<b>12071</b>	<b>145044</b>	<b>144941</b>
2.4	20461	<b>13027</b>	<b>299222</b>	<b>12448</b>	<b>143976</b>	<b>141277</b>
2.5	22248	<b>12772</b>	<b>273979</b>	<b>12625</b>	<b>142175</b>	<b>137445</b>
2.6	25285	<b>12773</b>	<b>235020</b>	<b>12926</b>	<b>141012</b>	<b>133001</b>
2.7	28740	<b>13201</b>	<b>202320</b>	<b>13313</b>	<b>138439</b>	<b>126839</b>
2.8	35516	<b>13332</b>	<b>170797</b>	<b>13359</b>	<b>135045</b>	<b>121998</b>
2.9	39624	<b>13707</b>	<b>138788</b>	<b>13597</b>	<b>133015</b>	<b>114066</b>
3	42048	<b>13778</b>	<b>113962</b>	<b>13573</b>	<b>127611</b>	<b>109446</b>
3.1	45416	<b>14322</b>	<b>85369</b>	<b>13496</b>	<b>123398</b>	<b>102919</b>
3.2	48486	<b>14185</b>	<b>65013</b>	<b>13434</b>	<b>118677</b>	<b>96422</b>
3.3	50111	<b>14951</b>	<b>49701</b>	<b>13393</b>	<b>113249</b>	<b>90595</b>
3.4	51899	<b>16384</b>	<b>36638</b>	<b>13146</b>	<b>107407</b>	<b>85821</b>
3.5	53993	<b>18466</b>	<b>29182</b>	<b>12959</b>	<b>99671</b>	<b>81211</b>
3.6	54818	<b>21147</b>	<b>23568</b>	<b>12774</b>	<b>93629</b>	<b>77881</b>
3.7	56353	<b>24246</b>	<b>21101</b>	<b>12503</b>	<b>87123</b>	<b>74075</b>
3.8	<b>57294</b>	<b>27040</b>	<b>20828</b>	<b>12046</b>	<b>80834</b>	<b>71169</b>
3.9	<b>58053</b>	<b>30131</b>	<b>22044</b>	<b>12365</b>	<b>75202</b>	<b>67950</b>
4	<b>58354</b>	<b>33207</b>	<b>23853</b>	<b>12908</b>	<b>69284</b>	<b>65991</b>

4.1	56314	35931	27157	14074	64640	64234
4.2	53751	38605	30092	16024	60926	61575
4.3	49873	40406	33294	18292	57056	60708
4.4	45507	43202	36809	21595	55095	58407
4.5	40620	44877	40029	24685	52657	57206
4.6	36890	47132	43680	28899	50642	55711
4.7	34206	49174	46655	32595	50258	53924
4.8	32247	50780	50093	36288	50174	53053
4.9	29949	51684	51679	39804	50291	52529
5	27657	52054	52236	43589	51602	52115
5.1	26069	52125	52795	47119	53313	51287
5.2	24245	52074	52408	49549	54372	50469
5.3	22203	52093	52446	51247	54646	50150
5.4	20617	51687	52492	51685	54871	49391
5.5	19147	51743	51988	51801	54965	49164
5.6	17701	51458	52109	52358	55598	48678
5.7	16357	51563	51770	52057	55176	49683
5.8	15415	51599	51209	52326	54798	49711
5.9	14717	51804	51393	51785	54154	50104
6	14189	52318	50706	51986	53002	49937
6.1	13898	52099	51134	52069	52096	49921
6.2	13439	51754	51173	51682	51109	49774
6.3	13263	51106	50940	52055	51161	50383
6.4	12921	51095	50481	51809	51356	51004
6.5	12800	50151	50575	52057	51108	51667
6.6	12767	50088	50178	52395	51604	52271
6.7	12765	50171	50125	52545	52214	52267
6.8	13039	50166	50330	52261	53016	52379
6.9	13177	49846	50963	52200	52981	51975
7	13738	50506	50954	52303	53479	52623
7.1	14878	50749	51987	52791	53464	52618
7.2	15989	50886	51642	52437	53125	53224
7.3	17680	50841	52234	52090	53390	53313
7.4	20037	50957	52492	51979	52887	53490
7.5	22660	50348	52773	51801	53068	53816
7.6	24875	50634	52511	51900	53029	53579
7.7	27105	50662	52642	51409	52235	53271
7.8	31257	50900	52527	51072	52817	52938
7.9	33539	50885	52259	51633	52282	52673
8	35935	50572	52277	51256	51171	52849
8.1	39187	50695	52116	51858	50838	52762
8.2	42209	50216	52174	52128	49812	52996
8.3	45115	49845	52167	52139	49411	52286
8.4	46865	49452	51883	52446	48363	52923
8.5	49546	49334	51574	52919	47328	51958
8.6	51198	50127	51542	52983	46703	52156
8.7	52999	49622	51414	53014	46655	52130
8.8	53681	49598	51416	52677	46618	52134
8.9	53708	49605	51866	53500	46913	51263
9	53533	49493	51633	53396	47931	50174
9.1	53445	49498	51971	53506	48196	49668
9.2	53357	50373	51789	53175	49441	48458
9.3	53381	50548	51477	53371	50285	47979

9.4	53848	50021	51855	53744	51571	47154
9.5	53724	51059	52119	53528	52073	47238
9.6	53546	51334	52444	53617	53208	47785
9.7	53949	51815	52568	52994	53809	47942
9.8	53423	51660	52616	52869	54184	48206
9.9	53854	51638	52775	52442	54433	48127
10	54210	51315	53209	51969	54164	49085
10.1	53400	51172	52816	51119	53315	49900
10.2	54063	50811	52925	51105	53812	50426
10.3	54222	50819	53001	50970	52829	50977
10.4	53987	50613	52021	50445	52142	51363
10.5	54604	49995	51417	50419	52227	51906
10.6	54362	50416	51341	50663	51972	52140
10.7	54651	49924	50104	51060	51850	51925
10.8	54192	49830	49820	51030	51819	52362
10.9	53938	50181	49755	50594	51857	52704
11	53730	50583	49462	50081	51473	53030
11.1	53690	50495	49806	49487	52080	52862
11.2	54037	50240	49412	49507	51904	52857
11.3	53459	50449	49484	49440	51944	53161
11.4	53516	51148	49591	49278	51800	52920
11.5	53368	51024	49667	49518	52057	53065
11.6	53581	51617	50180	49461	51749	52829
11.7	53564	51510	50327	49183	51909	52871
11.8	53176	52097	50557	48973	51830	52748
11.9	53952	52496	50148	48679	51529	52800
12	53598	52183	50161	49054	51678	52132
12.1	53439	52257	49844	48883	51450	52209
12.2	53518	52292	49744	49503	50674	51975
12.3	54081	52351	49457	49667	51013	51406
12.4	53797	52517	49100	49593	50656	51621
12.5	53665	52511	50041	49897	50769	51573
12.6	53537	52347	49951	50674	50812	51703
12.7	53677	52330	50032	51027	50485	51412
12.8	52977	52608	50423	50896	50600	51139
12.9	52874	52190	49597	50998	51207	51545
13	52569	52394	49690	51726	51000	51390
13.1	52939	52003	49284	51147	51372	51510
13.2	52708	51866	49085	50912	51422	51085
13.3	52764	51640	49648	50555	51157	50833
13.4	52961	51462	50041	50338	51015	50930
13.5	52837	51892	50394	50302	50962	50590
13.6	52686	51147	49821	49753	51083	51150
13.7	52597	50996	49368	50102	51195	51491
13.8	52671	50772	49133	49623	51412	51583
13.9	53200	50508	49180	49863	51848	51554
14	53081	50580	49551	49968	51781	51926
14.1	53149	49884	49935	49993	52152	51273
14.2	53241	50316	49583	50374	52202	51228
14.3	53853	50438	49954	50446	52848	50606
14.4	53894	49893	49676	50297	53164	50863
14.5	53727	50477	49238	50711	53305	50747
14.6	54517	51025	49944	50607	52944	50673
14.7	54114	50432	49516	50648	52284	49976

14.8	54634	51289	50422	51157	51549	49887
14.9	54397	50980	50447	51028	51301	48982
15	54827	51623	50887	51516	50571	48723
15.1	54754	51299	51042	51407	50990	48339
15.2	54620	51494	51223	51667	50931	47641
15.3	54682	51753	51564	51813	50315	47626
15.4	54630	52027	51255	51574	50978	48418
15.5	54690	51932	51352	52049	50782	49425
15.6	54935	52252	51261	52000	51047	49681
15.7	54607	52117	51309	52130	51783	50208
15.8	54750	52188	52212	52350	52313	50752
15.9	54739	51901	51442	52321	52614	50811
16	54311	52328	51536	52710	52730	51406
16.1	54561	52141	51080	52703	52432	51876
16.2	54273	52093	50635	52722	52769	52296
16.3	54055	51969	50530	52494	52933	52026
16.4	53902	52158	48775	52775	53030	52153
16.5	53531	52354	47743	52713	53116	52485
16.6	53645	52201	47070	52610	53471	52364
16.7	53995	52343	46788	51790	53888	51791
16.8	53631	52395	45546	52271	53849	52403
16.9	53725	52219	45267	51769	54094	52104
17	53503	51954	44972	51296	53918	51471
17.1	53844	51509	45037	51119	54238	50961
17.2	53363	51422	45189	50626	53873	50708
17.3	53228	51112	45209	50310	53850	50765
17.4	53452	51196	45466	49905	54032	50508
17.5	53558	51126	46349	48715	53791	50289
17.6	53657	50952	47211	48785	54135	50085
17.7	53031	51364	47768	48712	53740	49762
17.8	53115	51031	48070	48792	54154	49577
17.9	53162	51188	48770	48266	54341	48933
18	53172	50343	49554	48666	54072	48397
18.1	53057	50243	49822	48737	54353	47583
18.2	53090	50260	50726	48905	54142	47542
18.3	53414	50274	51280	48972	53500	48127
18.4	53702	50100	51796	48417	53318	48288
18.5	53096	49718	51511	48586	52641	49060
18.6	52975	50007	51832	47975	52044	48670
18.7	53417	50011	52443	48058	51856	49216
18.8	53112	49771	51886	48138	51223	49717
18.9	53806	50282	51814	48289	50450	50398
19	52937	49535	51961	48703	50273	50889
19.1	53554	50322	51530	49009	50569	51365
19.2	53669	50181	51246	49795	50162	52048
19.3	53697	50446	51651	49583	50708	52317
19.4	53075	51350	51435	50333	50399	52392
19.5	53378	51316	51141	50452	50806	52526
19.6	53596	51550	51400	50846	50244	52666
19.7	53319	51911	50692	51552	50302	52246
19.8	53474	51303	50980	51833	50265	52147
19.9	53647	51996	51106	51506	50415	52201

**Table C3.** Data from EMA line scan of sample E2 and E2 regarding titanium.

Titanium						
Distance from start [μm]	E2			F2		
	SI (Position 1)	SI (Position 2)	MRS Top (Position 1)	MRS Top (Position 2)	MRS Low (Position 1)	MRS Low (Position 2)
0	6390	20248	4315	19905	107775	101521
0.1	7958	22604	4284	21809	107863	101128
0.2	9468	25621	4273	24569	106945	101227
0.3	11151	29486	4271	26910	107370	100404
0.4	12838	34512	4426	29565	107480	99612
0.5	14395	40014	4606	32506	107304	99138
0.6	16210	45930	4964	34464	106843	97860
0.7	18042	53491	5467	36656	107011	97481
0.8	20421	59779	6185	38640	106008	96023
0.9	22859	67065	7097	40965	105541	94292
1	25954	73319	8116	42681	105562	92942
1.1	30767	78889	9657	45847	105400	91952
1.2	35339	88852	11292	47909	105423	90886
1.3	41605	93459	12601	50845	104686	89543
1.4	47717	99129	14595	53775	104154	88352
1.5	54402	103182	16866	57101	103444	86420
1.6	65114	105964	18887	60468	103066	83927
1.7	69732	107707	22005	64538	102334	82510
1.8	77722	108762	25018	68615	101889	80400
1.9	84749	108874	29448	72664	101470	77936
2	90947	109364	33651	75766	100181	75474
2.1	97230	109648	38271	78911	99602	72465
2.2	101556	109425	43152	81452	99195	69260
2.3	103725	109390	48076	86118	98581	66199
2.4	106504	109873	53399	88377	97587	62733
2.5	106918	109937	59535	92224	96289	59574
2.6	107950	109809	64845	96457	94495	55718
2.7	107533	109684	71303	99874	93577	52719
2.8	107014	109577	76311	101849	92092	49216
2.9	106019	109684	81746	106291	90481	46096
3	103435	109492	86410	106994	89205	42062
3.1	99143	108706	90773	108469	88064	38195
3.2	94716	108623	95185	109921	85470	34821
3.3	88267	106293	99067	110681	83492	31259
3.4	81629	102218	102190	111152	81037	27531
3.5	75138	98088	105105	110963	79287	24458
3.6	65947	92939	107667	112348	76902	20586
3.7	58253	85952	110007	112810	73610	17975
3.8	48796	78436	111105	112388	70755	15214
3.9	40672	69306	111398	113176	67854	12191
4	32845	60643	111996	114013	64896	10271
4.1	24157	52272	112561	113055	61735	7786
4.2	16974	42167	112708	112938	58212	6312
4.3	9658	34245	112627	113334	55315	5071
4.4	5021	25070	111473	112371	51328	3842
4.5	2660	17077	109652	113122	47054	3167

4.6	1628	10361	108130	112758	42274	2482
4.7	1152	4639	105962	112081	38733	2076
4.8	990	2670	101240	111716	34314	1640
4.9	980	1844	98217	111979	30172	1337
5	882	1361	92909	111279	26282	1177
5.1	812	1236	87119	108165	22796	1120
5.2	821	1054	79369	106154	19212	1042
5.3	759	979	72194	101274	15874	976
5.4	720	938	65815	95978	12719	962
5.5	714	925	58960	88907	10150	899
5.6	668	830	52502	81166	8094	921
5.7	644	820	45270	75240	6602	930
5.8	688	803	38456	68462	5040	914
5.9	658	755	32196	61893	3855	846
6	641	738	26766	54443	3143	844
6.1	607	745	20234	46749	2406	790
6.2	564	732	15751	40523	1918	796
6.3	557	732	11974	34963	1756	751
6.4	532	681	8565	28076	1557	774
6.5	552	646	6485	22436	1452	719
6.6	605	660	4731	17040	1392	731
6.7	544	588	3450	11797	1282	699
6.8	599	622	2745	7603	1211	672
6.9	557	585	1887	4951	1106	626
7	510	599	1686	3616	1059	677
7.1	553	549	1477	2832	837	680
7.2	477	549	1342	2399	771	640
7.3	460	555	1252	2023	657	625
7.4	485	519	1233	1807	543	617
7.5	481	567	1224	1703	442	620
7.6	500	550	1112	1528	457	581
7.7	482	510	1147	1442	437	614
7.8	445	528	1155	1409	442	613
7.9	441	518	1045	1268	415	604
8	459	493	1007	1259	412	558
8.1	460	512	1073	1213	436	586
8.2	446	495	985	1254	422	606
8.3	469	527	1012	1134	403	560
8.4	459	486	944	1133	440	595
8.5	463	497	924	1156	404	581
8.6	487	522	910	1127	427	587
8.7	492	473	976	1097	398	573
8.8	423	460	966	1120	404	524
8.9	439	465	881	1077	415	561
9	445	422	853	1006	421	501
9.1	431	426	850	1034	442	523
9.2	394	432	778	970	426	520
9.3	409	460	818	982	392	535
9.4	407	434	768	980	422	545
9.5	431	459	757	993	417	516
9.6	401	435	755	907	422	479
9.7	415	415	763	878	393	526
9.8	434	450	732	851	386	494

9.9	419	450	713	869	413	476
10	387	469	715	852	396	496
10.1	375	461	697	847	396	507
10.2	395	441	723	826	444	449
10.3	390	446	687	872	395	519
10.4	426	430	671	840	409	470
10.5	399	445	661	843	379	514
10.6	358	426	616	749	355	492
10.7	397	441	621	765	384	454
10.8	381	414	636	784	376	478
10.9	406	408	618	792	360	486
11	409	425	591	737	388	454
11.1	373	430	621	766	367	481
11.2	419	433	637	696	357	461
11.3	384	427	587	733	370	426
11.4	393	451	561	710	417	461
11.5	386	419	616	712	342	488
11.6	376	419	569	793	418	506
11.7	391	458	576	666	392	509
11.8	399	414	551	675	374	458
11.9	404	421	546	701	422	476
12	388	428	585	674	376	484
12.1	384	416	562	707	408	459
12.2	391	423	525	662	368	428
12.3	397	395	525	638	364	452
12.4	414	411	567	698	376	448
12.5	385	379	538	633	400	454
12.6	386	390	551	676	399	483
12.7	396	416	540	609	396	479
12.8	422	405	547	618	375	468
12.9	406	412	530	628	377	434
13	352	451	479	582	395	480
13.1	400	399	554	588	415	446
13.2	377	412	496	649	369	411
13.3	369	390	506	643	373	453
13.4	381	390	471	613	371	429
13.5	390	395	520	618	351	419
13.6	399	410	500	606	389	458
13.7	406	401	492	604	376	396
13.8	380	407	540	633	365	457
13.9	392	368	482	557	347	468
14	398	387	508	576	392	410
14.1	370	373	473	578	384	416
14.2	378	368	449	541	390	445
14.3	401	389	497	568	353	441
14.4	392	373	478	528	416	438
14.5	413	369	499	534	392	396
14.6	382	405	481	543	372	379
14.7	357	369	437	589	359	452
14.8	352	401	538	564	404	417
14.9	352	416	453	563	377	398
15	346	406	444	535	376	410
15.1	389	359	449	580	360	441
15.2	385	386	413	578	354	391

15.3	414	403	438	552	401	423
15.4	386	392	455	568	379	390
15.5	387	416	454	552	338	394
15.6	364	390	460	522	358	442
15.7	418	420	426	545	368	411
15.8	380	388	442	467	390	406
15.9	364	373	479	505	357	391
16	427	379	442	505	381	415
16.1	375	380	428	471	361	444
16.2	348	388	441	480	412	394
16.3	388	380	445	487	418	406
16.4	380	394	413	472	398	395
16.5	412	391	454	529	376	418
16.6	384	385	421	544	361	411
16.7	367	385	414	459	358	387
16.8	368	361	457	484	389	421
16.9	377	356	477	472	382	400
17	375	395	468	494	380	391
17.1	385	411	420	492	398	363
17.2	402	397	429	443	375	435
17.3	363	411	437	531	383	447
17.4	402	391	403	494	364	385
17.5	385	413	404	449	376	384
17.6	375	370	471	461	399	404
17.7	420	391	437	509	350	366
17.8	380	374	412	451	374	402
17.9	362	354	409	493	334	386
18	376	359	399	471	359	384
18.1	385	389	415	444	354	392
18.2	364	368	435	487	381	413
18.3	391	362	407	453	359	395
18.4	345	357	408	490	368	410
18.5	382	358	410	452	359	399
18.6	390	396	418	468	373	407
18.7	374	362	432	462	366	392
18.8	350	382	413	445	365	392
18.9	377	394	403	417	359	409
19	374	382	432	454	339	413
19.1	360	394	419	447	360	431
19.2	383	369	415	452	360	391
19.3	358	344	447	437	381	383
19.4	365	378	423	454	355	387
19.5	372	387	393	452	360	394
19.6	380	377	402	447	348	425
19.7	390	394	427	414	341	368
19.8	367	370	445	458	384	414
19.9	371	355	397	409	339	415

**Table C4.** Data from EMA line scan of sample E2 and F2 regarding carbon.

Distance from start [μm]	Carbon					
	E2			F2		
	SI (Position 1)	SI (Position 2)	MRS Top (Position 1)	MRS Top (Position 2)	MRS Low (Position 1)	MRS Low (Position 2)
0	<b>850226</b>	593844	595666	481755	13100	9596
0.1	<b>840628</b>	552322	596683	460425	13194	10150
0.2	<b>831212</b>	502207	600328	436001	13510	<b>10280</b>
0.3	<b>819628</b>	<b>463214</b>	601790	412117	13709	<b>10454</b>
0.4	<b>806238</b>	<b>419074</b>	602748	386711	14124	<b>10776</b>
0.5	<b>786748</b>	<b>382658</b>	604133	360834	14424	<b>11055</b>
0.6	<b>755674</b>	<b>346978</b>	605858	332230	14604	<b>11542</b>
0.7	<b>721501</b>	<b>304866</b>	605421	305579	15053	<b>12049</b>
0.8	<b>676107</b>	<b>274495</b>	603714	278802	15188	<b>12531</b>
0.9	<b>626462</b>	<b>244232</b>	599763	255402	15779	<b>13278</b>
1	<b>574139</b>	<b>225518</b>	594204	234314	16776	<b>13909</b>
1.1	<b>513399</b>	<b>213746</b>	582661	215836	17364	<b>14732</b>
1.2	<b>465869</b>	<b>194226</b>	571548	204520	18361	<b>15311</b>
1.3	<b>413581</b>	<b>182103</b>	560176	194435	19322	<b>16202</b>
1.4	<b>373881</b>	<b>159907</b>	545530	190415	20300	<b>17458</b>
1.5	<b>338519</b>	<b>134090</b>	531369	187803	21030	<b>18486</b>
1.6	<b>284018</b>	<b>106048</b>	517356	187900	22080	<b>20409</b>
1.7	<b>264825</b>	<b>76154</b>	501671	186376	23056	<b>22092</b>
1.8	<b>244153</b>	<b>57167</b>	483798	181654	<b>24362</b>	<b>24231</b>
1.9	<b>231091</b>	<b>41597</b>	463029	175928	<b>25021</b>	<b>26521</b>
2	<b>222532</b>	<b>32730</b>	444485	171067	<b>26609</b>	<b>29279</b>
2.1	<b>213290</b>	<b>26941</b>	426652	166525	<b>27737</b>	<b>32694</b>
2.2	<b>198471</b>	<b>22234</b>	406584	161782	<b>28375</b>	<b>35798</b>
2.3	<b>162564</b>	<b>20411</b>	<b>386345</b>	158199	<b>29698</b>	<b>39022</b>
2.4	<b>129841</b>	<b>18727</b>	<b>364470</b>	155754	<b>30531</b>	<b>44205</b>
2.5	<b>99179</b>	<b>18054</b>	<b>341851</b>	152456	<b>31282</b>	<b>49175</b>
2.6	<b>70300</b>	<b>17484</b>	<b>317972</b>	147716	<b>32428</b>	<b>56778</b>
2.7	<b>52722</b>	<b>17093</b>	<b>290646</b>	<b>137252</b>	<b>33432</b>	<b>63942</b>
2.8	<b>38011</b>	<b>16585</b>	<b>266467</b>	<b>127630</b>	<b>34175</b>	<b>73776</b>
2.9	<b>29375</b>	<b>16560</b>	<b>242529</b>	<b>107739</b>	<b>35239</b>	<b>90064</b>
3	<b>23740</b>	<b>16125</b>	<b>220447</b>	<b>95875</b>	<b>36202</b>	<b>106844</b>
3.1	<b>19116</b>	<b>15534</b>	<b>197810</b>	<b>81016</b>	<b>36763</b>	<b>132407</b>
3.2	<b>17668</b>	<b>14979</b>	<b>175227</b>	<b>65706</b>	<b>38117</b>	<b>154693</b>
3.3	<b>17244</b>	<b>14566</b>	<b>154762</b>	<b>53669</b>	<b>39373</b>	<b>179583</b>
3.4	<b>17926</b>	<b>15134</b>	<b>134308</b>	<b>43310</b>	<b>40572</b>	<b>206769</b>
3.5	<b>19746</b>	<b>15812</b>	<b>116683</b>	<b>35489</b>	<b>41141</b>	<b>225926</b>
3.6	<b>22600</b>	<b>17428</b>	<b>97285</b>	<b>28113</b>	<b>42831</b>	<b>244184</b>
3.7	<b>25247</b>	<b>19598</b>	<b>81216</b>	<b>24019</b>	<b>45253</b>	<b>253330</b>
3.8	<b>28878</b>	<b>22416</b>	<b>66750</b>	<b>20499</b>	<b>47017</b>	<b>258720</b>
3.9	<b>32006</b>	<b>25356</b>	<b>53418</b>	<b>18077</b>	<b>49215</b>	<b>259800</b>
4	<b>36206</b>	<b>28494</b>	<b>42426</b>	<b>16387</b>	<b>51610</b>	<b>256700</b>
4.1	<b>40059</b>	<b>31895</b>	<b>33790</b>	<b>14972</b>	<b>54542</b>	<b>247561</b>
4.2	<b>43653</b>	<b>35473</b>	<b>26798</b>	<b>14028</b>	<b>57188</b>	<b>235091</b>
4.3	<b>47467</b>	<b>38463</b>	<b>21663</b>	<b>13550</b>	<b>60148</b>	<b>219248</b>
4.4	<b>51071</b>	<b>42155</b>	<b>17929</b>	<b>12932</b>	<b>63983</b>	<b>192265</b>
4.5	<b>53517</b>	<b>46276</b>	<b>15192</b>	<b>12669</b>	<b>67500</b>	<b>169231</b>

4.6	54824	48848	14082	12380	70495	138397
4.7	55261	52079	13719	12463	72358	116235
4.8	55386	53580	13823	12159	73142	92634
4.9	55110	54073	14599	12092	73678	72775
5	55320	54636	16041	12116	72438	64360
5.1	54988	54464	18197	12234	71133	56064
5.2	55344	54995	21033	12874	69438	52169
5.3	55096	54764	23905	13856	66382	50114
5.4	55359	55175	26585	15783	64372	49374
5.5	55397	54573	29640	17896	62179	49568
5.6	55555	54539	32109	20718	60685	49336
5.7	55180	54719	34871	24086	58150	49966
5.8	55833	54977	38186	26825	56817	50420
5.9	56216	54852	40698	30048	54763	50915
6	56550	54430	42626	32807	53337	50643
6.1	56785	55190	45584	35717	51140	50960
6.2	56379	54451	47701	38073	49969	51414
6.3	57265	55080	49328	41121	48263	51400
6.4	56870	54771	50774	43499	47504	51657
6.5	57073	54303	51378	45600	47799	51481
6.6	56567	54491	52148	47968	47953	51839
6.7	56733	54078	52298	50506	48920	51776
6.8	56406	53622	52251	52455	49825	51106
6.9	56047	53756	52403	53768	49649	50507
7	55930	54002	52320	55137	50690	50649
7.1	55463	53705	52136	55063	51191	50090
7.2	55261	53899	51951	55543	51667	50329
7.3	54504	53517	50979	55626	52138	50715
7.4	53985	53253	50190	55954	52462	50517
7.5	53860	53932	50055	55640	52744	51010
7.6	53663	53450	49626	56038	53379	50880
7.7	53056	53674	49496	56081	54589	51341
7.8	53724	53747	49088	55919	55295	51425
7.9	53452	53953	49257	56141	55791	51294
8	53302	53939	48669	56544	55275	51238
8.1	53302	54097	48667	56531	54785	51507
8.2	53489	53454	48683	56798	55598	51732
8.3	54325	53277	49230	55506	55264	51996
8.4	54153	53407	49475	55728	55173	51055
8.5	54162	53114	49358	54933	55086	50820
8.6	54467	52850	49499	54691	55412	50114
8.7	54795	52327	49532	54927	55291	50677
8.8	54219	51907	49275	54743	55921	50271
8.9	54727	51201	49548	54811	55197	50010
9	54434	51020	49926	54465	56171	50037
9.1	54790	50442	50502	54536	55785	50395
9.2	54438	50819	50558	53965	55337	50348
9.3	54810	51082	51029	54163	55558	50094
9.4	54274	51043	51089	53547	55916	50012
9.5	53911	50957	51328	52584	55659	50134
9.6	53685	51333	50984	52288	55735	49674
9.7	53405	51931	51025	51673	55991	49856
9.8	53029	52343	51283	51194	56290	50338

9.9	53244	53310	51481	50767	56118	50995
10	53356	53097	51263	51062	55890	51278
10.1	52854	53816	51722	51056	56140	51680
10.2	53193	54164	52092	50585	55749	52083
10.3	52649	54745	51780	50955	55329	52552
10.4	52451	55068	52253	51332	55231	52180
10.5	51985	54597	52699	51582	55301	52310
10.6	51989	54205	52979	51363	55140	52878
10.7	52462	54335	53502	51789	55605	53204
10.8	52483	54313	53113	51845	55408	54115
10.9	52507	54456	53632	52070	55754	54187
11	53060	53768	53569	52575	55892	54508
11.1	53175	53904	53504	52918	55679	55080
11.2	53112	53592	53914	52300	55351	54821
11.3	53387	53892	53202	53483	55355	55368
11.4	53694	52902	53128	53136	54934	54816
11.5	53738	52899	52755	53176	54829	54844
11.6	54397	51931	52254	53634	55137	54951
11.7	54804	52204	52615	54218	55156	55811
11.8	54824	51778	52322	53988	55381	55408
11.9	55491	51814	52159	53549	55585	55542
12	55551	51704	52416	53929	55748	55828
12.1	56001	51677	52328	54457	56150	55853
12.2	55228	51561	52661	54729	55650	55761
12.3	55497	51355	52515	54617	55842	56680
12.4	55459	52293	52672	54852	55993	56459
12.5	55826	51962	52871	54944	56043	56201
12.6	55729	52389	52642	55449	56050	56164
12.7	55845	52841	53470	55636	55684	55523
12.8	55703	53228	53255	55732	56036	54660
12.9	56026	53620	53181	56273	56172	54071
13	55237	54323	54358	55698	55837	53705
13.1	55253	54403	53776	56062	56186	53448
13.2	54936	54207	54303	55557	55784	53723
13.3	55326	54291	54822	55725	55203	53064
13.4	55094	54159	54444	55856	55237	53236
13.5	55150	53853	54480	54317	53968	53011
13.6	55104	54065	54916	53763	52974	52960
13.7	54756	53182	54458	53691	52436	53353
13.8	55169	52752	53673	53837	52400	53096
13.9	55079	51912	53575	53356	52392	53340
14	55233	51458	53240	53308	52716	53075
14.1	54760	51405	52527	53676	52727	53346
14.2	54537	50324	51733	53137	52950	52966
14.3	54244	50182	51272	52965	52657	53424
14.4	53821	50293	51642	53590	53030	54471
14.5	53958	50237	50566	53413	53682	53441
14.6	53929	50483	50732	53437	54081	53445
14.7	53238	50352	50249	53292	53639	53593
14.8	53294	50943	50117	53471	54244	53461
14.9	53045	50866	49583	53620	54865	53250
15	52303	51451	49060	53841	55346	53105
15.1	52300	51948	48329	53863	55840	52411
15.2	52543	51894	48014	54223	56059	51897

15.3	52270	52801	48130	54504	55919	52212
15.4	52993	52970	48286	54631	55970	52468
15.5	52656	53467	48419	54747	56558	52251
15.6	52977	53503	48451	54899	56780	51271
15.7	52247	53676	49276	54763	57155	51605
15.8	52535	53530	50145	54730	57001	51655
15.9	52179	53248	50484	54616	56893	51560
16	51916	52445	51084	54652	57062	52482
16.1	52333	52388	50685	55020	57168	52699
16.2	52718	52018	50934	55011	57628	53318
16.3	52254	51695	51438	55251	56805	53162
16.4	52463	51137	50975	54397	57151	53935
16.5	52163	51290	51391	54591	57100	53923
16.6	52512	51212	51140	54412	56329	53731
16.7	52292	51095	51400	54356	56866	54470
16.8	52494	51046	51499	54102	56688	54676
16.9	52257	51078	52136	54348	56185	54056
17	53041	51388	52498	54489	55992	54698
17.1	52705	51632	52414	54611	55590	54320
17.2	52934	51646	52358	54910	55067	54256
17.3	52978	51848	53111	54792	54591	54739
17.4	53128	52033	53041	54605	54899	54944
17.5	53186	52608	53233	54676	54220	54739
17.6	52854	52878	53277	55325	53095	54310
17.7	52672	52563	53038	54947	52188	53800
17.8	52601	53044	52899	54976	51039	53818
17.9	52615	52978	52627	54948	50003	53889
18	52589	52712	53275	54763	50228	53684
18.1	52262	52796	53026	54536	49727	53761
18.2	51873	52457	53204	55101	49759	54068
18.3	52062	52191	53593	54672	49478	54188
18.4	51989	52347	52887	54205	49245	54048
18.5	52010	52086	52889	54138	48962	54043
18.6	51346	52270	53073	53605	48124	54473
18.7	51982	52777	52634	53337	47003	54559
18.8	52118	52312	52497	53096	47121	54819
18.9	52085	52902	52617	52919	46047	54538
19	51595	52892	52662	52679	46480	55169
19.1	52095	52924	53021	52242	47070	54373
19.2	52554	52757	52890	51908	47383	53940
19.3	52313	53047	53411	51912	47917	53512
19.4	52070	53175	53165	51490	48343	53434
19.5	52531	53026	53002	51654	48788	52809
19.6	52427	52854	53238	51505	50004	53445
19.7	52716	53392	53147	51269	50238	53292
19.8	52899	52816	53006	51464	51328	53264
19.9	52811	53036	52917	50932	51149	53131

**Table C5.** Data from EMA line scan of sample G3 and H3 regarding titanium.

Distance from start [μm]	Titanium					
	G3			H3		
	SI (Position 1)	SI (Position 2)	MRS Top (Position 1)	MRS Top (Position 2)	MRS Low (Position 1)	MRS Low (Position 2)
0	778	408	529	3306	108609	109645
0.1	917	604	557	3752	108320	109735
0.2	1039	706	670	4560	108087	109133
0.3	1238	920	748	5452	107915	108655
0.4	1354	1147	823	7210	108524	108249
0.5	1727	1512	987	8702	107287	108172
0.6	2001	2109	1058	10149	108189	108421
0.7	2604	2538	1092	12282	107620	107564
0.8	3177	3514	1241	14557	107987	107213
0.9	3886	4386	1401	16777	108248	107378
1	5159	5299	1438	19245	108291	107101
1.1	6598	6404	1650	21472	107772	106198
1.2	9118	7851	1881	24544	107772	105835
1.3	12531	9239	1949	27778	108189	105485
1.4	17170	10530	2155	31391	108154	104970
1.5	26749	12225	2464	35319	108243	104725
1.6	32475	14440	2615	38936	108006	104212
1.7	40098	16196	2781	43465	107797	104530
1.8	47361	17496	3312	48408	107772	103864
1.9	54700	18158	3699	53238	106883	104170
2	63185	18572	4100	57875	107696	104307
2.1	69210	19848	4721	63839	107096	104113
2.2	76697	21989	5470	68173	107195	103361
2.3	82126	25206	6112	71942	107236	103690
2.4	84371	29374	7319	76812	107553	103511
2.5	86054	33322	8091	80442	106584	103226
2.6	84328	38021	9390	83823	106524	103008
2.7	80596	41619	10918	87478	106031	102864
2.8	74581	44704	12364	90525	105918	102714
2.9	68874	45794	14057	94347	106106	102952
3	60764	45629	15096	97484	105948	102639
3.1	54088	44614	16512	100465	105002	101960
3.2	45811	43242	17482	102605	105480	102092
3.3	39695	41696	18556	104167	105656	101062
3.4	32822	40112	19142	106147	105431	99868
3.5	25399	38345	20019	106808	105342	98933
3.6	19141	36303	20903	107609	105006	96920
3.7	12221	34470	21873	106650	104594	94662
3.8	7362	31515	22609	105275	104516	91667
3.9	4008	28070	23144	100541	103353	88066
4	1900	24067	23154	97126	103219	82925
4.1	1257	16974	22755	92448	101379	77931
4.2	1101	13316	22599	86009	100314	71657
4.3	925	9354	21917	80944	98167	66126
4.4	863	6203	21087	75626	94988	61584
4.5	918	3972	19771	69093	91627	56836
4.6	879	2210	18318	62220	87520	51444
4.7	844	1395	16290	56620	83233	46538
4.8	765	903	14784	51067	78574	41507
4.9	803	680	13450	45340	73256	36755
5	745	606	12222	40151	68322	32151
5.1	713	526	11041	34494	61835	27093
5.2	759	507	9952	29211	57243	22957

5.3	699	527	8884	24343	51926	19062
5.4	622	514	7592	18777	46413	15096
5.5	604	542	6797	14151	41418	11294
5.6	621	518	5495	10193	36548	8224
5.7	640	475	4168	6562	31385	5530
5.8	639	485	2812	3919	25562	3194
5.9	594	473	1660	2421	19962	1905
6	564	476	1063	1634	16008	1365
6.1	567	480	769	1258	11527	1148
6.2	551	448	624	1025	8094	1023
6.3	539	461	560	946	5150	993
6.4	544	459	498	922	3188	931
6.5	541	450	509	832	2161	902
6.6	534	477	473	799	1586	919
6.7	537	455	506	818	1283	853
6.8	523	458	488	774	1263	878
6.9	545	440	465	753	1152	756
7	558	491	482	727	1181	795
7.1	552	441	449	742	1018	731
7.2	475	406	445	681	989	695
7.3	510	396	486	660	1038	693
7.4	521	449	481	655	1039	661
7.5	504	432	477	672	916	657
7.6	460	419	454	680	922	662
7.7	458	419	439	615	829	664
7.8	476	403	432	621	853	643
7.9	536	429	433	576	790	624
8	481	414	471	586	823	608
8.1	429	426	447	582	797	618
8.2	498	403	393	578	779	621
8.3	462	426	439	569	750	585
8.4	444	381	370	581	779	561
8.5	433	413	427	539	705	562
8.6	458	398	432	503	666	560
8.7	467	406	421	508	697	558
8.8	479	409	409	521	669	559
8.9	448	377	416	547	626	533
9	453	369	407	537	690	562
9.1	443	359	426	493	641	544
9.2	427	400	461	502	631	508
9.3	432	392	426	476	631	489
9.4	435	387	392	500	599	518
9.5	411	393	414	537	631	496
9.6	464	376	442	496	642	529
9.7	445	366	439	468	580	503
9.8	408	405	428	516	588	524
9.9	426	401	410	518	583	502
10	394	385	437	487	558	447
10.1	434	364	441	487	607	457
10.2	422	403	386	477	572	500
10.3	452	385	416	492	586	471
10.4	381	405	405	458	560	475
10.5	439	410	403	434	517	466
10.6	394	397	397	431	538	495
10.7	402	356	407	454	528	463
10.8	428	411	378	485	544	475
10.9	418	387	391	426	513	424
11	367	383	429	421	513	455
11.1	422	382	392	474	555	478
11.2	399	375	403	411	488	455
11.3	412	405	396	480	490	459

11.4	405	352	405	400	510	465
11.5	398	350	414	434	537	443
11.6	389	365	435	471	491	446
11.7	412	376	417	458	518	460
11.8	389	371	393	413	508	459
11.9	379	365	411	433	502	468
12	373	392	430	399	481	438
12.1	401	366	398	428	513	494
12.2	405	374	409	440	450	442
12.3	387	367	359	437	480	456
12.4	394	387	401	392	464	469
12.5	421	341	376	384	441	436
12.6	404	401	405	412	455	437
12.7	380	354	403	419	478	439
12.8	401	394	409	393	445	463
12.9	409	370	393	413	422	408
13	397	367	384	405	468	405
13.1	382	380	411	406	500	447
13.2	389	423	407	410	430	395
13.3	362	359	382	421	461	434
13.4	404	374	418	402	437	427
13.5	377	384	370	392	386	407
13.6	386	406	363	423	426	414
13.7	367	382	397	405	454	408
13.8	394	388	391	416	442	436
13.9	387	349	414	416	437	443
14	393	378	378	407	455	407
14.1	375	395	398	412	424	439
14.2	427	359	393	421	451	413
14.3	420	356	421	414	411	455
14.4	389	349	427	400	435	421
14.5	376	357	392	399	441	394
14.6	365	369	397	413	421	411
14.7	380	378	334	370	413	407
14.8	383	357	374	396	445	403
14.9	372	376	395	411	427	408
15	395	378	381	385	442	424
15.1	383	364	379	412	402	413
15.2	384	349	372	388	429	419
15.3	361	379	370	399	425	393
15.4	380	392	387	409	435	390
15.5	362	379	405	407	417	383
15.6	369	400	378	419	459	424
15.7	429	369	413	373	420	436
15.8	360	332	388	426	378	427
15.9	371	395	424	418	410	377
16	356	390	397	383	407	387
16.1	402	364	429	412	404	416
16.2	398	399	408	411	388	397
16.3	409	390	374	392	410	372
16.4	388	378	391	425	422	394
16.5	350	386	405	388	390	373
16.6	342	374	370	407	380	376
16.7	374	389	409	423	428	369
16.8	396	373	387	388	416	392
16.9	399	377	398	405	368	424
17	426	397	392	419	430	360
17.1	383	380	355	395	391	379
17.2	366	338	378	374	355	376
17.3	434	375	390	392	404	402
17.4	391	357	393	372	402	385

17.5	361	357	366	395	<b>371</b>	355
17.6	377	389	404	368	<b>378</b>	396
17.7	380	383	367	433	<b>404</b>	342
17.8	366	368	395	394	<b>343</b>	400
17.9	378	378	352	411	<b>397</b>	386
18	410	347	381	372	<b>389</b>	395
18.1	391	385	388	376	391	408
18.2	381	396	364	370	407	411
18.3	377	344	393	412	379	404
18.4	342	362	394	419	387	389
18.5	393	385	364	391	390	393
18.6	410	380	354	383	426	346
18.7	392	381	387	396	407	379
18.8	396	377	382	408	379	433
18.9	385	362	375	336	399	383
19	355	347	339	398	374	380
19.1	370	418	383	426	393	380
19.2	377	358	364	404	370	391
19.3	377	345	408	408	399	417
19.4	400	380	378	378	401	423
19.5	369	340	361	388	368	388
19.6	382	381	397	376	367	376
19.7	374	365	337	414	377	352
19.8	375	387	380	388	383	370
19.9	379	351	408	400	407	394

**Table C6.** Data from EMA line scan of sample G3 and H3 regarding carbon.

Distance from start [μm]	G3			H3		
	SI (Position 1)	SI (Position 2)	MRS Top (Position 1)	MRS Top (Position 2)	MRS Low (Position 1)	MRS Low (Position 2)
0	<b>817711</b>	884586	797401	751341	17458	15988
0.1	<b>807049</b>	891697	791857	742086	17736	16088
0.2	<b>797465</b>	894938	785148	733815	17903	16142
0.3	<b>787720</b>	899782	774227	721954	18213	16026
0.4	<b>777792</b>	904246	762185	705544	18528	15911
0.5	<b>766712</b>	905115	748972	689988	19191	15872
0.6	<b>759504</b>	<b>907434</b>	733909	672390	19303	15774
0.7	<b>751554</b>	<b>908927</b>	721447	651836	20592	15918
0.8	<b>751613</b>	<b>909464</b>	707481	625971	21663	15329
0.9	<b>750101</b>	<b>904908</b>	690341	599730	23096	15145
1	<b>755002</b>	<b>902104</b>	674913	570197	24293	15049
1.1	<b>758035</b>	<b>893692</b>	658719	538483	25665	15227
1.2	<b>762151</b>	<b>883612</b>	640941	503366	27301	14845
1.3	<b>767792</b>	<b>871769</b>	623658	474803	29548	14589
1.4	<b>770874</b>	<b>859255</b>	607145	450792	31230	14763
1.5	<b>772566</b>	<b>843255</b>	594778	427812	33364	14633
1.6	<b>767625</b>	<b>821522</b>	582458	403237	35544	14785
1.7	<b>757790</b>	<b>799808</b>	573940	379773	37883	14721
1.8	<b>743421</b>	<b>772282</b>	562245	355299	40015	14942
1.9	<b>721437</b>	<b>741365</b>	<b>555054</b>	326883	43196	<b>14936</b>
2	<b>683588</b>	<b>702823</b>	<b>546416</b>	<b>298998</b>	44674	<b>15038</b>
2.1	<b>643446</b>	<b>654307</b>	<b>539181</b>	<b>264781</b>	46812	<b>15256</b>
2.2	<b>589721</b>	<b>609328</b>	<b>532713</b>	<b>237500</b>	48770	<b>15104</b>
2.3	<b>537959</b>	<b>561382</b>	<b>529701</b>	<b>211014</b>	50451	<b>15459</b>
2.4	<b>481577</b>	<b>521270</b>	<b>528166</b>	<b>183077</b>	51921	<b>15450</b>

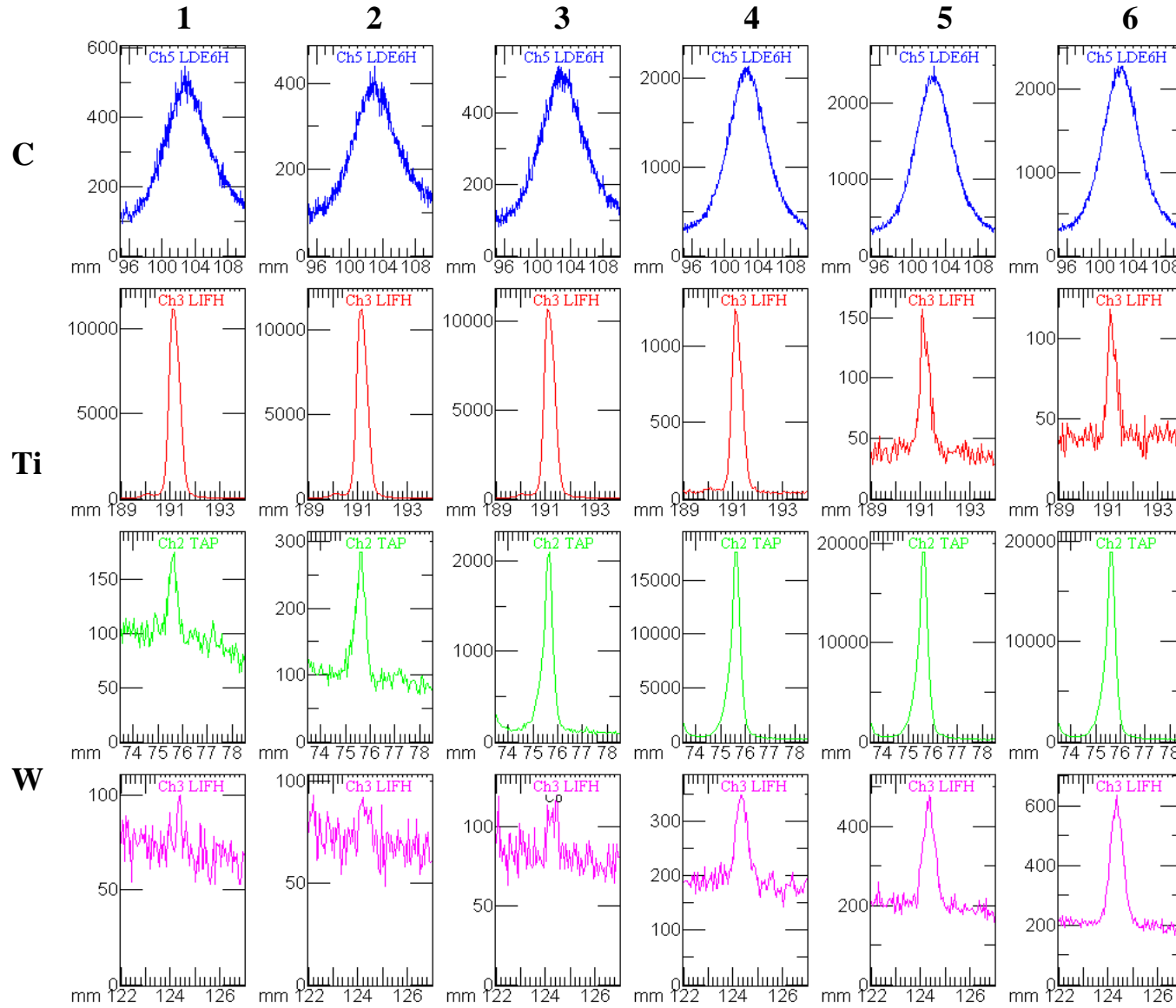
2.5	407289	480114	527201	161004	53409	15684
2.6	349023	429744	523328	140566	55064	15490
2.7	281181	385231	516451	124199	55898	15450
2.8	231273	335563	508620	111304	57099	15758
2.9	185473	292309	496463	104130	57762	15653
3	138370	256143	483267	97672	58938	15740
3.1	106645	221548	463659	92442	59682	15884
3.2	78768	199430	445808	84213	60475	15997
3.3	63066	175559	428174	73969	60927	16156
3.4	52791	161600	405928	61753	62105	16692
3.5	45627	154762	382870	51781	63378	17612
3.6	43455	150555	359847	41909	65022	18001
3.7	43014	147322	336360	34568	67046	19463
3.8	44174	136533	310367	29829	69206	21028
3.9	46189	118794	284443	24674	72099	22657
4	49140	99038	263054	23460	75039	24460
4.1	51644	72666	241400	23475	79504	27151
4.2	53220	64324	221326	24030	83358	30146
4.3	53617	57064	200505	24921	88224	32401
4.4	53651	54178	180987	26464	91429	34857
4.5	53470	52020	161704	28304	95186	36815
4.6	53419	50705	142138	30958	98825	39390
4.7	53065	49926	124658	32835	102737	41696
4.8	53475	49188	112479	34686	106040	43869
4.9	53149	49403	102809	36365	108415	45833
5	53283	50035	95479	38415	110961	48051
5.1	53253	49884	90041	40649	112731	50127
5.2	53498	49623	86993	41905	113794	52055
5.3	53161	50168	84198	43871	115500	53869
5.4	53107	50474	80770	45517	116729	55273
5.5	52516	50232	78177	47617	117970	56421
5.6	52338	50578	74789	49108	118761	57951
5.7	52144	50755	72075	50940	118731	58726
5.8	51855	50899	67994	52316	119259	58421
5.9	51490	51668	62091	52540	118302	59619
6	51756	51777	56951	53662	116997	59115
6.1	51854	52200	54170	53718	113486	59024
6.2	51101	51500	53093	53592	111029	58520
6.3	50999	52523	52300	53525	107306	58293
6.4	50298	51867	52513	53218	104369	57786
6.5	50610	51795	52459	53311	101996	57258
6.6	51206	52280	52813	53879	99450	57292
6.7	51076	52455	52125	52896	97031	57002
6.8	51544	52623	52609	53112	96080	56379
6.9	51633	52315	53091	52617	95373	55730
7	51887	51566	53263	52658	95468	55625
7.1	51848	51745	52903	52972	95623	55527
7.2	51765	51677	53155	52535	95814	55345
7.3	51907	51259	52926	52415	95597	55695
7.4	51719	51236	53117	52480	94921	56073
7.5	52234	51333	53066	52535	95256	55867
7.6	52685	51320	53076	52649	93533	55761
7.7	53111	51407	53514	52868	93313	55773
7.8	53470	51390	54058	53191	93033	55961
7.9	52966	51142	53461	53448	92707	56031
8	53272	51143	53792	52542	92154	55699
8.1	53935	51241	54336	52957	92087	55897
8.2	54028	51177	53558	52605	91856	56492
8.3	53989	50914	54447	52636	91611	55975
8.4	54100	50741	54206	52695	92514	56336
8.5	54567	50242	54449	53246	93076	56242

8.6	54352	49503	54314	53759	93317	56468
8.7	54264	49427	54590	53975	94295	56559
8.8	53844	48782	54353	53720	93506	56674
8.9	54347	48928	54467	54066	93815	56232
9	53646	47767	54665	53900	93127	56849
9.1	52979	47590	55225	54375	92020	56618
9.2	52331	47132	54928	54118	90785	56551
9.3	52096	46754	54558	54418	90036	56878
9.4	51813	46697	54532	55040	89327	56753
9.5	51814	46931	54261	54750	88604	56745
9.6	51497	46581	54355	54475	88245	56612
9.7	50729	47034	54549	54611	88018	56609
9.8	50666	47180	54116	55164	87713	56679
9.9	50531	47772	54131	55249	88324	57072
10	50033	47819	54256	55556	88742	56126
10.1	50410	48603	53801	55268	88056	56516
10.2	50386	48548	53853	55132	87917	56410
10.3	50383	49568	54003	55026	86318	56173
10.4	50939	49760	53760	54078	85511	56005
10.5	50834	50274	54501	54213	83780	56510
10.6	50822	50869	54260	54602	83401	56267
10.7	50103	51532	54317	53994	81649	56636
10.8	49254	52344	54453	54092	80346	56525
10.9	49084	52429	54042	53904	79680	56749
11	49027	51620	54459	54044	78288	56497
11.1	49240	51748	54386	53454	77246	56894
11.2	49791	50915	54284	53167	76301	57187
11.3	49658	50749	54657	53503	75581	57320
11.4	49687	50459	54312	53501	75405	57037
11.5	49574	50506	54335	53590	74016	57643
11.6	49931	50009	54435	53173	73243	57086
11.7	49647	50495	54315	53209	71897	57079
11.8	49551	49683	54613	53268	70892	57430
11.9	50236	49624	54425	53116	68223	57657
12	50747	49084	54736	53384	66829	57653
12.1	51038	49131	54900	53719	65464	57770
12.2	51389	48647	55143	53812	64801	57456
12.3	52127	49348	54879	53845	63818	57633
12.4	51896	49684	55082	54464	62549	57377
12.5	52202	49925	54913	54855	62530	57601
12.6	52032	50902	55201	54902	62173	57158
12.7	51566	50844	54871	54966	61681	57301
12.8	51293	51204	55004	55137	60650	56559
12.9	51309	51167	54751	55293	60070	56681
13	51177	52022	54917	55699	59545	56384
13.1	51098	52023	54505	55004	58713	56582
13.2	51173	52309	55056	54748	57766	55817
13.3	51074	52294	55468	54704	57695	55653
13.4	51007	52799	54967	54618	57010	55836
13.5	50724	53107	55082	54575	56222	55958
13.6	51057	53266	55247	54837	56027	55623
13.7	50563	53174	55142	54367	55548	55517
13.8	51285	53205	54801	54595	55567	55514
13.9	51500	52520	54580	54240	55081	55166
14	51678	52198	54584	54762	55242	55611
14.1	51167	51906	54383	54352	55669	55211
14.2	51906	51156	54035	54488	55372	55449
14.3	51794	50793	54407	54020	55333	54884
14.4	51935	50232	53966	54155	56002	55077
14.5	52016	49999	54395	54030	56020	55311
14.6	52272	49893	54169	53733	56000	55389
14.7	51895	49544	54238	53214	56029	55538

14.8	52179	49846	54262	53112	56006	55590
14.9	51974	49945	54159	53636	55954	55989
15	52223	49820	54319	53321	56246	55724
15.1	52089	49967	54344	53251	56156	56672
15.2	52352	49470	54423	53376	55997	55779
15.3	52201	50041	54349	53677	56148	55664
15.4	52075	50134	53903	53822	56414	55350
15.5	52205	50393	53927	54086	56386	55542
15.6	52249	50058	53956	54403	56412	55606
15.7	52319	50645	54290	54097	56881	54759
15.8	51998	50224	54318	54386	56952	54568
15.9	51938	49962	54768	53945	56425	54925
16	51971	49734	55105	54482	56169	54523
16.1	52022	49893	54948	54357	56485	54676
16.2	52037	49801	55480	54043	56859	54720
16.3	51649	49809	54768	54584	56898	54057
16.4	51817	49883	54797	54416	57570	54288
16.5	51407	49925	54846	54353	58042	54113
16.6	51480	49884	54319	54614	59036	53953
16.7	51920	49674	53760	54794	59584	54056
16.8	51433	49882	53728	55380	59918	53888
16.9	52144	50421	53154	55444	61522	53574
17	52230	50247	53030	55330	61226	53721
17.1	51865	49760	52815	55970	61720	53692
17.2	52282	50532	52962	55647	62234	53641
17.3	52462	50548	52000	55499	63132	53892
17.4	52771	50652	51951	55739	63306	54148
17.5	53218	50797	52171	56223	63490	53838
17.6	52907	51613	51983	56752	64792	53956
17.7	53017	51222	51874	56678	65041	53364
17.8	53298	51234	51816	56408	65789	53570
17.9	53391	51843	52046	56804	66183	53705
18	53406	51287	51918	57061	65774	53567
18.1	53212	51235	51745	56719	65362	52891
18.2	52875	51430	51844	56601	64622	53347
18.3	52779	51565	52027	56841	63186	53248
18.4	52692	51169	52312	57166	62167	53435
18.5	52607	50811	52707	57112	61352	53139
18.6	52466	50435	52383	57305	60147	53480
18.7	52491	50130	52770	57296	59440	53459
18.8	52133	49749	53088	56759	57962	53238
18.9	52269	49848	53385	56801	56718	53403
19	52367	49981	53661	56807	56663	53977
19.1	52130	49064	54396	56480	55209	53952
19.2	51429	49588	54148	56412	54280	53659
19.3	51537	48951	53962	56179	53266	53543
19.4	51468	48624	54526	56088	52557	53669
19.5	51773	47900	54719	56237	51998	53300
19.6	51327	47462	55175	56036	51179	53331
19.7	51551	47656	54976	55989	50763	52886
19.8	51485	47271	54938	55383	50678	53484
19.9	51330	47399	54698	55722	50493	53831

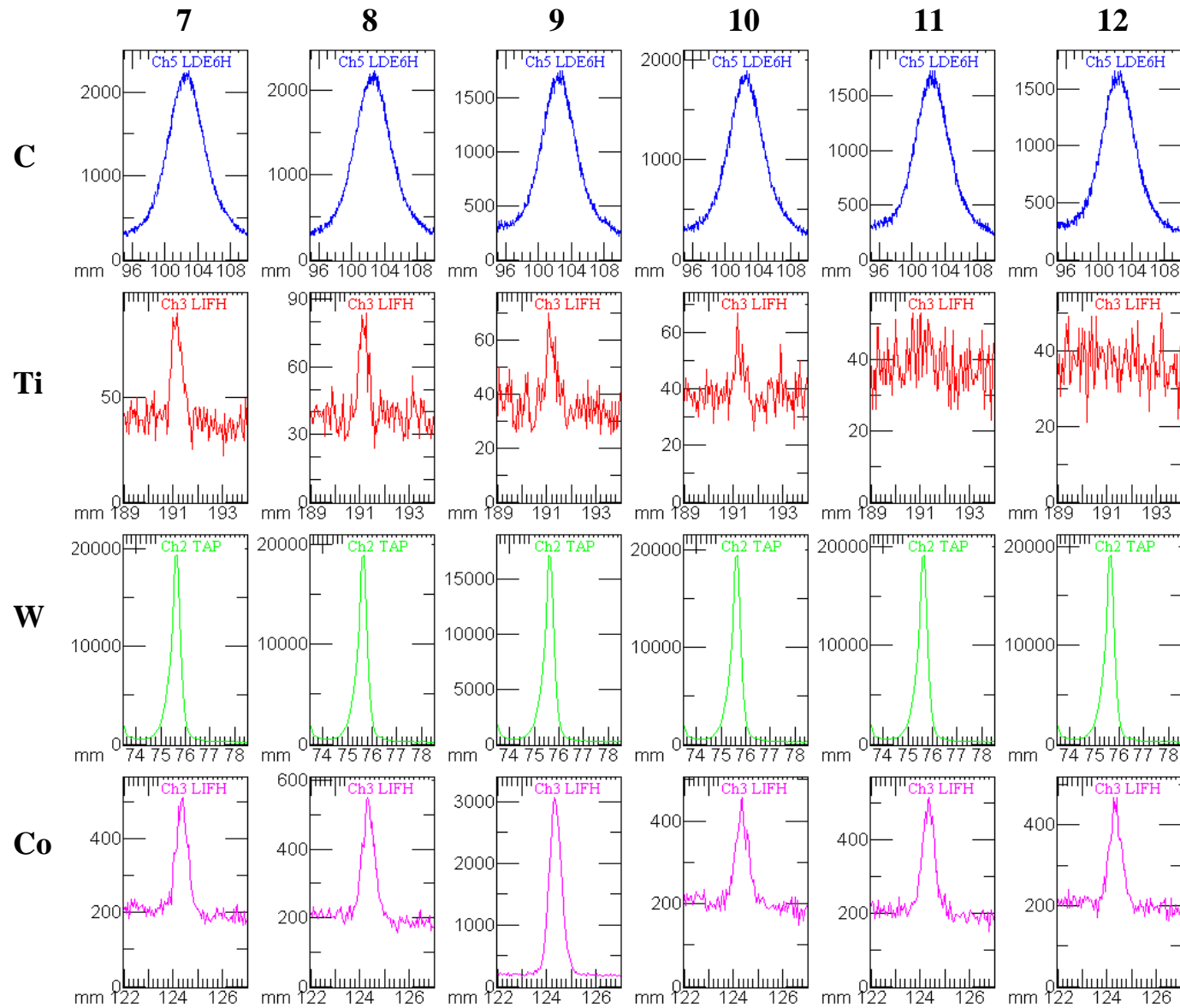
## **APPENDIX C2 – POINT-TO-POINT ANALYSIS WITH EMA**

Raw data from the point-to-point analysis, performed with electron microprobe analyzer (EMA), are presented in Fig. C1–16. Test G3 (Fig. C1–4), H3 (Fig. C5–8), I3 (Fig. C9–12) and J3 (Fig. C13–16) were analyzed along two lines at different locations. Carbon (C), titanium (Ti), tungsten (W) and cobalt (Co) were analyzed and are represented with blue, red, green and pink colors, respectively. The maximum (Max), minimum (Min) and average (Av.) values from respective diagram are displayed in tables next to each collage of spectra.



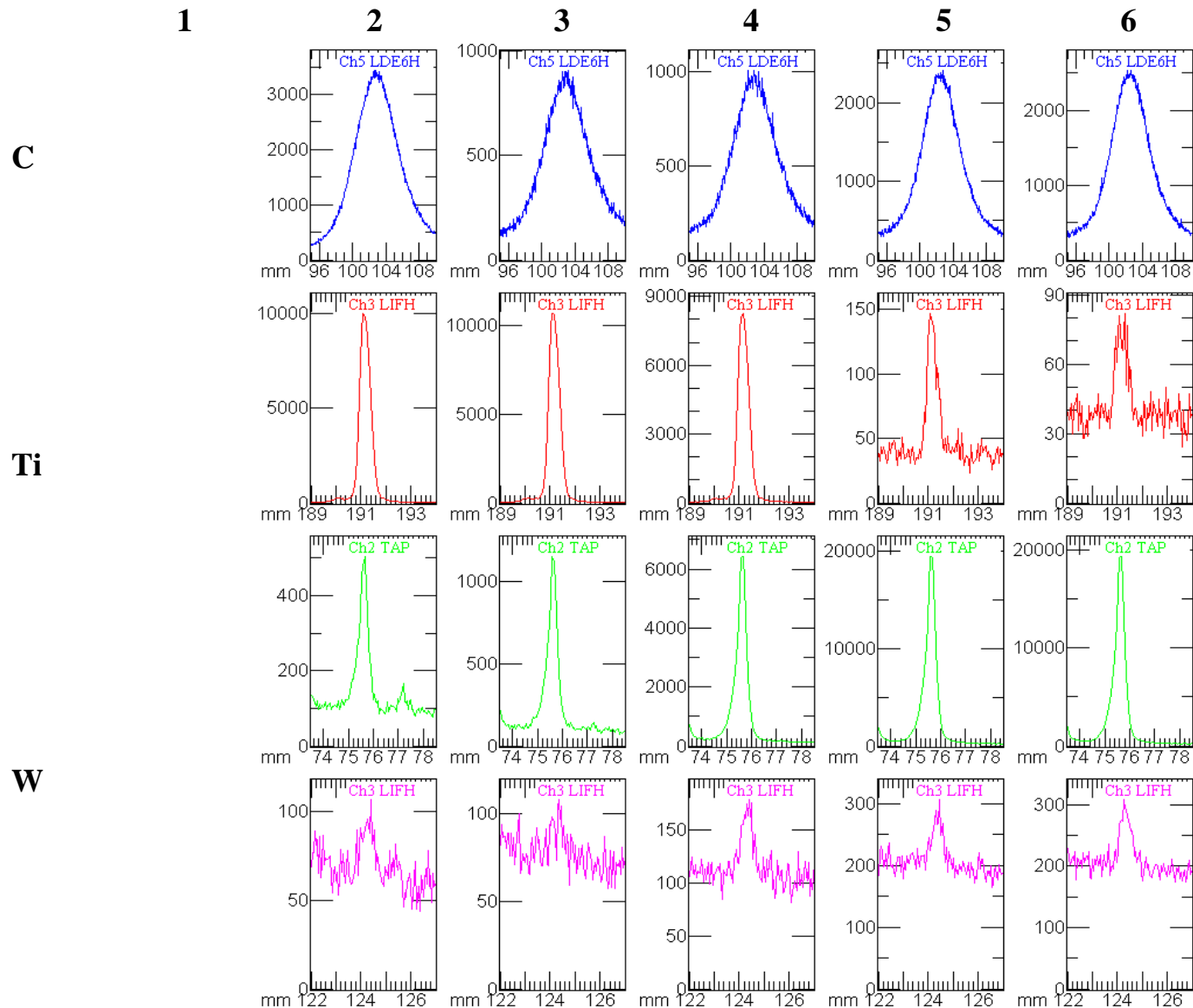
	C	Ti	
	Max 546	Max 11157	
<b>1</b>	Min 93	Min 22	
	Av. 275	Av. 1217	
	Max 440	Max 11254	
<b>2</b>	Min 74	Min 23	
	Av. 226	Av. 1225	
	Max 532	Max 10673	
<b>3</b>	Min 81	Min 28	
	Av. 274	Av. 1169	
	Max 2139	Max 1239	
<b>4</b>	Min 266	Min 29	
	Av. 979	Av. 159	
	Max 2484	Max 157	
<b>5</b>	Min 273	Min 27	
	Av. 1064	Av. 48	
	Max 2275	Max 118	
<b>6</b>	Min 292	Min 25	
	Av. 1014	Av. 44	
	W	Co	
	Max 175	Max 100	
<b>1</b>	Min 64	Min 53	
	Av. 101	Av. 72	
	Max 284	Max 93	
<b>2</b>	Min 71	Min 48	
	Av. 113	Av. 72	
	Max 2096	Max 120	
<b>3</b>	Min 83	Min 63	
	Av. 310	Av. 84	
	Max 17588	Max 349	
<b>4</b>	Min 191	Min 142	
	Av. 2054	Av. 204	
	Max 19180	Max 479	
<b>5</b>	Min 198	Min 147	
	Av. 2236	Av. 229	
	Max 18948	Max 635	
<b>6</b>	Min 199	Min 160	
	Av. 2212	Av. 253	

**Figure C1.** Test G3, line 1. Spectra from EMA point-to-point analysis of C (blue), Ti (red), W (green) and Co (pink) to the left.



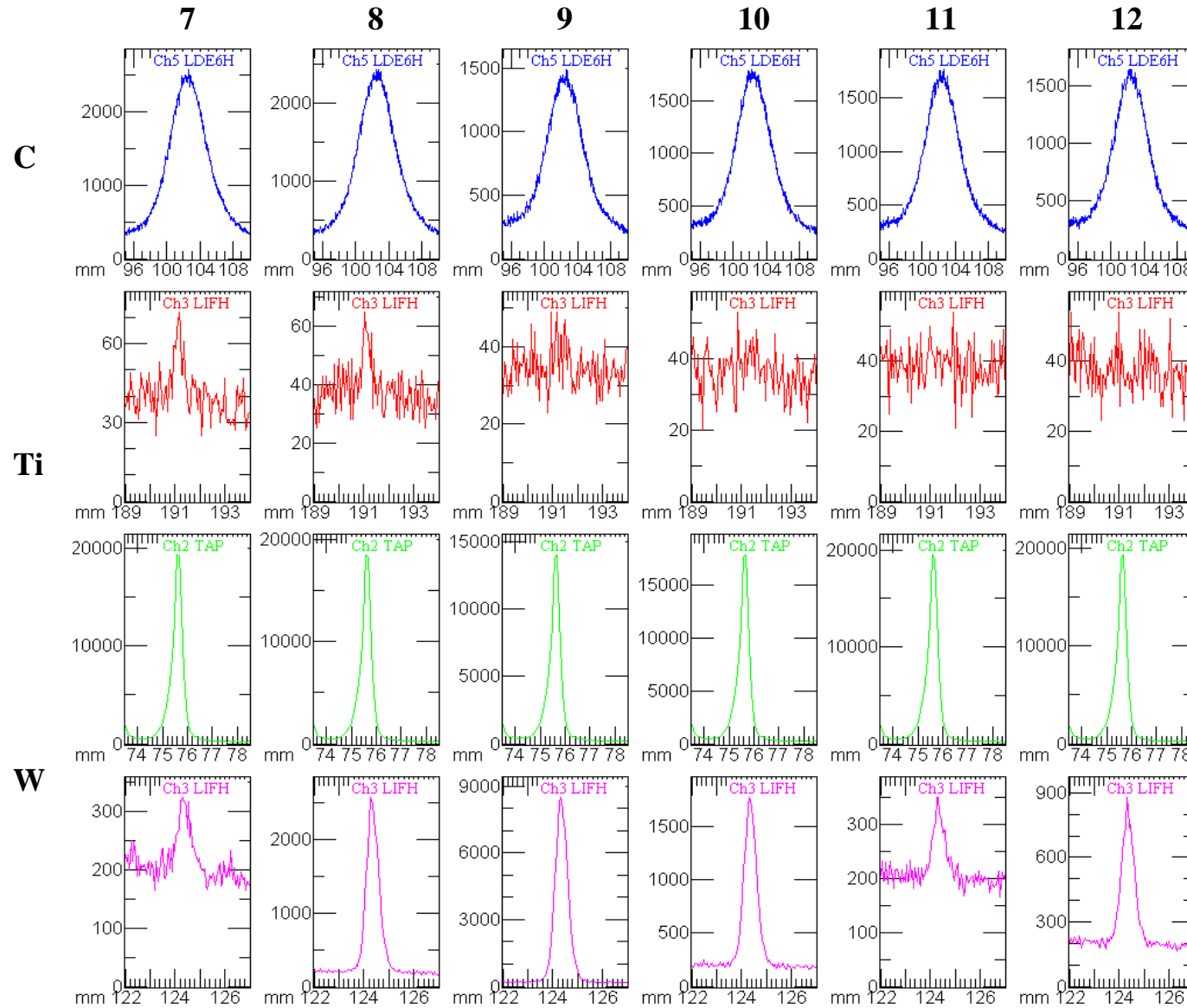
	C	Ti		
7	Max 2255 Min 275 Ave 1002	Max 90 Min 22 Ave 43		
8	Max 2234 Min 285 Ave 988	Max 84 Min 24 Ave 41		
9	Min 220 Ave 762 Max 1896	Min 25 Ave 37 Max 67		
10	Min 241 Ave 827 Max 1734	Min 25 Ave 39 Max 53		
11	Min 221 Ave 756 Max 1661	Min 23 Ave 39 Max 50		
12	Min 240 Ave 726	Min 21 Ave 37		
	W	Co		
7	Max 19297 Min 195 Ave 2232	Max 513 Min 165 Ave 236		
8	Max 18931 Min 192 Ave 2204	Max 550 Min 157 Ave 238		
9	Min 185 Ave 2021 Max 19506	Min 158 Ave 538 Max 457		
10	Min 204 Ave 2265 Max 19136	Min 149 Ave 227 Max 514		
11	Min 202 Ave 2238 Max 19088	Min 150 Ave 236 Max 468		
12	Min 203 Ave 2217	Min 163 Ave 230		

**Figure C2.** Test G3, line 1. Spectra from EMA point-to-point analysis of C (blue), Ti (red), W (green) and Co (pink) to the left.



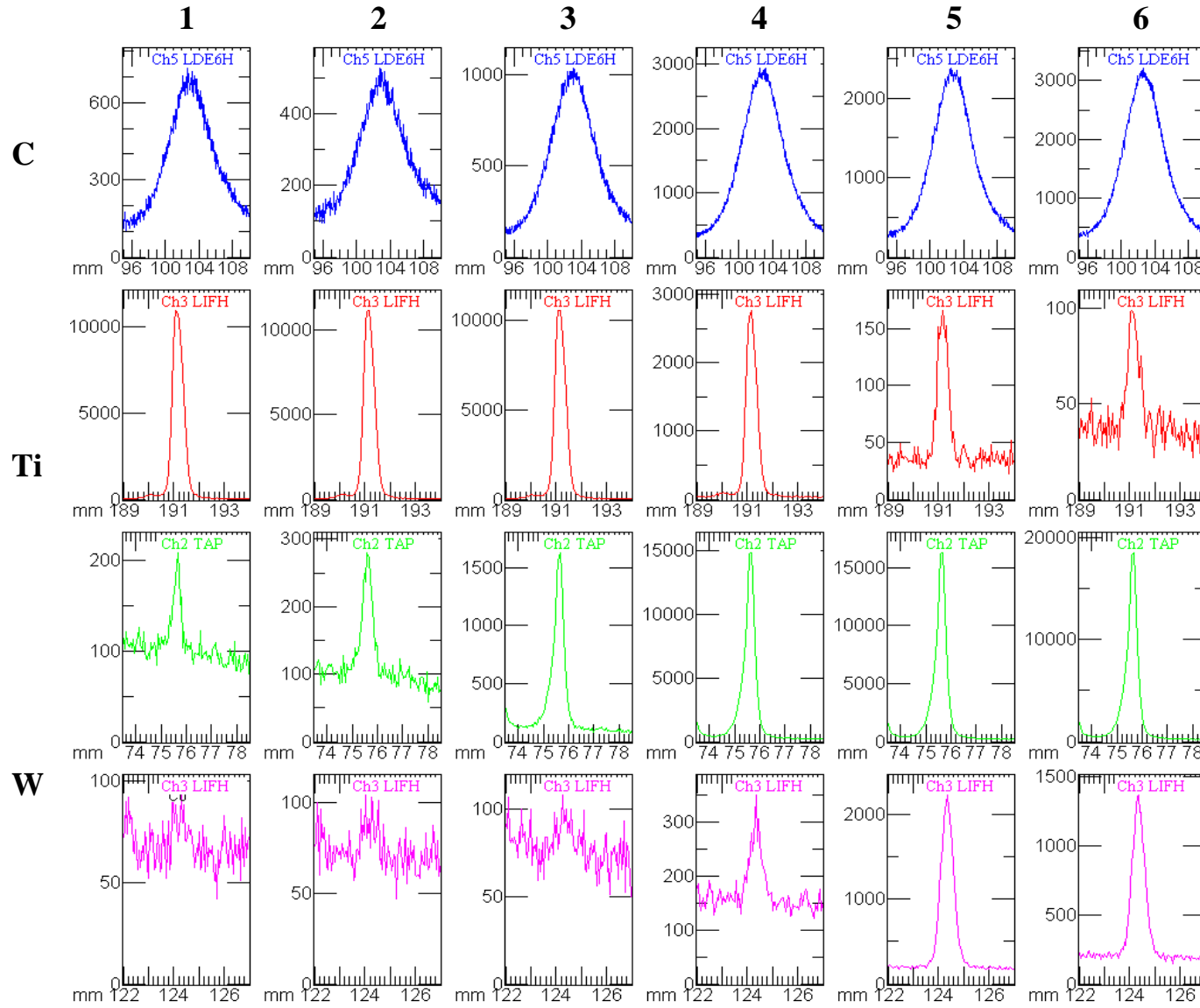
	C	Ti	
<b>1</b>	Max 3437	Max 9980	
<b>2</b>	Min 267	Min 23	
	Ave 1580	Ave 1098	
	Max 909	Max 10702	
<b>3</b>	Min 111	Min 21	
	Ave 443	Ave 1179	
	Max 1009	Max 8262	
<b>4</b>	Min 143	Min 33	
	Ave 492	Ave 922	
	Max 2411	Max 147	
<b>5</b>	Min 291	Min 23	
	Ave 1069	Ave 48	
	Max 2535	Max 82	
<b>6</b>	Min 303	Min 24	
	Ave 1132	Ave 42	
	W	Co	
<b>1</b>	Max 504	Max 107	
<b>2</b>	Min 77	Min 44	
	Ave 139	Ave 69	
	Max 1155	Max 108	
<b>3</b>	Min 72	Min 57	
	Ave 206	Ave 78	
	Max 6432	Max 179	
<b>4</b>	Min 112	Min 82	
	Ave 800	Ave 115	
	Max 19420	Max 307	
<b>5</b>	Min 177	Min 164	
	Ave 2260	Ave 208	
	Max 19384	Max 309	
<b>6</b>	Min 189	Min 174	
	Ave 2250	Ave 210	

**Figure C3.** Test G3, line 2. Spectra from EMA point-to-point analysis of C (blue), Ti (red), W (green) and Co (pink) to the left.



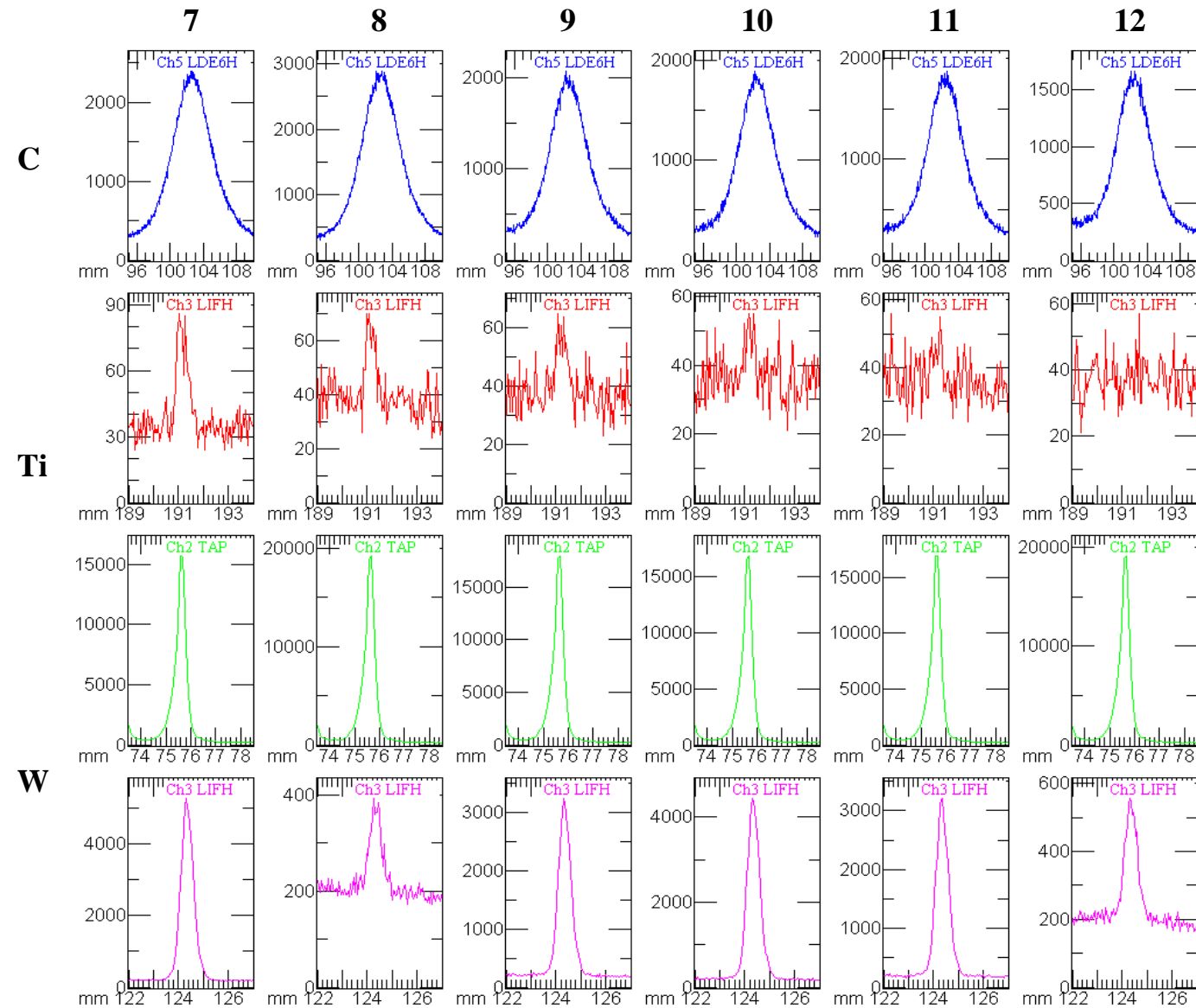
	C	Ti	W	Co
7	Max 2570 Min 313 Ave 1124 Max 2435	Max 72 Min 25 Ave 40 Max 65		
8	Min 309 Ave 1078 Max 1490	Min 25 Ave 38 Max 49		
9	Min 198 Ave 666 Max 1798	Min 23 Ave 34 Max 53		
10	Min 236 Ave 796 Max 1764	Min 20 Ave 36 Max 54		
11	Min 234 Ave 766 Max 1637	Min 21 Ave 39 Max 54		
12	Min 226 Ave 724	Min 19 Ave 37		
			Max 19313 Min 198 Ave 2247 Max 18574	Max 324 Min 164 Ave 213 Max 2571
			Min 198 Ave 2139 Max 14032	Min 156 Ave 477 Max 8517
			Min 168 Ave 1640 Max 17833	Min 155 Ave 1213 Max 1781
			Min 190 Ave 2069 Max 19513	Min 155 Ave 386 Max 351
			Min 196 Ave 2270 Max 19331	Min 165 Ave 217 Max 880
			Min 198 Ave 2241	Min 160 Ave 276

**Figure C4.** Test G3, line 2. Spectra from EMA point-to-point analysis of C (blue), Ti (red), W (green) and Co (pink) to the left.



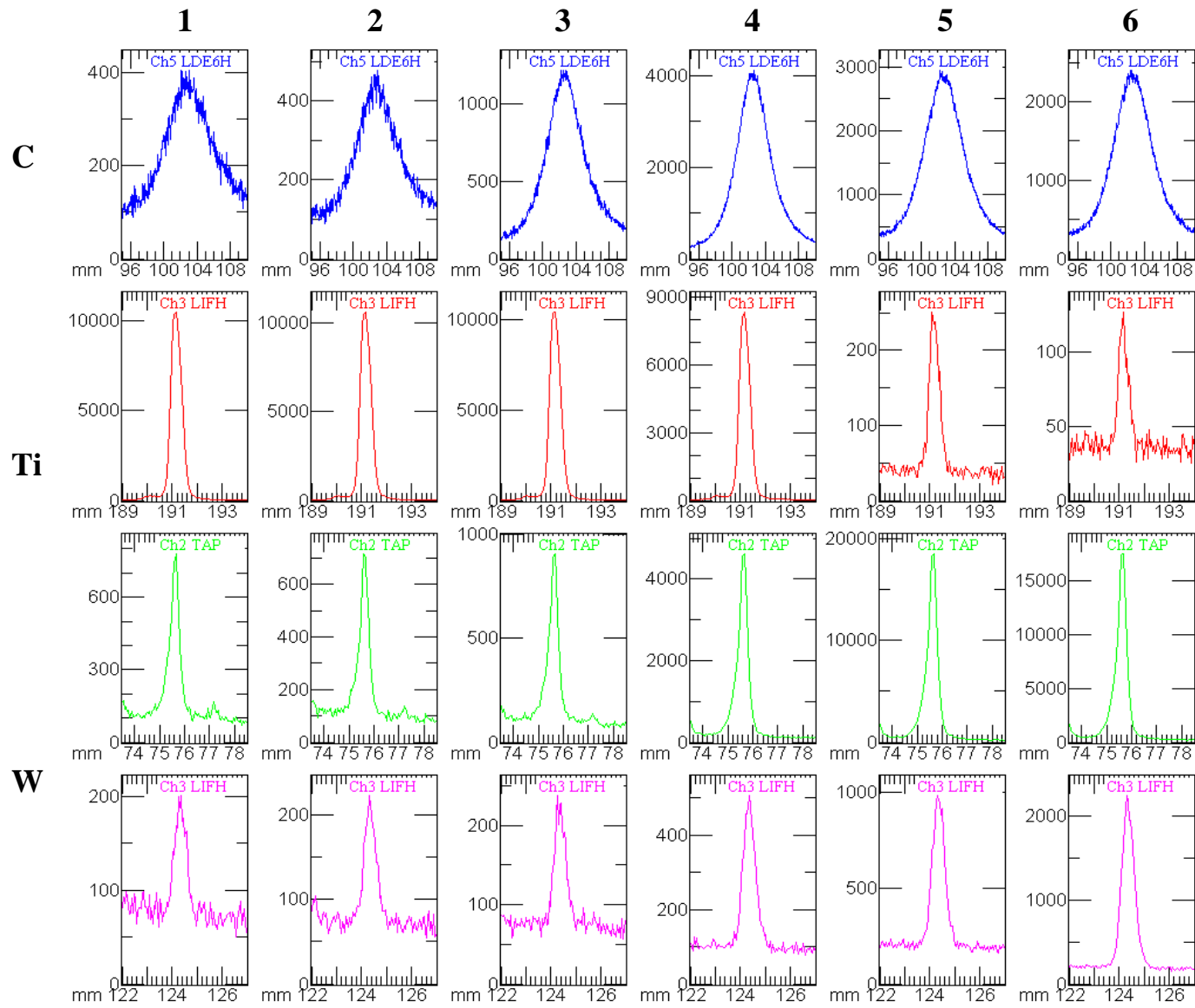
	C	Ti	W	Co
	Max 734	Max 10946	Max 209	Max 93
<b>1</b>	Min 105	Min 23	Min 68	Min 42
	Ave 361	Ave 1206	Ave 106	Ave 69
	Max 526	Max 11154	Max 280	Max 104
<b>2</b>	Min 95	Min 18	Min 58	Min 47
	Ave 276	Ave 1225	Ave 114	Ave 74
	Max 1035	Max 10580	Max 1631	Max 108
<b>3</b>	Min 126	Min 24	Min 73	Min 47
	Ave 503	Ave 1163	Ave 264	Ave 79
	Max 2936	Max 2767	Max 14850	Max 351
<b>4</b>	Min 313	Min 25	Min 173	Min 122
	Ave 1353	Ave 320	Ave 1756	Ave 171
	Max 2379	Max 166	Max 16281	Max 2232
<b>5</b>	Min 250	Min 22	Min 173	Min 168
	Ave 1072	Ave 48	Ave 1904	Ave 438
	Max 3211	Max 99	Max 18518	Max 1365
<b>6</b>	Min 333	Min 22	Min 174	Min 147
	Ave 1424	Ave 43	Ave 2140	Ave 336

**Figure C5.** Test H3, line 1. Spectra from EMA point-to-point analysis of C (blue), Ti (red), W (green) and Co (pink) to the left.



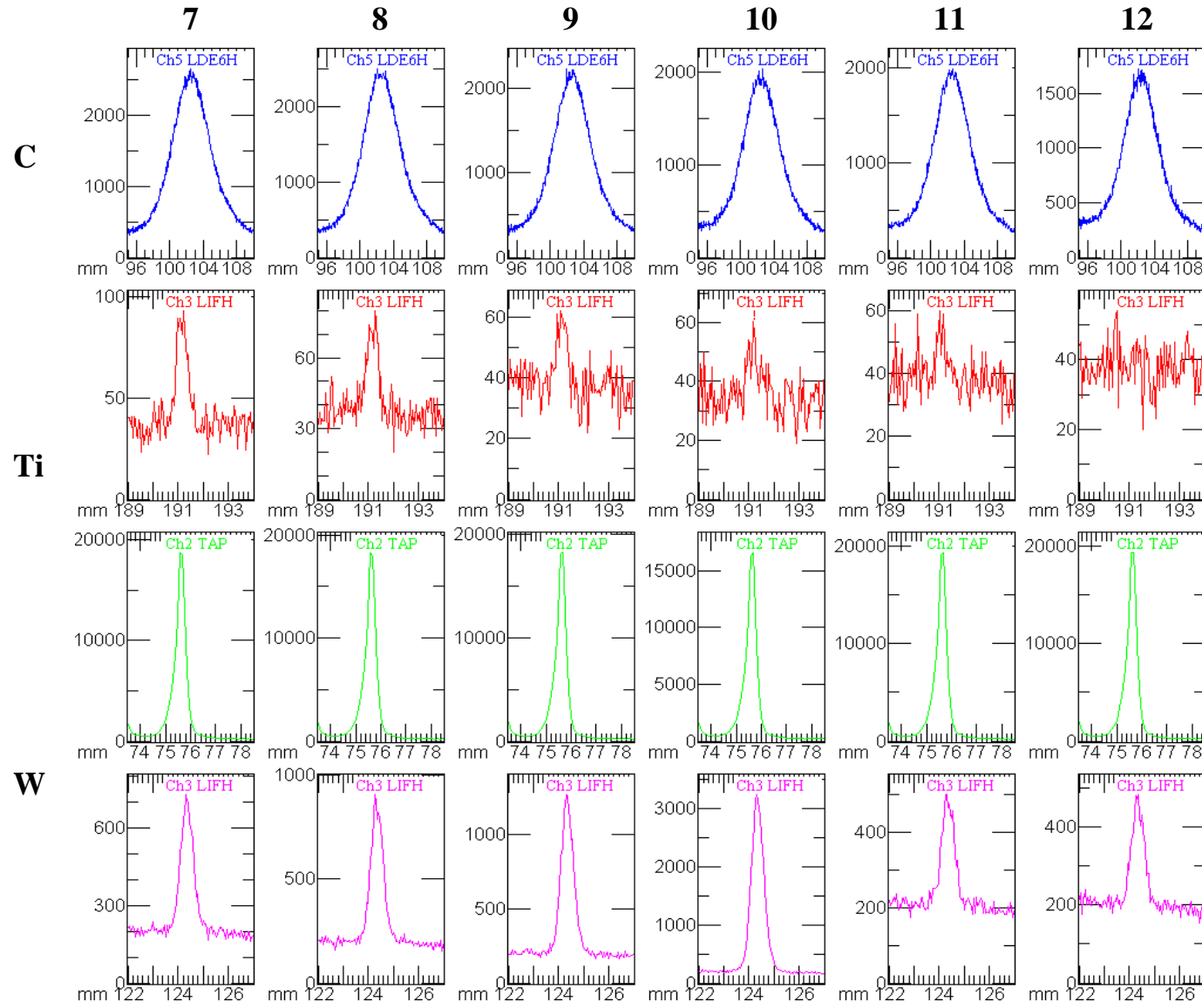
	C	Ti	W	Co
7	Max 2398 Min 295 Ave 1082	Max 86 Min 24 Ave 39	Max 15718 Min 186 Ave 1837	Max 5288 Min 157 Ave 814
8	Max 2886 Min 299 Ave 1292	Max 70 Min 24 Ave 40	Max 19209 Min 198 Ave 2225	Max 393 Min 172 Ave 220
9	Max 2070 Min 265 Ave 908	Max 65 Min 23 Ave 39	Max 1892 Min 255 Ave 821	Max 55 Min 24 Ave 37
10	Max 1877 Min 233 Ave 826	Max 56 Min 21 Ave 37	Max 17962 Min 198 Ave 2112	Max 3245 Min 172 Ave 4445
11	Max 1668 Min 255 Ave 821	Max 57 Min 24 Ave 37	Max 16921 Min 172 Ave 1979	Max 3213 Min 155 Ave 556
12	Max 236 Min 236 Ave 734	Max 21 Min 21 Ave 37	Max 16854 Min 180 Ave 2222	Max 4445 Min 163 Ave 241

**Figure C6.** Test H3, line 1. Spectra from EMA point-to-point analysis of C (blue), Ti (red), W (green) and Co (pink) to the left.



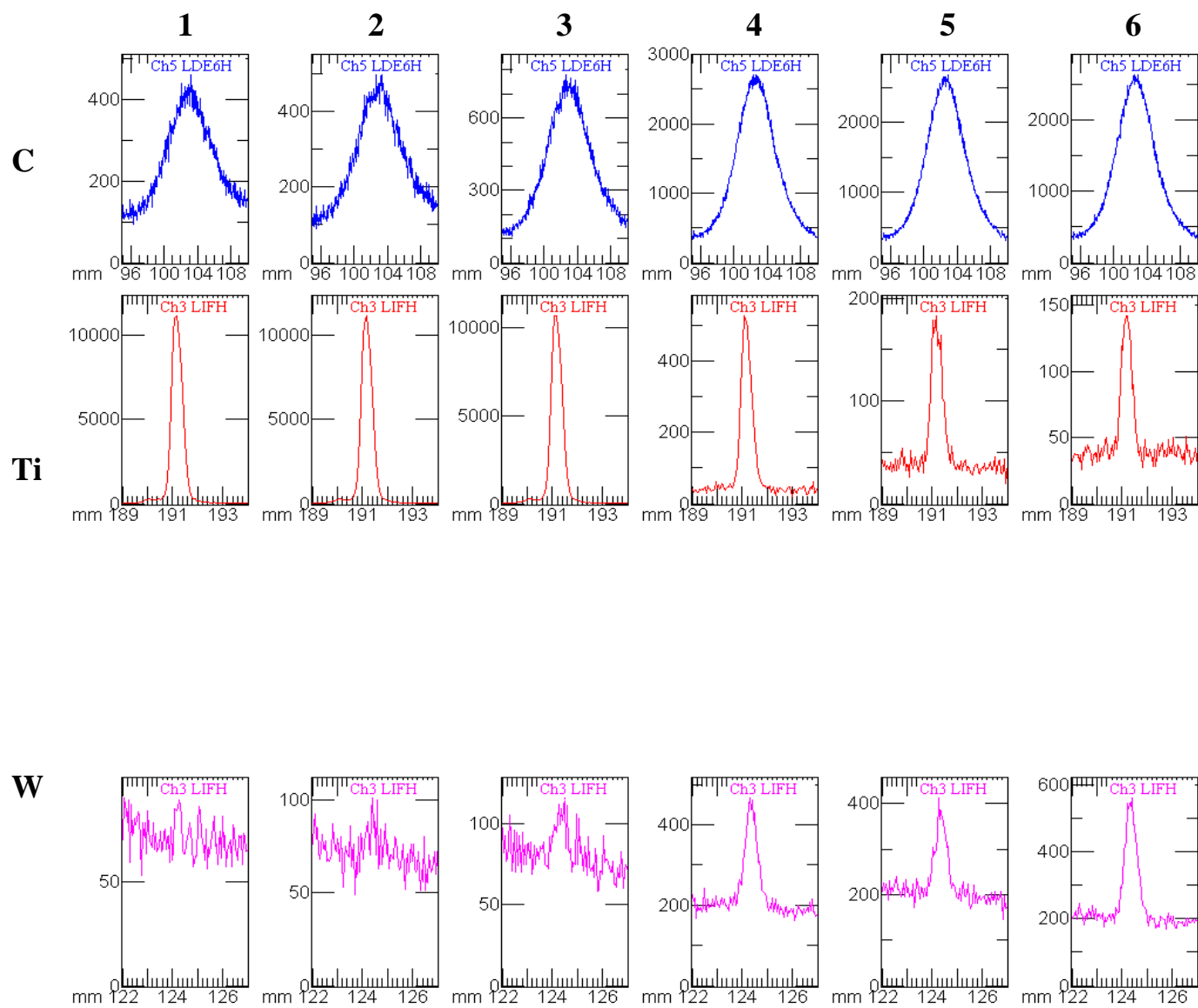
	C	Ti	W	Co
	Max 404	Max 10463	Max 780	Max 201
<b>1</b>	Min 86	Min 19	Min 71	Min 50
	Ave 223	Ave 1154	Ave 170	Ave 89
	Max 478	Max 10594	Max 716	Max 223
<b>2</b>	Min 88	Min 22	Min 73	Min 54
	Ave 240	Ave 1167	Ave 160	Ave 90
	Max 1216	Max 10394	Max 905	Max 238
<b>3</b>	Min 125	Min 24	Min 70	Min 57
	Ave 526	Ave 1151	Ave 178	Ave 92
	Max 4120	Max 8333	Max 4621	Max 507
<b>4</b>	Min 250	Min 25	Min 91	Min 76
	Ave 1539	Ave 909	Ave 587	Ave 146
	Max 2947	Max 251	Max 18566	Max 983
<b>5</b>	Min 338	Min 21	Min 185	Min 161
	Ave 1305	Ave 58	Ave 2160	Ave 292
	Max 2402	Max 127	Max 17531	Max 2245
<b>6</b>	Min 268	Min 25	Min 179	Min 154
	Ave 1073	Ave 43	Ave 2044	Ave 437

**Figure C7.** Test H3, line 2. Spectra from EMA point-to-point analysis of C (blue), Ti (red), W (green) and Co (pink) to the left.



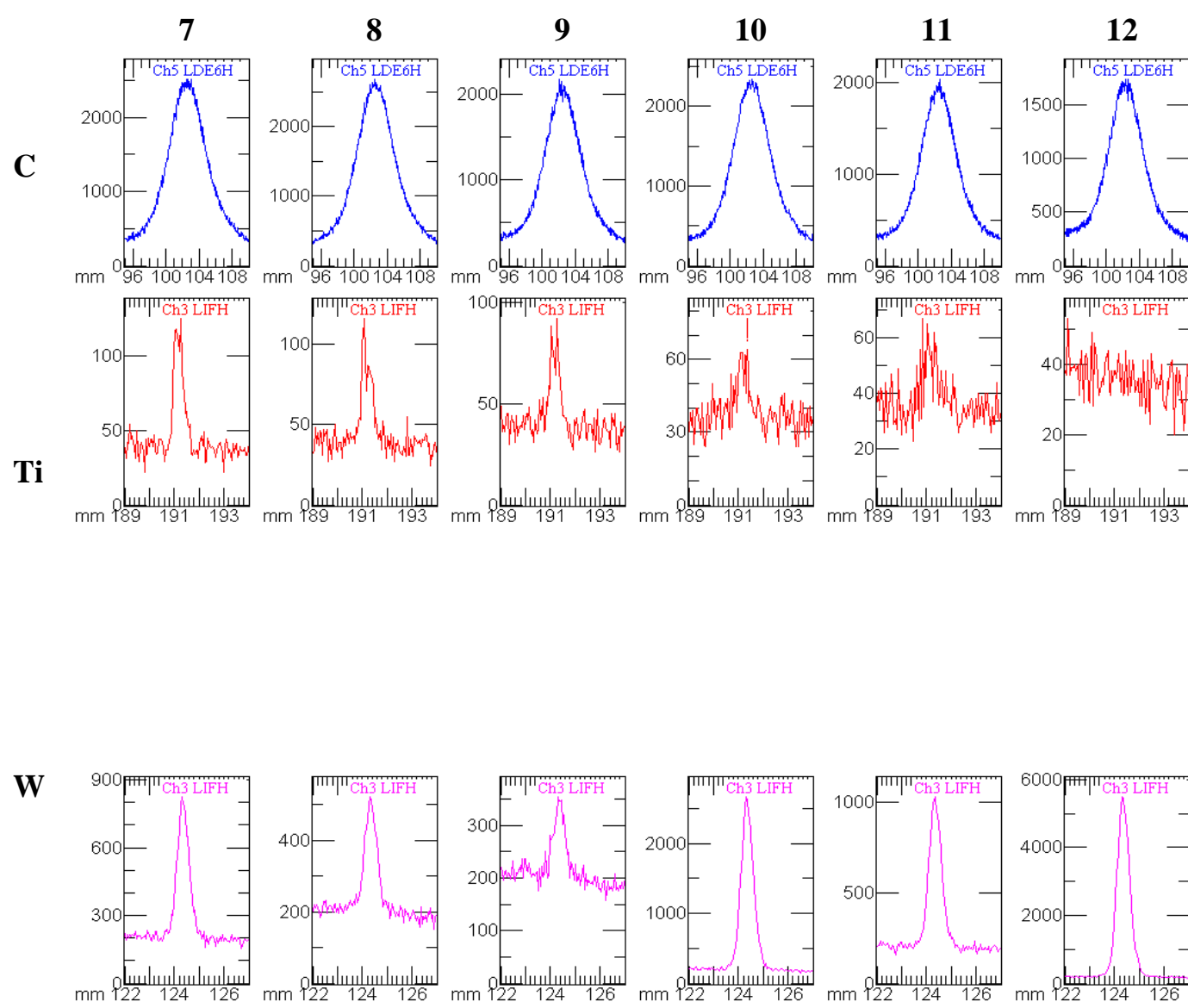
	C	Ti
7	Max 2652 Min 307 Ave 1175 Max 2495	Max 93 Min 22 Ave 42 Max 80
8	Min 318 Ave 1105 Max 2233	Min 20 Ave 41 Max 62
9	Min 263 Ave 988 Max 2033	Min 22 Ave 39 Max 64
10	Min 270 Ave 889 Max 1995	Min 19 Ave 36 Max 60
11	Min 267 Ave 888 Max 1725	Min 24 Ave 39 Max 54
12	Min 218 Ave 748	Min 20 Ave 38
	W	Co
7	Max 18737 Min 184 Ave 2167 Max 18306	Max 731 Min 163 Ave 261 Max 908
8	Min 175 Ave 2134 Max 18255	Min 156 Ave 277 Max 1269
9	Min 195 Ave 2136 Max 16613	Min 160 Ave 322 Max 3249
10	Min 184 Ave 1938 Max 19328	Min 156 Ave 558 Max 499
11	Min 179 Ave 2240 Max 19349	Min 174 Ave 240 Max 484
12	Min 194 Ave 2254	Min 155 Ave 232

**Figure C8.** Test H3, line 2. Spectra from EMA point-to-point analysis of C (blue), Ti (red), W (green) and Co (pink) to the left.



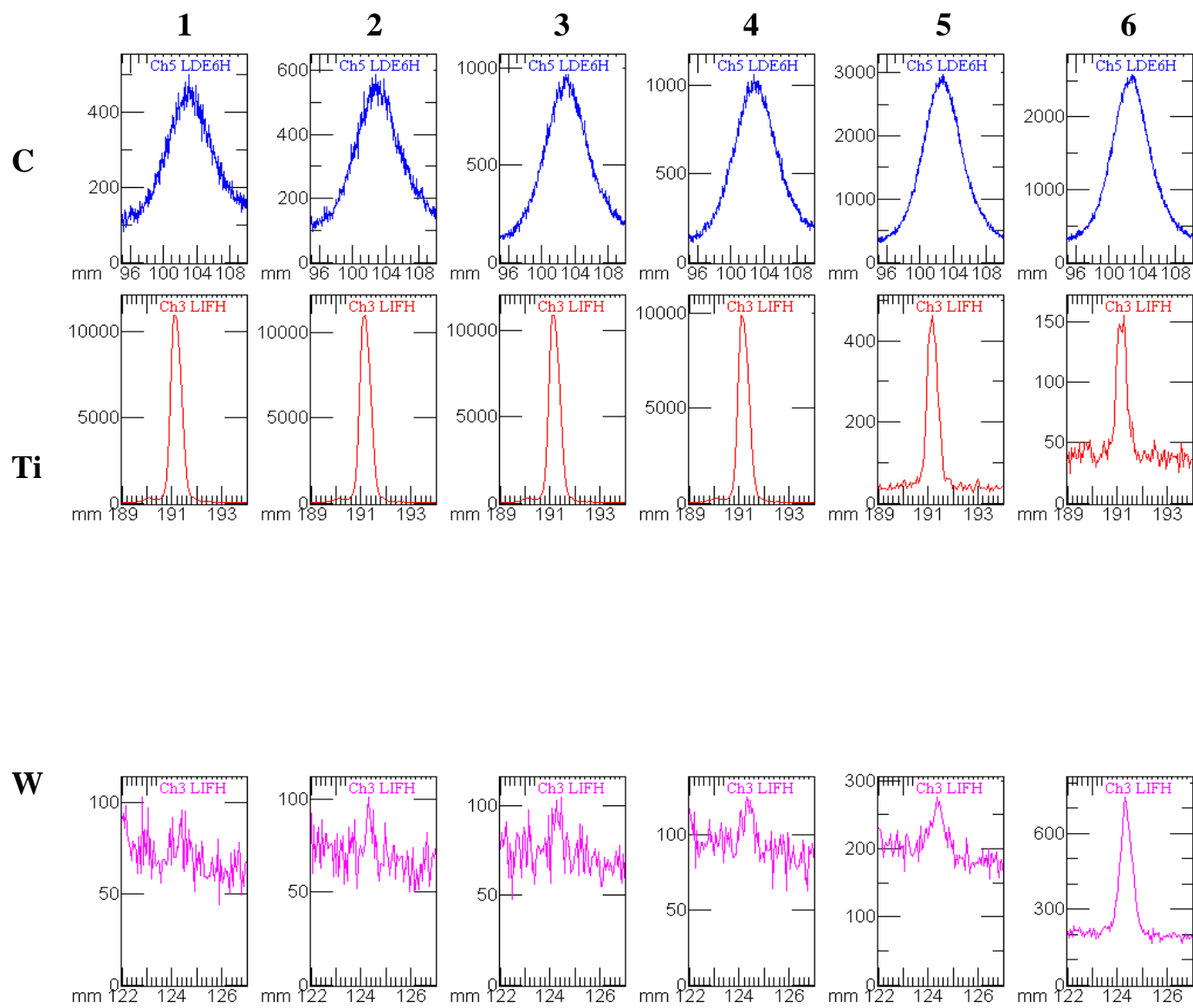
	C	Ti	W	Co
Max	461	Max 11129		
1 Min	94	Min 21		
Ave	243	Ave 1225		
Max	497	Max 11179		
2 Min	89	Min 22		
Ave	263	Ave 1218		
Max	780	Max 10701		
3 Min	110	Min 32		
Ave	380	Ave 1183		
Max	2709	Max 527		
4 Min	326	Min 21		
Ave	1223	Ave 88		
Max	2686	Max 183		
5 Min	321	Min 19		
Ave	1192	Ave 51		
Max	2637	Max 142		
6 Min	318	Min 26		
Ave	1176	Ave 48		
W Max		90		
1 Min		53		
Ave		71		
Max		101		
2 Min		49		
Ave		72		
Max		116		
3 Min		58		
Ave		82		
Max		467		
4 Min		161		
Ave		227		
Max		413		
5 Min		146		
Ave		221		
Max		563		
6 Min		169		
Ave		241		

**Figure C9.** Test I3, line 1. Spectra from EMA point-to-point analysis of C (blue), Ti (red), W (green) and Co (pink) to the left.



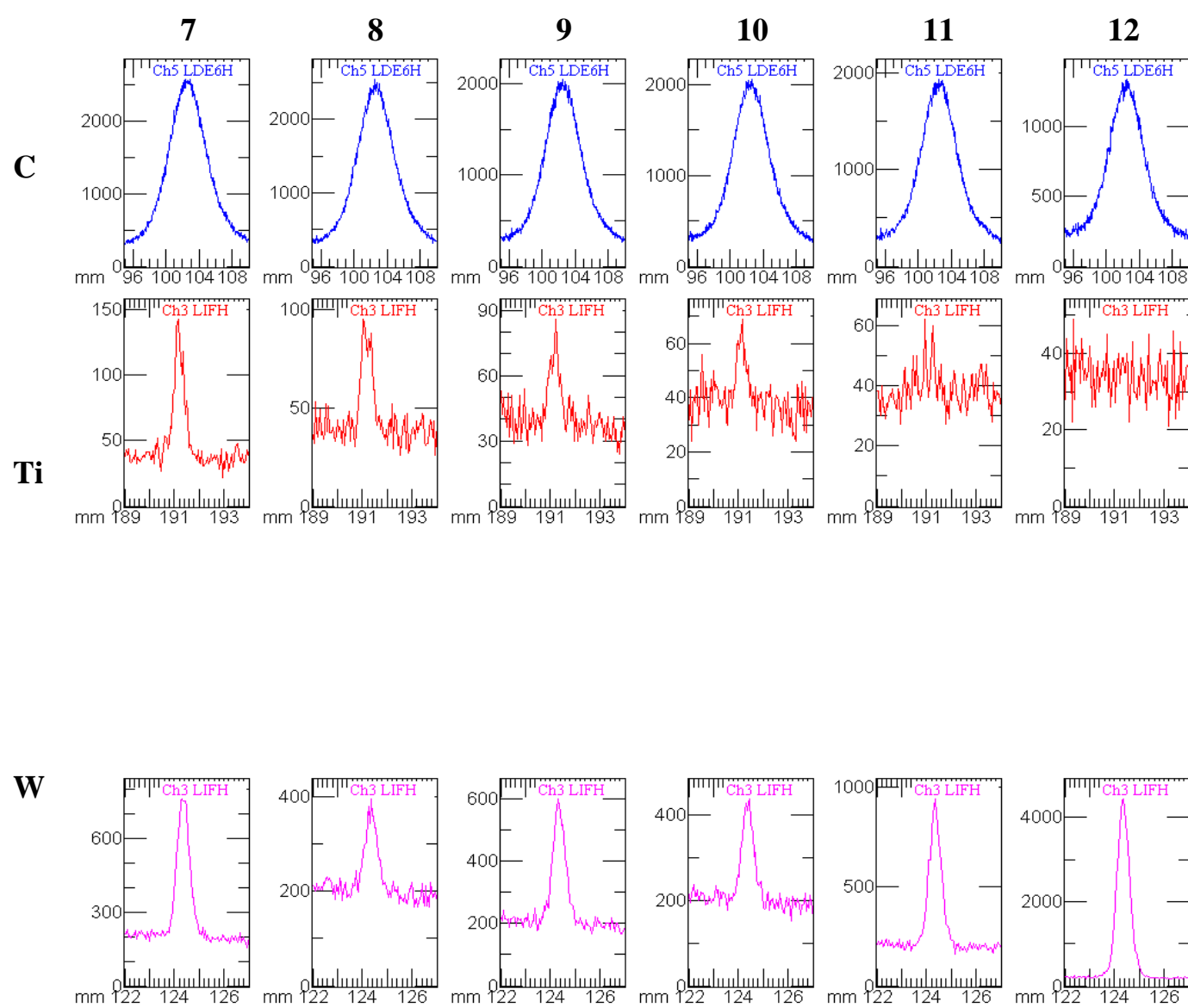
	C		Ti	
7	Max	2517	Max	125
7	Min	326	Min	22
7	Ave	1133	Ave	45
7	Max	2679	Max	116
8	Min	309	Min	24
8	Ave	1190	Ave	44
8	Max	2170	Max	92
9	Min	270	Min	26
9	Ave	933	Ave	42
9	Max	2339	Max	77
10	Min	311	Min	24
10	Ave	1052	Ave	39
10	Max	2036	Max	67
11	Min	282	Min	23
11	Ave	877	Ave	38
11	Max	1739	Max	53
12	Min	219	Min	20
12	Ave	765	Ave	36
	W		Co	
7	Max	825	Max	825
7	Min	154	Min	154
7	Ave	271	Ave	271
8	Max	522	Max	522
8	Min	150	Min	150
8	Ave	238	Ave	238
8	Max	354	Max	354
9	Min	158	Min	158
9	Ave	217	Ave	217
9	Max	2667	Max	2667
10	Min	151	Min	151
10	Ave	487	Ave	487
10	Max	1033	Max	1033
11	Min	159	Min	159
11	Ave	302	Ave	302
11	Max	5496	Max	5496
12	Min	152	Min	152
12	Ave	839	Ave	839

**Figure C10.** Test I3, line 1. Spectra from EMA point-to-point analysis of C (blue), Ti (red), W (green) and Co (pink) to the left.



	C		Ti	
	Max	501	Max	10949
<b>1</b>	Min	82	Min	24
	Ave	261	Ave	1213
	Max	588	Max	10988
<b>2</b>	Min	96	Min	24
	Ave	302	Ave	1217
	Max	968	Max	10846
<b>3</b>	Min	118	Min	21
	Ave	470	Ave	1201
	Max	1062	Max	9899
<b>4</b>	Min	114	Min	24
	Ave	502	Ave	1097
	Max	2974	Max	463
<b>5</b>	Min	315	Min	24
	Ave	1325	Ave	83
	Max	2585	Max	155
<b>6</b>	Min	294	Min	24
	Ave	1144	Ave	50
	W		Co	
	Max	103	Max	103
<b>1</b>	Min	44	Min	44
	Ave	70	Ave	70
	Max	101	Max	101
<b>2</b>	Min	50	Min	50
	Ave	70	Ave	70
	Max	105	Max	105
<b>3</b>	Min	48	Min	48
	Ave	74	Ave	74
	Max	125	Max	125
<b>4</b>	Min	63	Min	63
	Ave	94	Ave	94
	Max	276	Max	276
<b>5</b>	Min	155	Min	155
	Ave	203	Ave	203
	Max	745	Max	745
<b>6</b>	Min	163	Min	163
	Ave	262	Ave	262

**Figure C11.** Test I3, line 2. Spectra from EMA point-to-point analysis of C (blue), Ti (red), W (green) and Co (pink) to the left.



	C	Ti
7	Max 2568 Min 303 Ave 1151 Max 2545	Max 143 Min 22 Ave 47 Max 95
8	Min 310 Ave 1108 Max 2047	Min 26 Ave 44 Max 86
9	Min 268 Ave 903 Max 2062	Min 24 Ave 42 Max 69
10	Min 260 Ave 915 Max 1937	Min 24 Ave 40 Max 62
11	Min 240 Ave 860 Max 1339	Min 27 Ave 39 Max 49
12	Min 194 Ave 594	Min 21 Ave 34
	W	Co
7		Max 762 Min 157 Ave 270 Max 396
8		Min 166 Ave 221 Max 601
9		Min 167 Ave 248 Max 439
10		Min 151 Ave 226 Max 942
11		Min 161 Ave 284 Max 4439
12		Min 164 Ave 719

**Figure C12.** Test I3, line 2. Spectra from EMA point-to-point analysis of C (blue), Ti (red), W (green) and Co (pink) to the left.

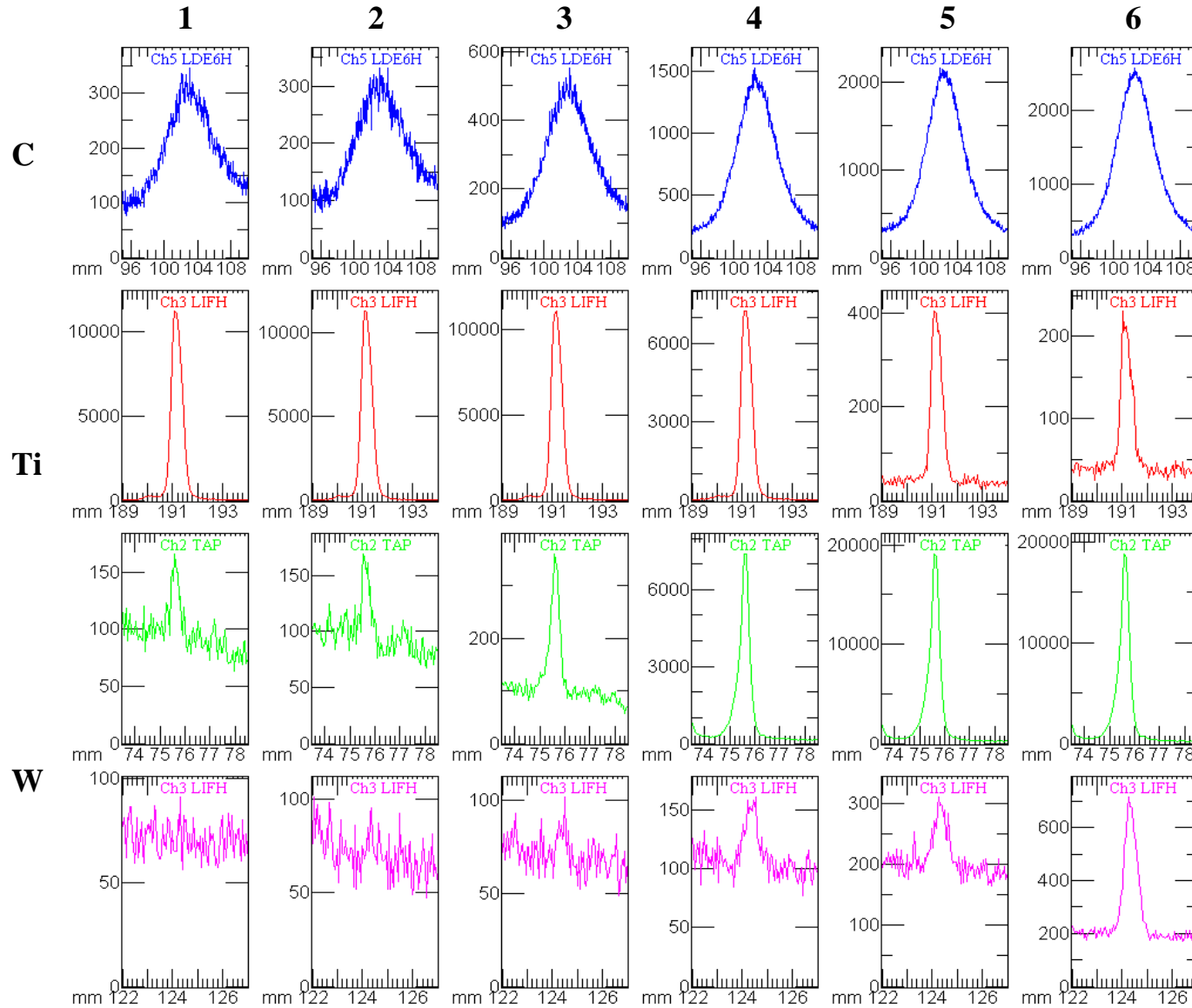
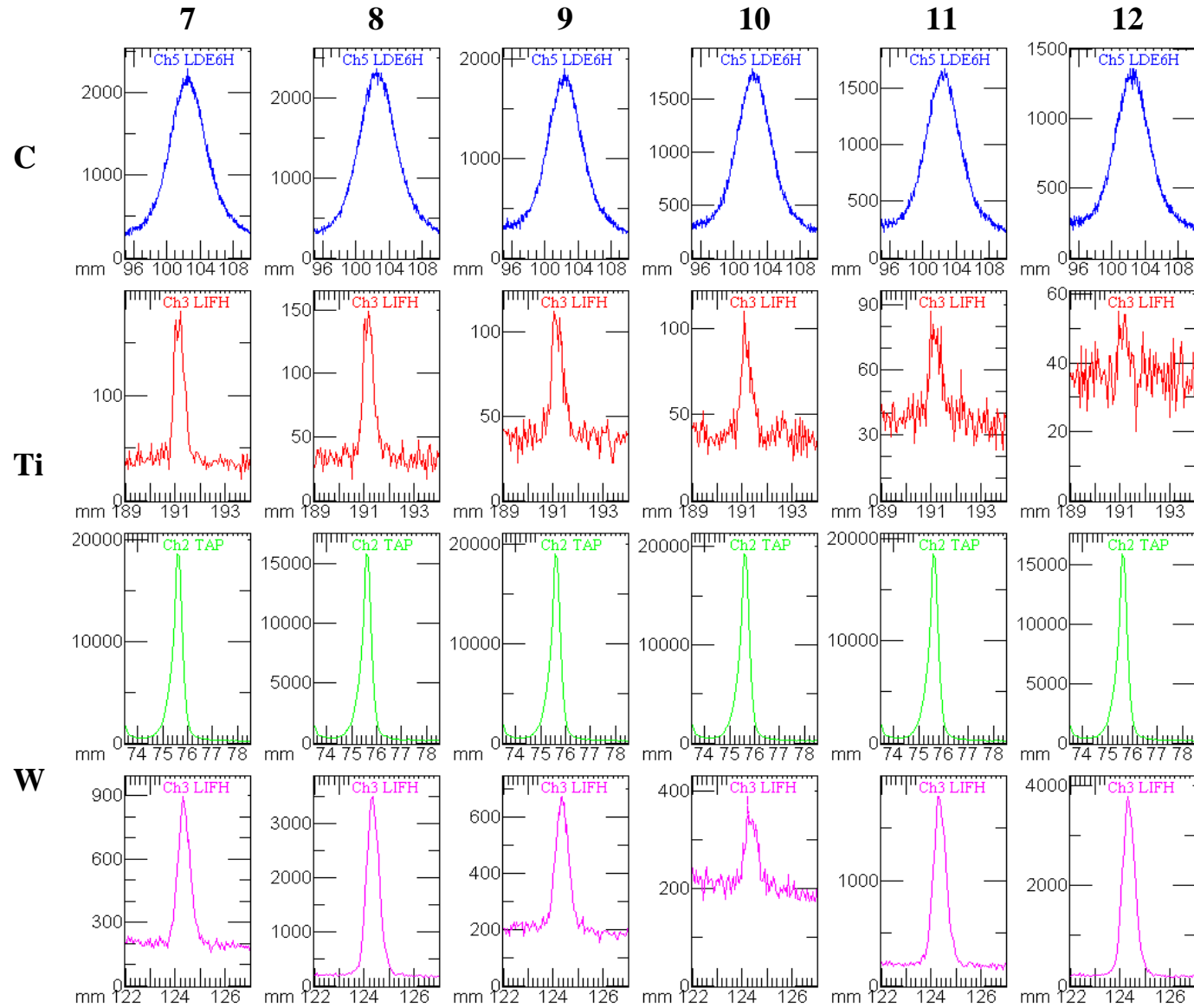


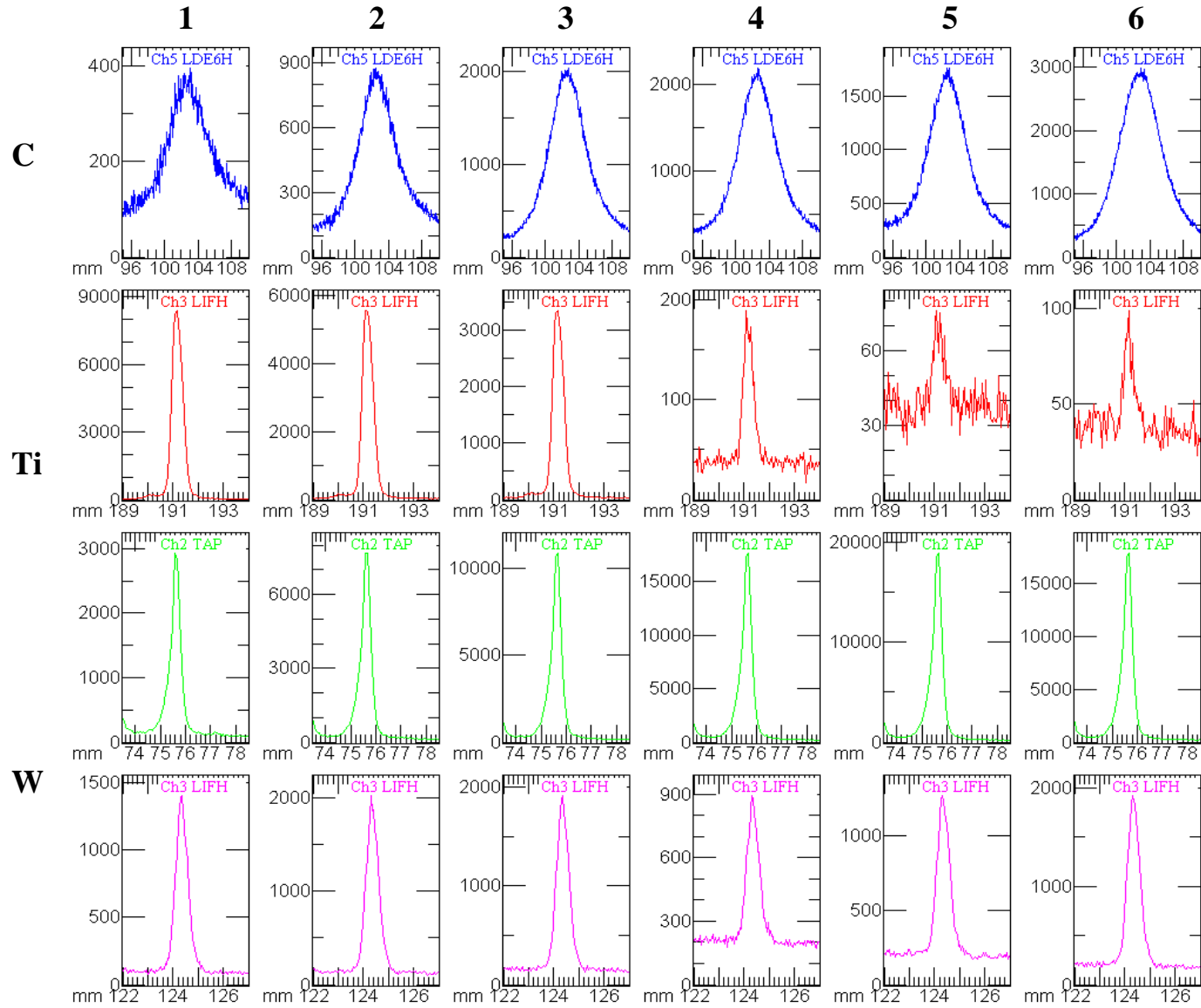
**Figure C13.** Test J3, line 1. Spectra from EMA point-to-point analysis of C (blue), Ti (red), W (green) and Co (pink) to the left.

	C	Ti	W	Co
	Max 346	Max 11263	Max 166	Max 91
<b>1</b>	Min 76	Min 18	Min 63	Min 56
	Ave 192	Ave 1235	Ave 97	Ave 71
	Max 332	Max 11297	Max 169	Max 101
<b>2</b>	Min 78	Min 22	Min 67	Min 47
	Ave 191	Ave 1227	Ave 98	Ave 71
	Max 552	Max 11082	Max 360	Max 102
<b>3</b>	Min 84	Min 19	Min 57	Min 49
	Ave 276	Ave 1214	Ave 117	Ave 71
	Max 1527	Max 7252	Max 7394	Max 161
<b>4</b>	Min 187	Min 24	Min 112	Min 77
	Ave 681	Ave 815	Ave 909	Ave 110
	Max 2163	Max 404	Max 19086	Max 310
<b>5</b>	Min 285	Min 25	Min 189	Min 165
	Ave 944	Ave 77	Ave 2219	Ave 208
	Max 2583	Max 231	Max 18776	Max 716
<b>6</b>	Min 296	Min 24	Min 196	Min 169
	Ave 1127	Ave 57	Ave 2172	Ave 256



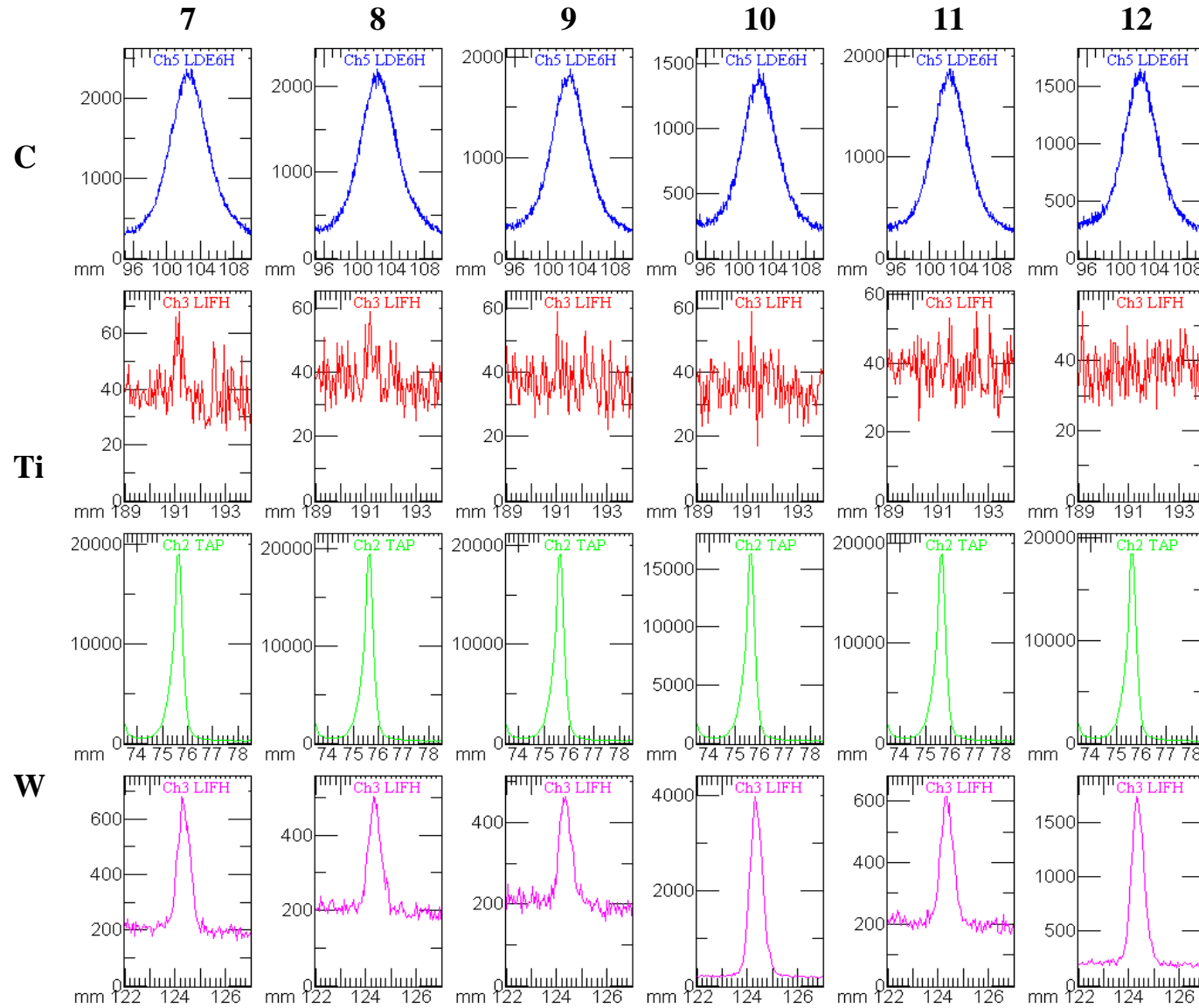
	C	Ti	W	Co
7	Max 2293 Min 271 Ave 980	Max 180 Min 20 Ave 51	Max 18598 Min 175 Ave 2156	Max 896 Min 156 Ave 276
8	Max 2360 Min 296 Ave 1054	Max 149 Min 17 Ave 45	Max 15847 Min 173 Ave 1848	Max 3493 Min 152 Ave 593
9	Max 244 Min 244 Ave 809	Max 112 Min 22 Ave 45	Max 19076 Min 197 Ave 2213	Max 673 Min 154 Ave 258
10	Max 1788 Min 238 Ave 775	Max 110 Min 23 Ave 43	Max 15847 Min 179 Ave 2250	Max 87 Min 23 Ave 43
11	Max 1357 Min 210 Ave 732	Max 55 Min 23 Ave 42	Max 18548 Min 185 Ave 2131	Max 55 Min 23 Ave 42
12	Max 179 Min 179 Ave 601	Max 20 Min 20 Ave 37	Max 15911 Min 167 Ave 1844	Max 3781 Min 157 Ave 631

**Figure C14.** Test J3, line 1. Spectra from EMA point-to-point analysis of C (blue), Ti (red), W (green) and Co (pink) to the left.



	C	Ti	W	Co
	Max 396	Max 8403	Max 2931	Max 1401
<b>1</b>	Min 84	Min 22	Min 80	Min 73
	Ave 206	Ave 923	Ave 398	Ave 249
	Max 875	Max 5546	Max 7675	Max 2024
<b>2</b>	Min 120	Min 28	Min 109	Min 104
	Ave 395	Ave 630	Ave 929	Ave 354
	Max 2040	Max 3348	Max 10901	Max 1916
<b>3</b>	Min 199	Min 25	Min 128	Min 123
	Ave 874	Ave 394	Ave 1274	Ave 361
	Max 2190	Max 189	Max 17660	Max 894
<b>4</b>	Min 274	Min 17	Min 164	Min 173
	Ave 960	Ave 51	Ave 2059	Ave 282
	Max 1758	Max 76	Max 18908	Max 1271
<b>5</b>	Min 258	Min 22	Min 181	Min 173
	Ave 788	Ave 41	Ave 2173	Ave 332
	Max 2993	Max 99	Max 17858	Max 1925
<b>6</b>	Min 273	Min 23	Min 175	Min 158
	Ave 1381	Ave 42	Ave 2069	Ave 403

**Figure C15.** Test J3, line 2. Spectra from EMA point-to-point analysis of C (blue), Ti (red), W (green) and Co (pink) to the left.



	C	Ti	W	Co
7	Max 2364 Min 287 Ave 1049 Max 2210	Max 68 Min 25 Ave 39 Max 59	Max 18981 Min 189 Ave 2207 Max 19439	Max 681 Min 162 Ave 257 Max 503
8	Min 285 Ave 963 Max 1879	Min 25 Ave 38 Max 59	Min 201 Ave 2236 Max 19180	Min 165 Ave 235 Max 464
9	Min 256 Ave 806 Max 1457	Min 22 Ave 37 Max 59	Min 190 Ave 2218 Max 16283	Min 159 Ave 231 Max 3984
10	Min 201 Ave 626 Max 1877	Min 17 Ave 36 Max 55	Min 169 Ave 1901 Max 18907	Min 156 Ave 652 Max 615
11	Min 236 Ave 806 Max 1649	Min 23 Ave 38 Max 54	Min 203 Ave 2199 Max 18471	Min 167 Ave 251 Max 1741
12	Min 227 Ave 712	Min 26 Ave 38	Min 186 Ave 2160	Min 160 Ave 387

Figure C16. Test J3, line 2. Spectra from EMA point-to-point analysis of C (blue), Ti (red), W (green) and Co (pink) to the left.

## APPENDIX D – IMAGES OF FLANK WEAR

Figures D1–5 illustrates the flank wear progression of test A–J at different times. Each image represents a new cutting edge due to the fact that continuous cutting was performed.

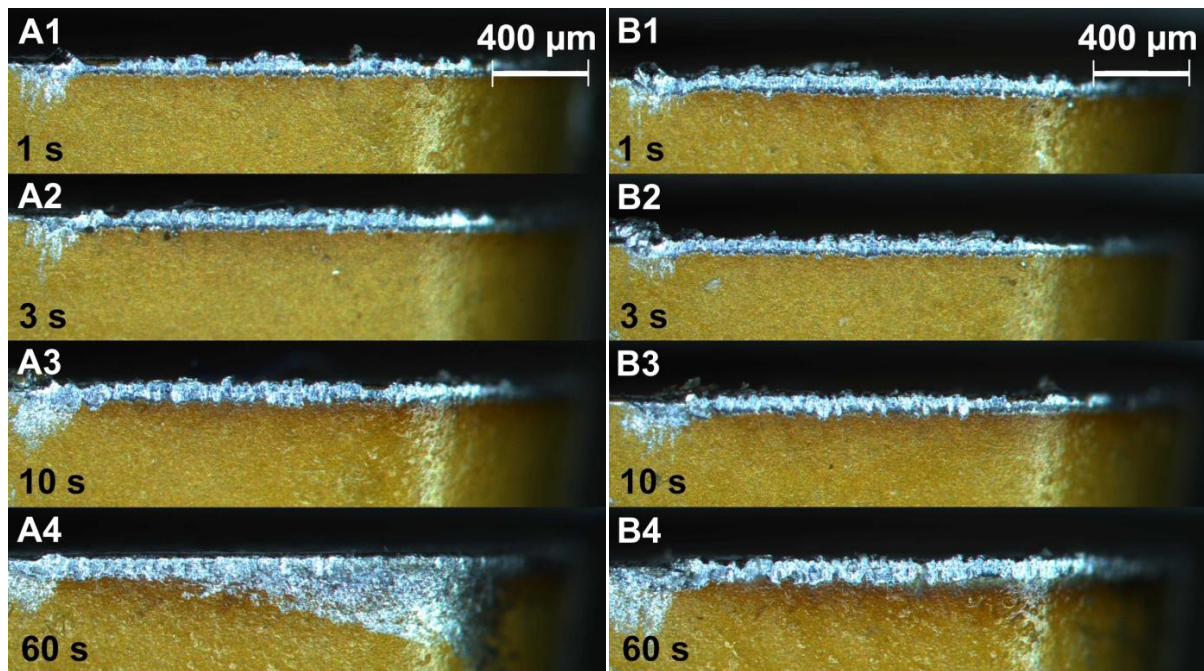


**Figure D1.** Flank wear progression of A1–4 (SI) to the left and B1–4 (MRS) to the right at 1, 3, 10 and 60 s.

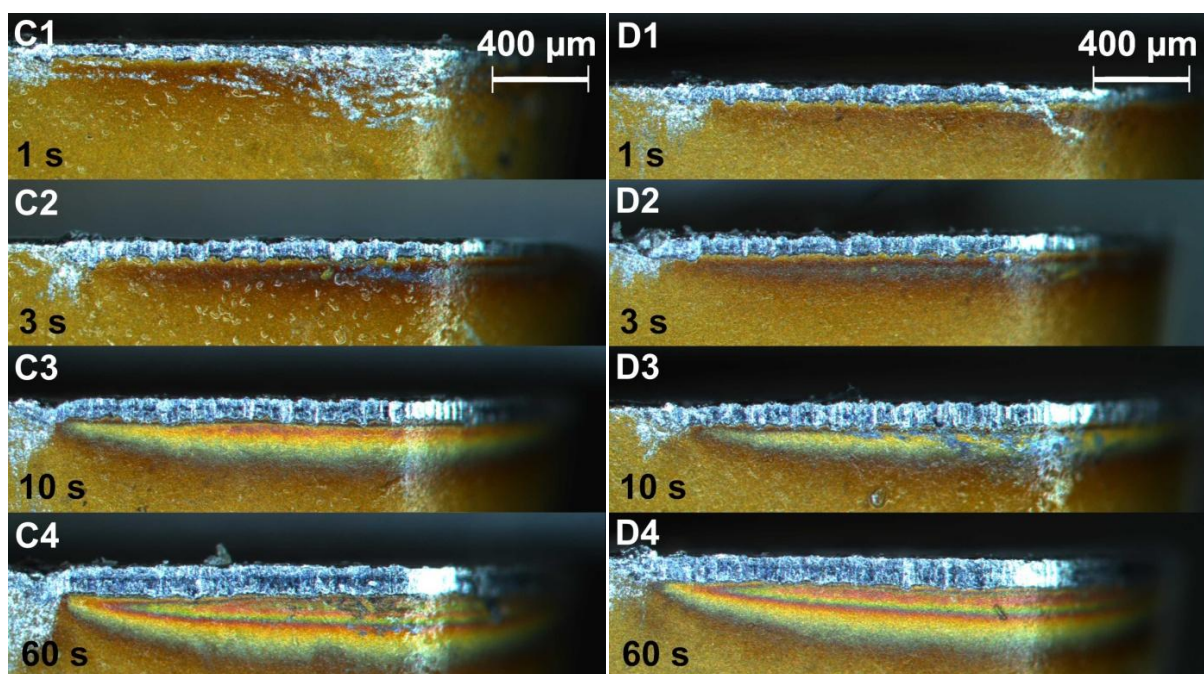


**Figure D2.** Flank wear progression of C1–4 (SI) to the left and D1–4 (MRS) to the right at 1, 3, 10 and 60 s.

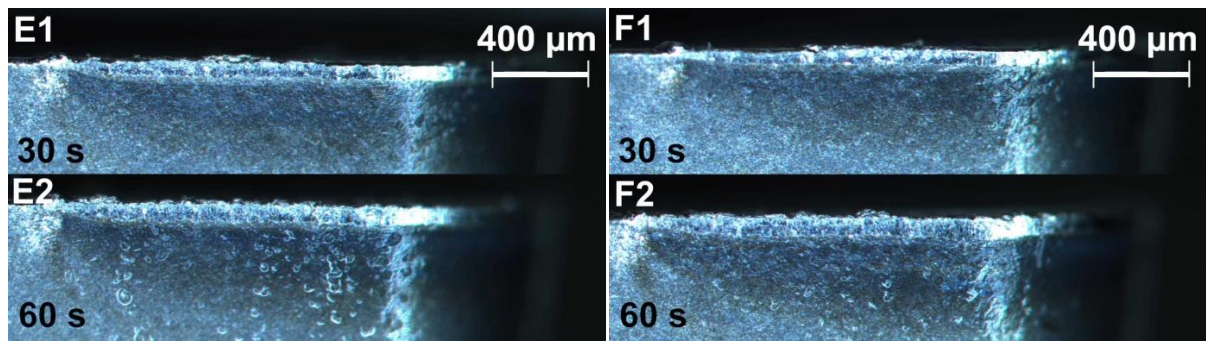


**Figure D3.** Flank wear progression of E1–2 (SI) to the left and F1–2 (MRS) to the right at 30 and 60 s.

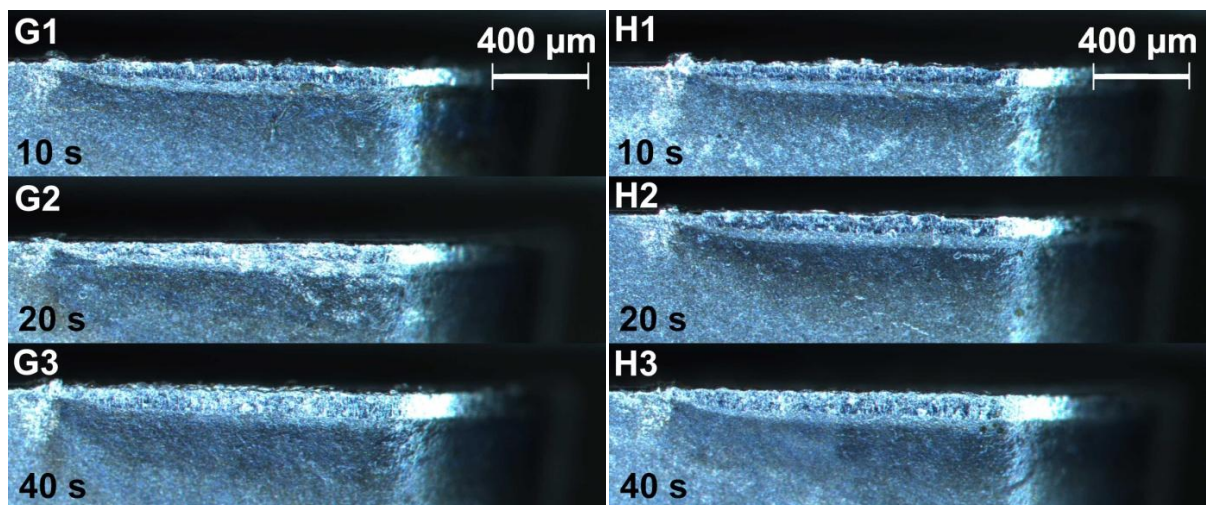


**Figure D4.** Flank wear progression of G1–3 (SI) to the left and H1–3 (MRS) to the right at 10, 20 and 40 s.

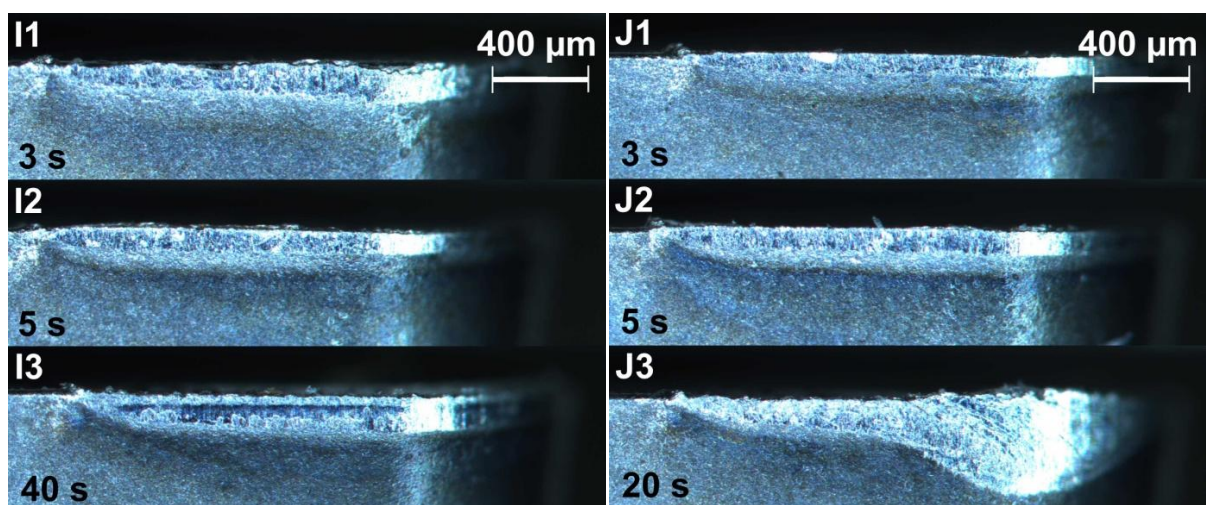


**Figure D5.** Flank wear progression of I1–3 (SI) to the left and J1–3 (MRS) to the right at 3, 5, 20 and 40 s.

## APPENDIX E1 – CHIP GEOMETRY ( $d_c$ , $p_c$ , $\phi_{seg}$ )

Table E1–3 represents mean shear band spacing, segment spacing and segmentation angle with mean values, standard deviation (SD), minimum (Min) and maximum (Max) values for each test procedure. Table E4 presents the raw data.

**Table E1.** Mean values, SD, Min and Max values calculated from the  $d_c$  data set.

Mean shear band spacing ( $d_c$ )								
	Coated with CVD				Uncoated			
	30 m/min SI	30 m/min MRS	75 m/min SI	75 m/min MRS	75 m/min SI	75 m/min MRS	90 m/min SI	90 m/min MRS
<b>Mean</b>	122.64	126.41	121.13	125.84	126.11	124.98	128.58	119.47
<b>SD</b>	21.17	45.32	17.64	13.15	18.53	18.09	16.27	17.06
<b>Min</b>	63.27	37.95	68.42	88.22	91.62	71.07	92.78	80.29
<b>Max</b>	173.98	221.26	161.27	153.42	181.03	177.54	160.96	158.13

**Table E2.** Mean values, SD, Min and Max values calculated from the  $p_c$  data set.

Segment spacing ( $p_c$ )								
	Coated with CVD				Uncoated			
	30 m/min SI	30 m/min MRS	75 m/min SI	75 m/min MRS	75 m/min SI	75 m/min MRS	90 m/min SI	90 m/min MRS
<b>Mean</b>	157.19	153.40	164.23	172.34	173.70	169.88	176.85	164.57
<b>SD</b>	24.55	53.94	22.92	15.87	16.55	18.22	20.20	21.36
<b>Min</b>	77.11	55.44	82.78	139.03	132.98	138.08	124.80	112.29
<b>Max</b>	220.54	298.72	211.88	204.50	211.51	221.64	226.18	204.53

**Table E3.** Mean values, SD, Min and Max values calculated from the  $\phi_{seg}$  data set.

Segmentation angle ( $\phi_{seg}$ )								
	Coated with CVD				Uncoated			
	30 m/min SI	30 m/min MRS	75 m/min SI	75 m/min MRS	75 m/min SI	75 m/min MRS	90 m/min SI	90 m/min MRS
<b>Mean</b>	50.47	51.86	46.40	46.78	45.08	46.45	45.86	47.77
<b>SD</b>	2.99	4.39	4.18	2.42	2.73	2.58	2.82	3.09
<b>Min</b>	42.48	42.76	35.53	42.12	39.81	40.96	39.64	41.05
<b>Max</b>	56.34	61.33	55.72	51.97	51.00	51.61	52.80	54.99



75 m/min, U (SI)			75 m/min, U (MRS)			90 m/min, U (SI)			90 m/min, U (MRS)		
$d_c$ [ $\mu\text{m}$ ]	$p_c$ [ $\mu\text{m}$ ]	$\phi_{seg}$ [°]	$d_c$ [ $\mu\text{m}$ ]	$p_c$ [ $\mu\text{m}$ ]	$\phi_{seg}$ [°]	$d_c$ [ $\mu\text{m}$ ]	$p_c$ [ $\mu\text{m}$ ]	$\phi_{seg}$ [°]	$d_c$ [ $\mu\text{m}$ ]	$p_c$ [ $\mu\text{m}$ ]	$\phi_{seg}$ [°]
125.02	197.37	40.46	129.82	163.64	44.06	152.15	204.40	44.55	135.09	204.53	42.93
132.54	160.72	39.81	136.23	183.50	43.40	143.28	194.19	46.22	132.98	121.64	41.05
118.02	206.65	43.68	136.58	179.80	41.15	125.25	190.42	45.95	89.24	183.35	42.52
109.06	144.56	44.27	132.85	189.37	42.46	131.21	165.07	41.84	135.93	197.52	51.09
117.41	145.10	45.52	133.38	192.79	45.91	126.75	194.02	45.05	148.70	166.55	47.98
101.22	150.76	46.17	130.27	165.87	42.58	150.96	189.13	43.77	141.06	200.44	44.29
110.65	168.46	49.78	126.64	183.25	48.23	138.73	203.45	43.67	117.34	168.88	44.83
146.52	168.46	44.39	133.59	178.24	47.98	117.67	150.76	46.25	137.89	149.66	41.69
126.21	155.26	44.27	148.59	157.71	46.37	104.48	145.79	46.21	97.80	142.88	44.76
101.76	178.72	49.54	113.60	181.80	46.21	120.07	199.41	41.48	116.48	148.72	47.49
146.49	188.21	42.26	130.11	178.38	43.53	144.35	185.19	50.20	100.86	112.29	49.31
124.24	170.85	40.57	116.09	149.76	44.05	140.91	188.21	50.66	88.68	137.66	54.99
130.65	185.13	51.00	121.71	142.02	47.60	148.21	158.13	46.10	110.12	187.14	47.87
116.39	132.98	44.90	110.33	188.12	49.64	109.67	172.48	44.41	158.13	193.22	47.10
111.84	185.88	48.97	112.82	173.78	48.89	117.54	148.86	43.01	122.82	178.69	47.17
139.48	159.41	44.91	151.32	138.08	45.89	104.04	171.38	44.86	129.99	156.01	45.52
123.96	173.41	46.73	128.52	161.24	46.35	119.73	194.02	44.94	114.52	180.20	48.94
127.30	174.90	44.50	92.11	157.35	46.95	128.18	173.78	45.94	114.92	171.52	47.40
159.83	194.63	46.22	132.54	152.80	42.27	127.63	176.92	49.16	125.56	174.51	46.70
117.50	173.03	47.26	96.15	188.51	49.47	135.97	183.20	45.67	114.49	136.20	49.86
113.15	184.56	47.35	129.88	161.92	47.49	128.57	124.80	44.77	104.15	122.35	44.18
181.03	211.51	43.07	113.07	165.74	46.02	95.21	201.74	46.75	80.29	138.84	45.73
137.79	182.36	43.85	113.38	161.92	46.48	151.87	168.20	48.43	95.21	153.02	48.67
124.57	194.48	47.05	128.98	171.38	43.40	133.78	175.56	43.14	107.12	158.58	51.31
133.83	174.21	43.84	110.40	147.48	46.40	125.95	189.87	48.01	128.08	178.12	50.59
109.22	172.42	45.24	134.35	161.43	46.46	148.68	199.28	47.60	129.57	183.12	48.13
130.65	192.62	43.87	125.95	221.64	44.71	142.40	174.98	48.50	123.81	188.70	46.13
158.13	166.65	41.72	112.18	188.93	45.53	141.03	164.22	39.64	118.08	161.61	44.65
120.82	183.46	45.20	114.75	186.71	43.89	113.15	179.64	46.18	126.13	187.55	42.73
121.93	180.30	41.87	150.02	219.94	40.96	99.72	208.74	41.92	126.61	162.72	47.24
133.07	181.96	42.65	152.70	189.55	45.06	139.13	168.79	42.28	115.70	161.84	45.35
116.31	161.58	47.45	115.12	171.97	45.17	134.37	202.12	52.80	118.90	167.62	49.85
148.35	180.47	45.63	120.82	163.00	41.02	129.49	196.05	47.60	122.75	151.36	53.45
119.32	161.09	41.45	177.54	145.66	49.26	131.40	158.49	45.86	137.15	171.97	46.00
96.15	180.09	46.22	84.52	182.36	44.85	134.65	174.29	44.47	111.11	185.29	47.77
147.81	175.09	45.11	156.81	181.47	48.36	107.22	149.66	46.02	114.83	173.76	49.77
139.54	186.58	43.48	71.07	152.34	45.85	104.43	164.58	44.61	135.08	158.11	50.98
100.42	170.91	41.79	132.09	152.80	49.39	134.48	226.18	51.95	115.35	166.79	51.00
108.24	173.30	47.01	146.75	163.07	49.27	160.96	163.07	45.32	127.78	175.79	47.09
136.05	171.87	48.61	109.22	164.49	44.12	149.64	141.63	43.77	135.67	151.84	52.82
125.02	158.49	47.89	119.05	177.12	49.20	114.25	171.33	44.66	123.32	131.26	49.94
127.02	184.59	45.15	103.09	151.82	47.50	131.14	195.22	48.86	85.01	130.14	48.71
105.52	134.41	44.95	123.02	192.28	48.63	126.39	174.21	42.58	97.34	171.58	48.38
91.62	164.07	46.61	133.11	152.99	48.23	141.48	186.80	44.81	101.26	185.77	43.17
132.73	173.26	50.29	127.96	168.78	48.13	145.15	191.15	41.35	152.70	174.51	50.40
148.59	177.52	41.46	139.96	138.08	48.44	120.19	164.05	49.96	113.87	167.02	49.96
106.61	158.49	41.58	117.54	173.03	45.84	144.56	154.03	49.51	129.57	145.36	48.87
106.03	186.71	48.20	118.86	157.13	44.98	92.78	159.75	48.65	108.39	162.02	48.89
139.99			97.09	158.28	47.76	107.50	169.45	47.20	121.28	151.36	50.12
159.84			138.73	169.17	50.92	125.25	155.94	45.71	108.02	178.92	49.27
			127.16	143.90	47.37	133.63			129.01	184.72	51.70
			135.11	186.10	47.07	110.71			146.69		
			120.52	175.09	48.39				109.24		
			122.54		50.79						
			136.92		51.61						
			125.12		49.51						

## APPENDIX E2 – CHIP GEOMETRY ( $t_{2\min}$ , $t_{2\max}$ , $G$ )

Table E5 represent  $G$ , with mean values, standard deviation (SD), minimum (Min) and maximum (Max) values for each test procedure. Table E6 presents the raw data of  $t_{2\max}$ ,  $t_{2\min}$  and calculated values of  $G$ .

**Table E5.** Mean values, SD, Min and Max values calculated from the  $G$  data set.

Degree of segmentation (G)								
	Coated with CVD				Uncoated			
	30 m/min SI	30 m/min MRS	75 m/min SI	75 m/min MRS	75 m/min SI	75 m/min MRS	90 m/min SI	90 m/min MRS
<b>Mean</b>	0.42	0.39	0.45	0.48	0.49	0.48	0.49	0.45
<b>SD</b>	0.10	0.12	0.09	0.05	0.07	0.08	0.07	0.08
<b>Min</b>	0.12	0.11	0.18	0.35	0.34	0.18	0.32	0.25
<b>Max</b>	0.62	0.58	0.63	0.57	0.63	0.71	0.59	0.56

**Table E6.** Raw data of  $t_{2\max}$  and  $t_{2\min}$ , together with the calculated values of  $G$  from LOM measurements of Ti–6Al–4V chips. The highlighted data were outliers, and excluded from further calculations.

30 m/min, CVD (SI)	
Tooth thickness [µm]	G
$t_{2\max}$ 278.45	0.51
$t_{2\min}$ 137.34	
$t_{2\max}$ 251.49	0.43
$t_{2\min}$ 142.46	
$t_{2\max}$ 299.30	0.46
$t_{2\min}$ 161.57	
$t_{2\max}$ 202.42	0.16
$t_{2\min}$ 170.00	
$t_{2\max}$ 309.39	0.38
$t_{2\min}$ 191.66	
$t_{2\max}$ 246.98	0.34
$t_{2\min}$ 164.11	
$t_{2\max}$ 296.53	0.40
$t_{2\min}$ 177.98	
$t_{2\max}$ 258.66	0.47
$t_{2\min}$ 137.32	
$t_{2\max}$ 295.72	0.46
$t_{2\min}$ 158.39	
$t_{2\max}$ 273.79	0.38
$t_{2\min}$ 171.10	
$t_{2\max}$ 259.39	0.38
$t_{2\min}$ 159.56	
$t_{2\max}$ 225.71	0.16
$t_{2\min}$ 190.46	
$t_{2\max}$ 293.60	0.44
$t_{2\min}$ 164.08	

$t_{2\max}$ 282.65	0.44	$t_{2\min}$ 154.38	
$t_{2\min}$ 159.01		$t_{2\max}$ 253.11	0.46
$t_{2\max}$ 267.06	0.49	$t_{2\min}$ 136.50	
$t_{2\min}$ 136.68		$t_{2\max}$ 306.94	0.49
$t_{2\max}$ 292.98	0.52	$t_{2\min}$ 156.38	
$t_{2\min}$ 140.15		$t_{2\max}$ 273.36	0.46
$t_{2\max}$ 288.71	0.61	$t_{2\min}$ 146.73	
$t_{2\min}$ 113.01		$t_{2\max}$ 258.72	0.62
$t_{2\max}$ 284.25	0.47	$t_{2\min}$ 98.90	
$t_{2\min}$ 150.63		$t_{2\max}$ 299.30	0.51
$t_{2\max}$ 286.66	0.50	$t_{2\min}$ 145.72	
$t_{2\min}$ 142.95		$t_{2\max}$ 231.86	0.38
$t_{2\max}$ 278.66	0.38	$t_{2\min}$ 143.87	
$t_{2\min}$ 173.38		$t_{2\max}$ 265.61	0.43
$t_{2\max}$ 280.12	0.44	$t_{2\min}$ 150.42	
$t_{2\min}$ 157.10		$t_{2\max}$ 237.89	0.33
$t_{2\max}$ 240.25	0.48	$t_{2\min}$ 159.01	
$t_{2\min}$ 124.53		$t_{2\max}$ 294.12	0.52
$t_{2\max}$ 312.19	0.39	$t_{2\min}$ 142.48	
$t_{2\min}$ 189.12		$t_{2\max}$ 230.76	0.25
$t_{2\max}$ 240.06	0.44	$t_{2\min}$ 174.20	
$t_{2\min}$ 134.27		$t_{2\max}$ 270.02	0.38
$t_{2\max}$ 251.70	0.37	$t_{2\min}$ 166.20	
$t_{2\min}$ 158.66		$t_{2\max}$ 302.00	0.51
$t_{2\max}$ 309.87	0.54	$t_{2\min}$ 147.59	
$t_{2\min}$ 141.92		$t_{2\max}$ 298.55	0.45
$t_{2\max}$ 299.24	0.43	$t_{2\min}$ 164.03	
$t_{2\min}$ 169.60		$t_{2\max}$ 260.98	0.42
$t_{2\max}$ 298.26	0.48	$t_{2\min}$ 150.40	

t <sub>2</sub> max	251.42	
t <sub>2</sub> min	134.81	0.46
t <sub>2</sub> max	262.69	
t <sub>2</sub> min	139.74	0.47
t <sub>2</sub> max	253.81	
t <sub>2</sub> min	168.90	0.33
t <sub>2</sub> max	262.84	
t <sub>2</sub> min	166.55	0.37
t <sub>2</sub> max	302.80	
t <sub>2</sub> min	160.22	0.47
t <sub>2</sub> max	237.03	
t <sub>2</sub> min	191.78	0.19
t <sub>2</sub> max	270.71	
t <sub>2</sub> min	148.89	0.45
t <sub>2</sub> max	302.62	
t <sub>2</sub> min	155.14	0.49
t <sub>2</sub> max	278.80	
t <sub>2</sub> min	163.39	0.41
t <sub>2</sub> max	308.17	
t <sub>2</sub> min	156.48	0.49
t <sub>2</sub> max	232.49	
t <sub>2</sub> min	162.64	0.30
t <sub>2</sub> max	266.57	
t <sub>2</sub> min	146.08	0.45
t <sub>2</sub> max	251.38	
t <sub>2</sub> min	148.73	0.41
t <sub>2</sub> max	264.01	
t <sub>2</sub> min	131.61	0.50
t <sub>2</sub> max	291.95	
t <sub>2</sub> min	139.11	0.52
t <sub>2</sub> max	241.00	
t <sub>2</sub> min	150.40	0.38
t <sub>2</sub> max	252.01	
t <sub>2</sub> min	154.38	0.39
t <sub>2</sub> max	240.40	
t <sub>2</sub> min	173.93	0.28
t <sub>2</sub> max	237.69	
t <sub>2</sub> min	194.16	0.18
t <sub>2</sub> max	227.42	
t <sub>2</sub> min	199.46	0.12
t <sub>2</sub> max	231.16	
t <sub>2</sub> min	146.42	0.37

30 m/min, CVD (MRS)		
Tooth thickness [µm]	G	
t <sub>2</sub> max	265.87	
t <sub>2</sub> min	153.18	0.42
t <sub>2</sub> max	259.94	
t <sub>2</sub> min	174.98	0.33
t <sub>2</sub> max	292.47	
t <sub>2</sub> min	176.14	0.40
t <sub>2</sub> max	251.49	
t <sub>2</sub> min	146.70	0.42
t <sub>2</sub> max	213.75	
t <sub>2</sub> min	189.36	0.11
t <sub>2</sub> max	226.02	0.54

75 m/min, CVD (SI)		
Tooth thickness [µm]	G	
t <sub>2</sub> max	308.17	
t <sub>2</sub> min	142.45	0.54
t <sub>2</sub> max	263.47	
t <sub>2</sub> min	176.62	0.33
t <sub>2</sub> max	239.77	
t <sub>2</sub> min	196.95	0.18
t <sub>2</sub> max	272.15	
t <sub>2</sub> min	125.95	0.54
t <sub>2</sub> max	274.40	
t <sub>2</sub> min	155.70	0.43
t <sub>2</sub> max	252.86	
t <sub>2</sub> min	181.92	0.28
t <sub>2</sub> max	245.57	
t <sub>2</sub> min	188.54	0.23
t <sub>2</sub> max	267.77	
t <sub>2</sub> min	126.88	0.49
t <sub>2</sub> max	273.01	
t <sub>2</sub> min	154.52	0.43
t <sub>2</sub> max	229.53	
t <sub>2</sub> min	163.45	0.29
t <sub>2</sub> max	237.02	
t <sub>2</sub> min	111.65	0.53
t <sub>2</sub> max	235.31	
t <sub>2</sub> min	126.01	0.46
t <sub>2</sub> max	219.63	
t <sub>2</sub> min	147.53	0.33
t <sub>2</sub> max	247.85	
t <sub>2</sub> min	119.72	0.52

t <sub>2</sub> min	156.05	
t <sub>2</sub> max	293.39	0.42
t <sub>2</sub> min	171.10	
t <sub>2</sub> max	285.10	0.49
t <sub>2</sub> min	144.16	
t <sub>2</sub> max	278.69	0.47
t <sub>2</sub> min	147.04	
t <sub>2</sub> max	271.40	0.51
t <sub>2</sub> min	132.93	
t <sub>2</sub> max	281.29	0.36
t <sub>2</sub> min	180.14	
t <sub>2</sub> max	297.78	0.45
t <sub>2</sub> min	164.28	
t <sub>2</sub> max	308.21	0.52
t <sub>2</sub> min	148.48	
t <sub>2</sub> max	261.13	0.39
t <sub>2</sub> min	159.85	
t <sub>2</sub> max	322.10	0.55
t <sub>2</sub> min	143.47	
t <sub>2</sub> max	211.81	0.24
t <sub>2</sub> min	160.06	
t <sub>2</sub> max	274.02	0.36
t <sub>2</sub> min	176.67	
t <sub>2</sub> max	251.21	0.27
t <sub>2</sub> min	182.94	
t <sub>2</sub> max	204.09	0.24
t <sub>2</sub> min	154.82	
t <sub>2</sub> max	288.21	0.50
t <sub>2</sub> min	143.86	
t <sub>2</sub> max	281.98	0.52
t <sub>2</sub> min	134.64	
t <sub>2</sub> max	289.70	0.49
t <sub>2</sub> min	146.87	
t <sub>2</sub> max	291.71	0.51
t <sub>2</sub> min	142.36	
t <sub>2</sub> max	280.61	0.50
t <sub>2</sub> min	140.63	
t <sub>2</sub> max	249.95	0.43
t <sub>2</sub> min	141.25	
t <sub>2</sub> max	279.40	0.49
t <sub>2</sub> min	141.88	
t <sub>2</sub> max	269.42	0.45
t <sub>2</sub> min	148.05	
t <sub>2</sub> max	316.86	0.59
t <sub>2</sub> min	129.45	
t <sub>2</sub> max	286.06	0.49
t <sub>2</sub> min	146.20	
t <sub>2</sub> max	297.52	0.52
t <sub>2</sub> min	143.11	
t <sub>2</sub> max	282.76	0.39
t <sub>2</sub> min	172.37	
t <sub>2</sub> max	340.20	0.63
t <sub>2</sub> min	125.49	
t <sub>2</sub> max	247.47	0.31
t <sub>2</sub> min	170.89	
t <sub>2</sub> max	326.44	0.60
t <sub>2</sub> min	130.81	
t <sub>2</sub> max	274.31	0.37
t <sub>2</sub> min	173.96	

t <sub>2</sub> max	321.99	0.53
t <sub>2</sub> min	150.09	
t <sub>2</sub> max	273.75	0.42
t <sub>2</sub> min	157.41	
t <sub>2</sub> max	298.59	0.48
t <sub>2</sub> min	155.84	
t <sub>2</sub> max	280.09	0.44
t <sub>2</sub> min	156.09	
t <sub>2</sub> max	297.91	0.51
t <sub>2</sub> min	145.10	
t <sub>2</sub> max	261.67	0.42
t <sub>2</sub> min	151.48	
t <sub>2</sub> max	296.55	0.49
t <sub>2</sub> min	150.95	
t <sub>2</sub> max	247.25	0.36
t <sub>2</sub> min	159.36	
t <sub>2</sub> max	290.05	0.45
t <sub>2</sub> min	158.95	
t <sub>2</sub> max	255.39	0.40
t <sub>2</sub> min	152.37	
t <sub>2</sub> max	253.08	0.34
t <sub>2</sub> min	167.99	
t <sub>2</sub> max	302.30	0.52
t <sub>2</sub> min	144.35	
t <sub>2</sub> max	266.51	0.44
t <sub>2</sub> min	149.83	
t <sub>2</sub> max	268.72	0.43
t <sub>2</sub> min	153.99	
t <sub>2</sub> max	273.53	0.52
t <sub>2</sub> min	130.83	
t <sub>2</sub> max	254.73	0.31
t <sub>2</sub> min	175.70	
t <sub>2</sub> max	291.83	0.45
t <sub>2</sub> min	160.04	
t <sub>2</sub> max	257.10	0.32
t <sub>2</sub> min	174.83	
t <sub>2</sub> max	235.20	0.37
t <sub>2</sub> min	147.44	

75 m/min, CVD (MRS)		
	Tooth thickness [µm]	G
t <sub>2</sub> max	265.42	0.51
t <sub>2</sub> min	128.94	
t <sub>2</sub> max	260.53	0.52
t <sub>2</sub> min	125.13	
t <sub>2</sub> max	296.45	0.57
t <sub>2</sub> min	128.50	
t <sub>2</sub> max	254.52	0.35
t <sub>2</sub> min	165.43	
t <sub>2</sub> max	291.23	0.52
t <sub>2</sub> min	139.16	
t <sub>2</sub> max	284.67	0.52
t <sub>2</sub> min	138.05	
t <sub>2</sub> max	261.06	0.50
t <sub>2</sub> min	130.56	
t <sub>2</sub> max	249.97	0.41
t <sub>2</sub> min	146.44	

t <sub>2</sub> max	252.95	0.48
t <sub>2</sub> min	132.06	
t <sub>2</sub> max	287.27	0.49
t <sub>2</sub> min	147.44	
t <sub>2</sub> max	272.47	0.51
t <sub>2</sub> min	133.53	
t <sub>2</sub> max	273.32	0.53
t <sub>2</sub> min	128.52	
t <sub>2</sub> max	276.43	0.52
t <sub>2</sub> min	132.47	
t <sub>2</sub> max	276.94	0.46
t <sub>2</sub> min	148.67	
t <sub>2</sub> max	274.12	0.47
t <sub>2</sub> min	144.69	
t <sub>2</sub> max	283.01	0.44
t <sub>2</sub> min	158.63	
t <sub>2</sub> max	285.76	0.48
t <sub>2</sub> min	149.38	
t <sub>2</sub> max	293.20	0.48
t <sub>2</sub> min	152.05	
t <sub>2</sub> max	303.24	0.42
t <sub>2</sub> min	174.83	
t <sub>2</sub> max	293.43	0.49
t <sub>2</sub> min	148.91	
t <sub>2</sub> max	289.19	0.46
t <sub>2</sub> min	156.19	
t <sub>2</sub> max	294.65	0.52
t <sub>2</sub> min	142.48	
t <sub>2</sub> max	304.20	0.46
t <sub>2</sub> min	164.58	
t <sub>2</sub> max	278.55	0.52
t <sub>2</sub> min	132.69	
t <sub>2</sub> max	283.18	0.48
t <sub>2</sub> min	145.92	
t <sub>2</sub> max	284.12	0.52
t <sub>2</sub> min	136.97	
t <sub>2</sub> max	279.84	0.55
t <sub>2</sub> min	124.71	
t <sub>2</sub> max	252.67	0.51
t <sub>2</sub> min	123.75	
t <sub>2</sub> max	258.64	0.45
t <sub>2</sub> min	140.97	
t <sub>2</sub> max	289.94	0.50
t <sub>2</sub> min	144.85	
t <sub>2</sub> max	260.00	0.44
t <sub>2</sub> min	145.76	
t <sub>2</sub> max	269.11	0.49
t <sub>2</sub> min	137.34	
t <sub>2</sub> max	285.63	0.43
t <sub>2</sub> min	163.71	
t <sub>2</sub> max	292.10	0.50
t <sub>2</sub> min	147.21	
t <sub>2</sub> max	282.21	0.37
t <sub>2</sub> min	177.89	
t <sub>2</sub> max	280.34	0.48
t <sub>2</sub> min	147.02	
t <sub>2</sub> max	273.09	0.39
t <sub>2</sub> min	165.75	
t <sub>2</sub> max	277.70	0.51

t <sub>2</sub> min	135.45	
t <sub>2</sub> max	274.90	0.46
t <sub>2</sub> min	147.70	
t <sub>2</sub> max	280.12	0.44
t <sub>2</sub> min	155.72	
t <sub>2</sub> max	278.51	0.43
t <sub>2</sub> min	160.12	
t <sub>2</sub> max	276.46	0.42
t <sub>2</sub> min	161.19	
t <sub>2</sub> max	265.87	0.45
t <sub>2</sub> min	147.06	
t <sub>2</sub> max	286.85	0.53
t <sub>2</sub> min	135.88	
t <sub>2</sub> max	264.80	0.41
t <sub>2</sub> min	155.38	
t <sub>2</sub> max	278.70	0.48
t <sub>2</sub> min	145.70	
t <sub>2</sub> max	264.23	0.52
t <sub>2</sub> min	128.04	
t <sub>2</sub> max	308.07	0.54
t <sub>2</sub> min	142.14	
t <sub>2</sub> max	271.33	0.48
t <sub>2</sub> min	140.55	
t <sub>2</sub> max	299.95	0.55
t <sub>2</sub> min	134.38	
t <sub>2</sub> max	277.87	0.46
t <sub>2</sub> min	149.83	
t <sub>2</sub> max	318.69	0.55
t <sub>2</sub> min	144.70	

t <sub>2</sub> min	120.56	
t <sub>2</sub> max	276.41	0.48
t <sub>2</sub> min	144.28	
t <sub>2</sub> max	233.03	0.42
t <sub>2</sub> min	134.67	
t <sub>2</sub> max	290.66	0.54
t <sub>2</sub> min	133.38	
t <sub>2</sub> max	262.09	0.52
t <sub>2</sub> min	125.80	
t <sub>2</sub> max	277.39	0.53
t <sub>2</sub> min	131.20	
t <sub>2</sub> max	300.21	0.62
t <sub>2</sub> min	114.05	
t <sub>2</sub> max	255.54	0.50
t <sub>2</sub> min	127.54	
t <sub>2</sub> max	258.59	0.38
t <sub>2</sub> min	159.17	
t <sub>2</sub> max	326.42	0.63
t <sub>2</sub> min	122.35	
t <sub>2</sub> max	255.91	0.54
t <sub>2</sub> min	118.53	
t <sub>2</sub> max	252.48	0.61
t <sub>2</sub> min	98.31	
t <sub>2</sub> max	288.50	0.58
t <sub>2</sub> min	122.50	
t <sub>2</sub> max	266.48	0.44
t <sub>2</sub> min	148.97	
t <sub>2</sub> max	267.27	0.42
t <sub>2</sub> min	154.37	
t <sub>2</sub> max	276.97	0.58
t <sub>2</sub> min	115.97	
t <sub>2</sub> max	253.41	0.50
t <sub>2</sub> min	126.67	
t <sub>2</sub> max	237.29	0.43
t <sub>2</sub> min	134.45	
t <sub>2</sub> max	268.90	0.55
t <sub>2</sub> min	120.28	
t <sub>2</sub> max	252.03	0.46
t <sub>2</sub> min	135.34	
t <sub>2</sub> max	275.58	0.58
t <sub>2</sub> min	116.31	
t <sub>2</sub> max	238.91	0.49
t <sub>2</sub> min	122.50	
t <sub>2</sub> max	225.13	0.38
t <sub>2</sub> min	139.25	
t <sub>2</sub> max	267.19	0.51
t <sub>2</sub> min	131.26	
t <sub>2</sub> max	273.74	0.55
t <sub>2</sub> min	122.16	
t <sub>2</sub> max	257.27	0.40
t <sub>2</sub> min	154.96	
t <sub>2</sub> max	250.22	0.42
t <sub>2</sub> min	146.24	
t <sub>2</sub> max	281.15	0.50
t <sub>2</sub> min	141.62	
t <sub>2</sub> max	271.83	0.49
t <sub>2</sub> min	138.73	
t <sub>2</sub> max	263.19	0.55
t <sub>2</sub> min	117.41	

t <sub>2</sub> max	260.33	0.42
t <sub>2</sub> min	151.35	
t <sub>2</sub> max	221.37	0.34
t <sub>2</sub> min	145.02	
t <sub>2</sub> max	288.71	0.49
t <sub>2</sub> min	148.68	
t <sub>2</sub> max	293.51	0.60
t <sub>2</sub> min	118.10	
t <sub>2</sub> max	227.76	0.40
t <sub>2</sub> min	137.20	
t <sub>2</sub> max	234.09	0.40
t <sub>2</sub> min	140.05	

75 m/min, U (MRS)		
Tooth thickness [µm]	G	
t <sub>2</sub> max	267.77	0.44
t <sub>2</sub> min	151.29	
t <sub>2</sub> max	278.04	0.51
t <sub>2</sub> min	135.67	
t <sub>2</sub> max	267.06	0.61
t <sub>2</sub> min	102.97	
t <sub>2</sub> max	269.87	0.45
t <sub>2</sub> min	148.92	
t <sub>2</sub> max	261.07	0.39
t <sub>2</sub> min	159.35	
t <sub>2</sub> max	280.31	0.71
t <sub>2</sub> min	80.63	
t <sub>2</sub> max	298.35	0.49
t <sub>2</sub> min	151.75	
t <sub>2</sub> max	265.23	0.46
t <sub>2</sub> min	143.20	
t <sub>2</sub> max	285.39	0.56
t <sub>2</sub> min	126.12	
t <sub>2</sub> max	249.02	0.48
t <sub>2</sub> min	129.42	
t <sub>2</sub> max	270.18	0.52
t <sub>2</sub> min	131.02	
t <sub>2</sub> max	261.06	0.47
t <sub>2</sub> min	137.15	
t <sub>2</sub> max	270.22	0.41
t <sub>2</sub> min	158.62	
t <sub>2</sub> max	265.08	0.51
t <sub>2</sub> min	131.05	
t <sub>2</sub> max	275.87	0.49
t <sub>2</sub> min	141.03	
t <sub>2</sub> max	288.07	0.55
t <sub>2</sub> min	128.49	
t <sub>2</sub> max	266.57	0.56
t <sub>2</sub> min	116.99	
t <sub>2</sub> max	240.04	0.50
t <sub>2</sub> min	119.10	
t <sub>2</sub> max	292.22	0.53
t <sub>2</sub> min	137.31	
t <sub>2</sub> max	249.59	0.35
t <sub>2</sub> min	162.81	
t <sub>2</sub> max	267.54	0.48

t <sub>2</sub> min	140.05
t <sub>2</sub> max	254.79
t <sub>2</sub> min	140.67
t <sub>2</sub> max	283.25
t <sub>2</sub> min	163.64
t <sub>2</sub> max	295.83
t <sub>2</sub> min	167.12
t <sub>2</sub> max	259.00
t <sub>2</sub> min	155.62
t <sub>2</sub> max	293.16
t <sub>2</sub> min	139.88
t <sub>2</sub> max	260.42
t <sub>2</sub> min	128.71
t <sub>2</sub> max	268.52
t <sub>2</sub> min	147.53
t <sub>2</sub> max	274.21
t <sub>2</sub> min	116.34
t <sub>2</sub> max	292.92
t <sub>2</sub> min	121.67
t <sub>2</sub> max	258.97
t <sub>2</sub> min	135.81
t <sub>2</sub> max	283.08
t <sub>2</sub> min	161.30
t <sub>2</sub> max	326.02
t <sub>2</sub> min	110.33
t <sub>2</sub> max	249.72
t <sub>2</sub> min	170.53
t <sub>2</sub> max	318.92
t <sub>2</sub> min	139.56
t <sub>2</sub> max	237.11
t <sub>2</sub> min	195.03
t <sub>2</sub> max	278.25
t <sub>2</sub> min	187.94
t <sub>2</sub> max	296.22
t <sub>2</sub> min	137.08
t <sub>2</sub> max	263.90
t <sub>2</sub> min	146.72
t <sub>2</sub> max	273.02
t <sub>2</sub> min	165.22
t <sub>2</sub> max	279.07
t <sub>2</sub> min	166.07
t <sub>2</sub> max	305.24
t <sub>2</sub> min	145.56
t <sub>2</sub> max	302.63
t <sub>2</sub> min	142.36
t <sub>2</sub> max	280.12
t <sub>2</sub> min	142.40
t <sub>2</sub> max	264.88
t <sub>2</sub> min	160.84
t <sub>2</sub> max	291.69
t <sub>2</sub> min	150.29
t <sub>2</sub> max	284.08
t <sub>2</sub> min	139.62
t <sub>2</sub> max	271.55
t <sub>2</sub> min	134.26
t <sub>2</sub> max	255.89
t <sub>2</sub> min	135.39
t <sub>2</sub> max	292.55

t <sub>2</sub> min	154.05
t <sub>2</sub> max	292.10
t <sub>2</sub> min	149.76
t <sub>2</sub> max	291.33
t <sub>2</sub> min	131.86
t <sub>2</sub> max	286.01
t <sub>2</sub> min	147.71
t <sub>2</sub> max	280.52
t <sub>2</sub> min	157.54
t <sub>2</sub> max	304.42
t <sub>2</sub> min	155.74

t <sub>2</sub> max	211.58
t <sub>2</sub> min	144.38
t <sub>2</sub> max	301.05
t <sub>2</sub> min	133.73
t <sub>2</sub> max	274.78
t <sub>2</sub> min	133.01
t <sub>2</sub> max	282.50
t <sub>2</sub> min	145.01
t <sub>2</sub> max	305.47
t <sub>2</sub> min	126.22
t <sub>2</sub> max	292.92
t <sub>2</sub> min	128.94
t <sub>2</sub> max	242.13
t <sub>2</sub> min	138.09
t <sub>2</sub> max	217.95
t <sub>2</sub> min	140.51
t <sub>2</sub> max	288.54
t <sub>2</sub> min	134.04
t <sub>2</sub> max	254.47
t <sub>2</sub> min	125.22
t <sub>2</sub> max	226.75
t <sub>2</sub> min	144.96
t <sub>2</sub> max	291.12
t <sub>2</sub> min	149.39
t <sub>2</sub> max	273.70
t <sub>2</sub> min	136.14
t <sub>2</sub> max	262.92
t <sub>2</sub> min	146.96
t <sub>2</sub> max	253.33
t <sub>2</sub> min	159.74
t <sub>2</sub> max	283.63
t <sub>2</sub> min	138.61
t <sub>2</sub> max	294.55
t <sub>2</sub> min	123.20
t <sub>2</sub> max	297.23
t <sub>2</sub> min	151.04
t <sub>2</sub> max	237.88
t <sub>2</sub> min	150.65
t <sub>2</sub> max	273.73
t <sub>2</sub> min	128.52
t <sub>2</sub> max	255.39
t <sub>2</sub> min	135.41
t <sub>2</sub> max	302.58
t <sub>2</sub> min	140.04
t <sub>2</sub> max	283.73
t <sub>2</sub> min	128.70
t <sub>2</sub> max	241.32
t <sub>2</sub> min	126.22
t <sub>2</sub> max	248.69
t <sub>2</sub> min	120.46
t <sub>2</sub> max	223.24
t <sub>2</sub> min	134.33
t <sub>2</sub> max	249.10
t <sub>2</sub> min	150.35
t <sub>2</sub> max	264.89
t <sub>2</sub> min	148.11
t <sub>2</sub> max	273.75
t <sub>2</sub> min	126.43

90 m/min, U (SI)		
Tooth thickness [μm]	G	
t <sub>2</sub> max	284.63	0.54
t <sub>2</sub> min	131.59	
t <sub>2</sub> max	278.76	0.54
t <sub>2</sub> min	127.97	
t <sub>2</sub> max	269.57	0.54
t <sub>2</sub> min	123.51	
t <sub>2</sub> max	292.29	0.49
t <sub>2</sub> min	150.07	
t <sub>2</sub> max	266.21	0.54
t <sub>2</sub> min	121.86	
t <sub>2</sub> max	305.13	0.56
t <sub>2</sub> min	134.40	
t <sub>2</sub> max	284.36	0.58
t <sub>2</sub> min	118.96	
t <sub>2</sub> max	272.54	0.49
t <sub>2</sub> min	139.39	
t <sub>2</sub> max	245.76	0.40
t <sub>2</sub> min	147.10	
t <sub>2</sub> max	250.18	0.51
t <sub>2</sub> min	123.31	
t <sub>2</sub> max	280.02	0.49
t <sub>2</sub> min	142.14	
t <sub>2</sub> max	252.68	0.48
t <sub>2</sub> min	131.59	
t <sub>2</sub> max	302.80	0.58
t <sub>2</sub> min	127.67	
t <sub>2</sub> max	230.97	0.43
t <sub>2</sub> min	130.72	
t <sub>2</sub> max	237.53	0.43
t <sub>2</sub> min	134.73	
t <sub>2</sub> max	238.85	0.42
t <sub>2</sub> min	138.47	
t <sub>2</sub> max	273.80	0.53
t <sub>2</sub> min	128.93	
t <sub>2</sub> max	267.09	0.49
t <sub>2</sub> min	136.00	
t <sub>2</sub> max	271.85	0.50
t <sub>2</sub> min	135.45	
t <sub>2</sub> max	281.50	0.54
t <sub>2</sub> min	128.70	
t <sub>2</sub> max	288.41	0.48
t <sub>2</sub> min	150.22	

90 m/min, U (MRS)		
Tooth thickness [µm]		G
t <sub>2</sub> max	271.11	0.50
t <sub>2</sub> min	135.31	
t <sub>2</sub> max	276.66	0.56
t <sub>2</sub> min	121.83	
t <sub>2</sub> max	240.84	0.39
t <sub>2</sub> min	147.52	
t <sub>2</sub> max	289.79	0.49
t <sub>2</sub> min	147.34	
t <sub>2</sub> max	307.06	0.54
t <sub>2</sub> min	140.46	
t <sub>2</sub> max	285.04	0.53
t <sub>2</sub> min	134.07	
t <sub>2</sub> max	295.29	0.53
t <sub>2</sub> min	140.04	
t <sub>2</sub> max	273.95	0.52
t <sub>2</sub> min	130.22	
t <sub>2</sub> max	252.89	0.35
t <sub>2</sub> min	165.51	
t <sub>2</sub> max	256.34	0.42
t <sub>2</sub> min	148.56	
t <sub>2</sub> max	266.93	0.38
t <sub>2</sub> min	166.26	
t <sub>2</sub> max	225.98	0.25
t <sub>2</sub> min	168.95	
t <sub>2</sub> max	271.62	0.37
t <sub>2</sub> min	170.22	
t <sub>2</sub> max	299.41	0.56
t <sub>2</sub> min	131.45	
t <sub>2</sub> max	284.82	0.51
t <sub>2</sub> min	140.63	
t <sub>2</sub> max	264.58	0.46
t <sub>2</sub> min	142.11	
t <sub>2</sub> max	283.32	0.49

t <sub>2</sub> min	145.01	
t <sub>2</sub> max	271.90	0.38
t <sub>2</sub> min	168.57	
t <sub>2</sub> max	302.95	0.50
t <sub>2</sub> min	152.81	
t <sub>2</sub> max	268.08	0.41
t <sub>2</sub> min	159.43	
t <sub>2</sub> max	259.20	0.43
t <sub>2</sub> min	146.82	
t <sub>2</sub> max	217.61	0.30
t <sub>2</sub> min	151.74	
t <sub>2</sub> max	246.55	0.35
t <sub>2</sub> min	160.57	
t <sub>2</sub> max	260.50	0.43
t <sub>2</sub> min	148.54	
t <sub>2</sub> max	299.52	0.53
t <sub>2</sub> min	139.44	
t <sub>2</sub> max	285.94	0.45
t <sub>2</sub> min	157.61	
t <sub>2</sub> max	246.19	0.48
t <sub>2</sub> min	128.47	
t <sub>2</sub> max	271.90	0.46
t <sub>2</sub> min	146.27	
t <sub>2</sub> max	282.73	0.50
t <sub>2</sub> min	140.09	
t <sub>2</sub> max	276.13	0.46
t <sub>2</sub> min	148.48	
t <sub>2</sub> max	288.84	0.48
t <sub>2</sub> min	151.06	
t <sub>2</sub> max	281.03	0.44
t <sub>2</sub> min	157.71	
t <sub>2</sub> max	295.78	0.54
t <sub>2</sub> min	137.11	
t <sub>2</sub> max	260.35	0.42
t <sub>2</sub> min	151.74	
t <sub>2</sub> max	250.47	0.33
t <sub>2</sub> min	166.86	
t <sub>2</sub> max	286.56	0.54
t <sub>2</sub> min	133.15	
t <sub>2</sub> max	290.63	0.44
t <sub>2</sub> min	161.90	
t <sub>2</sub> max	293.35	0.50
t <sub>2</sub> min	146.87	
t <sub>2</sub> max	290.47	0.44
t <sub>2</sub> min	162.10	
t <sub>2</sub> max	284.63	0.52
t <sub>2</sub> min	135.38	
t <sub>2</sub> max	232.25	0.30
t <sub>2</sub> min	163.73	
t <sub>2</sub> max	250.08	0.25
t <sub>2</sub> min	188.09	
t <sub>2</sub> max	252.09	0.43
t <sub>2</sub> min	143.40	
t <sub>2</sub> max	283.83	0.56
t <sub>2</sub> min	123.75	
t <sub>2</sub> max	266.90	0.45
t <sub>2</sub> min	146.60	
t <sub>2</sub> max	281.72	0.51
t <sub>2</sub> min	139.04	
t <sub>2</sub> max	274.90	0.49
t <sub>2</sub> min	141.16	
t <sub>2</sub> max	264.41	0.45
t <sub>2</sub> min	144.97	
t <sub>2</sub> max	279.91	0.49
t <sub>2</sub> min	143.02	
t <sub>2</sub> max	288.95	0.47
t <sub>2</sub> min	152.72	
t <sub>2</sub> max	283.54	0.51
t <sub>2</sub> min	140.22	

### APPENDIX E3 – CHIP GEOMETRY MEASUREMENTS ( $p_{sb}$ , $\delta_{sb}$ , $\rho_{seg}$ )

Tables E7–9 contains raw data of shear band projection ( $p_{sb}$ ), shear band width ( $\delta_{sb}$ ) and bulge angle ( $\rho_{seg}$ ) measurements. Values in bold are averages and outliers are highlighted in red.

**Table E7.** Shear band projection measurements.

Shear band projection ( $p_{sb}$ ) [ $\mu\text{m}$ ]								
Coated with CVD				Uncoated				
$30 \text{ m/min}$ <i>SI</i>	$30 \text{ m/min}$ <i>MRS</i>	$75 \text{ m/min}$ <i>SI</i>	$75 \text{ m/min}$ <i>MRS</i>	$75 \text{ m/min}$ <i>SI</i>	$75 \text{ m/min}$ <i>MRS</i>	$90 \text{ m/min}$ <i>SI</i>	$90 \text{ m/min}$ <i>MRS</i>	
198.32	160.48	209.44	179.23	188.94	168.62	205.29	167.59	
138.58	250.09	183.61	176.10	232.84	303.50	169.52	212.68	
198.24	214.02	157.78	188.76	205.99	156.03	229.98	235.07	
<b>65.37</b>	144.99	165.53	192.97	211.02	167.24	237.05	270.52	
175.69	173.75	188.65	181.25	187.78	216.91	207.09	211.56	
<b>177.71</b>	<b>188.67</b>	<b>181.00</b>	<b>183.66</b>	<b>205.31</b>	<b>202.46</b>	<b>209.79</b>	<b>219.48</b>	

**Table E8.** Shear band width measurements.

Shear band width ( $\delta_{sb}$ ) [ $\mu\text{m}$ ]								
Coated with CVD				Uncoated				
$30 \text{ m/min}$ <i>SI</i>	$30 \text{ m/min}$ <i>MRS</i>	$75 \text{ m/min}$ <i>SI</i>	$75 \text{ m/min}$ <i>MRS</i>	$75 \text{ m/min}$ <i>SI</i>	$75 \text{ m/min}$ <i>MRS</i>	$90 \text{ m/min}$ <i>SI</i>	$90 \text{ m/min}$ <i>MRS</i>	
17.53	17.03	13.70	13.83	16.63	13.12	24.48	18.99	
21.64	23.45	11.63	17.09	21.30	22.01	14.94	14.92	
18.01	14.19	18.31	19.72	20.82	15.51	25.76	15.44	
28.59	14.01	13.03	18.05	12.74	15.62	25.84	18.78	
17.10	13.53	14.32	11.82	12.23	21.18	19.82	17.13	
<b>18.57</b>	<b>16.44</b>	<b>14.20</b>	<b>16.10</b>	<b>16.74</b>	<b>17.49</b>	<b>22.17</b>	<b>17.05</b>	

**Table E9.** Bulge angle measurements.

Bulge angle ( $\rho_{seg}$ ) [°]								
Coated with CVD				Uncoated				
$30 \text{ m/min}$ <i>SI</i>	$30 \text{ m/min}$ <i>MRS</i>	$75 \text{ m/min}$ <i>SI</i>	$75 \text{ m/min}$ <i>MRS</i>	$75 \text{ m/min}$ <i>SI</i>	$75 \text{ m/min}$ <i>MRS</i>	$90 \text{ m/min}$ <i>SI</i>	$90 \text{ m/min}$ <i>MRS</i>	
29.94	27.16	23.38	22.25	17.84	22.93	27.50	25.68	
19.93	26.40	16.90	32.64	22.59	18.62	18.50	17.32	
<b>45.21</b>	26.56	20.47	27.24	26.09	24.63	24.25	16.14	
19.01	36.08	20.82	30.87	31.69	25.61	27.00	19.56	
21.69	33.79	21.19	15.61	28.28	22.09	25.10	16.08	
<b>22.64</b>	<b>30.00</b>	<b>20.55</b>	<b>25.72</b>	<b>25.30</b>	<b>22.78</b>	<b>24.47</b>	<b>18.96</b>	

## APPENDIX F1 – DIFFERENCES BETWEEN COLLECTED CHIPS

Mean shear band spacing ( $d_c$ ), segment spacing ( $p_c$ ), segmentation angle ( $\phi_{seg}$ ), and degree of segmentation ( $G$ ) after raw data were separated between the two collected chips from each tests are illustrated in Fig. F1. MRSs are red and SIs are blue. LOM images are presented in figures F2–9.

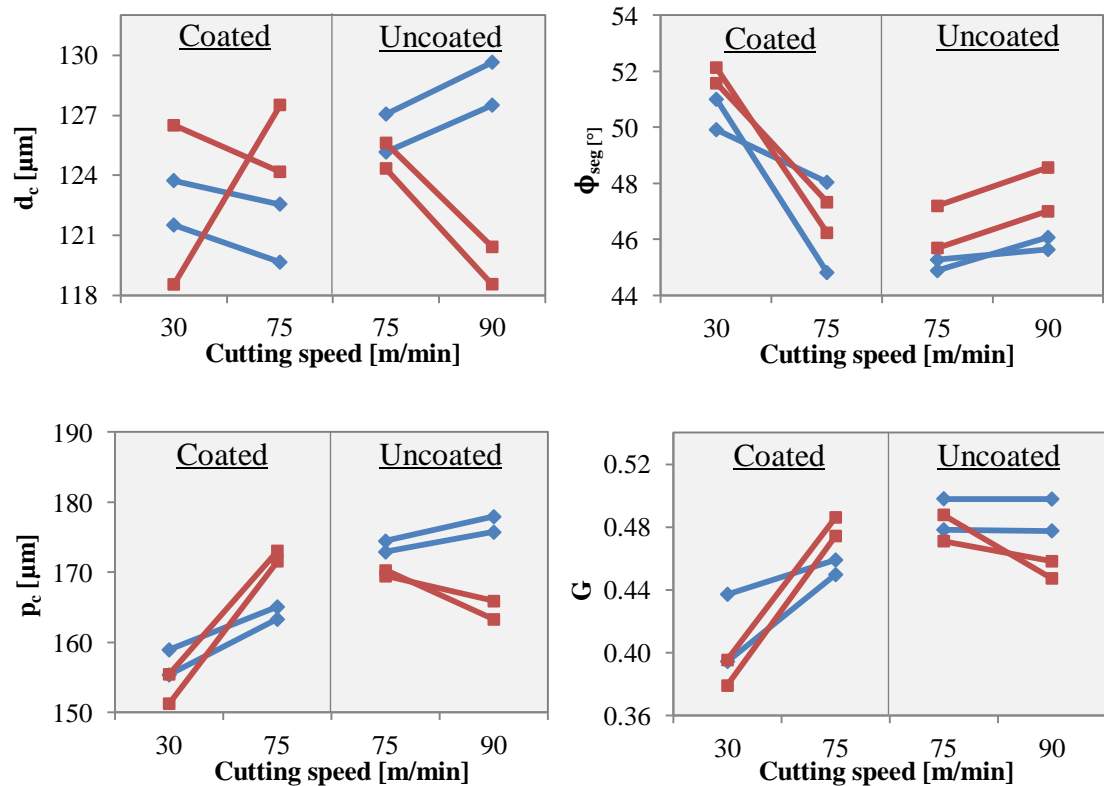


**Figure F1.** Differences between the two collected chips for respective test sample, for  $d_c$ ,  $p_c$ ,  $\phi_{seg}$  and  $G$ .

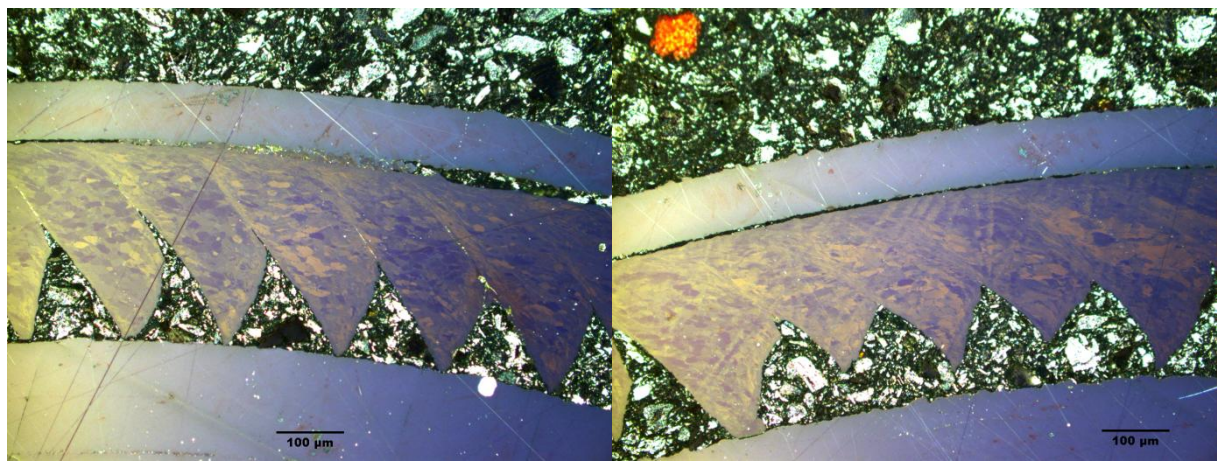


**Figure F2.** LOM images of different chips from CVD (SI) at 30 m/min cutting speed.

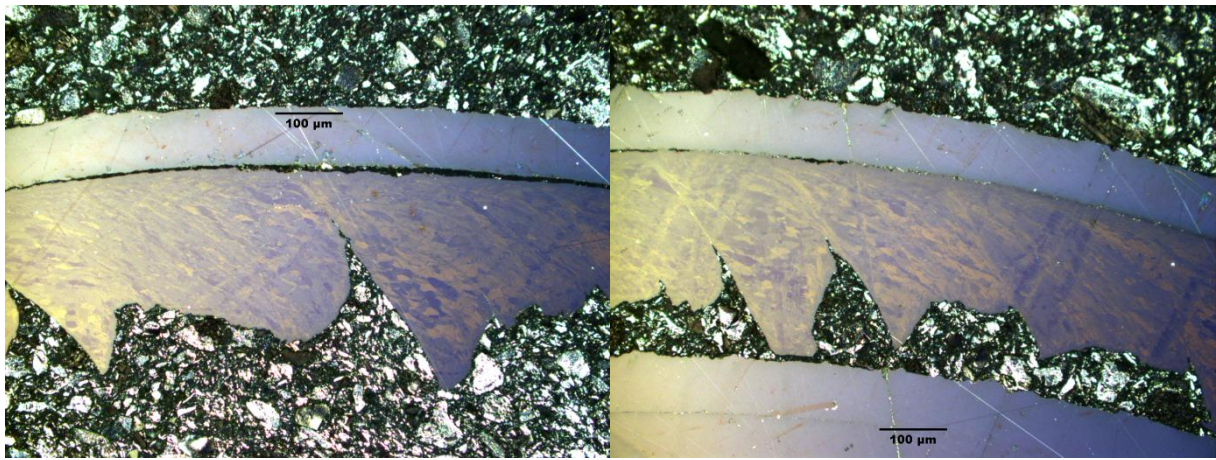


**Figure F3.** LOM images of different chips from CVD (MRS) at 30 m/min cutting speed.

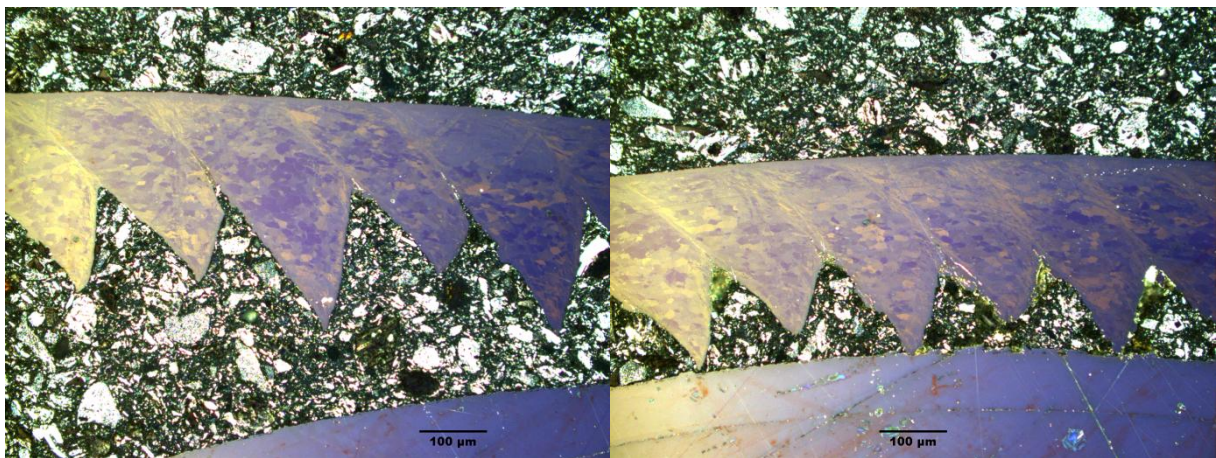


**Figure F4.** LOM images of different chips from CVD (SI) at 75 m/min cutting speed.

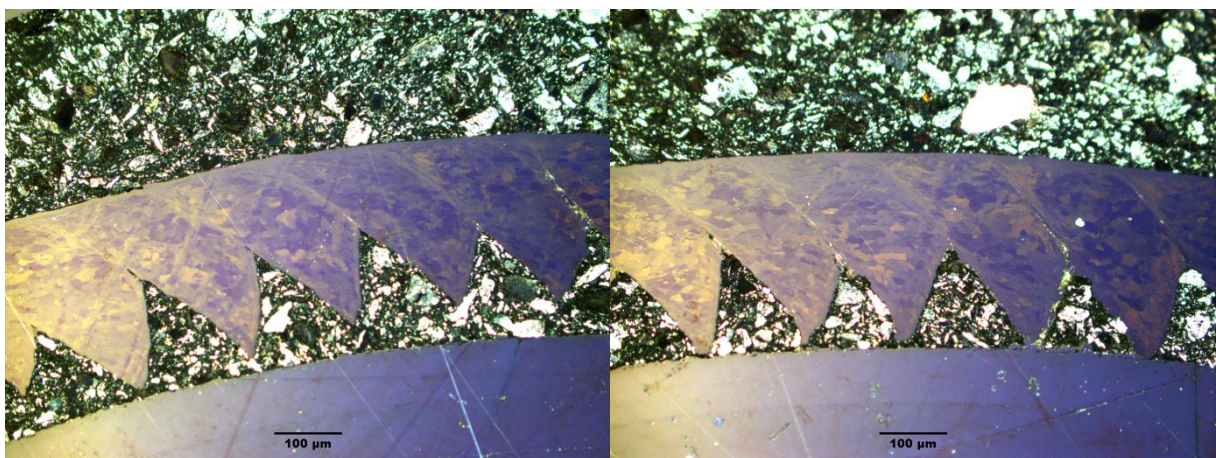


**Figure F5.** LOM images of different chips from CVD (MRS) at 75 m/min cutting speed.

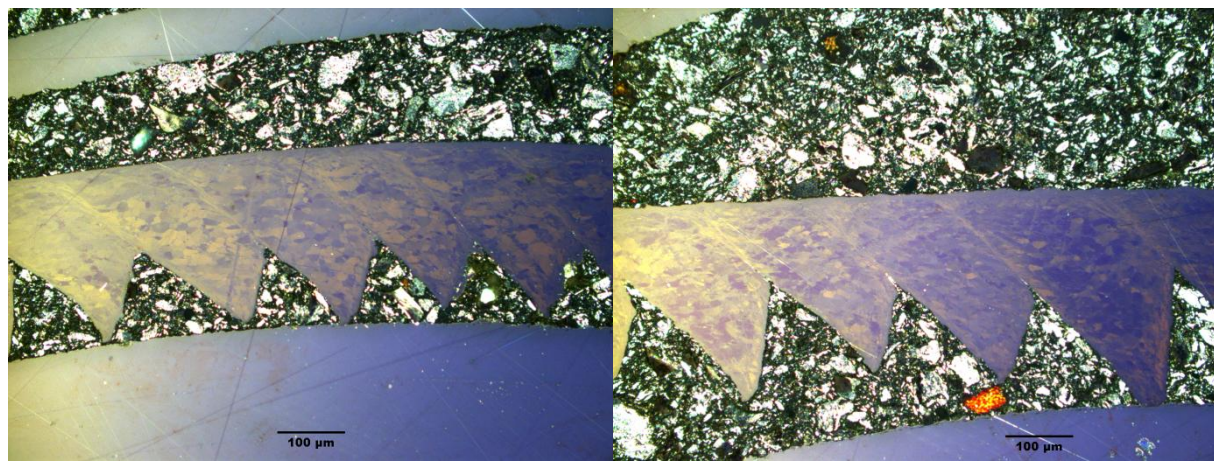


**Figure F6.** LOM images of different chips from U (SI) at 75 m/min cutting speed.

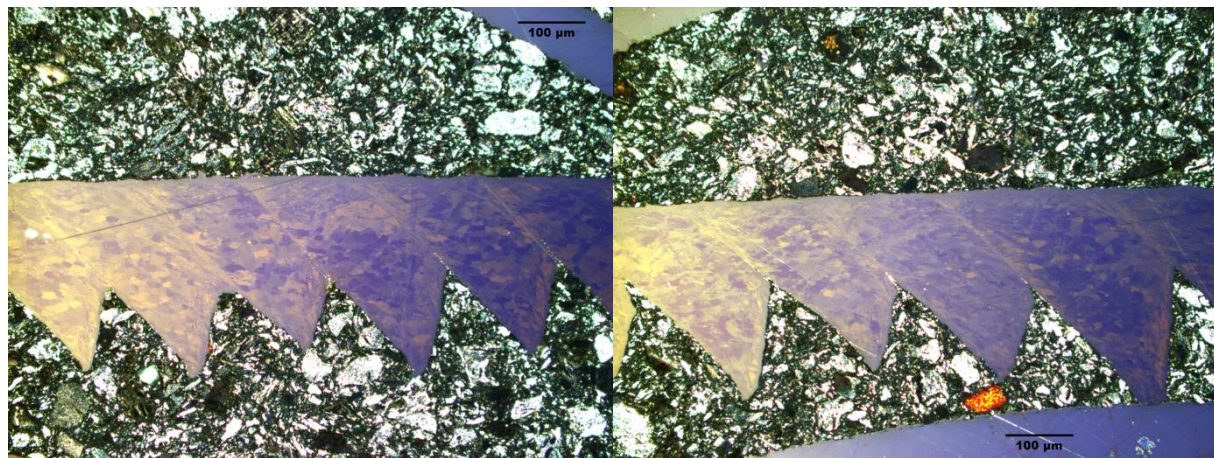


**Figure F7.** LOM images of different chips from U (MRS) at 75 m/min cutting speed.

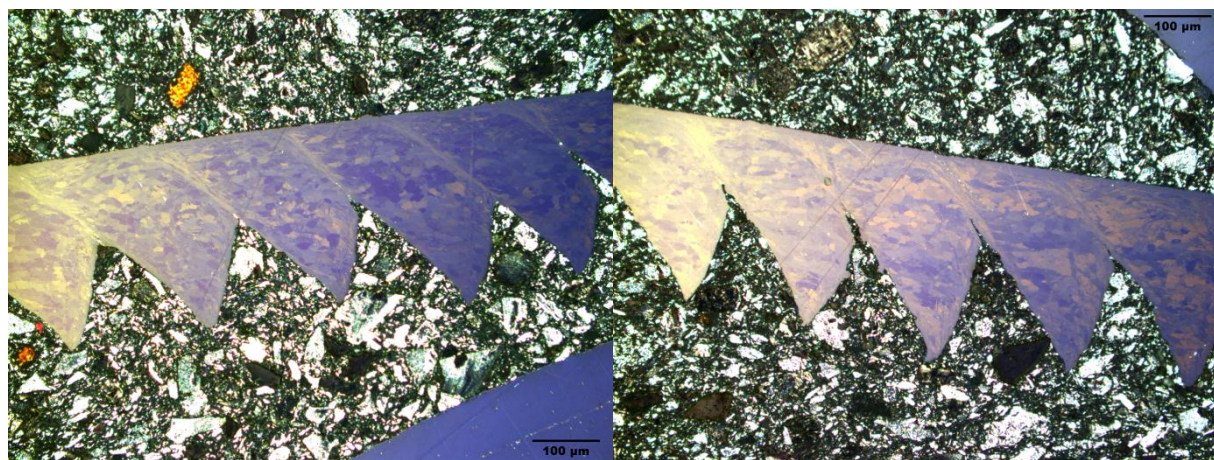


**Figure F8.** LOM images of different chips from U (SI) at 90 m/min cutting speed.

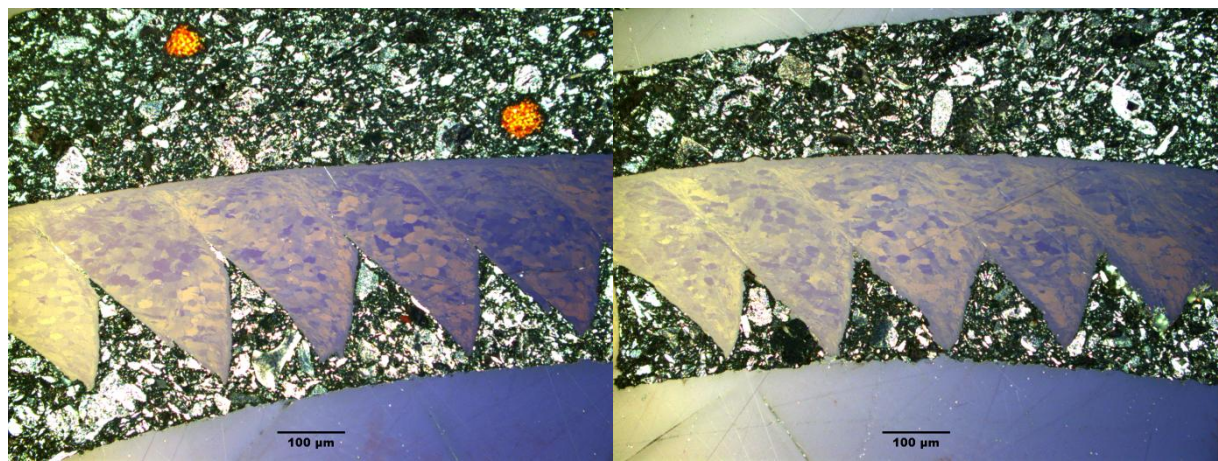


**Figure F9.** LOM images of different chips from U (MRS) at 90 m/min cutting speed.

## APPENDIX F2 – SEM IMAGES OF COLLECTED CHIPS

Figures F10–13 presents SEM images of cutting speeds between 30–90 m/min.

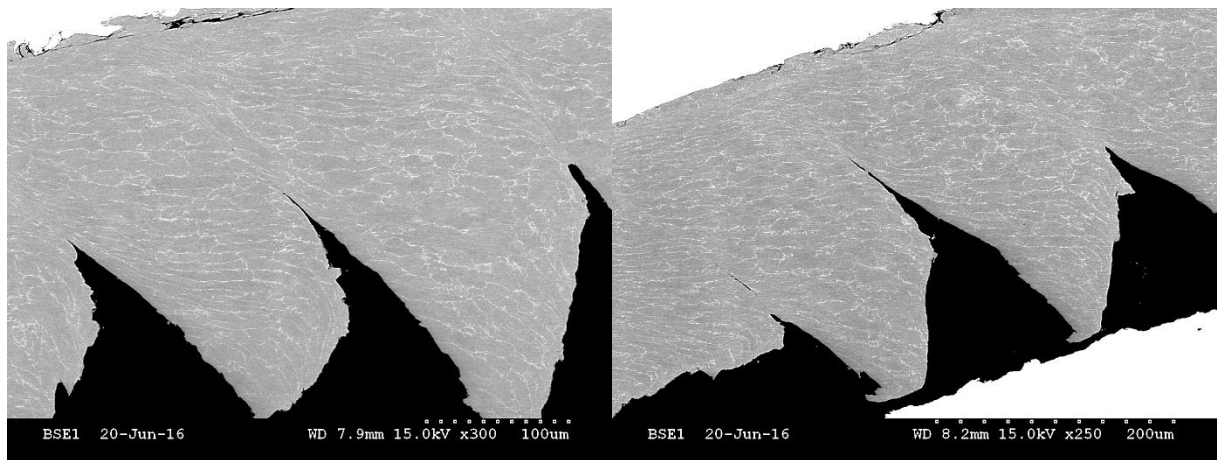


**Figure F10.** SEM images of chips of CVD (SI) to the left and CVD (MRS) to the right at 30 m/min.

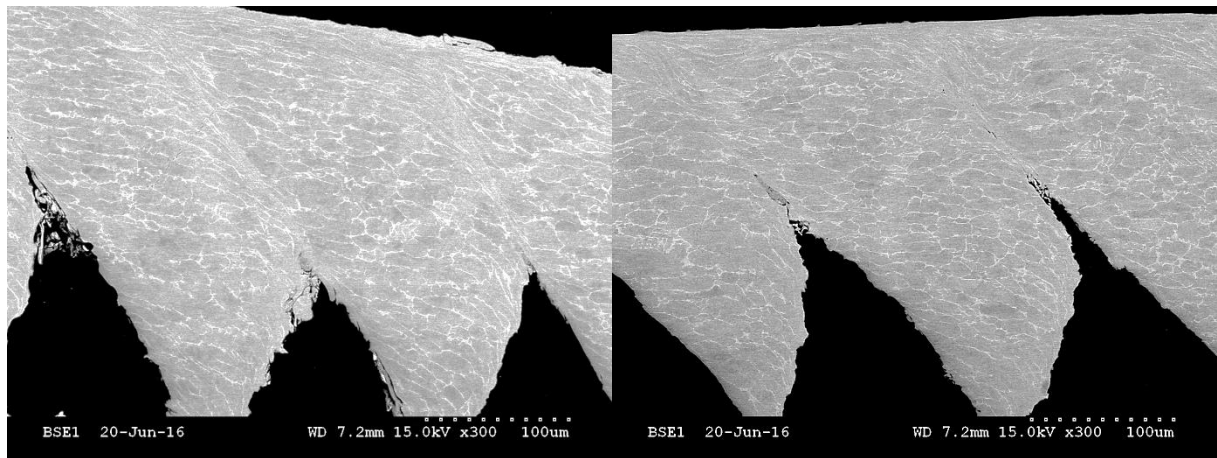


**Figure F11.** SEM images of chips of CVD (SI) to the left and CVD (MRS) to the right at 75 m/min.

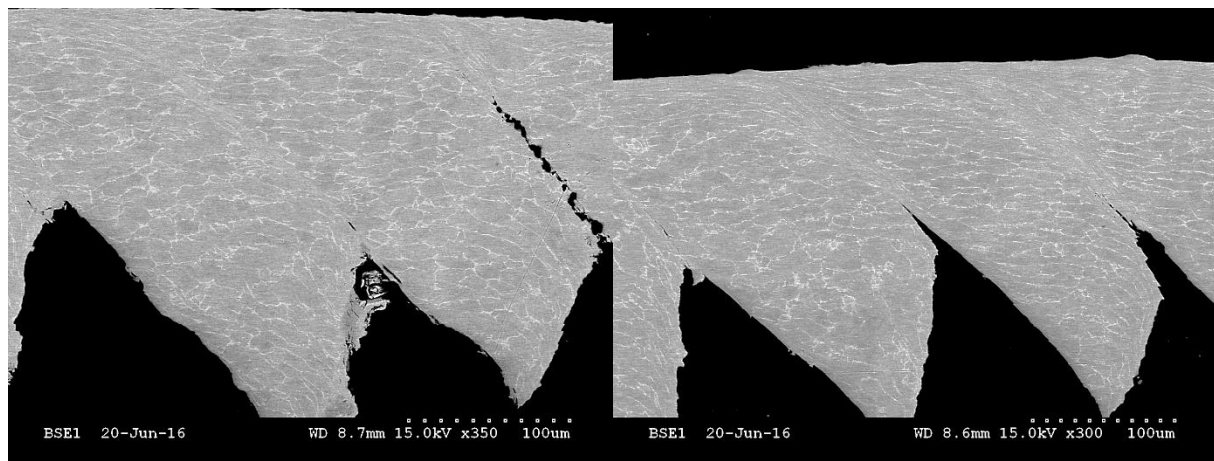


**Figure F12.** SEM images of chips of U (SI) to the left and U (MRS) to the right at 75 m/min.

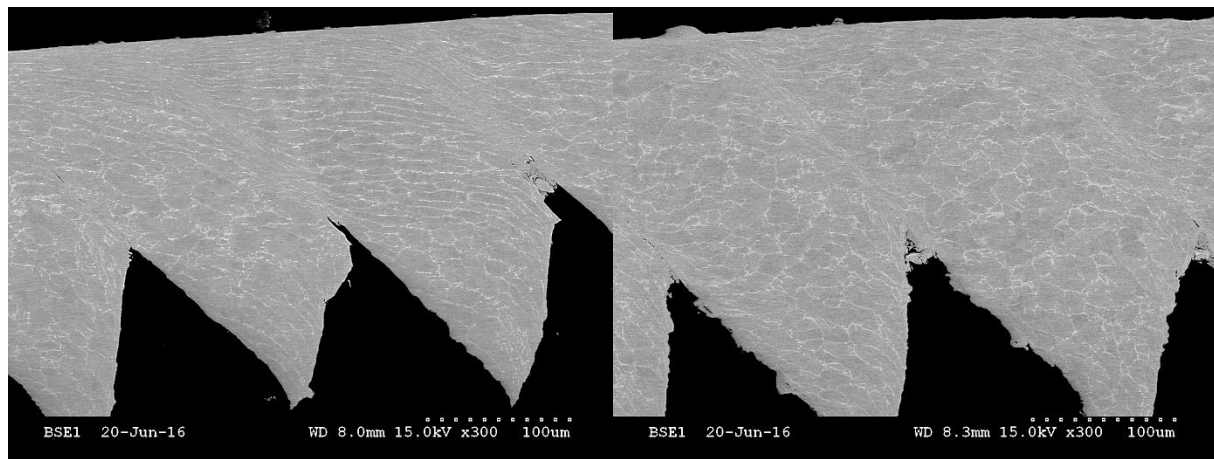


**Figure F13.** SEM images of chips of U (SI) to the left and U (MRS) to the right at 90 m/min.

## APPENDIX G1 – CALCULATIONS REGARDING CROSS-SECTIONS

Figure G1 is a schematic illustration of the rake face crater.  $x$  notifies how far into the crater the cross-section is present and how much of the crater that was grinded away.  $h$  responds the difference between the cross-section and reference point,  $h_0$  represents the difference between the starting point of L (length of crater) and reference point, and  $h_{max}$  corresponds to the difference between the ending point of L and reference point.  $r_\varepsilon$  denotes the nose radius, and a and b are variables. Equations 23–24 were used to calculate where on the crater the cross-section is located. Height measurements are found in tables G1–2.

$$h_0 = r_\varepsilon - \sqrt{r_\varepsilon^2 + r_\varepsilon^2}$$

\* sin 15°

*Eq. Fel! Bokmärket är inte definierat.*

$$x = \frac{h - h_0}{\sin 60^\circ} \quad \text{Eq. Fel! Bokmärket är inte definierat.}$$

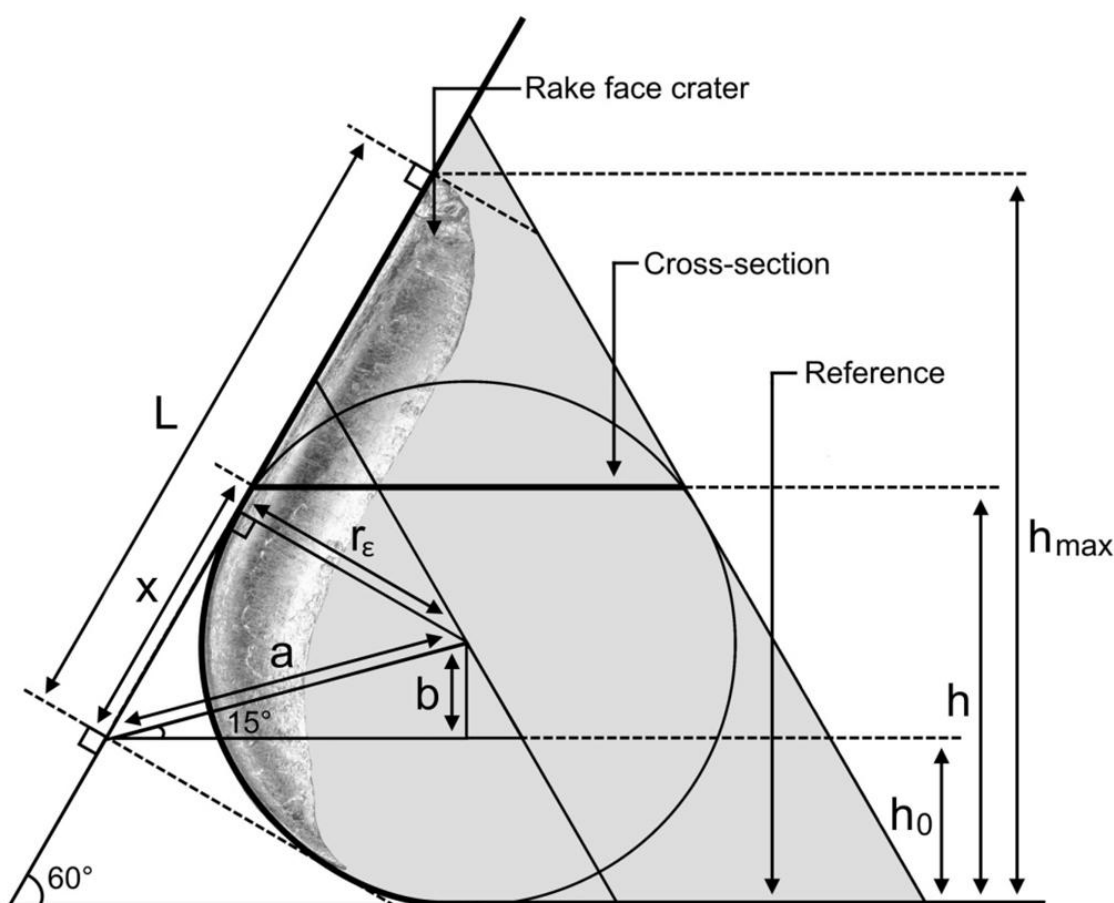


**Figure G1.** Schematic illustration of the rake face crater.  $x$  = length of removed crater.  $h$  = difference between cross-section and reference point,  $h_0$  = difference between starting point of L

and reference point, and  $h_{\max}$  = difference between ending point of L and reference point.  $r_e$  = nose radius.

**Table G1.** Height measurement of insert pellets.

Pellet			Height measurement of pellets					
Cutting speed [m/min]	Coating	Grade	Time of cut [s]	Reference [mm]	Cross section [mm]	Grinded away (h) [mm]	± From mean value [mm]	Grinded away from crater (x) [mm]
30	CVD	SI	60	14.7555	13.407	1.35	0.08	<b>0.97</b>
	CVD	MRS	60					
75	CVD	SI	3	16.0835	14.6565	1.43	0.16	<b>1.06</b>
	CVD	MRS	3					
75	-	SI	60	14.4115	13.311	1.10	0.16	<b>0.69</b>
	-	MRS	60					
90	-	SI	40	16.098	14.9245	1.17	0.09	<b>0.77</b>
	-	MRS	40					
115	-	SI	3	14.8515	13.6775	1.17	0.09	<b>0.77</b>
	-	MRS	3					
115	-	SI	40	14.4215	13.063	1.36	0.09	<b>0.98</b>
	-	MRS	20					

**Table G2.** Height measurement of chip pellets.

Pellet			Height measurement of pellets			
Cutting speed [m/min]	Coating	Grade	Reference [mm]	Cross section [mm]	Grinded away from chips [mm]	± From mean value [mm]
30	CVD	SI	16.028	14.461	<b>1.57</b>	0.39
	CVD	MRS				
75	CVD	SI	16.164	15.191	<b>0.97</b>	0.21
	CVD	MRS				
75	-	SI	16.197	15.027	<b>1.17</b>	0.01
	-	MRS				
90	-	SI	15.446	14.435	<b>1.01</b>	0.17
	-	MRS				

## APPENDIX G2 – ANALYSIS OF VARIATION AND CHIP STATISTICS

F-tests, T-tests and ANOVAs are presented in tables G3–7. Measurements with asterisk (\*) are significant values. The distribution of data for  $d_c$ ,  $p_c$ ,  $\phi_{seg}$  and  $G$ ; one standard deviation from mean, and error bars are max and min values are presented in Fig. G2.

**Table G3.** F-tests of measured geometrical parameters and calculated shears.

	30 m/min			75 m/min		
	F	F crit.	p	F	F crit.	p
$d_c$	4,583*	1.542	0.000	1,799*	1.558	0.015
$p$	4,829*	1.542	0.000	2,086*	1.569	0.004
$\phi_{seg}$	2.147	1.559	0.002	2,988*	1.571	0.000
$t_2$	2,073*	1.555	0.003	1.127	1.569	0.332
$G$	1.449	1.555	0.084	3,411*	1.569	0.000
$\delta_{sb}$	2.806	6.388	0.171	1.645	6.388	0.321
$p_{sb}$	1.700	6.388	0.310	8,468*	6.388	0.031
$\rho_{seg}$	5.732	6.388	0.060	8,747*	6.388	0.029
$\gamma_c$	1.782	6.388	0.295	1.087	6.388	0.469
$\gamma_{seg}$	1.210	6.388	0.429	9,676*	6.388	0.025
$\gamma_{sb}$	1.832	6.388	0.286	1.128	6.388	0.455

**Table G4.** F-tests of measured geometrical parameters and calculated shears.

	75 m/min			90 m/min		
	F	F crit.	p	F	F crit.	p
$d_c$	1.049	1.580	0.430	1.100	1.589	0.368
$p$	1.212	1.610	0.253	1.118	1.604	0.349
$\phi_{seg}$	1.121	1.586	0.340	1.207	1.604	0.256
$t_2$	1.299	1.605	0.181	1,684*	1.602	0.035
$G$	1.390	1.605	0.126	1.377	1.604	0.132
$\delta_{sb}$	1.218	6.388	0.427	6,440*	6.388	0.049
$p_{sb}$	10,947*	6.388	0.020	2.017	6.388	0.257
$\rho_{seg}$	3.883	6.388	0.109	1.249	6.388	0.417
$\gamma_c$	5.521	6.388	0.063	2.351	6.388	0.214
$\gamma_{seg}$	3.794	6.388	0.112	1.649	6.388	0.320
$\gamma_{sb}$	5.766	6.388	0.059	2.393	6.388	0.209

**Table G5.** t-tests of measured geometrical parameters and calculated shears.

	30 m/min			75 m/min		
	t	t crit.	p	t	t crit.	p
$d_c$	-0.566	1.993	0.573	-1.653	1.981	0.101
$p$	-0.479	1.993	0.633	-2,224*	1.982	0.028
$\phi_{seg}$	1.905	1.990	0.060	-0.602	1.984	0.549
$t_2$	0.370	1.989	0.712	1.279	1.981	0.203
$G$	-1.364	1.982	0.175	-1,988*	1.985	0.050
$\delta_{sb}$	1.416	2.306	0.194	1.044	2.306	0.327
$p_{sb}$	-1.062	2.306	0.319	-0.277	2.571	0.793
$\rho_{seg}$	-0.534	2.306	0.608	1.586	2.571	0.174
$\gamma_c$	-1.866	2.306	0.099	0.846	2.306	0.422
$\gamma_{seg}$	-1.354	2.306	0.213	1.436	2.571	0.211
$\gamma_{sb}$	-1.883	2.306	0.096	0.829	2.306	0.431

**Table G6.** t-tests of measured geometrical parameters and calculated shears.

	75 m/min			90 m/min		
	t	t crit.	p	t	t crit.	p
$d_c$	0.318	1.983	0.751	-2,927*	1.984	0.004
$p$	-1.099	1.984	0.274	-2,967*	1.984	0.004
$\phi_{seg}$	-2,623*	1.983	0.010	3,249*	1.984	0.002
$t_2$	5,547*	1.983	0.000	-3,919*	1.986	0.000
$G$	-0.551	1.984	0.583	-2,429*	1.984	0.017
$\delta_{sb}$	-0.287	2.306	0.782	2.249	2.571	0.074
$p_{sb}$	-0.100	2.571	0.924	0.472	2.306	0.650
$\rho_{seg}$	0.943	2.306	0.373	-2.288	2.306	0.051
$\gamma_c$	-0.392	2.306	0.705	2,601*	2.306	0.032
$\gamma_{seg}$	0.625	2.306	0.550	-2.135	2.306	0.065
$\gamma_{sb}$	0.871	2.306	0.409	2,605*	2.306	0.031

**Table G7.** ANOVAs of measured geometrical parameters and calculated shears.

	F	F crit.	p
$d_c$	0.966	2.030	0.456
$p_c$	4,670*	2.031	0.000
$\phi_{seg}$	28,221*	2.031	0.000
$t_2$	10,335*	2.031	0.000
$G$	9,606*	2.031	0.000
$\delta_{sb}$	2.127	2.313	0.069
$p_{sb}$	1.427	2.313	0.229
$\rho_{seg}$	1.950	2.313	0.094
$\gamma_c$	2.155	2.313	0.066
$\gamma_{seg}$	4,717*	2.313	0.001
$\gamma_{sb}$	2.090	2.313	0.074

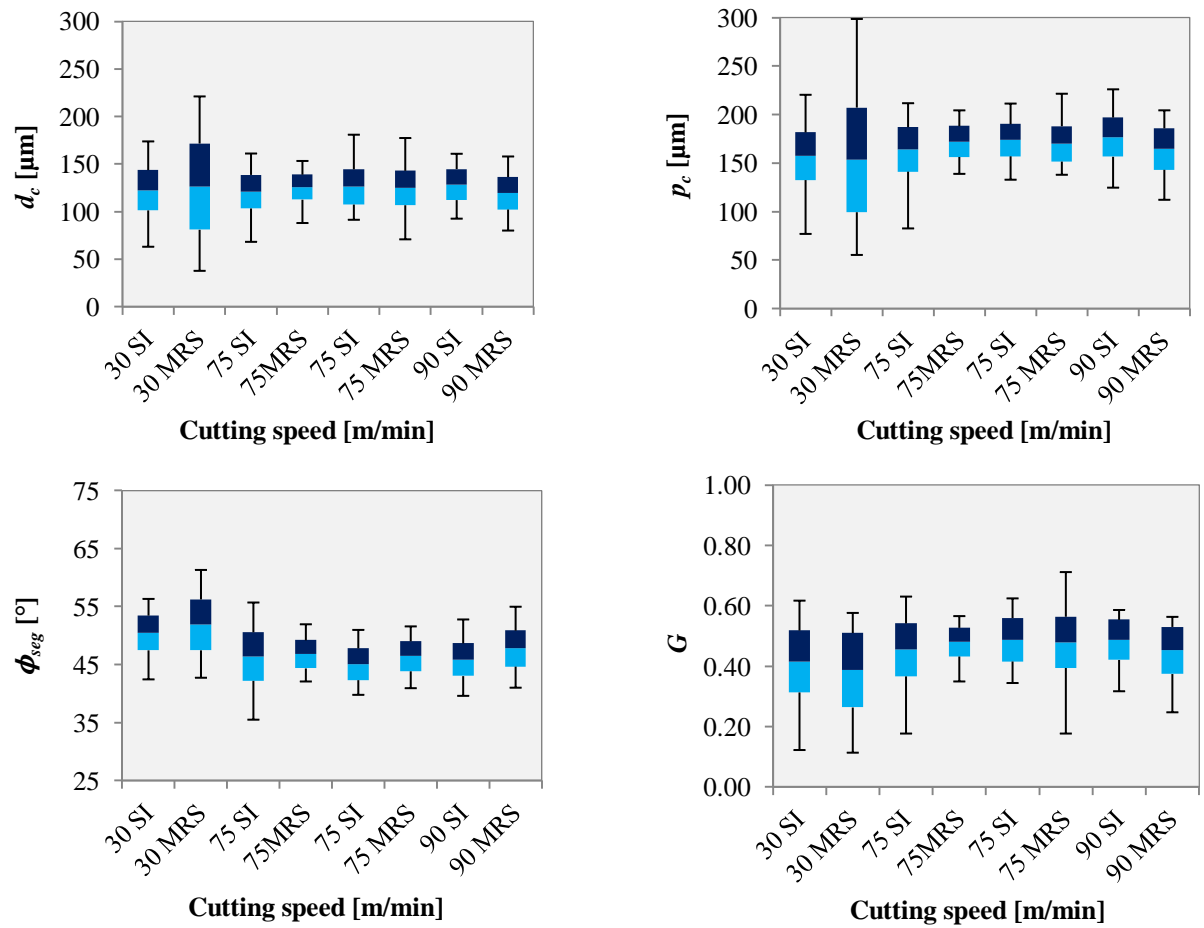


**Figure G2.** Distribution of data for  $d_{ch}$ ,  $p_c$ ,  $\phi_{seg}$  and  $G$ .

### APPENDIX G3 – CALUCULATION OF THE SHEAR ANGLE

Calculation of the shear angle ( $\phi$ ).

$$\frac{t_1}{\bar{t}_2} = \frac{\sin(\phi)}{\cos(\phi - \gamma)} \Rightarrow \left| x = \frac{t_1}{\bar{t}_2} \right| \Rightarrow x = \frac{\sin(\phi)}{\cos(\phi - \gamma)}$$

$$\Rightarrow x = \frac{\sin(\phi)}{\sin(\gamma) \sin(\phi) + \cos(\gamma) \cos(\phi)}$$

$$x(\sin(\gamma) \sin(\phi) + \cos(\gamma) \cos(\phi)) = \sin(\phi)$$

$$\Rightarrow x \sin(\gamma) \sin(\phi) + x \cos(\gamma) \cos(\phi) = \sin(\phi)$$

$$\Rightarrow |\alpha = x \sin(\gamma), \beta = x \cos(\gamma)|$$

$$\Rightarrow \sin(\phi) = \alpha \sin(\phi) + \beta \cos(\phi)$$

$$\Rightarrow \beta \cos(\phi) = \sin(\phi) - \alpha \sin(\phi)$$

$$\Rightarrow \beta \cos(\phi) = \sin(\phi)(1 - \alpha)$$

$$\Rightarrow \frac{\sin(\phi)}{\cos(\phi)} = \frac{\beta}{1 - \alpha} \Rightarrow \tan(\phi) = \frac{\beta}{1 - \alpha}$$

$$\Rightarrow \tan(\phi) = \frac{x \cos(\gamma)}{1 - x \sin(\gamma)} = \frac{\left(\frac{t_1}{\bar{t}_2}\right) \cos(\gamma)}{1 - \left(\frac{t_1}{\bar{t}_2}\right) \sin(\gamma)}$$

$$\Rightarrow \phi = \tan^{-1} \left( \frac{\left(\frac{t_1}{\bar{t}_2}\right) \cos(\gamma)}{1 - \left(\frac{t_1}{\bar{t}_2}\right) \sin(\gamma)} \right) \quad Eq. 20$$

## APPENDIX H – EDS ANALYSIS

Raw data from EDS analysis. Elemental composition of titanium, aluminum and vanadium are presented in Table H1. Respective EDS spectra are illustrated in Fig. H1.

**Table H1.** Results in atomic percent from EDS analysis of the back side of the chips.

Spectrum	In stats.	Al	Ti	V
30 SW (SI)	Yes	11.99	84.86	3.15
30 SW (MRS)	Yes	10.39	86.12	3.49
75 SW (SI)	Yes	12.44	84.06	3.50
75 SW (MRS)	Yes	10.26	86.10	3.64
75 U (SI)	Yes	10.72	85.79	3.49
75 U (MRS)	Yes	7.81	88.64	3.55
90 U (SI)	Yes	10.90	85.95	3.14
90 U (MRS)	Yes	11.53	85.06	3.41
Mean		10.76	85.82	3.42
Std. deviation		1.42	1.35	0.18
Max.		12.44	88.64	3.64
Min.		7.81	84.06	3.14
All results in atomic%				



**Figure H1.** EDS analysis of the back side of the chips eight chips at different cutting conditions.



